# Design of Lanthanide Coordination Compounds with Unusual Ligands and High Symmetry for Molecular Magnetism

Zur Erlangung des akademischen Grades eines

DOKTORS DER NATURWISSENSCHAFTEN

(Dr. rer. nat.)

von der KIT-Fakultät für Chemie und Biowissenschaften

des Karlsruher Instituts für Technologie (KIT)

genehmigte

DISSERTATION

von

Rouven Felix Pfleger, M.Sc.

1. Referentin: Prof. Dr. Annie K. Powell
2. Referentin: Prof. Dr. Karin Fink
Tag der mündlichen Prüfung: 14.04.2021

*For my dear husband Thiemo*

# ACKNOWLEDGEMENT

This thesis was carried out from January 2017 to March 2021 at the Institute for Inorganic Chemistry at Karlsruhe Institute of Technology under supervision of Prof. Dr. Annie K. Powell.

In this chapter I want to say thank you.

There were many people I worked together with in my time as a PhD student. There were also many people who supported me not only in terms of teaching me interesting things about chemistry but also helping me to be able to put so much effort in this thesis. This is why I need to structure this maybe a bit unusual. Please believe me that the order in which I want to say thank you cannot be correlated to who was more important or less. (Although I know how much you all like good correlations.)

Thank you, Karlsruhe.

Of course, you all come first to mind when I think about my thesis since I spent most of the time there working together with you. The Powell group became something like my work family which always is undeniable when somebody leaves for other positions.

Special thanks to you, Prof. Dr. Annie K. Powell, not only for being my "Doktormutter" as such spending a lot of time helping me and your other students to improve but also for supporting such a social and positive work environment. You gave me the chance to do my PhD with you and you helped me find my way in science.

Also, special thanks to you, Dr. Chris Anson, showing me a lot about crystallography and helping me translating my cryptic Denglisch to English that is suitable for a PhD thesis.

Thank you, my dear colleagues.

Thank you for the ones who welcomed me when I started in the Powell group who were Dr. Sebastian Habermann who taught me a lot about SMMs, Dr. Yan Peng who

also helped me with understanding this difficult topic but also Nadine, Martin and Irina who were always nice and positive and gave among others reasons for starting a PhD in the group.

Thank you to my dear colleagues who were working parallel with me on their PhD project. Thank you, Umaira Shuaib for the big help with setting up a measurement routine for cyclic voltammetry on lanthanide compounds. Thank you, Dr. Masooma Ibrahim, Dr. Krisana Pewasan and Dr. Marcel Merkel for the help when I had to measure something at INT. Special thanks also to Dr. Olaf Fuhr, Prof. Dieter Fenske and Dr. Andreas Eichhöfer for the big help with single crystal and powder X-ray measurements. Special thanks also to Thomas Ruppert helping me out with measuring powder patterns when I could not go to INT myself. And also special thanks to you, Jonas Braun, for the spectroelectro chemical measurements you did together with Dr. Claudia Bizzarri. Thank you for the administrative help, Gertraud Amschlinger. It is always good to know that you might have an answer how to manage things if I already lost every clue. Thank you, Dr. Markus Schroth for any help with any technique when I needed one. Thank you, Hagen, Blue and all the others in the group for supporting and having supported this positive environment.

Thank you, København.

With a special thank you to Prof. Jesper Bendix who supported me and inspired me a lot. Thank you for the great collaboration and for having me at your institute and your group.

The two stays in København were financed by the Karlsruhe House of Young Scientists (KHYS) (Die Auslandsaufenthalte wurden vom Karlsruhe House of Young Scientists (KHYS) gefördert.)

I also want to thank the people of the institute at Københavns Universitet who helped me with various measurements, especially Stergios Piligkos, Høgni Weihe, Niels Vissing Holst, Theis, Emil and Christian. But I also want to thank all the other people at the institute who welcomed me and treated me like I was always part of the group.

My biggest thanks I indeed saved. This to some extent because I cannot thank him enough. My beloved husband Thiemo Zehle. I am happy to have him. My work did not only have an influence on my life but also on his. I am happy that he took all this in the last four years. My honest thank you for helping me, especially for proofreading, and supporting me. I am lucky to have you!

# ABSTRACT

In the field of single molecule magnetism, big improvements on controlling relaxation phenomena have led to creating systems where high energy barriers are actually an obstacle to magnetisation reversal. Key here is to control the symmetry and lattice based processes such as spin-phonon coupling. In this thesis both these aspects are investigated.

Dysprosium ions which are most commonly used for lanthanide single molecule magnets were chosen in order to develop a testbed system. Such a testbed system is important because it allows the impact of seemingly small structural changes to be gaged. The system is always five-fold coordinated to 2,6-diacetylpyridinebis(2'-pyridylhydrazone) ($H_2$dapp) in the equatorial plane leaving axial sites available for coordination by secondary ligands such as $H_2O$, $Cl^-$, $NO_3^-$ and $OAc^-$. The first compound described is $[Dy(H_2dapp)(H_2O)_4]Cl_3$. For all compounds, the pentadentate ligand shows a helical distortion which can be quantified and is correlated to further factors. Expanding on this, the mononuclear units were coupled by fluoride or peroxide bridges which are rarely seen for lanthanide complexes. It is shown that the nature of the bridge can have positive or negative effects on the slow relaxation depending on the nature of the coupling.

In a second section, molecules with higher symmetry are investigated. The optimised synthesis for an isotopically enriched sample of a literature known pentagonal bipyramidal compound is presented which was used for investigations on the vibrational mode of the central dysprosium ion. It could be shown that the gadolinium derivative has single molecule magnet properties which is rare for gadolinium which usually has an isotropic magnetic ground state.

Finally, a case study on two new octahedral dysprosium compounds is presented to show the limits of low level calculations on lanthanide single ion complexes.

# ZUSAMMENFASSUNG

Auf dem Gebiet des Einzelmolekülmagnetismus haben große Fortschritte bei der Kontrolle von Relaxationsprozesse dazu geführt, dass Systeme erschaffen werden, in denen die hohen Energiebarrieren die eigentlichen Hindernisse der Magnetisierungsumkehr sind. Der Schlüssel hierbei ist es, die Symmetrie und die gitterabhängigen Prozesse wie Spin-Phonon-Kopplung zu kontrollieren. Diese Dissertation untersucht beide dieser Aspekte.

Dysprosium-Ionen, welche am meisten für Lanthanid-Einzelmolekülmagneten genutzt werden, wurden zur Entwicklung eines Modellsystems gewählt. Solch ein Modellsystem ist wichtig, da es ermöglicht, die Auswirkungen scheinbar kleiner struktureller Änderungen einzuschätzen. Das System ist immer fünffachgefaltet koordiniert an 2,6-Diacetylpyridinbis(2'-pyridylhydrazon) ($H_2$dapp) auf der äquatorialen Ebene, die axiale Punkte für die Koordination sekundärer Liganden wie $H_2O$, $Cl^-$, $NO_3^-$ und $OAc^-$ ermöglicht. Das erste beschriebene Molekül ist $[Dy(H_2dapp)(H_2O)_4]Cl_3$. Bei allen Molekülen zeigt der Pentadentatligand helikale Verzerrung, welche quantifiziert und zu anderen Faktoren korreliert werden kann. Hierauf aufbauend wurden die mononuklearen Einheiten mit Fluorid- und Peroxidbrücken gekoppelt, welche in Lanthanidkomplexen selten sind. Es wurde gezeigt, dass die Art der Verbrückung positive und negative Effekte auf die langsame Relaxation abhängig von der Art der Kopplung haben kann.

In einem zweiten Abschnitt wurden Moleküle mit großer Symmetrie untersucht. Der optimierte Syntheseweg für eine isotopisch angereicherte Probe einer literaturbekannten pentagonal-bipyramidalen Probe wurde vorgestellt. Diese Probe wurde für Untersuchungen der Schwingungsmodi der zentralen Dysprosium-Ionen genutzt. Es konnte gezeigt werden, dass das Gadolinium-Derivat Einzelmoleküleigenschaften besitzt, welche bei Gadolinium selten auftreten, die normalerweise einen isotropen magnetischen Grundzustand haben.

Zuletzt wurde eine Fallstudie mithilfe zweier oktaedrischer Dysprosium-Strukturen durchgeführt, um die Grenzen der Basisberechnungsmethoden von Lanthanid-Einzelion-Komplexen zu zeigen.

# EIDESSTATTLICHE ERKLÄRUNG

Eidesstattliche Versicherung gemäß § 13 Absatz 2 Ziffer 3 der Promotionsordnung des Karlsruher Instituts für Technologie für die KIT-Fakultät für Chemie und Biowissenschaften:

1. Bei der eingereichten Dissertation zu dem Thema Design of Lanthanide Coordination Compounds with Unusual Ligands and High Symmetry for Molecular Magnetism handelt es sich um meine eigenständig erbrachte Leistung.

2. Ich habe nur die angegebenen Quellen und Hilfsmittel benutzt und mich keiner unzulässigen Hilfe Dritter bedient. Insbesondere habe ich wörtlich oder sinngemäß aus anderen Werken übernommene Inhalte als solche kenntlich gemacht.

3. Die Arbeit oder Teile davon habe ich bislang nicht an einer Hochschule des In- oder Auslands als Bestandteil einer Prüfungs- oder Qualifikationsleistung vorgelegt.

4. Die Richtigkeit der vorstehenden Erklärungen bestätige ich.

5. Die Bedeutung der eidesstattlichen Versicherung und die strafrechtlichen Folgen einer unrichtigen oder unvollständigen eidesstattlichen Versicherung sind mir bekannt.

Ich versichere an Eides statt, dass ich nach bestem Wissen die reine Wahrheit erklärt und nichts verschwiegen habe.


Ort und Datum                                    Unterschrift

# INDEX

# LIST OF FIGURES

# LIST OF TABLES

# LIST OF ABBREVIATIONS

| | |
|---|---|
| Å | angstrom |
| AC | alternating current |
| bh | bottom half |
| BTPR | biaugmented trigonal prism |
| °C | degrees Celsius |
| CCU | capped relaxed cube |
| cm | centimetre(s) |
| Cp | cyclopentadien |
| CSAPR | spherical capped square antiprism |
| CSD | Cambridge Structural Database |
| CShM | continuous symmetry measurements |
| CV | cyclic voltammetry |
| 1D | one dimensional |
| 2D | two dimensional |
| DC | direct current |
| DMF | dimethylformamide |
| DOTA | 1,4,7,10-Tetraazacyclododecane-1,4,7,10-tetraacetic acid |
| EPR | electron paramagnetic resonance |
| h | hours |
| $H_2dapp$ | 2,6-Diacetylpyridinebis(2'-pyridylhydrazone) |
| HSAB | hard and soft acids and bases |
| Hz | Hertz |
| INS | inelastic neutron scattering |
| K | Kelvin |
| Ln | lanthanide |
| M | molar |
| MFF | muffin structure type |
| $m_J$ | magnetic state with quantum number J |
| nm | nanometre(s) |
| NRVS | nuclear resonance vibrational spectroscopy |
| OC | octahedron |

| | |
|---|---|
| Oe | oersted |
| Pc | phathalocyanine |
| QTM | quantum tunnelling of magnetisation |
| RT | room temperature |
| s | second(s) |
| SAPR | square antiprism |
| SIM | single ion magnet |
| SMM | single molecule magnet |
| SOC | spin-orbit coupling |
| SQUID | super conducting interference device |
| T | temperature |
| TBA | tetrabutylammonium |
| TBAP | tetrabutyleammonium phosphite |
| TCTPR | spherical capped trigonal prism |
| TDD | triangular dodecahedron |
| th | top half |
| V | volts |
| ZFC | zero field cooling |
| ZFS | zero field splitting |

# 1 INTRODUCTION

I would not have thought that chemistry is so much about patterns and symmetry before my studies. Sure, I knew the Periodic Table but I did not know the essence of it. Fermions that would not allow two of them being in the same state.[1] In 2019 the international year of the Periodic Table was celebrated. Mendeleev, Meyer and Newlands did not have this knowledge but still saw that pattern caused by the fermions because of the chemical behaviour of the atoms composed from them.[2,3] Again and again, one encounters symmetry and structure related properties. While the Thalidomide case is maybe the most prominent and terrifying example showing that symmetry and structure play a key role, this is also the case for spectroscopy and even some physical properties can only be achieved with the correct symmetry. Piezoelectricity, for example, can only occur in compounds with non-centrosymmetric space groups whereas pyroelectricity and ferroelectricity can only occur in polar space groups.[4] However, when I started with coordination chemistry on lanthanides, I thought that this may be the furthest you can get from high symmetry within the field of chemistry since lanthanide complexes tend not to favour high coordination symmetry. Much to my surprise, I quickly became aware that in the field of Single Molecule Magnets (SMMs), it is actually quite relevant. In the 1990s a modern generation of the highly sensitive magnetometers led to renewed interest in the $Mn_{12}$ carboxylate system from the groups of Gatteschi and Christou.[5-8] Contrary to the intuition of many at that time, the results showed that a single molecule could have magnetic remanence and it sparked the dream of creating materials that were able to preserve magnetic information on molecular scales.[5,8] These materials could potentially find applications in data storage and quantum computing. Keeping in mind that data storage devices are quite common in everyday life, one can imagine that a bit the size of a molecule would be able to solve problems like storing and processing data which occur due to increasing cyber traffic. It could also decrease the amount of energy that is needed for that purpose since smaller spaces would be needed with reduced cooling requirements.[9-12]

While the ideas of possible usage are manifold, the design of molecules showing good single molecule properties turned out to be challenging. The first attempts of just tailoring magnetic transition metal centres together to form molecules with high total spin values sparked from the idea to separate the magnetic states from each other

giving the magnetic moment obstacles to go over the energy barrier $U_{eff}$ which is proportional to the square of the ground state spin to the absolute value of the uniaxial anisotropy D.[13,14] After some initial synthetic success designing molecules with high total spins, Oliver Waldmann pointed out that the uniaxial anisotropy has an inverse S dependence which makes the $U_{eff}$ only proportional to S.[14] More dramatically, Eliseo Ruiz et al. elaborated that at a certain point of including more and more spin centres, the anisotropy drops with every spin centre added in that amount which the spin and the anisotropy of the system compensate.[15] Moreover, the energy barrier of spin reversal is directly dependent on the anisotropy of the system. However, anisotropy of the wrong sort is also detrimental to probability to the system going over this barrier and tunnelling effects start to take charge.

Research began to focus on lanthanides which can have very high uniaxial anisotropies, especially pronounced for $Dy^{3+}$, but also show strong spin-orbit coupling (SOC). This means that the magnetic levels are determined by the J-values with the microstates $m_J$ promising a large number of excited magnetic states often with very large energy differences.[11,16] Soon, the first lanthanide single ion complexes outbid transition metal clusters in their effective energy barriers. The phthalocyanine terbium complexes, for example, showed a relaxation barrier of 230 $cm^{-1}$ which outcompeted the famous $Mn_{12}$ acetate (42 $cm^{-1}$) easily.[8,17] However, nature decided the magnetic relaxation of lanthanide ion complexes could not completely go over the energy barrier.[11] Although the $\pm m_J$ states should be formally well separated for Kramers ions and non-Kramers ions in axial crystal field symmetries, relaxation processes occur that do not go completely over the energy barrier.[12,16] The quantum tunnelling of magnetisation (QTM) related relaxation pathways occur when mixing of the $\pm m_J$ states takes place for the single ion. This mixing can only be suppressed by constraining the system to high symmetries.[18,19] Who would have thought that chemistry is so much about patterns and symmetry?

# 2 THEORETICAL BACKGROUND

## 2.1 Lanthanide Coordination Compounds

In contrast to transition metal complexes, lanthanides have a big variety in their coordination number. A quick Cambridge Structural Database (CSD) search shows that there is a concentration of abundance in the numbers eight to ten. Although the data needs to be considered with some caution, since some entries in the CSD are wrong or imprecise, you can see in the distribution in the statistics in Figure 2.1 that the difference in dimension towards the other coordination numbers is significant. However, no coordination number has a significantly higher abundance as is the case for transition metals.[20] While the valence orbitals in transition metals, more precisely their electrons in d-orbitals, are involved in their coordination bonding, the valence orbitals in lanthanides, the f-orbitals, are lying closer to the core than the 5s and 5p shells in their noble gas configuration.[21] Thus, the forces that hold the lanthanide complexes together are more of an electrostatic nature.
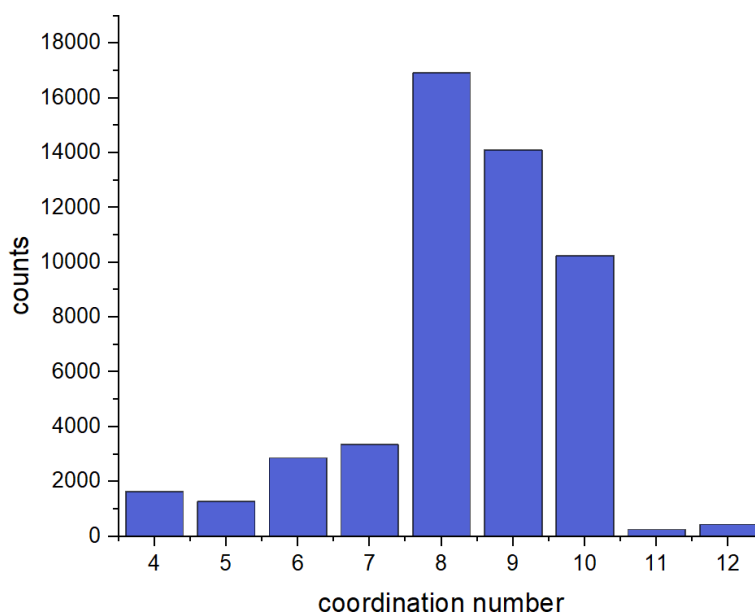
Figure 2.1: Statistics on the CSD search result for different coordination numbers of lanthanides.

Another effect of the buried valence electrons is that all lanthanides most commonly appear in the III+ oxidation state. The most exposed two electrons from the high energy 6s shell are easily given away. The same happens to the electrons in the 5d shell in lanthanum, gadolinium and lutetium. For the rest, the third electron is ejected from the

4f shell because of inter electron repulsion.[22] This leaves the lanthanides 3+ charged and with a dense shell structure.

For their reactivity in coordination chemistry, this means very hard central ions with valence electrons that only have a weak ability to contribute to bonding with ligands.[23] The consequence is that it is hard to bind soft or monodentate ligands but easy to bind hard or polydentate ligands.[24] Especially, negatively charged oxygen as in oxide, hydroxide, carboxylate, alcoholate ions or similar species work well as ligands. With oxalate ions, a fast complexation of dissolved lanthanide ions occurs precipitating a white amorphous solid. Also with fluoride ions and hydroxide ions, precipitates are formed easily. This gives strong restrictions on the pH of aqueous lanthanide ion solutions and on reagents that can be used. By combining all these properties described above, it is easy to understand why the initial design of lanthanide complexes is so challenging.

## 2.2 Molecular Magnetism

Although the rational design of lanthanide complexes is not an easy task, it makes sense to put effort in it because there is a strong structure-property relationship for molecular magnetism.[24] Although this is true for both transition metal and lanthanide complexes, the origin of the magnetic properties and therefore the structural targets are, to some extent, different.[25]

In general, magnetism can arise from moving charges and from spins.[4] Spins can be found as intrinsic properties of all elementary particles except from Higgs Bosons and represent a non-classical movement.[26,27] Conclusively, the total magnetic moment that an atom or a molecule has, stems from all its electrons, protons and neutrons. This sounds complicated but luckily most of the magnetic moments cancel out. As a result of the Pauli principle, the fermions (electrons, protons and neutrons) pair their spin moments antiparallel to one another to prevent the occurrence of the same quantum numbers.[28,29]

The other simplification regarding the magnetic moments of the electrons can be made because the mass enters the equation of the magnetic moment in the denominator seen in equation (1). Since the mass of protons and neutrons is about $1.8 \times 10^3$ larger, the magnetic moment they gain is lower by the same magnitude. This means, most of the magnetic moment stems from the unpaired electrons.[30]

$$\mu = -\frac{e}{m_e} \cdot \hat{l} = \mu_B \sqrt{l(l+1)} \tag{1}$$

From here, magnetism in transition metal and lanthanide compounds has to be considered differently due to the positions of the valence electrons and their possibilities to contribute to the resulting magnetic moment.[31]

In transition metal complexes, the ligand field splitting is quite strong. The reason for this is the fact that valence electrons are in the exposed d-shells. When ligands assumed as negative point charges disturb the crystal field this has a much bigger impact on the d-electrons of transition metals than on the f-electrons in the lanthanide ions which are protected by the larger 5s and 5p orbitals. There are two different limiting cases for transition metal complexes. Either the crystal field is stronger than the electron-electron repulsion or vice versa. In the case of a stronger crystal field, shown in Figure 2.2 on the left-hand side, the d-orbitals can be assumed to be split first by the crystal field removing their degeneracy. Afterwards, the electron-electron repulsion mixes the orbitals of each electron to terms which are also influenced in different ways by the ligand field. This is also the reason why SOC is so weak for most transition metals.[23] The degeneracy that would allow the movement of electrons through rotation related orbitals or terms is removed by the strong crystal field.[32] Consequently, the magnetic moment arises only from the spin of the system. Thus, S is a good quantum number to describe the magnetic moment of the system and equation (1) changes to equation (2) with the expansion by the Landé factor g taking into account the non-classical physics.

$$\mu = g_S \mu_B \sqrt{S(S+1)} \tag{2}$$

However, despite this removal of degeneracy, SOC takes place to a much weaker extent. As one factor of interactions between energy levels in a molecule, this contributes to the zero field splitting (ZFS) which removes the degeneracy of the $m_S$ sublevels.[33] There is a strong correlation between the separation of these sublevels, which reflects the magnetic anisotropy and the symmetry of the system. This is not

---

(1): Magnetic moment μ simplified by a general operator of angular momentum $\hat{l}$ with the electron charge e, the mass of the electron $m_e$, the Bohr magneton $\mu_B$ and the angular momentum quantum number l.[23]
(2): Spin only formula for the magnetic moment μ. The Landé factor for the spin $g_S$ is approximately 2.[23]

surprising because the extent of mixing of the energy levels depends directly on symmetry considerations.[34] The other limiting case is an electron-electron repulsion that is stronger than the ligand field splitting. In this case, the splitting into terms because of electron-electron repulsion precedes the ligand field splitting, but still the SOC and therefore the ZFS is weaker as depicted in Figure 2.2.

This means the energy barrier of the system U is directly dependent on the total spin of the system as $S^2$ and the ZFS parameter D expressing a quantitative dimension of the magnetic anisotropy of the system shown in equation (3) and equation (4).[35]

$$U = DS^2 \tag{3}$$

$$U = D\left(S^2 - \frac{1}{4}\right) \tag{4}$$

Regardless, to raise the total spin of a system by coupling the transition metal spin centres via suitable ligands is achievable. The positive effect on the energy barrier of the spin reversal is finite. On the one hand, as explained well and in detail by Oliver Waldmann, for a big number of spin centres the energy barrier is independent of S since the projection coefficients $d_i$ of the spin centres i scale with $S^{-2}$ and compensate the $S^2$ through the ZFS parameter D seen in equation (5) and equation (6) meaning the energy barrier would only grow monotonically with every spin centre added.[14]

$$D = \sum_{i=1}^{N} d_i D_i \tag{5}$$

$$d_i = \frac{S_i(2S_i - 1)}{S(2S - 1)} \tag{6}$$

In contrast, Eliseo Ruiz et al. showed empirically that spins and the ZFS parameter value D simply compensate one another and thus optimising one of them

---

(3): Energy barrier for an integer spin system.[35]
(4): Energy barrier for a half integer system.[35]
(5): Composition of the molecules zero field splitting parameter.[14]
(6): Dependence of $d_i$ on the total spin of the system S and the spins of each spin centre $S_i d_i$ scales with $S^{-2}$ since S becomes a constant factor.[14]

independently would not result in a higher energy barrier.[15] This means that the best way to enhance transition metal SMMs is to align paramagnetic centres with a strong individual anisotropy arising from strong SOC and/or ZFS to give a system with strong total anisotropy.[36]
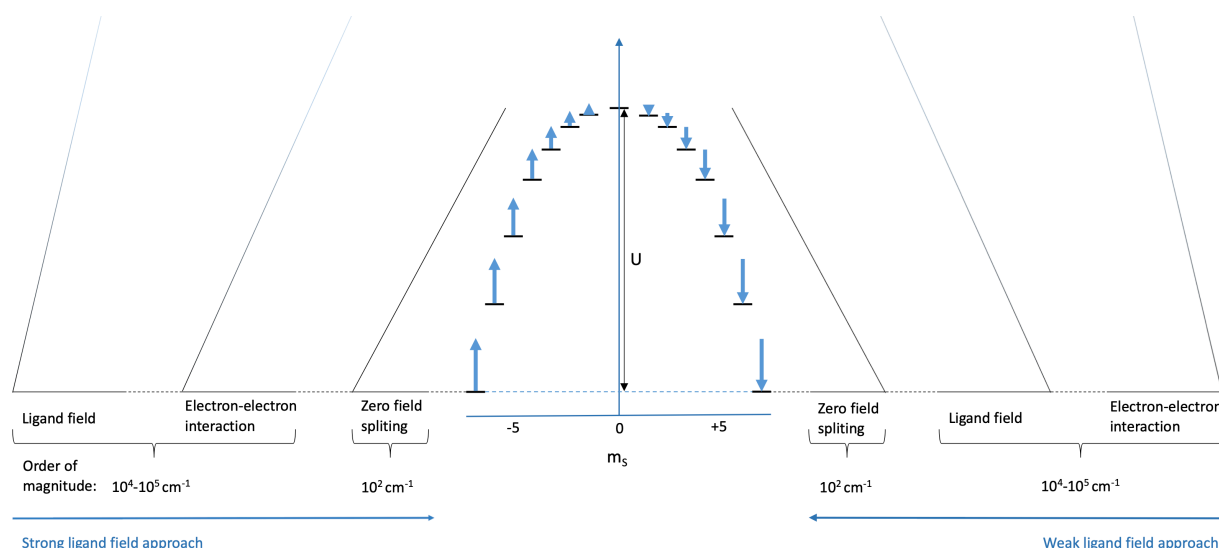


Figure 2.2: Schematic depiction of splitting of energy states as it usually occurs in 3d metals. The size of the arrows illustrates proportionally the projection of the spin moment of the system in direction of the anisotropy axis.

For lanthanides, the influences on the energy barrier for spin reversals are different. Lanthanides as a base for SMM behaviour were considered because of the inherent anisotropy of the magnetic states in the free lanthanide ion.[37] These stem from the strong SOC or the low influence of the crystal field that makes strong SOC possible. [38] Hence, S is no longer a good quantum number to describe the magnetic states. The difference between coupling l and s as individual j-values and coupling the L and S to give J is negligible and it is commonly found from the Russell-Saunders coupling according to equation (7).[4,23]

$$J = \begin{cases} |L - S| \\ L + S \end{cases} \tag{7}$$

Consequently, the calculation of the magnetic moment changes to $\mu_J$ as in equation (8).

(7): J-value for up to half filled shells (top) and more than half filled shells (bottom).[4]

$$\mu_J = g_J \mu_B \sqrt{J(J+1)} \tag{8}$$

Only the components of the magnetic moment that come from the orbit angular momentum $\mu_J$ and from the spin $\mu_S$, which are parallel to the coupled moment $\mu_J$, can have an impact. This is compensated by a new g-factor calculated as in equation (9).

$$g = 1 + \frac{S(S+1) + J(J+1) - L(L+1)}{2J(J+1)} \tag{9}$$

At the present, we have already discussed terms as electron-electron interactions being stronger than both SOC and crystal field interaction. In Figure 2.3, the order and order of magnitude of the different splittings of lanthanide ions can be seen.
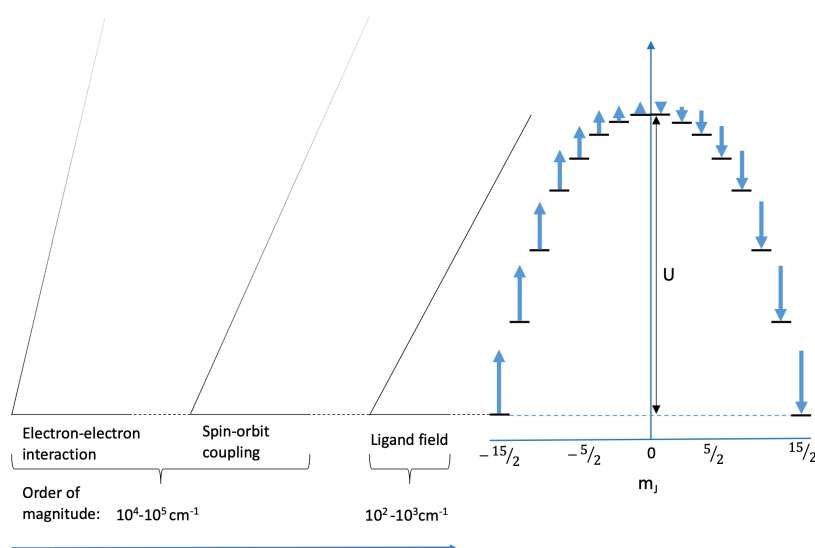


Figure 2.3: Scheme of the optimal splitting for dysprosium in an axial ligand field. The highest $|m_J|$ states form the ground states of the system. The size of the arrows illustrates proportionally the projection of the magnetic moment of the system in direction of the anisotropy axis.

Having the crystal field as the weakest splitting here means that the separation of the magnetic states, and as a consequence the energy barrier, strongly relies on a strong crystal field splitting. In essence, this means that although the 4 f-electrons are buried under the 5s and 5p shell and do not participate much in coordination bonding, the crystal field has a strong influence on the energy levels they can populate. Following synthetic chemistry carried out in that field, the famous lanthanide phthalocyanine was

---

(8): Magnetic moment for a Russel-Saunders coupled system.[4]
(9): g-factor in systems with strong spin-orbit coupling.[38]

discovered, and Jeffrey Reinhart and Jeffrey Long published a qualitative approach based on Siever's work on how to arrange the crystal field to separate the magnetic states well.[17,37] They showed that the different magnetic states can actually be described very well by the spatial shape of the ion's $m_J$ states electron distribution since the f-electrons are so shielded and have a strong angular dependence. To gain a high energy barrier, the magnetic states have to be well separated from each other. Ideally the state with the highest magnetic moment should be the ground state. The perturbation of the ground state by the ligand field needs to be minimised while for all excited states it has to be maximised. Thus, $Ln^{3+}$ ions with their highest $|m_J|$ states being of oblate shape, like dysprosium and terbium (Figure 2.7), should be placed ideally in an axial ligand field while $Ln^{3+}$ ions with their highest $m_J$ states being of prolate shape like erbium, thulium and ytterbium should preferably be placed in an equatorial ligand field.[16] In Figure 2.3, an optimal splitting for dysprosium is depicted. Here, the highest $|m_J|$ state is stabilised and well separated from the excited states. This model was refined by others with the conclusion that the influence by ligands is actually not in line with the spectrochemical series, but that negatively charged ligands with high electrostatic potential have a much higher impact on the anisotropy axis.[39-41] The excited states can be of different shape meaning that the energy levels are not always increasing in order from the highest to the lowest $|m_J|$ of a system. The order of the energy levels depends strongly on the ligand field and is not easy to predict for non-symmetrical coordination environments. Even in dysprosium complexes with axial symmetry and ligand field, it can happen that the $m_J$ states are not perfectly sorted or that a lower $m_J$ state forms the ground state. In Figure 2.4, the splitting is illustrated close to the measured energy levels of the $m_J$ states in the dysprosium phthalocyanine complex.[16]
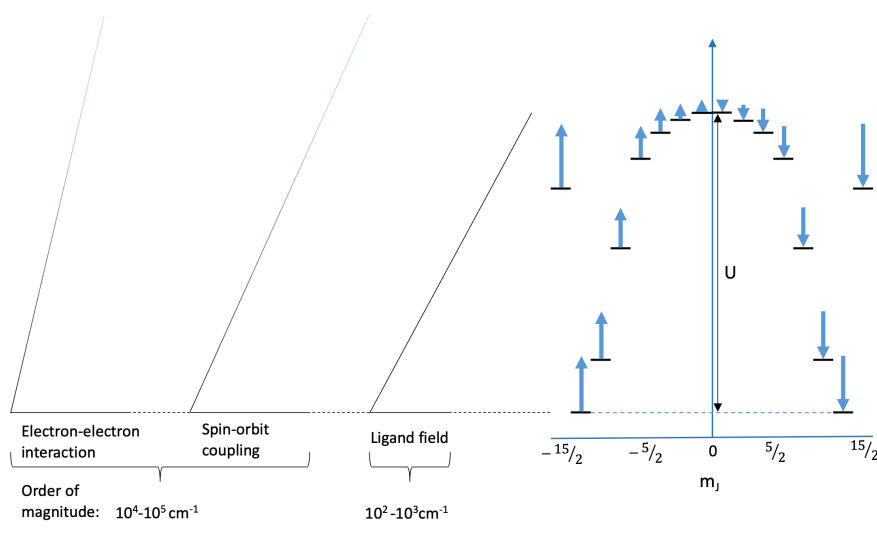
Figure 2.4: Schematic illustration of the splitting in the dysprosium phthalocyanine complex.[42]

At this point, it should be said that a bistability of states is intrinsically given for the half integer Kramers ions and for non-Kramers ions in axial symmetry fields.[43] These qualitative approaches have led to tremendous success in synthesising lanthanide SMMs in the last decade, which will be discussed later. A small disadvantage is that contrary to transition metal SMMs coupling, more than one magnetic centre is quite difficult due to the low ability of f-electrons to participate in strong coordination bonding.[44] Rather than leading to higher magnetic total states, weak bonding leads to mixing of states in an order of magnitude that allows faster relaxation processes described later.[45] Despite the success in improving on transition metal SMMs and even crossing the liquid nitrogen threshold, all molecular magnets are subject to problems with magnetic relaxation.[46-49]

## 2.3  Relaxation of Magnetic Moments

To date, lanthanide SMMs show huge energy barriers $U_{eff}$ for the reversal of the magnetisation. 1261 cm$^{-1}$ has been obtained even in air stable complexes.[50] However, the blocking temperatures that indicate a real inhibition of magnetic relaxation at a certain temperature are always much lower than what would be expected from the energy barriers. To understand this, one needs to have a look into the relaxation pathways depicted in Figure 2.5.[11]
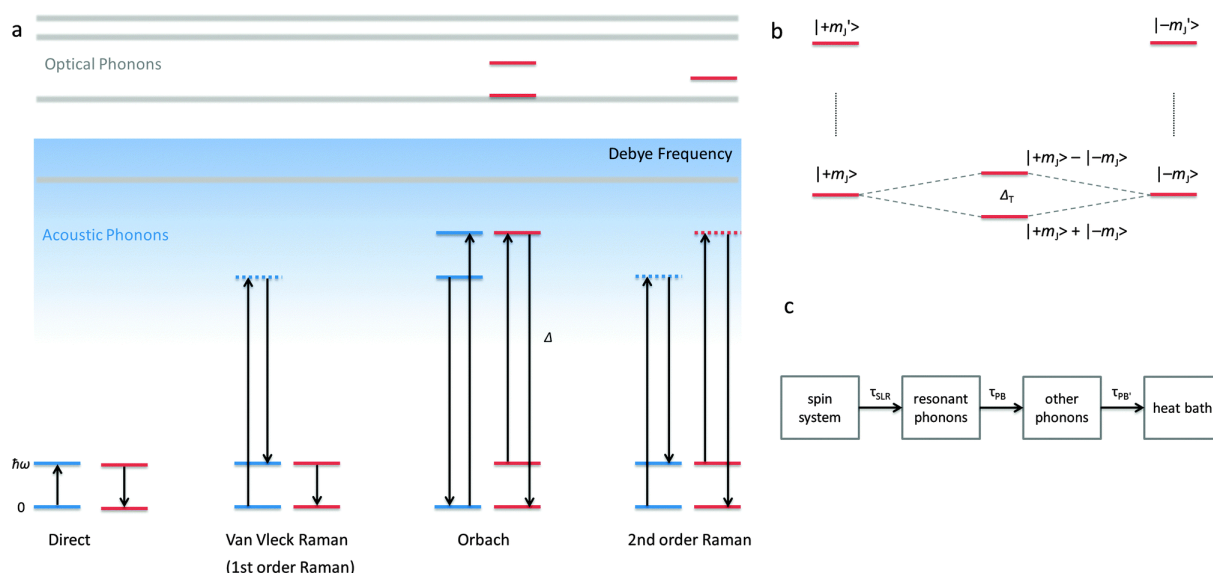
Figure 2.5: **(a)** Relaxation pathways that occur for the magnetisation in Kramers doublets. The density of states for the acoustic phonons are shown as an increase of blue colour up to the Debye frequency. Optical phonon states are depicted as grey lines. The blue lines show lattice energy states and the red lines $m_j$ states of the lanthanide ion. The Orbach process can be seen as two consecutive direct transitions and the Raman process as incorporating a virtual energy level to take up the energy being released by the process of spin reversal. **(b)** Schematic representation of the transvers interaction (e.g. hyperfine interaction, crystal field splitting, vibrational modes) induced mixing of states leading to superposition of states with opposite $m_J$ projections. $\Delta_T$ represents the tunnelling gap. **(c)** Processes involved in the relaxation with energy of the heat bath. If $\tau_{PB}$ and $\tau_{PB'}$ are slow compared to $\tau_{SLR}$, magnetic hysteresis can occur which is of nonmolecular origin.[11] – Published by The Royal Society of Chemistry.

Whilst for transition metal SMMs tunnelling processes can be observed, for example in the hysteresis of $Mn_{12}$ acetate, they play a much bigger role for lanthanide SMMs.[7] Additionally, temperature dependent spin-lattice relaxation pathways occur which seem to become predominant for high temperature SMMs.[51,52] Direct processes involve single acoustic phonons. These are rare since the density of states in that energy range is low. Orbach and Raman processes incorporate higher energy states and two phonons. In Orbach processes, the energy for the state transition is given or taken up by lattice phonon states whereas in Raman processes, the required energy for the state transition is given or taken up by a superposition of two phonons forming a virtual state. In a second order Raman process, the transition via a virtual superposition energy state of the magnetic states at the lanthanide also occurs. This illustrates very clearly where the temperature dependence of these relaxation processes comes from. As more of these phonons get thermally activated and as a broadening of vibrational modes occurs with higher temperatures, transitions become more efficient and a wider range of transitions are possible. The relaxation time is composed of contributions of all these processes. It can be described as a sum of the relaxation times of each process as described in equation (10).

$$\tau(T,H)^{-1} = AH^m T + CT^n + \tau_0^{-1} e^{\frac{U_{eff}}{k_B T}} + \frac{B_1}{1 + B_2 H^2} \tag{10}$$

The relaxation dynamics of the phonons are usually described using the Debye model. The two Cole-Cole equations (11) and (12) describe the Debye relaxation as quantified by $\tau$ values.

$$\chi'(\omega) = \chi_S + (\chi_T - \chi_S) \frac{1 + (\omega\tau)^{1-\alpha} \sin\left(\frac{\pi}{2}\alpha\right)}{1 + 2(\omega\tau)^{1-\alpha} \sin\left(\frac{\pi}{2}\alpha\right) + (\omega\tau)^{2-2\alpha}} \tag{11}$$

$$\chi''(\omega) = (\chi_T - \chi_S) \frac{(\omega\tau)^{1-\alpha} \cos\left(\frac{\pi}{2}\alpha\right)}{1 + 2(\omega\tau)^{1-\alpha} \sin\left(\frac{\pi}{2}\alpha\right) + (\omega\tau)^{2-2\alpha}} \tag{12}$$

By simultaneously fitting the in phase $\chi'$ and the out of phase signals $\chi''$ to the Debye relaxation, the $\tau$ values for each temperature can be obtained.[60] In an Arrhenius plot, temperature dependences can be made visible and therefore, occurring relaxation processes can be assigned to one of the terms in equation (10) shown in Figure 2.5. For better comparison of the properties, $\tau_0$ and $U_{eff}$ from the Orbach term of equation (10) are used as benchmarks. Also, the presence of a hysteresis at a certain temperature is used frequently. However, it has to be critically remarked that there is a lack of comparability of the hysteresis measurements since there are no standard measurement parameters like for example the sweep rate. The literature sometimes refers to the blocking temperature as the maximum temperature where open hysteresis can be observed although there is this inaccuracy. Another definition uses the temperature at which the relaxation time is 100 s. Because this is obviously arbitrary, the blocking temperature will be understood and used in this thesis like in the traditional definition of the zero field cooling (ZFC) as the temperature where the ZFC curve

---

(10): Arrhenius function with terms for direct processes ($AH^m T$), Raman processes ($CT^n$), Orbach processes $\left(\tau_0 e^{\frac{U_{eff}}{k_B T}}\right)$ and tunnelling processes $\left(\frac{B_1}{1+B_2 H^2}\right)$ as one example for the many variations used in the literature.[11,43,51,53-56]

(11): Cole-Cole function for the Debye relaxation for the in phase signals.[57-59]

(12): Cole-Cole function for the Debye relaxation for the out of phase signals.[57-59]

shows a maximum.[61] Another rule of thumb is to quote the temperature at which maxima can still be seen at 1000 Hz frequency.

While QTM can be suppressed by tight bonding and special symmetries, which is explained later in detail, for Orbach and Raman processes theoretical approaches on how to supress them are missing.[62] The understanding of the coupling of the spins to the phonon bath is subject of contemporary studies and seems to be the key for the design of high temperature SMMs.[63] Some recent publications suggest stiffer metal ligand bonding incorporating light atoms, smaller molecules and higher symmetries as possible starting points for synthetic approaches to reduce spin lattice relaxation.[64,65]

## 2.4  Symmetry of Lanthanide Complexes

Speaking about symmetry in lanthanide compounds incorporates two aspects which have to be regarded separately. On the one hand, there is the point group symmetry around the lanthanide ions. While for d-block metals the crystal field splitting directs the position of the ligands, it does not apply for the lanthanides because of the inherent properties of lanthanide ions described in sections 2.1 and 2.2. Hence, the point group symmetries often significantly deviate from ideal symmetries. Additionally, the variety in coordination numbers leads to a big diversity in possible ideal symmetries.[66]

On the other hand, there is the space group symmetry in which the compound crystallises. As a result of the lack of point group symmetry, the space group symmetry is also not very high. In an analysis of entries in the CSD, it can be seen that most lanthanide compounds crystallise in triclinic and monoclinic space groups. The most abundant ones are $P\bar{1}$ and $P2_1/c$ highlighted in Figure 2.6.[67]
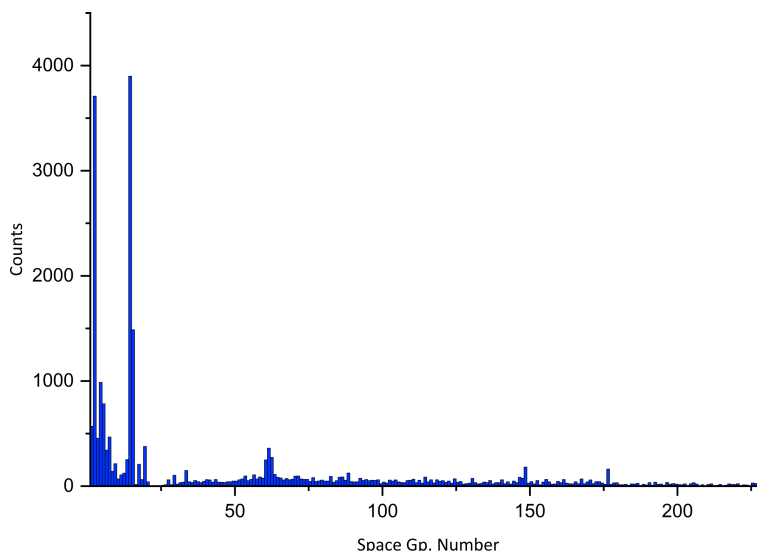
Figure 2.6: Counts of crystal structures on the CSD versus space group number.

As discussed earlier, symmetry plays a big role in the inhibition of quantum tunnelling and is discussed as a possibility to minimise Raman relaxation. More precisely, low and wrong point group symmetry is responsible for facilitating quantum tunnelling through mixing of states resulting from the presence of off-diagonal terms in the crystal field Hamiltonian $\widehat{H}_{CF}$ enabling forbidden transitions.[62] However, for some point group symmetries, which are depicted in Figure 2.7, the $m_J$ states do not mix due to linearity. This means, the Hamiltonian describing the ligand field is simplified because in certain symmetries some terms become zero. For $D_{4d}$ symmetry for example, the Hamiltonian is described in equation (13).[43,68]

$$\widehat{H}_{CF} = \sum_{q=-2}^{+2} B_2^q \hat{O}_2^q + \sum_{q=-4}^{+4} B_4^q \hat{O}_4^q + \sum_{q=-6}^{+6} B_6^q \hat{O}_6^q \tag{13}$$

Usually, it is hard to control the first order point symmetry. By this, the relative positions of the central ions and the directly connected ligand atoms are meant. Additionally, the first order point symmetry of a given metal centre can be broken by ligands further away. It is shown in the literature that even for higher order symmetry, perturbation can have a big influence on the quality of SMMs.[69] Hence, the favourable point symmetries from Figure 2.7 should ideally extend to the whole crystal system. Yet this is not possible for e.g. $D_{5h}$ since a 3D packing with this symmetry does not work.

---

(13): Crystal field Hamiltonian for the description of lanthanide complexes with the crystal field parameters ($B_n^q$) and Stevens operators ($\hat{O}_n^q$).[43,68]

**(A) Electronic Approach**

$Ce^{3+} m_j = 5/2$   $Pr^{3+} m_j = 4$   $Nd^{3+} m_j = 9/2$

$Pm^{3+} m_j = 4$   $Sm^{3+} m_j = 5/2$   $Gd^{3+} m_j \geq 7/2$

$Dy^{3+} m_j = 15/2$   $Tb^{3+} m_j = 6$   $Ho^{3+} m_j = 8$

$Er^{3+} m_j = 15/2$   $Tm^{3+} m_j = 6$   $Yb^{3+} m_j = 7/2$

$Eu^{3+} J = 0$

**(C) Symmetry Approach**

CF Parameters:
$B_2^0, B_4^0, B_6^0$

$C_5h / D_5h$

$S_{12} / D_6d$

$S_8 / D_4d$

$C_n (n \geq 7)$   $C_\infty$

**(B)**

$m_j = 15/2$   $m_j = 13/2$   $m_j = 11/2$   $m_j = 9/2$

$m_j = 7/2$   $m_j = 5/2$   $m_j = 3/2$   $m_j = 1/2$
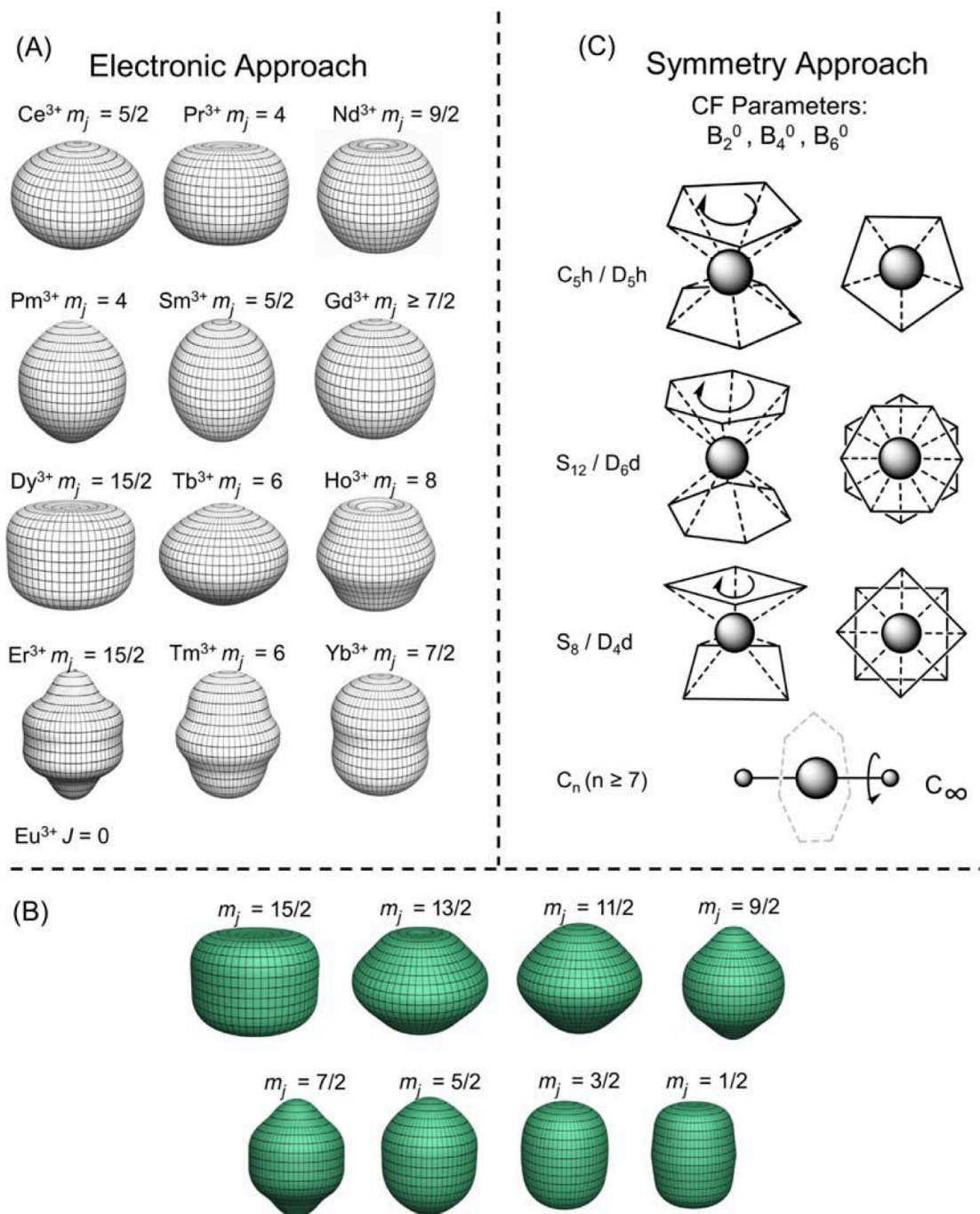
Figure 2.7: **(A)** Spatial projection for $m_j$ of different lanthanide ions. **(B)** Angular distributions for all $m_j$ states of Dy$^{3+}$. **(C)** Point groups with no transverse crystal field terms.[52]

Despite these difficulties, it has been shown that even with non-perfect coordination environments good results can be obtained. In the last years, vast improvements in applying theoretical symmetry and anisotropy considerations to single lanthanide ions have been made resulting in higher energy barriers and higher blocking temperatures.[25]

## 2.5 Applied Theory – Lanthanide Complexes with Slow Magnetic Relaxation

In this subchapter, some examples are given where it has been shown that a good but not perfect application of the theoretical demands can lead to promising results in improving the molecular magnetism of lanthanides.

The origin of the fast rise of lanthanide single molecule and single ion magnets (SIMs) is the aforementioned phthalocyanine-lanthanide system. It consists of a sandwich-like structure with two phthalocyanine ligands and a lanthanide ion trapped between them. The four inner nitrogen atoms of the ligand's macrocycle cap the lanthanide ion equidistantly while the two ligands are rotated 45° towards each other generating a square antiprismatic environment around the lanthanide ion. In the original system, each of the ligands is two times negatively charged and the crystalline [LnPc$_2$]$^-$ (Figure 2.8) is stabilised with one tetrabutylammonium (TBA) counter ion.[17] The structure had already been reported in the literature (as was also the case for Mn$_{12}$ acetate) when Ishikawa et al. did the magnetic investigation of the system and proved single molecule magnet behaviour of a lanthanide complex for the first time.[70-72]
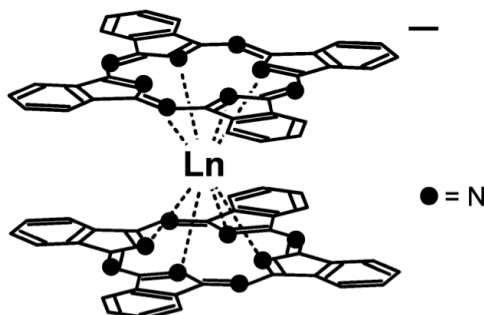


Figure 2.8: Scheme of the molecular structure of [TbPc$_2$][72] – Reprinted with permission from [72]. Copyright 2003 American Chemical Society.

Although the theory from above was developed after this discovery, the first example already was a good one. With 230 cm$^{-1}$, the [TbPc$_2$]$^-$ was among the [LnPc$_2$]$^-$ compounds with the highest energy barriers for many years. It even showed an open hysteresis up to 1.7 K. Initially, Ishikawa determined the energy of the m$_J$ sublevels. Subsequent calculations of triple deckers (two lanthanide ions and three macrocycles) revealed a large splitting for the m$_J$ states substantiated by AC measurements on the compound.[73,74] The assumption they made from the calculations that the splitting of the m$_J$ states would have the same effect on the magnetism of the lanthanide ion as the splitting of the spin states does for transition metal SMMs was proven by finding

the slow relaxation of magnetism.[17] What they had found was a perfect example for the later established theory. The ligand field was axial with the charge density above and below the lanthanide ion and the symmetry was almost perfect $D_{4d}$. Applying a more equatorial ligand field with this symmetry, on the other hand, stabilises the high $|m_J|$ ground states for erbium and destabilises it for terbium and dysprosium. This was shown in a compound where lanthanides were coordinated by polyoxometalates.[75]

The $TbPc_2$ system has been modified a lot thereafter searching for ways to improve the SMM behaviour. Oxidation of the system led to a higher energy barrier (410 cm$^{-1}$) but what had caused the increase was first discussed later when a modified version of the complex was investigated synthesised by single electron oxidation to the neutral and positively charged complex.[42] A shorter distance between the lanthanide and the ligand was thought to be responsible for the increase in energy barrier to 550 cm$^{-1}$ for the positively charged system.[76,77] It was also shown that taking the $[TbPc2]^0$ out of its phonon bath by putting it on a surface further raised the energy barrier.[78]

Great progress has been made on pentagonal bipyramidal complexes although this symmetry is not easy to obtain. Many groups have synthesised examples with approximately pentagonal bipyramidal symmetry. The different approaches here were on the one hand to find good templating chelating ligands that favour the $D_{5h}$ coordination environment and on the other hand to group strong electron density donor ligands in axial positions.[79-81] This seems to leave just enough space for small molecules like water or pyridine to self-assemble five ligands in the equatorial positions. From the compounds that have been made, it can be seen that the application of the theory shows the predicted results on oblate ground state shaped lanthanide ions. For the equatorial ligands, it is desirable to have small amounts of electron density on and long distances between the ligating atoms and the central ion. For the axial ligands, large amounts of electron density and short distances between the central ion and ligating atoms lead to higher energy barriers. Due to weak coupling of the magnetic moments, it has been shown to be the main factor for the heights of the energy barrier.[25,82] While $[Dy(OPCy_3)_2(H_2O)_5]Br_3$ with a coordination bond length of 2.35 Å to the water ligands and 2.2 Å to the phosphinoxide ligands has an energy barrier of only 377 cm$^{-1}$, it is increased to 1261 cm$^{-1}$ in $[Dy(O^tBu)_2(py)_5][BPh_4]$ with a coordination bond length of 2.56 Å to the pyridine ligands and 2.11 Å to the tert-butanolate ligands. However as widely stated in the literature, there is no simple structure-property relationship for the observed blocking temperature. What can be

noted though is that there is a strong dependence of the height of the blocking temperature to the symmetry and rigidity of the system. Despite the rather low energy barrier compared to other pentagonal bipyramidal dysprosium complexes [Dy(OPCy$_3$)$_2$(H$_2$O)$_5$]Br$_3$ has an exceptionally high blocking temperature with open hysteresis at 20 K. The symmetry-driven quenching of QTM in this compound is held responsible for this finding. It should be stressed that this case points out the challenges of generating a decent definition of the blocking temperature for the field of molecular magnetism. [Dy(O$^t$Bu)$_2$(py)$_5$][BPh$_4$] shows open hysteresis only up to 4 K but a blocking temperature from ZFC experiments up to 14 K while this blocking temperature for [Dy(OPCy$_3$)$_2$(H$_2$O)$_5$]Br$_3$ only is 11 K.[50,69] The compounds and their out of phase signals are shown in Figure 2.9.
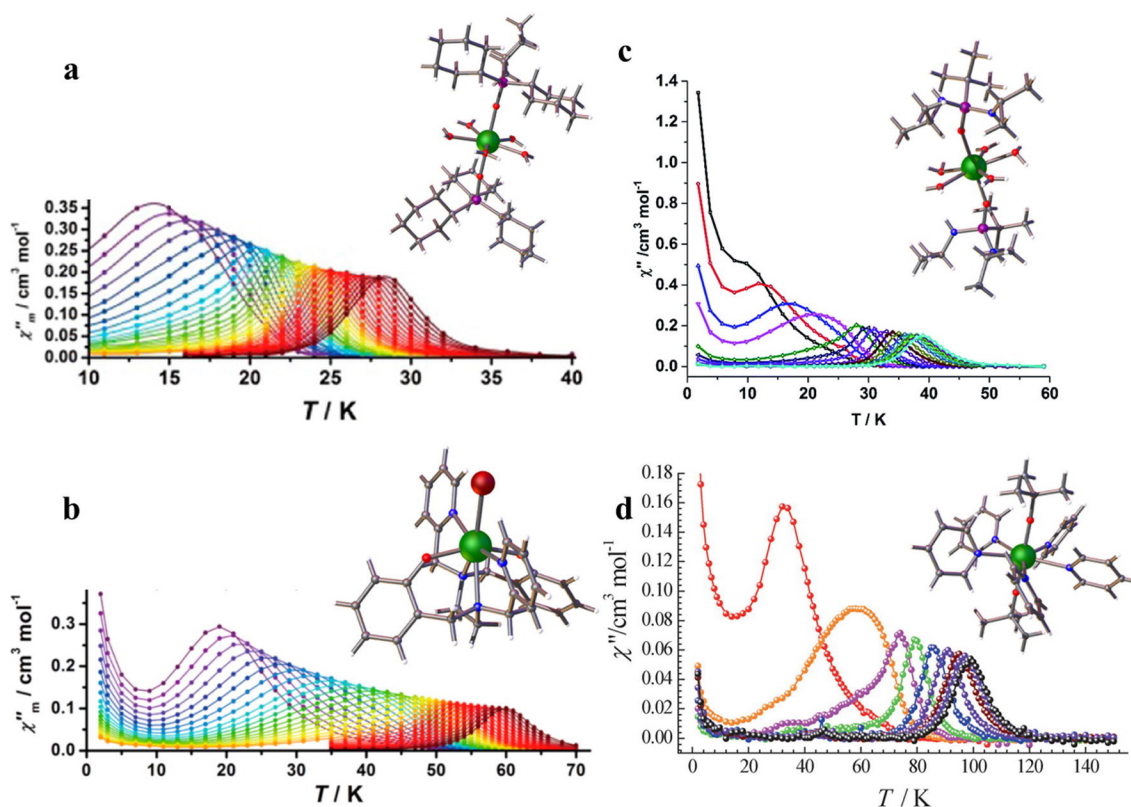


Figure 2.9: Pentagonal bipyramidal compounds from different groups put in comparison by Tuna et al.[25]

Recently, the group of Murrie employed triphenylsilyloxide as a stronger axial ligand. With this ligand, an energy barrier of 770 cm$^{-1}$ and open hysteresis up to 14 K was reported even for a compound that had deviations from D$_{5h}$ symmetry.[83] One year earlier, they had published a structure which had a 0.1-0.2 Å longer bond distance to the equatorial nitrogen atoms but D$_{6h}$ symmetry in the first order coordination sphere. For the optimised version, they obtained an energy barrier of 781 cm$^{-1}$ and an open

hysteresis up to 5 K.[84] Although this compound also deviates from idealised $D_{5h}$ symmetry, the much more symmetrical $D_{6h}$ compound with even longer bond distances in the equatorial plane shows almost the same energy barrier and a lower hysteresis temperature. Both compounds are shown in Figure 2.10.



**(a)**          **(b)**
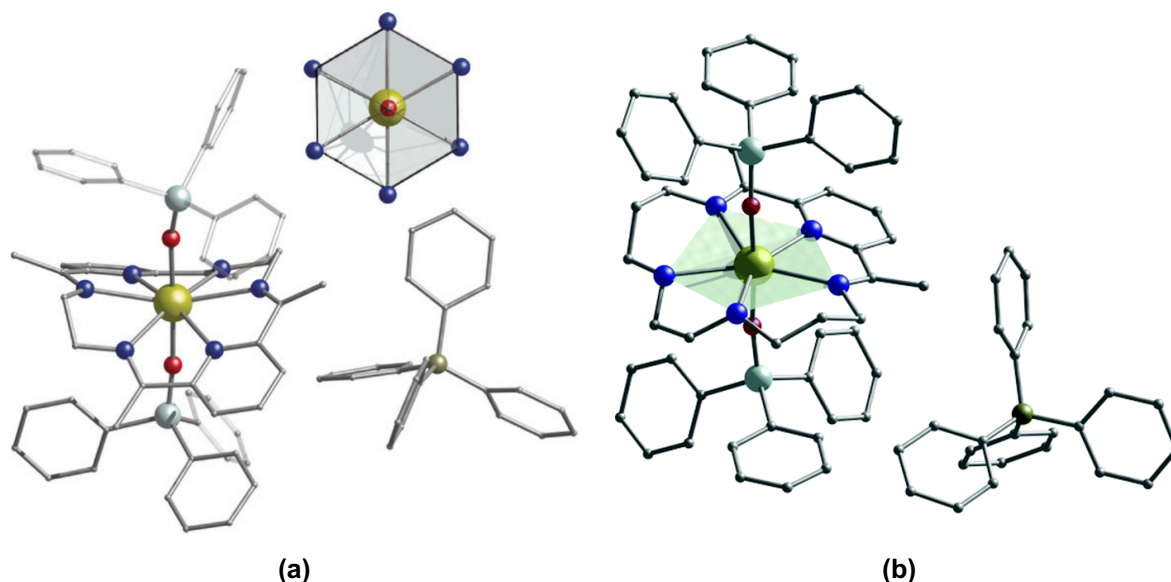
Figure 2.10: Structure of Murrie's **(a)** hexagonal and **(b)** pentagonal bipyramidal compounds with triphenylsilyloxide ligands.[83,84] – Published by The Royal Society of Chemistry.

Tight and ridged coupling to other magnetic moments is another big point that has been discussed for improving SMM properties by quenching of quantum tunnelling. With radical ligands and the combination of coaxiality and bridging ligands that enable strong intramolecular Ising interactions, this is possible.[85,86] The much shorter distance between the metal as a magnetic centre, the ligand as a magnetic S=1/2 centre, and the diffuse nature of the molecular orbitals of the radical ligand enhance the interactions with the f-electrons of the lanthanides.[87] This interaction is so strong that via such compounds, even for lanthanides, coupling can be so enhanced that radically coupled lanthanide ions cannot be regarded as single ions anymore. Most famous are the complexes with $N_2^{3-}$ and $N_2^{2-}$ bridging ligands of Rinehart et al. An incredibly strong coupling constant of -27 cm$^{-1}$ between the two Gd centres and the $N_2^{3-}$ radical was obtained for the radical bridged complex.[88] It was shown that the radical bridging is responsible for the high energy barrier and blocking temperature, which they could obtain in the Tb analogue by comparing it to the non-radical bridged version of the complex.[89] This example shows the much stronger effect by strong coupling via radical ligands compared with non-radical ones that only allow coupling of

$|m_l|>0$ orbitals. For the Gd-$N_2^{2-}$ complex, a coupling constant of -0.49 cm$^{-1}$ and a much lower energy barrier was obtained.[90] The terbium compound is shown in Figure 2.11.
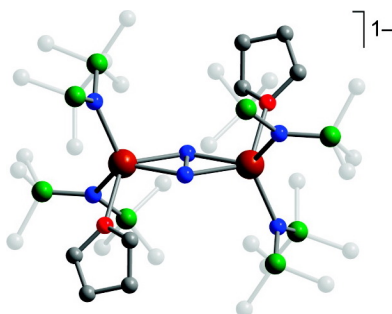


Figure 2.11: TbN$_2^{3-}$ bridged compound from Rinehart et al.[90] – Reprinted with permission from [90]. Copyright 2011 American Chemical Society.

Despite other approaches of lanthanide coupling, the coupling constant of the $N_2^{3-}$ system remains the highest. However, already weaker coupling via radicals can reduce QTM sufficiently and improve SMM properties as has been shown in many examples.[91,92]

The big breakthrough was the synthesis of the almost axial DyCp$_2$ complexes, which two groups claim to be responsible for. In the original compound, the cyclopentadienyl ligands are 1,2,4-substituted with -CMe$_3$ groups that shield the Dy ion of being bonded to other ligands beside the two Cp after the subtraction of the chloride ion present in the [Dy(Cp$^{ttt}$)$_2$Cl] intermediate. The resulting [Dy(Cp$^{ttt}$)$_2$]B(C$_6$F$_5$)$_4$ beats the previously discussed [Dy(O$^t$Bu)$_2$(py)$_5$] only slightly in terms of energy barrier (1277 cm$^{-1}$) but the blocking temperature of 60 K is unprecedented and much larger than observed in any compound before.[46,47]



[Dy(Cp$^{iPr4}$)$_2$]$^+$      [Dy(Cp$^{iPr4Me}$)$_2$]$^+$      [Dy(Cp$^{iPr4Et}$)$_2$]$^+$      [Dy(Cp$^{iPr5}$)$_2$]$^+$
**1**                          **2**                            **3**                            **4**
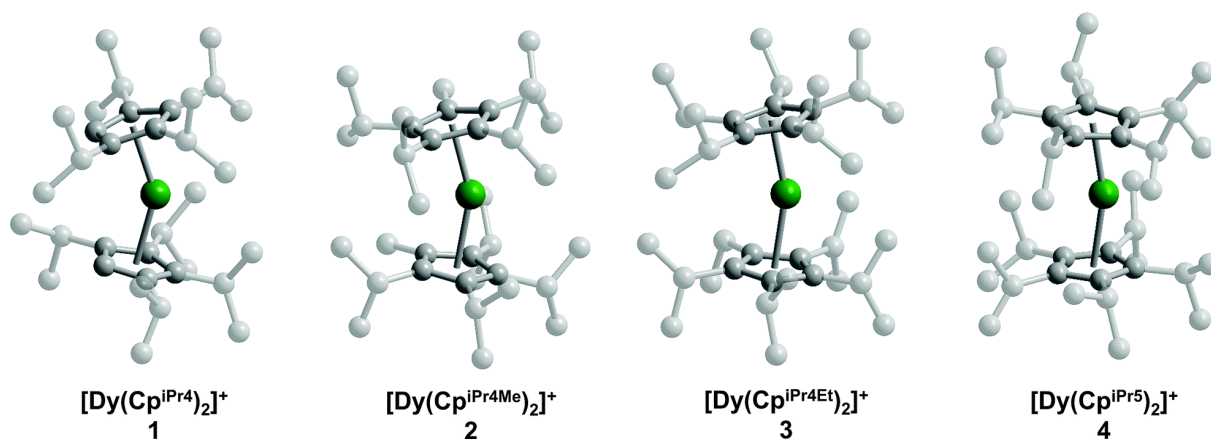
Figure 2.12: Different DyCp$_2^{-1}$ derivatives investigated by Long, Harvey et al.[48] – Published by The Royal Society of Chemistry.

While [Dy(Cp$^{ttt}$)$_2$Cl] shows strong mixing of m$_J$ states, in [Dy(Cp$^{ttt}$)$_2$]B(C$_6$F$_5$)$_4$ mixing of states was only present for m$_J$ states with higher energy. The authors of one of the papers explain this with the crystal field being closest to axiality than ever obtained for a dysprosium compound.[47] The still bent axis in which the ligands coordinate and the absence of symmetry hold against this and rather second the explanations of the authors of the other paper. The rigid coordination to the Cp ligands, contrary to more flexible metal-ligand bonds like with O$^t$Bu, seems to limit the accessible vibrational modes.[46] This explanation became even more reliable with the investigations of the magnetic properties of the system with modified ligands. These showed that although the consequent linearisation of the ligands' positions were conducted, no linear increase could be detected. From the compounds they investigated the one with one methyl group and four isopropyl groups on the Cp shows the best properties. The blocking temperature is significantly higher than with a hydrogen, an ethyl or an isopropyl group instead of the methyl group.[48] All this is topped by a modification of the Cp ligands with five methyl groups for only one of the ligands and five isopropyl groups for the other ligand. This [Dy(Cp$^{iPr5}$)(Cp$^*$)][B(C$_6$F$_5$)$_4$] has a blocking temperature of 78 K and an open hysteresis up to 80 K.[49] Different derivatives of DyCp$_2$$^{-1}$ derivatives are shown in Figure 2.12.

This short introduction outlines how successful interdisciplinary collaboration is for the field of molecular magnetism. The work of the inorganic chemists and the physicists build on each other to provide a leap from a basic idea and a first example of molecular magnetism to a bigger foundation of theoretical approaches and a system that works above the temperature of liquid nitrogen. All this was achieved in less than 30 years. However, not all work is done yet. Deeper understanding of spin-phonon coupling may be the next step on the physicists´ side and an air-stable system with comparable properties to [Dy(Cp$^{iPr5}$)(Cp$^*$)][B(C$_6$F$_5$)$_4$] may be the next step on the chemists' side.

# 3 OBJECTIVE

The field of single molecule magnets identified spin-phonon coupling as what needs to be understood in order to design molecules with slow magnetic relaxation at high temperatures. To date there is a lack of a suitable testbed to investigate these systematically. This testbed must provide enough flexibility for variations that can be set in comparison but it must be static enough that the comparisons remain meaningful. This thesis aims to deliberately modify the coordination environment of lanthanide complexes in order to investigate the impacts on the magnetic anisotropy and the relaxation paths of reversal of the magnetisation. As a second step the aim was to create high coordination symmetries on the lanthanide ion. To these ends, firstly, an asymmetric complex family with gradually varying coordination spheres at the lanthanide ion was designed. In order to function as a test bed system detailed structural descriptions were made. The basis for this system is a lanthanide ion chelated by a pentadentate Schiff-base ligand having a stable and essentially planar equatorial structure, which enables an easy exchange of the axial ligands. With these gradual variations, a test bed is created that makes the investigation of impacts on the magnetism and other properties caused by small changes of the coordination environment possible. Additionally, the symmetry of these systems is augmented by the coupling of the monomeric units via rare lanthanide-fluoride and lanthanide-peroxide bridges in a cooperative project with Prof. Jesper Bendix. Also here, the coupling atoms can be varied in order to explore the effects of the changes. Furthermore, higher symmetrical systems were targeted putting an emphasis on the influences of different structural factors on magnetic properties. For a 3-Met collaboration with Dr. Lena Scherthan and Prof. Dr. Volker Schünemann, a pentagonal bipyramidal lanthanide compound known from the literature was reproduced with $^{161}$Dy. The compound was used to investigate molecular vibrational modes. The same compound was synthesised with gadolinium as central ion showing that despite the isotropic ground state of the gadolinium slow magnetic relaxation can be observed.

# 4 RESULTS AND DISCUSSION

The research concept presented in this thesis is based on the idea of creating specific ligand fields around a given lanthanide ion which are favourable for slow magnetic relaxation. For $Dy^{3+}$, which has an oblate electron density in its $^6H_{15/2}$ ground state, it has been calculated that the ligand field with electrostatically strong ligands in the axial positions is suited to stabilise this ground state and reduce thermally activated processes by separating it from the other states.[16,93] However for applications, the blank equatorial sites cannot be without any ligands if the aim is to create a stable compound. With less negatively polarised and uncharged equatorial ligands, magnetic anisotropy can be retained. Grouping the ligands in certain symmetries quenches quantum tunnelling and forces the spin to use the anisotropically separated states for relaxation.[11,62]

## 4.1 Dysprosium Complexes with a Pentaaza Ligand

The research presented here builds on previous work performed at Karlsruhe Institute of Technology (KIT) and on results using this strategy in the chemical literature.[83,94-97] 2,6-Diacetylpyridinebis(2'-pyridylhydrazone) ($H_2$dapp) is a literature known pentadentate N5 ligand and was chosen to be used on dysprosium ions in order to create a stable environment that allows axial magnetic anisotropy and incremental structural variations for the investigation of the influence on the magnetic properties to be expected.[98-101]

The formation of the ligand was conducted *in situ* via a Schiff-base reaction in methanol.



Figure 4.1: Reaction scheme for the synthesis of the pentadentate Schiff-base ligand.

For all the complexes obtained, the chelate ligand formed the expected rather flat equatorial environment, but which was more or less helically-distorted around the lanthanide ion. Its tendency to be flat is due to the $sp^2$-hybridised hydrazone NH groups being involved in the huge, delocalised π-system of the ligand. As a result of the helicity, all the complexes obtained are of low symmetry. A video was prepared to aid in understanding the role of the helicity (see digital appendix) and the reader is also referred to some relevant literature.[99,102,103]

Because of the large variety of the synthesised complexes, they are divided into three groups for an easier overview but in terms of the scientific strategy to create a system that can provide deeper understanding in structure property relationship, they need to be seen as a whole.

### 4.1.1  Dysprosium Complexes with $H_2dapp$ and a Secondary Ligand

A general synthetic strategy for the formation of the compounds in this chapter is the one-pot synthesis of the complexes with 2-hydrazino pyridine and 2,6-diacetylpyridine $DyCl_3 \cdot 6H_2O$ and $Dy(NO_3)_3 \cdot 6H_2O$ as suitable dysprosium salts. For lanthanide-$H_2dapp$ complexes in the literature, the ligand was synthesised separately.[100,101] As second ligand type aquato, nitrate and acetate ligands were used for the complex synthesis. Depending on heating and crystallisation conditions, different crystal structures and molecular structures can be obtained using the same reaction mixture. Four different dysprosium complexes with homogenic second ligand type depicted in Figure 4.2 were synthesised.

$[Dy(H_2dapp)(H_2O)_4]Cl_3 \cdot 5H_2O$ **(1)** is only accessible via direct synthesis. The reaction with $DyCl_3 \cdot 6H_2O$ followed by evaporation of the solvent within one day leads to the formation of $[Dy(H_2dapp)(H_2O)_4]Cl_3 \cdot 5H_2O$ **(1)**. Single crystals were obtained when the evaporation of solvent was stopped with 1 ml of solvent remaining.

$[Dy(H_2dapp)(NO_3)_2]NO_3$ **(2)** and its chloride salt $[Dy(H_2dapp)(NO_3)_2]Cl_{0.92}(NO_3)_{0.08}$ **(3)** can both be obtained either directly using the $Dy(NO)_3 \cdot 6H_2O$ salt as starting material or by preparing a reaction mixture of $\{DyL(H_2O)_4\}$ **(1)** and adding two equivalents of $NaNO_3$. Mixing of a methanol solution of the ligand with a methanol 1:1 stoichiometric suspension of $Dy(NO_3)_3 \cdot 6H_2O$ at ambient conditions and subsequently heating gives trapezoid orange crystals after one day, which were suitable for single crystal measurements. If the solution is not heated, crystal structures with lattice water will be obtained having poorer crystallinity.

Figure 4.2: The four complexes with homogenic second ligand type {DyL(H$_2$O)$_4$} **(1)**, {DyL(NO$_3$)$_2$} **(2)**, {DyL(NO$_3$)$_2$} **(3)** and {DyL(Ac)$_2$} **(4)**. Colour code: white = H; grey = C; blue = N; red = O; light green = Cl; lilac = Dy.

[Dy(H$_2$dapp)(Ac)$_2$]Cl **(4)** was obtained by adding 2/3 equivalent of sodium acetate to the reaction mixture of {DyL(H$_2$O)$_4$} **(1)**. [Dy(H$_2$dapp)(Ac)$_2$]Ac cannot be synthesised directly with only Dy(Ac)$_3$·6H$_2$O and the ligand. Most probably, this is the case because the acetate anion cannot support hydrogen bonds in the same way the nitrate anions do. This will be discussed in more detail below where the crystal structures are described. As an overview, the reaction schemes are depicted in Figure 4.3.

Figure 4.3: Reaction scheme for dysprosium complex synthesis of $[Dy(H_2dapp)(H_2O)_4]Cl_3 \cdot 5H_2O$ **(1)**, $[Dy(H_2dapp)(NO_3)_2]NO_3$ **(2)**, $[Dy(H_2dapp)(NO_3)_2]Cl_{0.92}(NO_3)_{0.08}$ **(3)** and $[Dy(H_2dapp)(Ac)_2]Cl$ **(4)**.

The molecular structures of the complexes with these pentadentate chelate ligands require a more complicated description than is usually the case with macrocycles like porphyrins and phthalocyanines. In contrast to macrocyclic ligands, the terminal pyridines of this chelate ligand are not directly bonded, allowing an additional degree of freedom. It cannot only bend but also helically distort. The position of the lanthanide ion relative to the chelate ligand can vary not only considering the ligand as a whole but also relative to every single nitrogen ligand atom. This helical distortion comes from the steric constraints of the ligand has to overcome when it coordinates to an ion. If the ligand were perfectly flat the (6-)hydrogens on the terminal pyridine rings would already be close enough for unfavourable steric interaction, which can be seen in a space filling model after drawing the structure in Chem3D and minimising the steric energy with the MM2 software package (Figure 4.4).[104]



Figure 4.4: Space filling model of the ligand with minimised sterical energy. Green lines: area where the hydrogens on the 6-position of the terminal pyridine rings come close to each other.

On coordination to a lanthanide ion, the two terminal pyridine rings are pulled even closer together making this steric problem even worse. The ligand could either bend or helically distort to overcome this (Figure 4.5). In most cases, however, it is a helical distortion which is observed.

Figure 4.5: **(a)** Bending and **(b)** helical distortion of the chelate ligand.

This concept of helical distortion was developed and used by others for similar compounds such as the polycyclic aromatic molecules known as helicenes.[102,103] However, it is not easy to visualise from the static pictures and the reader is referred to the digital appendix.

The usual quantification methods for helices such as diameter and pitch cannot be used since there is no 360° coil and the distortion is not regular over the whole ligand. This might not be intuitive since the objection could be made that smaller than 360° helixes could be seen as 360/n part of a helix. However, this only works if it is a regular helix because only in these the slopes and the diameters always stay the same per definition of the word regular. If the helix is not regular in terms of slope and diameter the core problem can be seen as how to fit it best to the few reference points. More drastically described an optimal helix consists of infinite data points because the slope in every single point being the same. If one starts to decrease the number of points that describe the helix, steps will appear. As soon as it is smaller than 360° one can only assume that they stay regular to extract the information for a turn of 360°. If they are not regular, as in the case of these molecules, the assumption one makes about the rest of the helix becomes arbitrary because one can fit different helixes with varying diameters and relative angles to the object. In order to quantify the helical distortion in the irregular helical molecules, the two dihedral angles $\alpha$ and $\beta$ shown in Figure 4.6 (a) were measured.

Figure 4.6: Measuring strategy of the helical distortion. **(a)** Dihedral angles $\alpha$ and $\beta$ between the planes constructed by the position of three atoms. Each group of three is colour coded. **(b)** and **(c)** Two of these planes, the green and the blue one. **(c)** Angle $\alpha$ in the molecule. **(d)** and **(e)** Schemes of the 2D side view with the angles $\alpha$ and $\beta$. **(d)** Situation with dysprosium on the height of the middle pyridine. **(e)** Dysprosium shifted downwards. The dashed lines show the outlined positions of the Dy-N bonds without shifting. The red marked angle is the change in $\alpha$ and $\beta$ that does not compensate by taking the absolute value of the sum of the angles $\delta$.

In Figure 4.6 (b) and (e), it can be seen that one of the angles characterises the helical distortion of half the molecule from the central pyridine ring to one of the terminal pyridine nitrogens. Taking the absolute value of the sum of these torsion angles as

described in equation (14) $\delta$ as a measure of helicity has the advantage that the tilting of the central pyridine ring levels out. This can be seen in Figure 4.6 (d) and (e).

$$\delta = |\alpha + \beta| \tag{14}$$
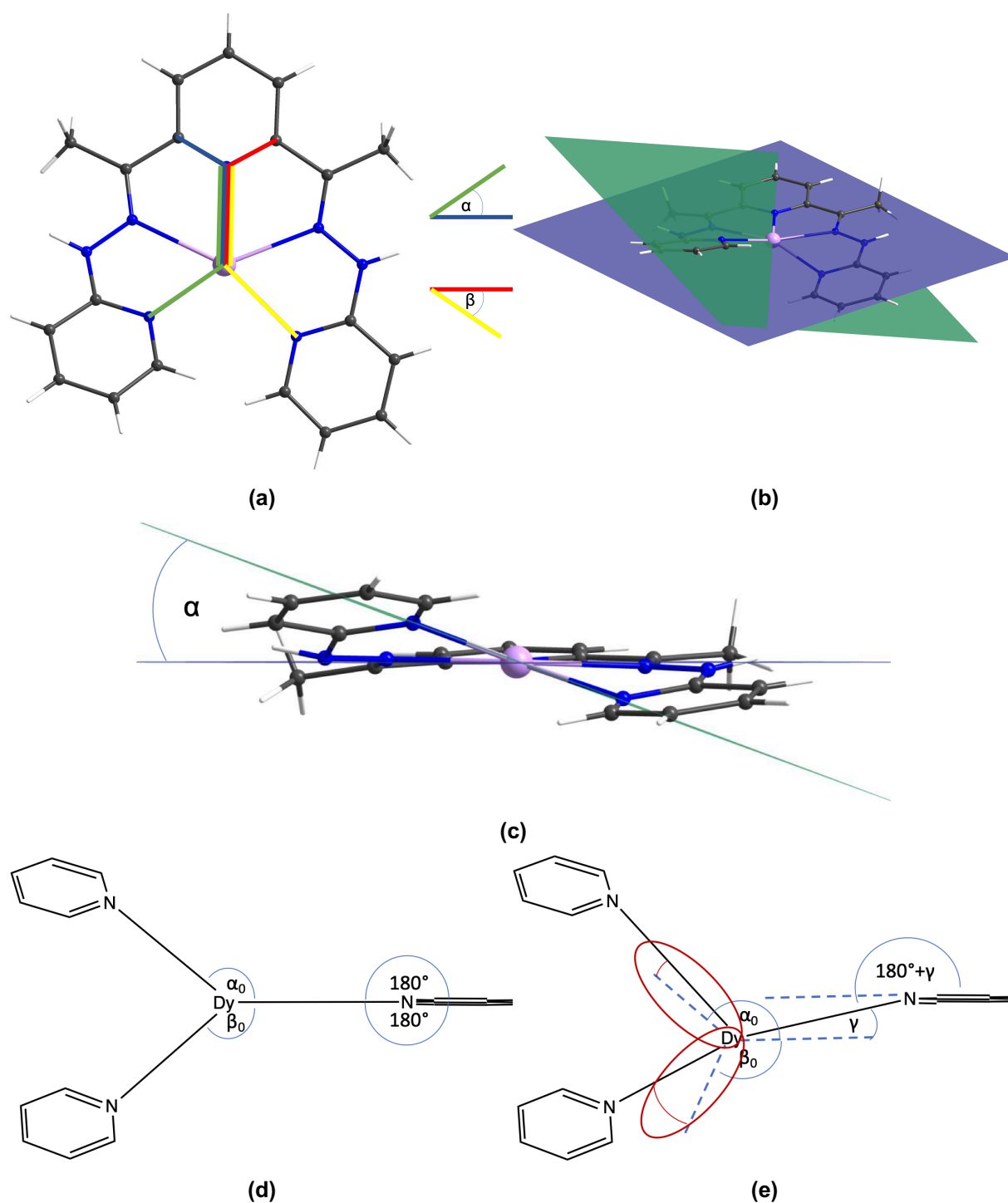
However, the relative position of the dysprosium does not level out completely as outlined by the red marked angles which represent the changes of $\alpha$ and $\beta$, respectively. As illustrated in the graphics in Figure 4.6, the changes in the two angles (here $\alpha$ and $\beta$) compensate to some extent but not completely. Since the relative position of the dysprosium ion relative to the ligand does not change dramatically and the influence of the position of the dysprosium ion is not huge, these inaccuracies can be accepted. The results are shown in Table 4.1.

Table 4.1: Helical distortion values for $\{DyL(H_2O)_4\}$ **(1)**, $\{DyL(NO_3)_2\}$ **(2)**, $\{DyL(NO_3)_2\}$ **(3)** and $\{DyL(Ac)_2\}$ **(4)**.
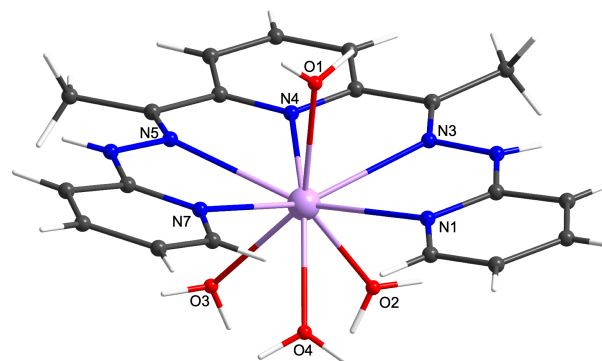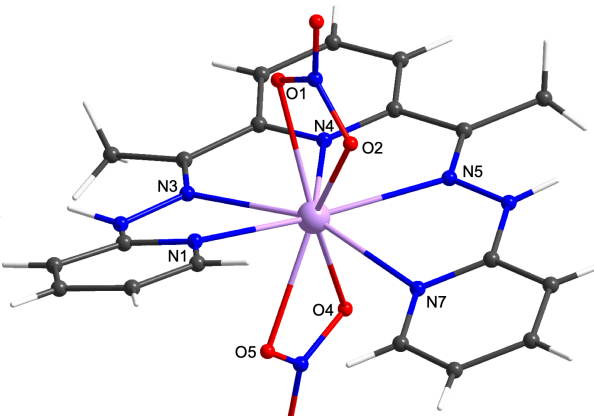
| Compound | $\alpha/°$ | $\beta/°$ | $\delta/°$ |
|:---:|:---:|:---:|:---:|
| **(1)** | 32.0 | -23.8 | **8.2** |
| **(2)** | -22.9 | -20.5 | **43.4** |
| **(3)** | -26.9 | -22.9 | **49.7** |
| **(4)** | -20.4 | -15.7 | **36.0** |

Comparing the values obtained for the helicity, it is noticable how much they vary. The lowest $\delta$ value found is 8.2° for complex $\{DyL(H_2O)_4\}$ **(1)** and the strongest helicity can be found in $\{DyL(NO_3)_2\}$ **(3)** showing a $\delta$ value of 49.7°. The other complexes $\{DyL(NO_3)_2\}$ **(2)** and $\{DyL(Ac)_2\}$ **(4)** also show strong helicity and big distortion $\delta$ values of 43.4° and 36.0°. From a first affect viewing these values, one could attribute the much smaller helical distortion in $\{DyL(H_2O)_4\}$ **(1)** to the fact that it is the only complex of the four which has its secondary ligands not equally distributed on both sides of the chelate ligand. In $\{DyL(H_2O)_4\}$ **(1)**, one water is on one side and the other three waters are on the other side while in $\{DyL(NO_3)_2\}$ **(2)**, $\{DyL(NO_3)_2\}$ **(3)** and $\{DyL(Ac)_2\}$ **(4)**, the ligands are distributed equally on both sides of the ligand. This could be seen as a better positioning of the dysprosium in the centre of the chelate ligand which results in a stronger helical distortion instead of a bending of the ligand. However in the next subchapters, there will be complexes described with non-equal distribution of the secondary ligands which also show strong helicity. It also needs to be regarded that in

---

(14): Calculation of the $\delta$ value as a measure of helicity.

some cases the signs of $\alpha$ and $\beta$ are both positive or both negative and in other cases one is positive and the other one is negative. Given that the signs reflect the relative motion of the arms of the ligand to each other, same signs show helicity whilst opposite signs show a folding rather than helicity. This means for {DyL(H$_2$O)$_4$} **(1)** although the helicity of the molecule is not particularly pronounced, it still shows a non negligible folding. Intriguingly, the distortion angles of the two different salts of the complex with nitrate as secondary ligand {DyL(NO$_3$)$_2$} **(2)** and {DyL(NO$_3$)$_2$} **(3)** differ significantly. As already mentioned, the $\delta$ value of {DyL(NO$_3$)$_2$} **(3)** is 49.7°. In contrast to that, it is only 43.4° in the nitrate salt {DyL(NO$_3$)$_2$} **(2)**. It can already be said that both crystallise in the same space group, which will be discussed later in detail, and that {DyL(NO$_3$)$_2$} **(3)** crystallises with a smaller unit cell and therefore higher density. Complex {DyL(Ac)$_2$} **(4)** is less helically distorted at 36.0° and also crystallises in the same space group but with larger unit cell parameters than {DyL(NO$_3$)$_2$} **(2)** and {DyL(NO$_3$)$_2$} **(3)**. From these findings, it can be said that the crystal packing with other counter ions has an influence on the coordination sphere of the complexes since effectively this is the only change between {DyL(NO$_3$)$_2$} **(2)** and {DyL(NO$_3$)$_2$} **(3)** and that smaller unit cell parameters can be correlated with the stronger distortions in the molecules presented.

Table 4.2: Bond lengths and angles for {DyL(H$_2$O)$_4$} **(1)**, {DyL(NO$_3$)$_2$} **(2)**, {DyL(NO$_3$)$_2$} **(3)** and {DyL(Ac)$_2$} **(4)**.



| (1) | | | (2) | | |
|-----|-----|-----|-----|-----|-----|
| Atom | Atom | Length/Å | Atom | Atom | Length/Å |
| Dy1 | O1 | 2.329(2) | Dy1 | O1 | 2.4534(13) |
| Dy1 | O2 | 2.360(2) | Dy1 | O2 | 2.3884(12) |
| Dy1 | O3 | 2.463(3) | Dy1 | O4 | 2.4648(12) |
| Dy1 | O4 | 2.392(2) | Dy1 | O5 | 2.4189(12) |
| Dy1 | N1 | 2.563(3) | Dy1 | N1 | 2.4900(14) |
| Dy1 | N3 | 2.543(3) | Dy1 | N3 | 2.4406(14) |
| Dy1 | N4 | 2.526(2) | Dy1 | N4 | 2.4193(13) |
| Dy1 | N5 | 2.563(3) | Dy1 | N5 | 2.4626(13) |
| Dy1 | N7 | 2.583(3) | Dy1 | N7 | 2.4522(13) |

| Atom | Atom | Atom | Angle/° |
|---|---|---|---|
| N1 | Dy1 | N3 | 63.36(8) |
| N3 | Dy1 | N4 | 62.46(8) |
| N4 | Dy1 | N5 | 61.95(8) |
| N5 | Dy1 | N7 | 62.17(8) |
| N1 | Dy1 | N7 | 98.39(9) |
| O2 | Dy1 | O4 | 72.84(9) |
| O3 | Dy1 | O4 | 72.49(9) |
| O1 | Dy1 | N1 | 75.82(9) |
| O1 | Dy1 | N3 | 73.89(9) |
| O1 | Dy1 | N4 | 80.69(9) |
| O1 | Dy1 | N5 | 76.91(9) |
| O1 | Dy1 | N7 | 75.32(9) |

| Atom | Atom | Atom | Angle/° |
|---|---|---|---|
| N1 | Dy1 | N3 | 65.17(5) |
| N3 | Dy1 | N4 | 66.09(5) |
| N4 | Dy1 | N5 | 65.45(5) |
| N5 | Dy1 | N7 | 65.16(4) |
| N1 | Dy1 | N7 | 102.69(4) |
| O1 | Dy1 | O2 | 52.77(4) |
| O4 | Dy1 | O5 | 52.42(4) |
| O1 | Dy1 | O4 | 144.23(4) |
| O1 | Dy1 | O5 | 146.59(5) |
| O2 | Dy1 | O4 | 151.25(5) |
| O2 | Dy1 | O5 | 131.96(4) |



**(3)**



**(4)**
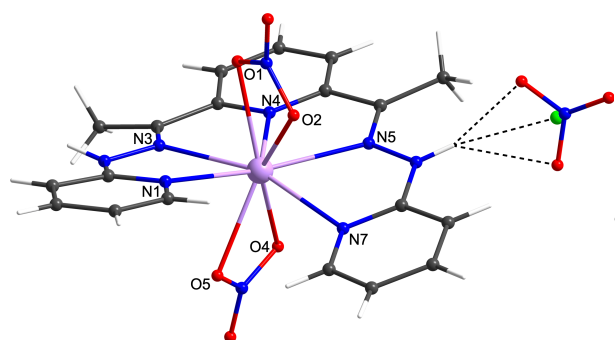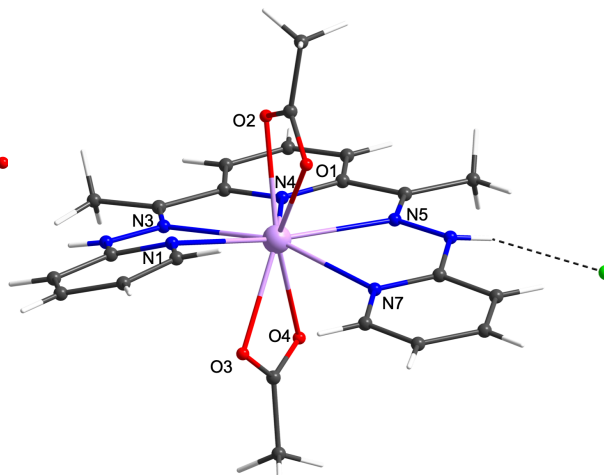
| Atom | Atom | Length/Å |
|---|---|---|
| Dy1 | O1 | 2.433(3) |
| Dy1 | O2 | 2.378(3) |
| Dy1 | O4 | 2.461(3) |
| Dy1 | O5 | 2.418(3) |
| Dy1 | N1 | 2.501(3) |
| Dy1 | N3 | 2.450(3) |
| Dy1 | N4 | 2.429(3) |
| Dy1 | N5 | 2.467(3) |
| Dy1 | N7 | 2.465(3) |

| Atom | Atom | Atom | Angle/° |
|---|---|---|---|
| N1 | Dy1 | N3 | 64.87(9) |
| N3 | Dy1 | N4 | 65.65(10) |
| N4 | Dy1 | N5 | 64.90(10) |
| N5 | Dy1 | N7 | 65.05(9) |
| N1 | Dy1 | N7 | 103.93(9) |
| O1 | Dy1 | O2 | 53.04(9) |
| O4 | Dy1 | O5 | 52.42(9) |
| O1 | Dy1 | O4 | 145.82(9) |
| O1 | Dy1 | O5 | 145.76(10) |
| O2 | Dy1 | O4 | 151.71(10) |
| O2 | Dy1 | O5 | 129.43(9) |

| Atom | Atom | Length/Å |
|---|---|---|
| Dy1 | O1 | 2.408(2) |
| Dy1 | O2 | 2.412(3) |
| Dy1 | O3 | 2.379(3) |
| Dy1 | O4 | 2.410(2) |
| Dy1 | N1 | 2.505(3) |
| Dy1 | N3 | 2.517(3) |
| Dy1 | N4 | 2.475(3) |
| Dy1 | N5 | 2.507(3) |
| Dy1 | N7 | 2.512(3) |

| Atom | Atom | Atom | Angle/° |
|---|---|---|---|
| N1 | Dy1 | N3 | 63.67(10) |
| N3 | Dy1 | N4 | 63.86(11) |
| N4 | Dy1 | N5 | 64.12(10) |
| N5 | Dy1 | N7 | 63.65(11) |
| N1 | Dy1 | N7 | 107.97(10) |
| O1 | Dy1 | O2 | 53.66(9) |
| O3 | Dy1 | O4 | 53.86(10) |
| O1 | Dy1 | O3 | 119.16(10) |
| O1 | Dy1 | O4 | 151.08(10) |
| O2 | Dy1 | O3 | 155.38(11) |
| O2 | Dy1 | O4 | 145.17(10) |

All four molecules {DyL(H$_2$O)$_4$} **(1)**, {DyL(NO$_3$)$_2$} **(2)**, {DyL(NO$_3$)$_2$} **(3)** and {DyL(Ac)$_2$} **(4)** have a dysprosium central ion coordinated to the five nitrogens of the pentadentate chelate ligand and to four oxygen atoms stemming from a second ligand type. For

{DyL(H$_2$O)$_4$} **(1)**, this second ligand type is water. For {DyL(NO$_3$)$_2$} **(2)** and for {DyL(NO$_3$)$_2$} **(3)**, this second ligand type is nitrate and for {DyL(Ac)$_2$} **(4)**, it is acetate. In Table 4.2, the bond lengths and bond angles are listed for **(1)-(4)**. The bond lengths between dysprosium and nitrogen are all in a range expected for a Dy-N coordination bond. With values between 2.4 Å and 2.6 Å, they are in a range which represents 54 % of the structures with Dy-N bond in the CSD. 92 % of the structures with Dy-N bond in the CSD have Dy-N bond lengths in the range 2.3 Å to 2.7 Å.

{DyL(H$_2$O)$_4$} **(1)** shows the longest dysprosium nitrogen bonds of the four compounds. The average Dy-N bond length in {DyL(H$_2$O)$_4$} **(1)** is 2.56 Å. In {DyL(Ac)$_2$} **(4)**, it is only 2.5 Å and in {DyL(NO$_3$)$_2$} **(3)** and {DyL(NO$_3$)$_2$} **(2)**, it is 2.46 Å and 2.45 Å, respectively. In each of the complexes, the Dy-N bond lengths vary. The shortest Dy-N bonds are the Dy-N4 bonds in all four complexes.

The dysprosium-oxygen bond lengths are shorter in the water complex than in the complexes with the anionic ligands, which is usual. 73 % of the dysprosium structures with a water ligand in the CSD have Dy-O bond lengths smaller than 2.4 Å while only 7 % of the structures with nitrate ligand have smaller Dy-O bond lengths than 2.4 Å. All four complexes have Dy-O bonds with comparatively small bond lengths. As already mentioned, the Dy-O bonds in {DyL(NO$_3$)$_2$} **(2)** and {DyL(NO$_3$)$_2$} **(3)** with bond lengths less than 2.4 Å are remarkably short. The Dy-O1 bond length in the water complex {DyL(H$_2$O)$_4$} **(1)** that is shorter than 2.35 Å falls under a group of reported structures with water ligands in the CSD with 31 % of the shortest bond lengths between dysprosium and the water oxygen. The fact that this bond is shorter can be expected since the chelate ligand leaves space for the single water coordinated from this side in relation to the ligand. On the other hand, complex {DyL(H$_2$O)$_4$} **(1)** has a Dy-O bond longer than 2.45 Å while only 21 % of the structures in the CSD with a dysprosium water bond contain a dysprosium water bond that is longer than 2.45 Å. Intriguingly, this bond in {DyL(H$_2$O)$_4$} **(1)** is Dy-O3 although the O3 water molecule is on the side where the arm of the ligand is distorted away from the water which should give it more space for a closer coordination. Complex {DyL(Ac)$_2$} **(4)** has a Dy-O bond length smaller than 2.4 Å while of the reported structures with acetate ligands in the CSD only 35 % have smaller than 2.4 Å Dy-O bond lengths between their dysprosium and their acetate ligand. The average Dy-O bond lengths in all complexes are within usual parameters. In {DyL(H$_2$O)$_4$} **(1)**, this is 2.39 Å, in {DyL(NO$_3$)$_2$} **(2)** 2.43 Å, in {DyL(NO$_3$)$_2$} **(3)** 2.42 Å and in {DyL(Ac)$_2$} **(4)** 2.40 Å.

If one looks at the bond angles, the ligand constrains the angles that can be expected between the dysprosium and two of the nitrogen atoms. The rigid ligand constrains this angle to ca 62°-66°. There are smaller angles between dysprosium and next neighbouring coordinating nitrogen atoms within the pentadentate ligand (green angles in Figure 4.7) and a bigger angle between the dysprosium and the terminal pyridine nitrogens. The green angles are all 62-66°, with two $sp^2$ ligand atoms between each pair of nitrogens. By a stronger helical distortion, these firstly mentioned angles increase as given the helicity they are not constraint to add up to 360°. This can be seen in Table 4.2 for the angles depicted in green in Figure 4.7.
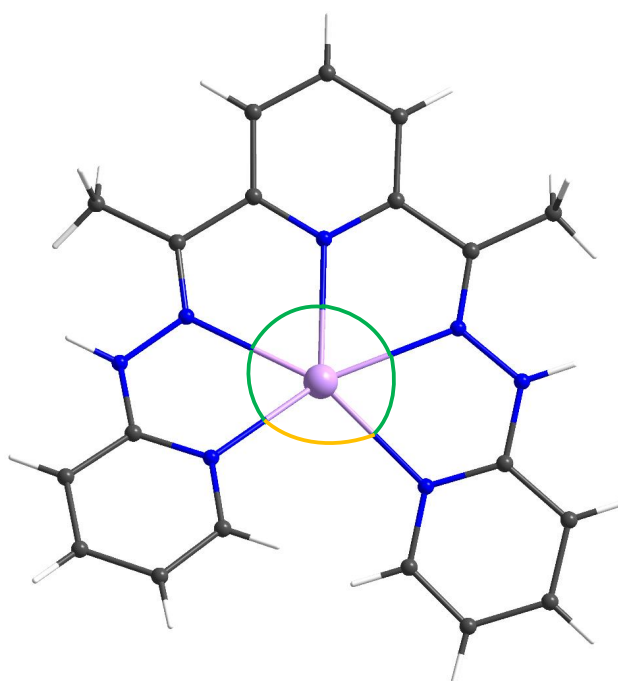


Figure 4.7: Bond angles between the dysprosium and the coordinating nitrogens. Angles depicted in green are within the ligand. The angle depicted in yellow is between the dysprosium and the two terminal pyridine nitrogens.

In {DyL(H$_2$O)$_4$} **(1)** the average of these angles is 62.5°. In {DyL(NO$_3$)$_2$} **(2)** it is 65.2°. In {DyL(NO$_3$)$_2$} **(3)** it is 65.1° and in {DyL(Ac)$_2$} **(4)** it is 63.8°. Although the difference between {DyL(NO$_3$)$_2$} **(2)** and {DyL(NO$_3$)$_2$} **(3)** is small, this concurs with the findings from the quantification of helicity by the dihedral angles qualitatively. The angle between dysprosium and the terminal pyridine nitrogen, which is depicted in yellow in Figure 4.7, has to be seen more as a compensation for all other distortions within the complexes. If for example there are two complexes with the same Dy-N bond lengths and one has a stronger helical distortion, the two terminal pyridine rings can move closer together because their 6-H atoms can avoid each other better. This means as a

result, the yellow angle in Figure 4.7 becomes smaller although the bond lengths are the same. Also, if the molecule folds instead of distorting helically, the yellow angle becomes smaller as a result. For all molecules an anchor axis can be defined in order to quantify the relative position of the secondary ligands.
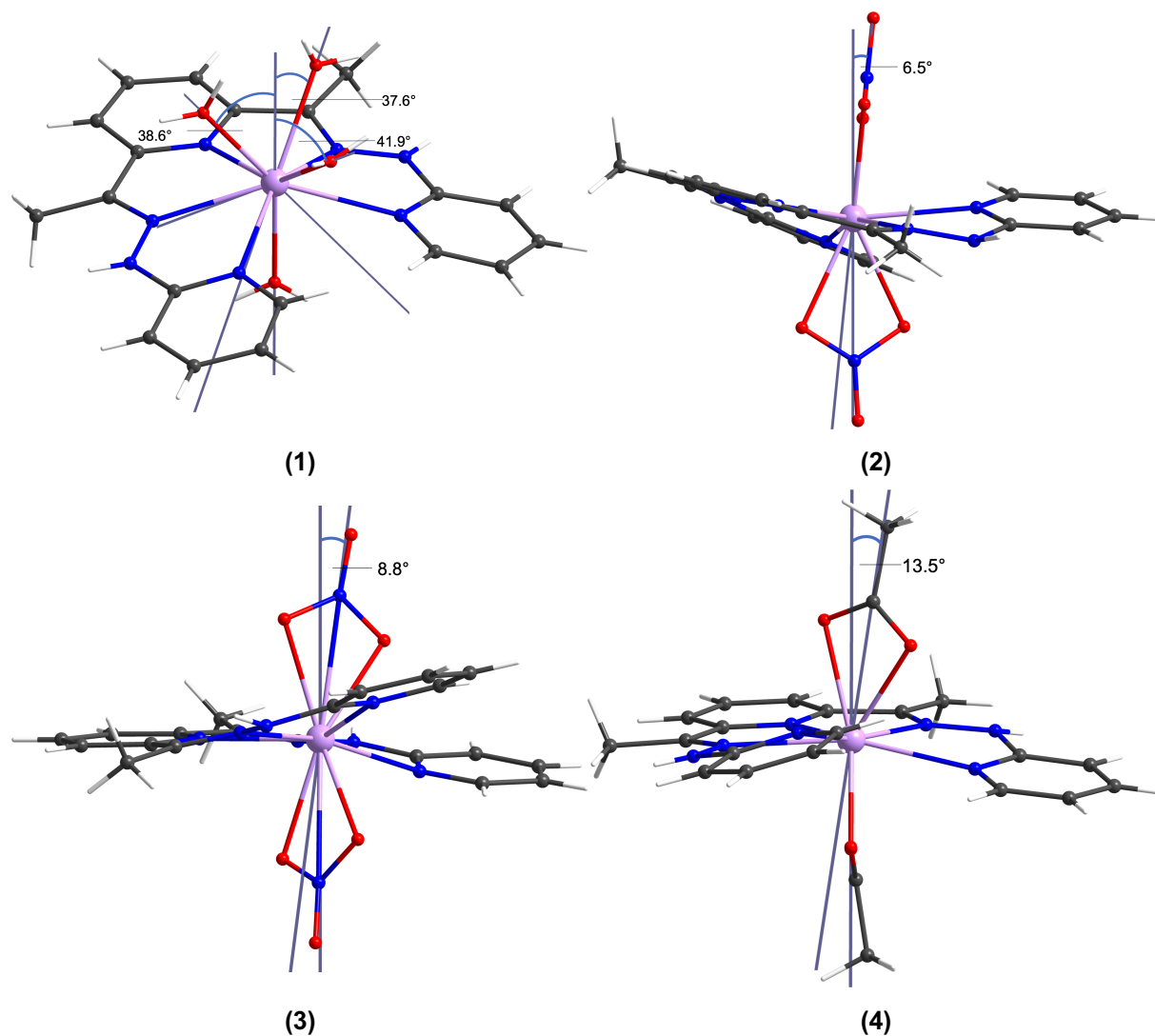


Figure 4.8: Angles between anchor axes and secondary ligands of {DyL($H_2O$)$_4$} **(1)**, {DyL($NO_3$)$_2$} **(2)**, {DyL($NO_3$)$_2$} **(3)** and {DyL(Ac)$_2$} **(4)**.

This anchor axis either represents the bond vector between the dysprosium and the single secondary ligand or, in the case with only two secondary ligands, one is chosen since the relative position of the two ligands is not influenced by this decision.

In Figure 4.8, it can be seen that the Dy-O bonds with the three water ligands on the other side relative to the pentadentate ligand in {DyL($H_2O$)$_4$} **(1)** vary in their deviation angle to the anchor axis. The water above the gap of the $H_2$dapp ligand has a Dy-O bond which deviates stronger than the other two. It can also be seen that the nitrate

ligands are closer to alignment than the acetate ligands in {DyL(Ac)$_2$} **(4)**. Concerning the O-Dy-O angles it can be seen that the bidentate capping ligands coordinate asymmetrically like it is known for lanthanide compounds with nitrate ligands.[105]
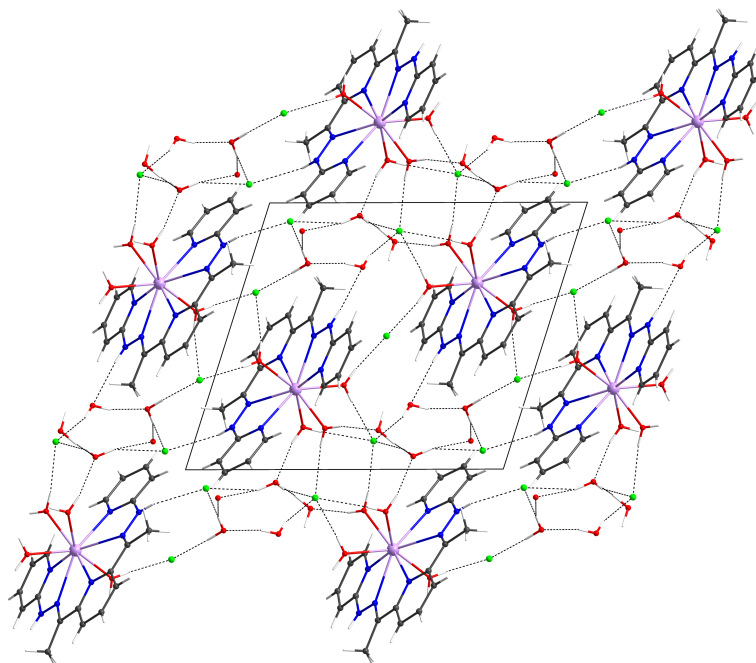


a

**(1)**
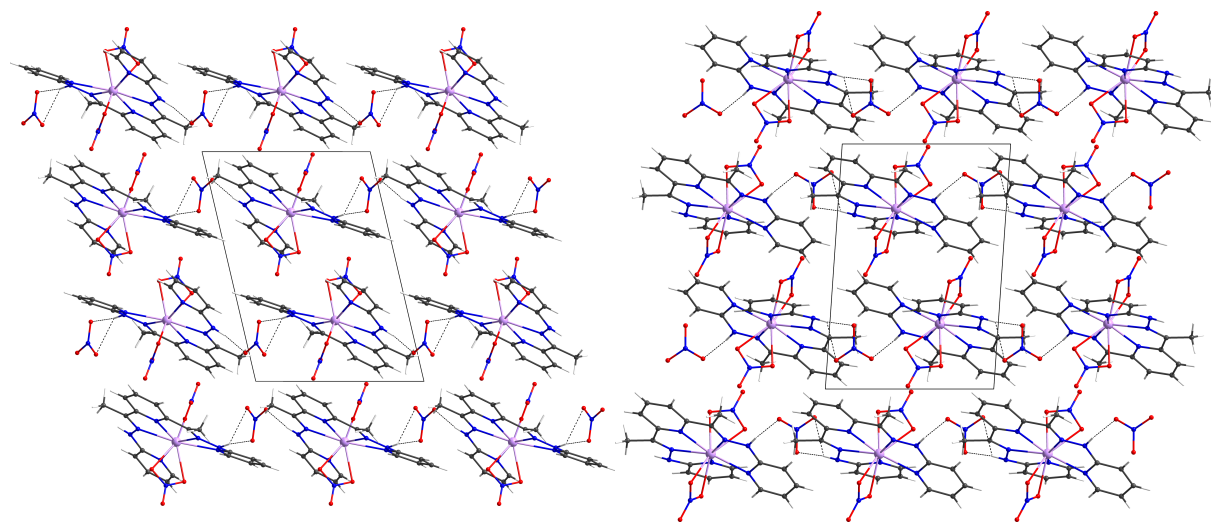


a                                                                          b

**(2)**
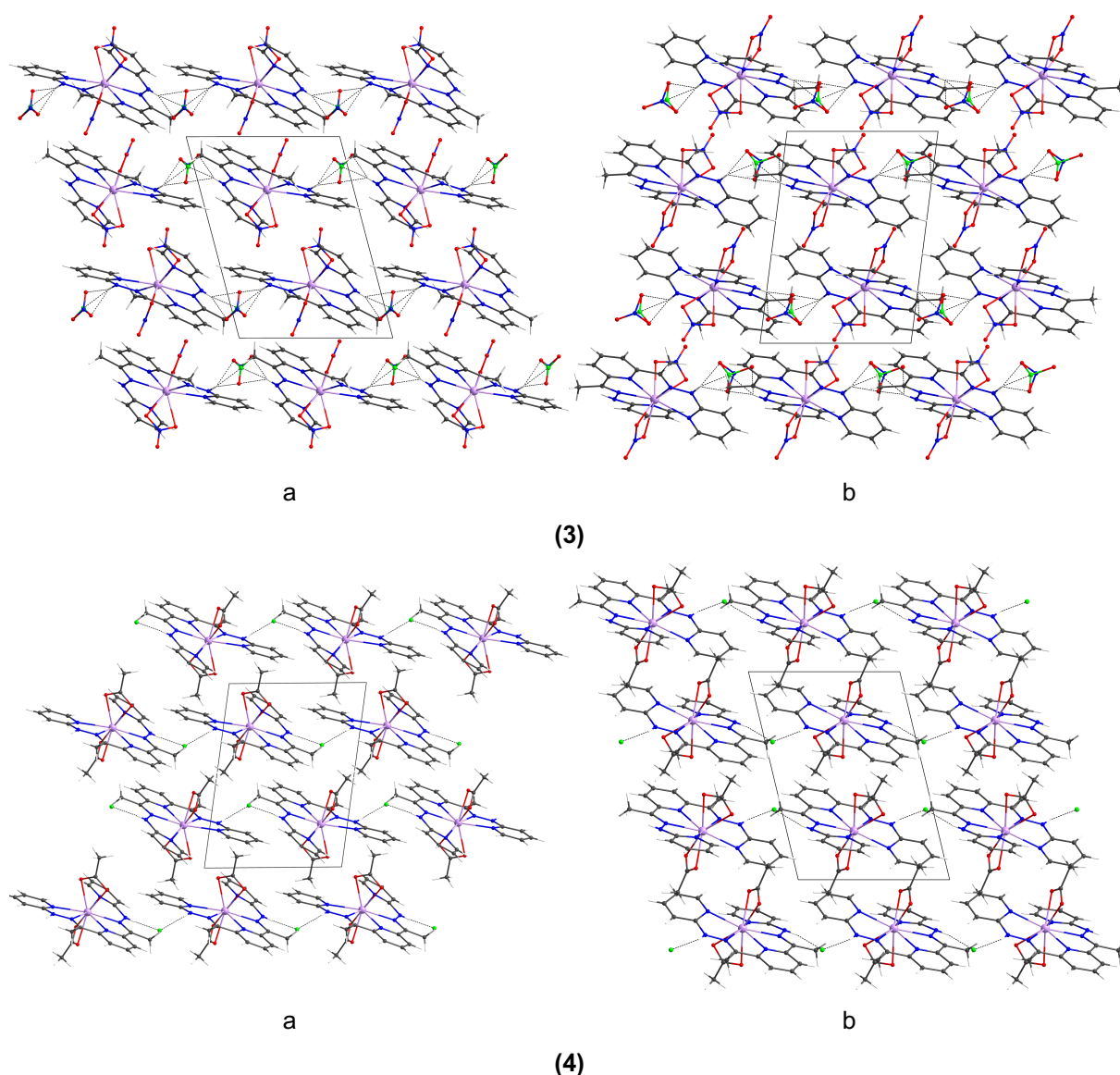
Figure 4.9: Crystal packing of {DyL(H$_2$O)$_4$} **(1)**, {DyL(NO$_3$)$_2$} **(2)**, {DyL(NO$_3$)$_2$} **(3)** and {DyL(Ac)$_2$} **(4)** with viewing direction underneath.

All four compounds crystallise in the space group P$\bar{1}$. A centrosymmetric space group is usual for enantiomeric compounds since it improves their packing. The asymmetric unit of {DyL(H$_2$O)$_4$} **(1)** contains [Dy(H$_2$dapp)(H$_2$O)$_4$]Cl$_3$·5H$_2$O with one chloride on the inversion centre and the other half of it disordered with a water molecule. Another half-occupied position of water leads to an integer number of water molecules. The other three crystal structures, {DyL(NO$_3$)$_2$} **(2)**, {DyL(NO$_3$)$_2$} **(3)** and {DyL(Ac)$_2$} **(4)**, are related and differ mostly in their density as the unit cell parameters reveal (section 8.1). In {DyL(Ac)$_2$} **(4)** the assignment of the axes is different to {DyL(NO$_3$)$_2$} **(2)** and {DyL(NO$_3$)$_2$} **(3)** in the way that axes a and b are changed. This can be seen in the figures of the packing. For {DyL(Ac)$_2$} **(4)** the difference to the corresponding pictures for {DyL(NO$_3$)$_2$} **(2)** and {DyL(NO$_3$)$_2$} **(3)** arises from a translation along the cell axis c

corresponding to half the interplanar distance (Figure 4.9). This is not necessarily intuitive since the methyl group of the acetate is bulkier than the oxygen of the nitrate. In all three crystal structures, the asymmetric units are free of lattice solvents. They contain $[Dy(H_2dapp)(NO_3)_2]NO_3$ **(2)**, $[Dy(H_2dapp)(NO_3)_2]Cl_{0.92}(NO_3)_{0.08}$ **(3)** and $[Dy(H_2dapp)(Ac)_2]Cl$ **(4)**. This dense packing leads to a very close contact of one of the coordinating nitrates with the nitrate ligand of a next neighbouring complex in the two nitrate complexes $\{DyL(NO_3)_2\}$ **(2)** and $\{DyL(NO_3)_2\}$ **(3)**. The contact between the nitrates is closer than the sum of the van der Waals radii in both structures. The denser packing of $\{DyL(NO_3)_2\}$ **(3)** is reflected by the smaller distance of the nitrates with 2.95 Å which is shown in detail in Figure 4.10 (b). This is 0.08 Å smaller than in $\{DyL(NO_3)_2\}$ **(2)** (3.03 Å, Figure 4.10 (a)) and 0.12 Å smaller than the sum of the van der Waals radii of oxygen and nitrogen (3.07 Å). This kind of stacking between nitrates is known but usually occurs intramolecular or for nitrate counter ions.[106] In $\{DyL(Ac)_2\}$ **(4)**, there is more steric hindrance due to the methyl group of the acetate ligands. In contrast, the bulky acetate methyls prevent such a close approach of two acetates. To put it another way, planar nitrates can be involved in π-stacking, particularly if the formally positive N of one nitrate lies close to a formally negative oxygen of the other with a nitrogen-oxygen distance of just over 3 Å being much shorter than typical π-stacking between aromatics (3.4-3.6 Å). The structure responds to this fact with a 4.19 Å distance between the acetates of the two neighbouring complexes (Figure 4.10 (c)) which seems to be a result of the influence of the hydrogen bonding to the lattice anion. This can also be concluded from the fact that, as already mentioned, with anions that are not able to form bridges via hydrogen bonding such as acetate the crystallisation of the complexes does not seem to work. Additionally, the exchange of the counter ion leads to a denser packing and stronger helicity in $\{DyL(NO_3)_2\}$ **(3)**.

**(2)**



**(3)**

**(4)**
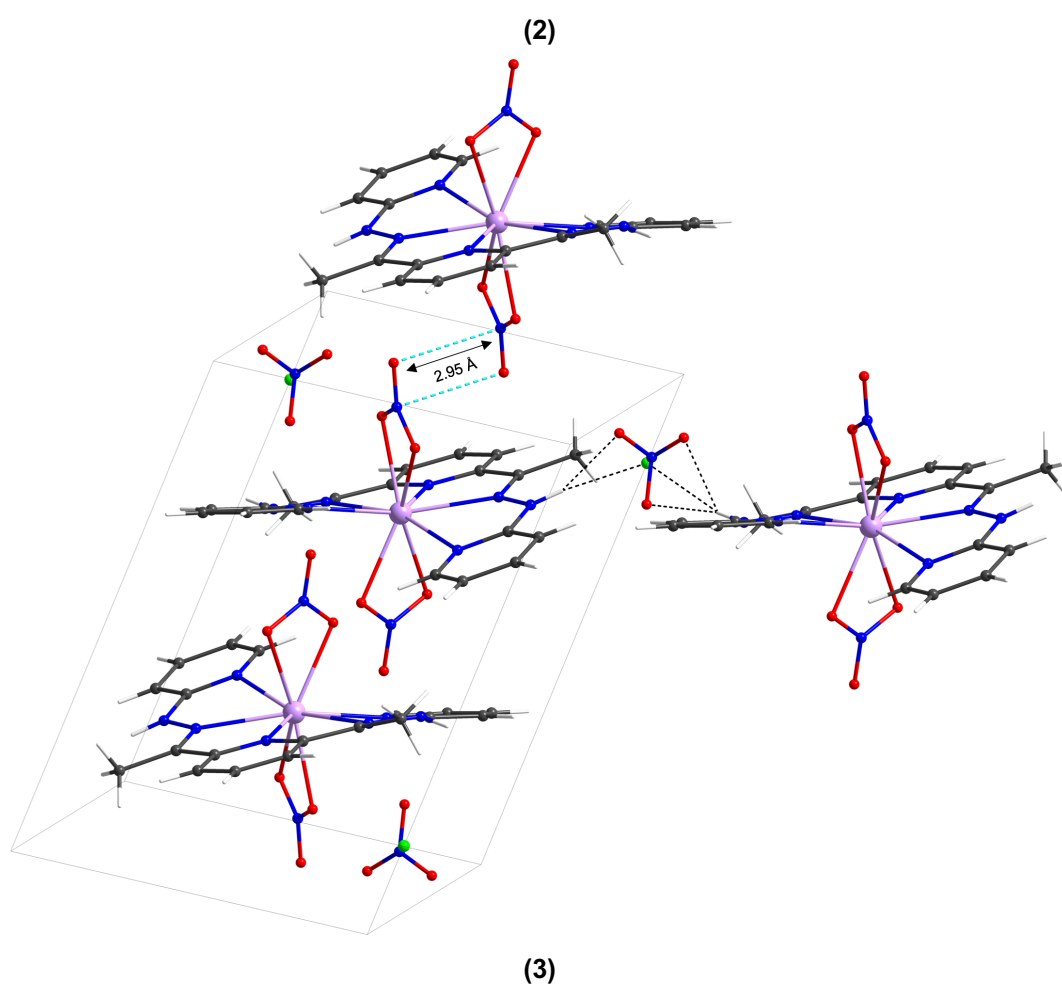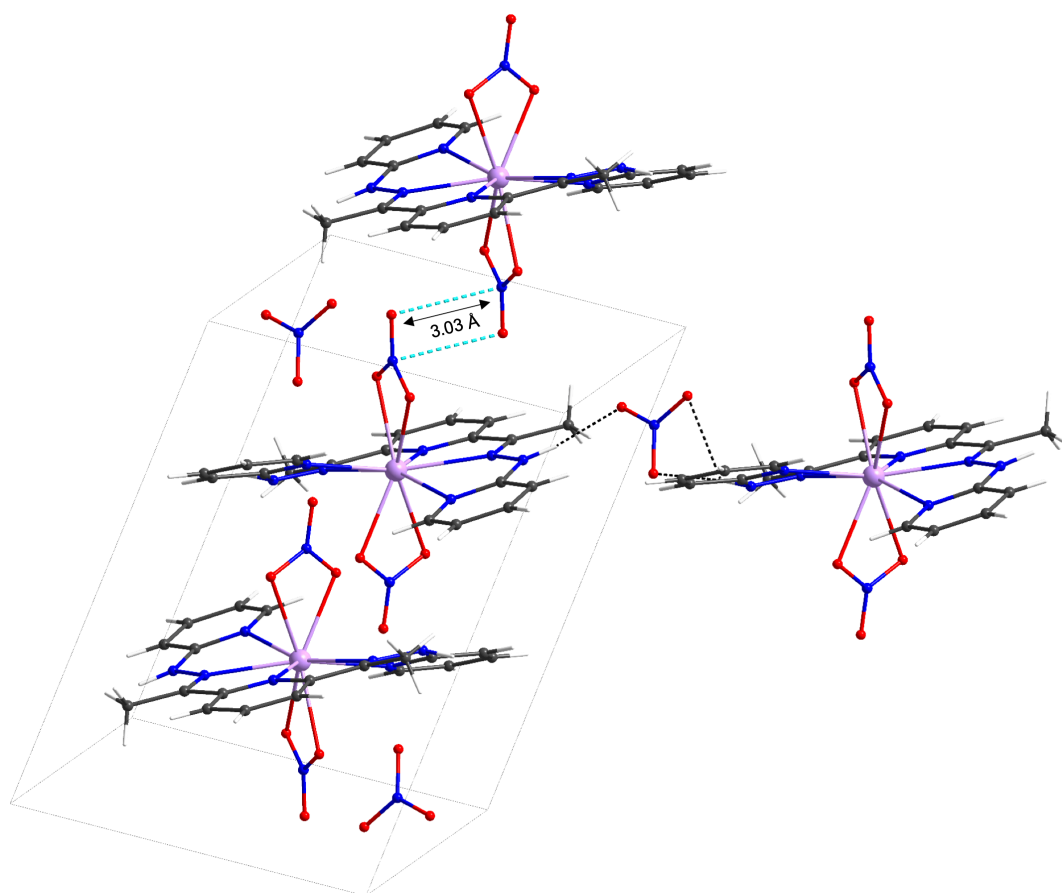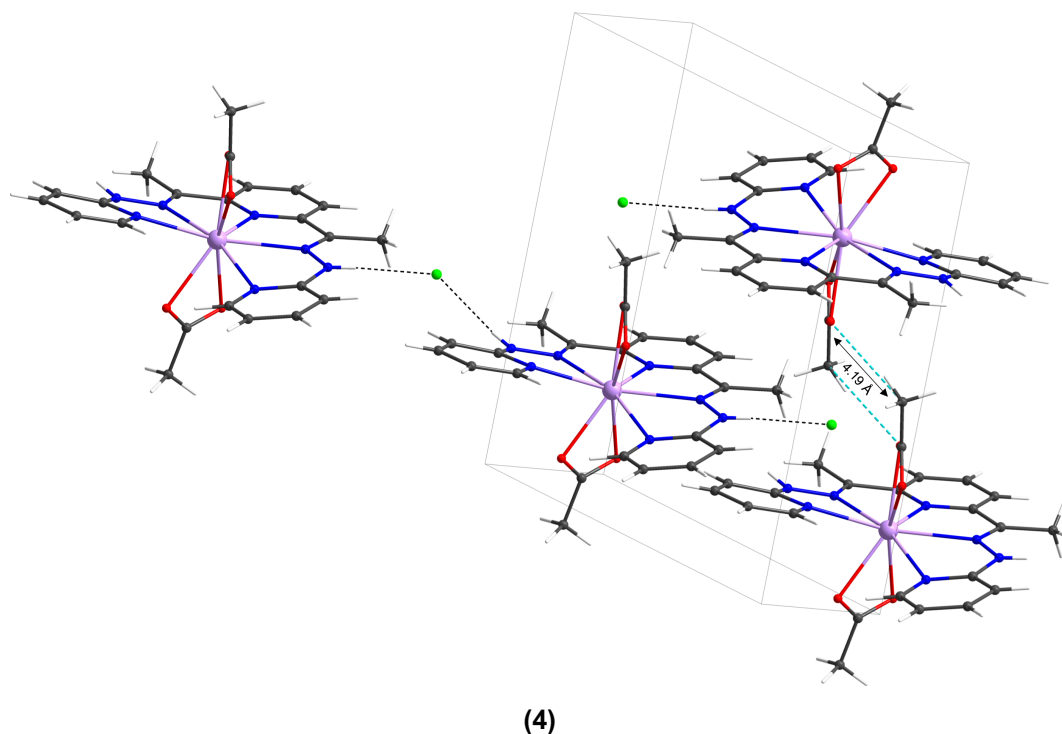
Figure 4.10: Distances between the secondary ligands in the crystal structures of the systems $\{DyL(NO_3)_2\}$ **(2)**, $\{DyL(NO_3)_2\}$ **(3)** and $\{DyL(Ac)_2\}$ **(4)**.

Hydrogen bonding also seems to be structure imposing in the crystal structure of $\{DyL(H_2O)_4\}$ **(1)** since a network of hydrogen bonds connects the molecules and the counter ions in the crystal structure. How much influence there is on the molecular structure can only be guessed due to the chicken-and-egg problem. As usual in coordination chemistry, there is not much known about the molecular structure in solution. However, since there is a significant difference in the helicity in $\{DyL(NO_3)_2\}$ **(2)** and $\{DyL(NO_3)_2\}$ **(3)** which can only stem from the different packing due to the different counter ion, some influence on the molecular structure must be considered.

The structures were designed for single molecule magnetic investigations. These properties are very structure sensitive as explained in depth in the theory. For this reason, a structure analysis by continuous symmetry measurements (CShM) with SHAPE 2.1 was conducted.[107] The program delivers deviation values in comparison to optimised polyhedra. These optimised polyhedra are mathematical objects with certain edge lengths and angles. This can sometimes be in conflict with real structures of complexes when there is a high variation in coordination bond lengths of the central atoms and lead to misleading values for chemical interpretation. However, this is not the case in these structures since all coordination bonds are of similar magnitude.
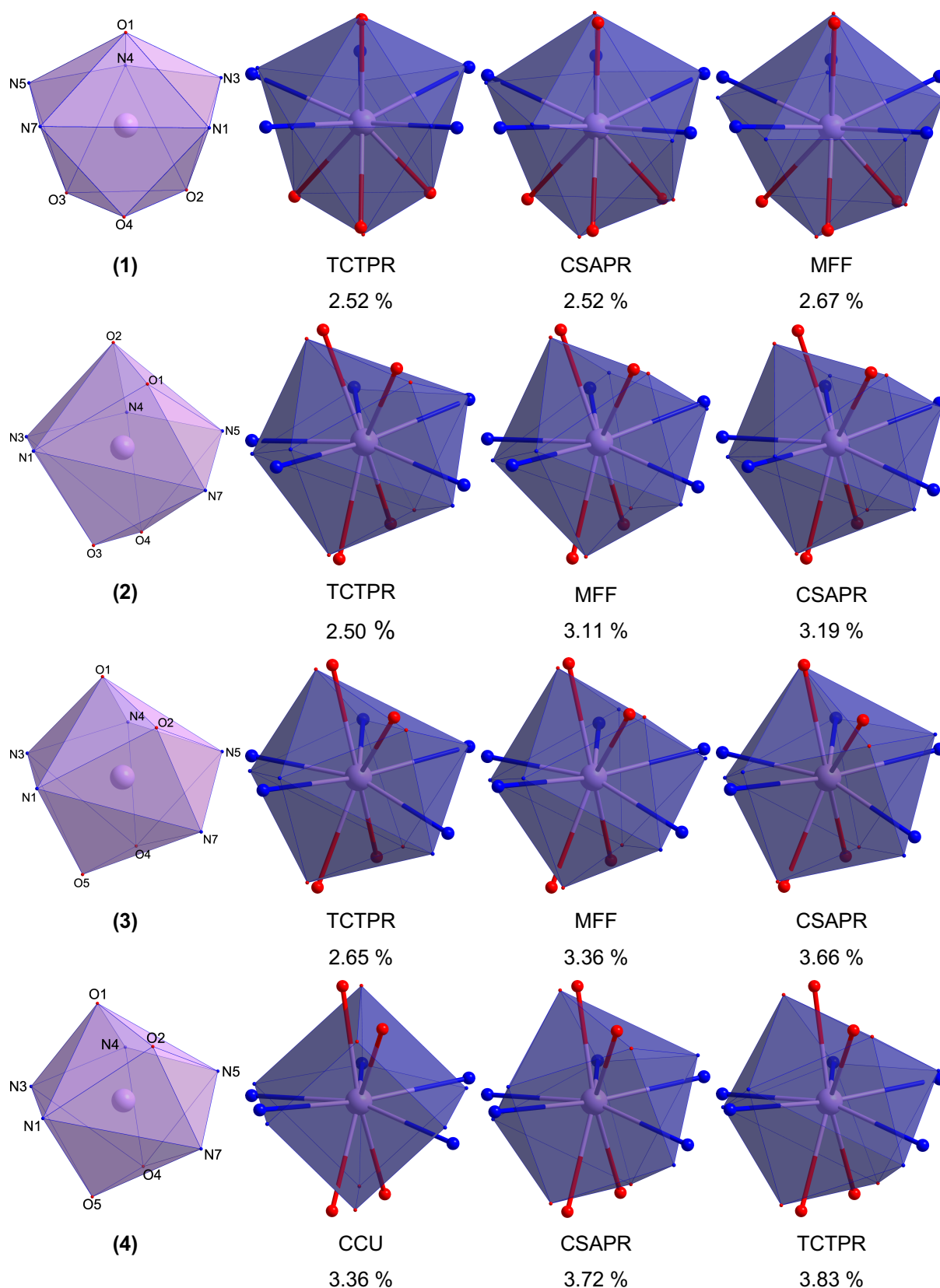
Figure 4.11: Lilac: coordination polyhedra of the complexes {DyL(H₂O)₄} **(1)**, {DyL(NO₃)₂} **(2)**, {DyL(NO₃)₂} **(3)** and {DyL(Ac)₂} **(4)**. Blue: coordination polyhedra of the best fitting ideal structures, spherical capped trigonal prism (TCTPR), spherical capped square antiprism (CSAPR), muffin structure type (MFF) and spherical capped relaxed cube (CCU) and the positions of the atoms in the original structure. Deviation values below ideal structures. The deviation values and the optimal polyhedra are obtained with SHAPE 2.1.[107]

All structures are low in symmetry as is usually the case for lanthanide complexes. In Figure 4.11, the coordination polyhedra of the real complexes is depicted in pink and the optimised polyhedra with the lowest deviation values are shown on the right. It can be seen that $\{DyL(H_2O)_4\}$ **(1)**, $\{DyL(NO_3)_2\}$ **(2)** and $\{DyL(NO_3)_2\}$ **(3)** agree most with the spherical capped trigonal prism (TCTPR, $D_{3h}$ symmetry), the spherical capped square antiprism (CSAPR, $C_{4v}$ symmetry) and the muffin structure type (MFF, $C_s$ symmetry). The order of the deviation values for the other optimised geometries are different for $\{DyL(H_2O)_4\}$ **(1)** compared to $\{DyL(NO_3)_2\}$ **(2)** and $\{DyL(NO_3)_2\}$ **(3)** as it can be seen rationalised in Figure 4.11.

However, although there is a completely different distribution of the secondary ligands in relation to the pentadentate chelate ligand, the TCTPR structure type is in all three structures the one with the smallest deviation value. On the other hand, in $\{DyL(Ac)_2\}$ **(4)** the best agreement can be found with the spherical capped relaxed cube (CCU, $C_{4v}$ symmetry), which is not among the most suitable optimal polyhedrons in any of the other structures. All deviation values are higher than in $\{DyL(H_2O)_4\}$ **(1)**, $\{DyL(NO_3)_2\}$ **(2)** and $\{DyL(NO_3)_2\}$ **(3)**. For this optimised CCU, it already is 3.36 %, which is a higher deviation value than with any of the three best fitting structures in $\{DyL(H_2O)_4\}$ **(1)** and $\{DyL(NO_3)_2\}$ **(2)**. The other two optimal structures among the best fitting ones for $\{DyL(Ac)_2\}$ **(4)** are CSAPR and TCTPR.

Although the low symmetry is not helpful for preventing mixing of states and, therefore, quantum tunnelling, it was shown that also for low symmetry dysprosium complexes, strong splitting of states due to strong anisotropy can provide the conditions for SMM properties. For the analysis of energy states in lanthanide complexes, spectroscopic methods can be used like electron paramagnetic resonance (EPR) or inelastic neutron scattering experiments (INS). However, they are disadvantageous with low symmetry compounds because an EPR spectrum will be too information rich for interpretation and INS experiments can only detect transitions allowed by the selection rules in a small range of energy and, as already explained in section 2.2, the energies of the $m_J$ states is not always in the order $|m_J|$ to $-|m_J|$. For computational approaches, the low symmetry can also be a big problem because it leads to over parameterisation.[108,109] *Ab initio* calculations are, therefore, only helpful for low symmetry compounds if enough parameters can be estimated from spectroscopic measurements. Hence for the presented compounds, the strengths of anisotropy and the anisotropy axes are estimated with an electrostatic model with aid of the MAGELLAN software.[40] This can,

however, only be a rough estimate since the model does not incorporate charge-shifting.[110] Although the absolute values for the reversal energies may not be accurate, comparing these values as relative values for the closely related complexes is legitimate and useful. This can enable ranking the anisotropy for the complexes with $H_2$dapp ligand from the realistically smallest to the largest. The results are depicted in Figure 4.12 showing the calculated anisotropy axes of each molecule in dark green and the estimated value for the strengths of the anisotropy below each picture of the molecules. These values reveal low anisotropy in {DyL($H_2O$)$_4$} **(1)**, which is to be expected since none of the ligands is charged. If a more sophisticated model could have been applied, it would probably detect easy plane anisotropy due to charge shifting in the pentadentate ligand towards the more electronegative and π-conjugated donor nitrogens. Complexes {DyL($NO_3$)$_2$} **(2)** and {DyL($NO_3$)$_2$} **(3)** show similar easy axis anisotropy as expected due to the very similar coordination sphere at the dysprosium. Complex {DyL(Ac)$_2$} **(4)** shows the strongest anisotropy most probably due to the shorter Dy-O and longer Dy-N bonds compared to {DyL($NO_3$)$_2$} **(2)** and {DyL($NO_3$)$_2$} **(3)**. As it will be discussed more in detail in the following sections the minimal reversal energy values obtained from MAGELLAN are not suited to predict good or bad properties in terms of blocking of the relaxation of the magnetic moment.

**(1)**
140 cm$^{-1}$

**(2)**
720 cm$^{-1}$

**(3)**
680 cm$^{-1}$

**(4)**
1050 cm$^{-1}$
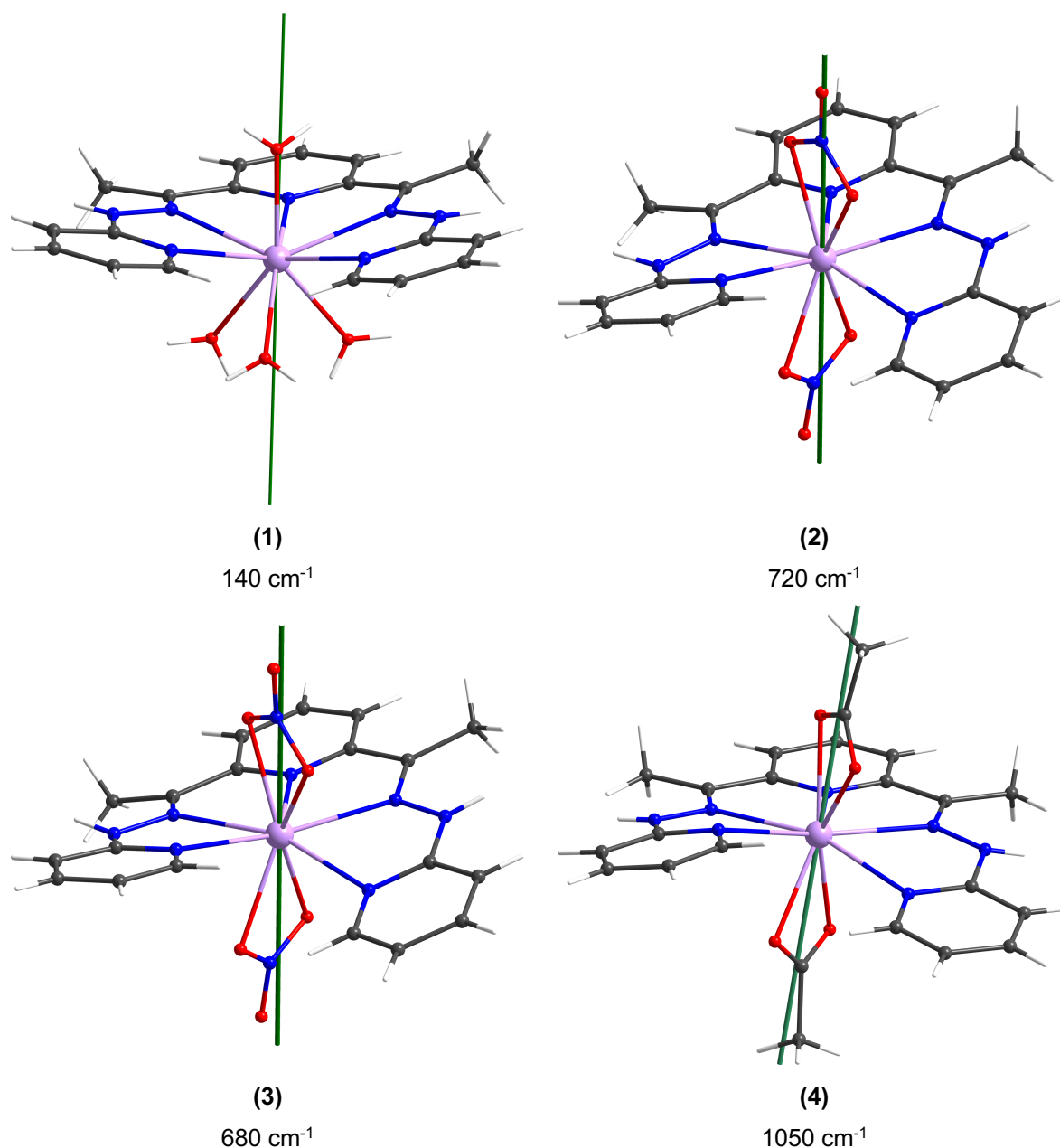
Figure 4.12: Molecules {DyL(H$_2$O)$_4$} **(1)**, {DyL(NO$_3$)$_2$} **(2)**, {DyL(NO$_3$)$_2$} **(3)** and {DyL(Ac)$_2$} **(4)** with anisotropy axes and minimal reversal energies obtained from MAGELLAN.[40]

From the structural data discussed so far it would still be the acetate version {DyL(Ac)$_2$} **(4)** that looks most promising. The methyl groups of the acetate shield the dysprosium from movements from the crystal packing because it does not hydrogen bond and urges more space in the packing. This means reduced spin-phonon coupling. It will be discussed in the following chapters that and why it is currently put in focus to consider about spin-phonon coupling.
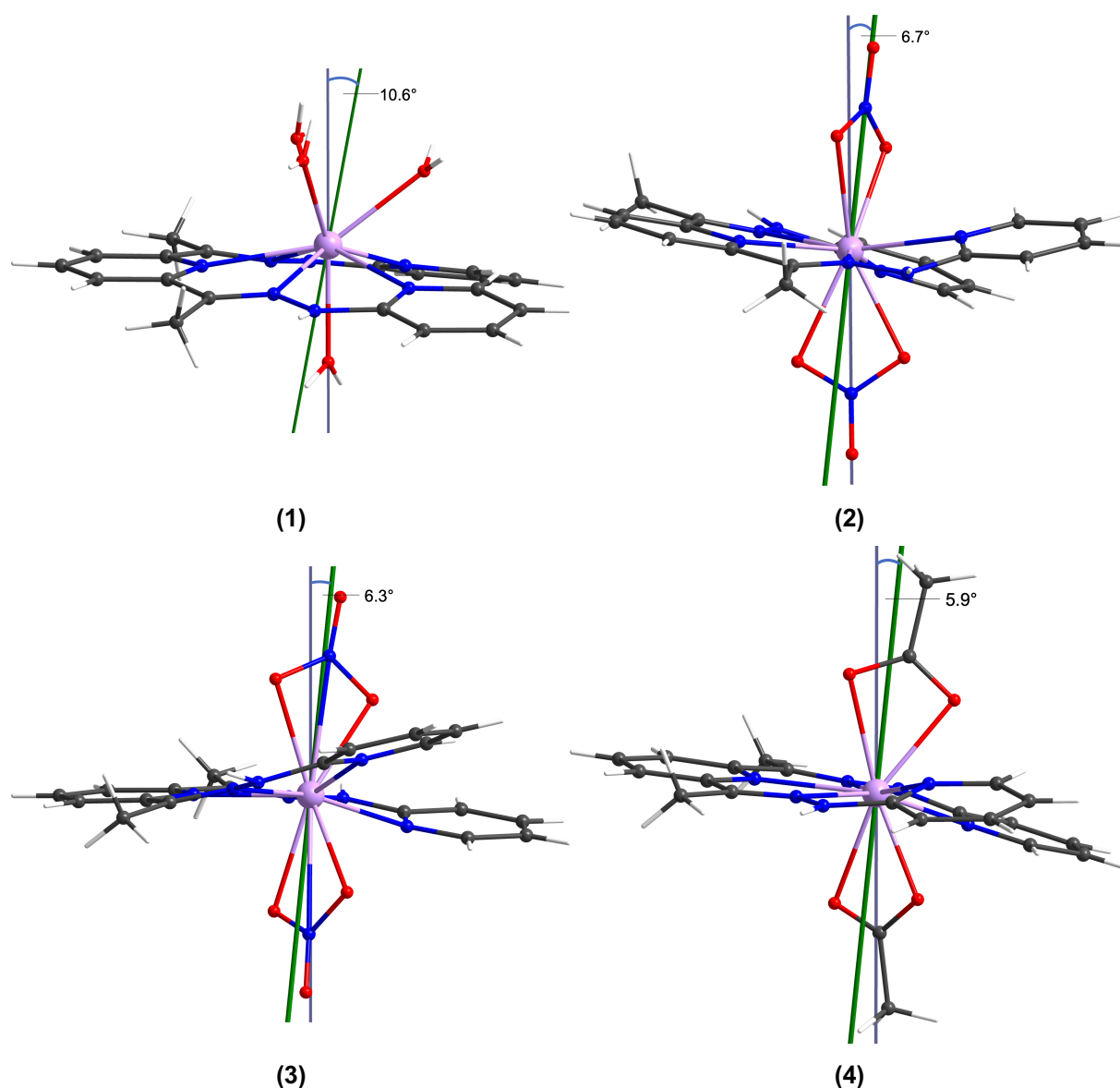
Figure 4.13: Angles between anchor axes and anisotropy axes of $\{DyL(H_2O)_4\}$ **(1)**, $\{DyL(NO_3)_2\}$ **(2)**, $\{DyL(NO_3)_2\}$ **(3)** and $\{DyL(Ac)_2\}$ **(4)**.

The calculated anisotropy axes have quite a good correlation with the previously defined anchor axes. Figure 4.13 shows that the angles between these axes are about 6° for the nitrate and the acetate capped compounds $\{DyL(NO_3)_2\}$ **(2)**, $\{DyL(NO_3)_2\}$ **(3)** and $\{DyL(Ac)_2\}$ **(4)** and around 10° for the complex with water ligands $\{DyL(H_2O)_4\}$ **(1)**. Magnetic data could only be collected for $\{DyL(NO_3)_2\}$ **(2)** because of lack of instrument time. They were collected at Københavns Universitet (University of Copenhagen) in the group of Prof. Jesper Bendix. This was done with a super conducting quantum interference device (SQUID), which is a superconductor separated in two halves by a Josephson contact. Changes of the magnetic field, for example induced by a magnetic sample moving in and out of the magnetic field of the SQUID, can therefore be measured as a voltage change between the two halves.
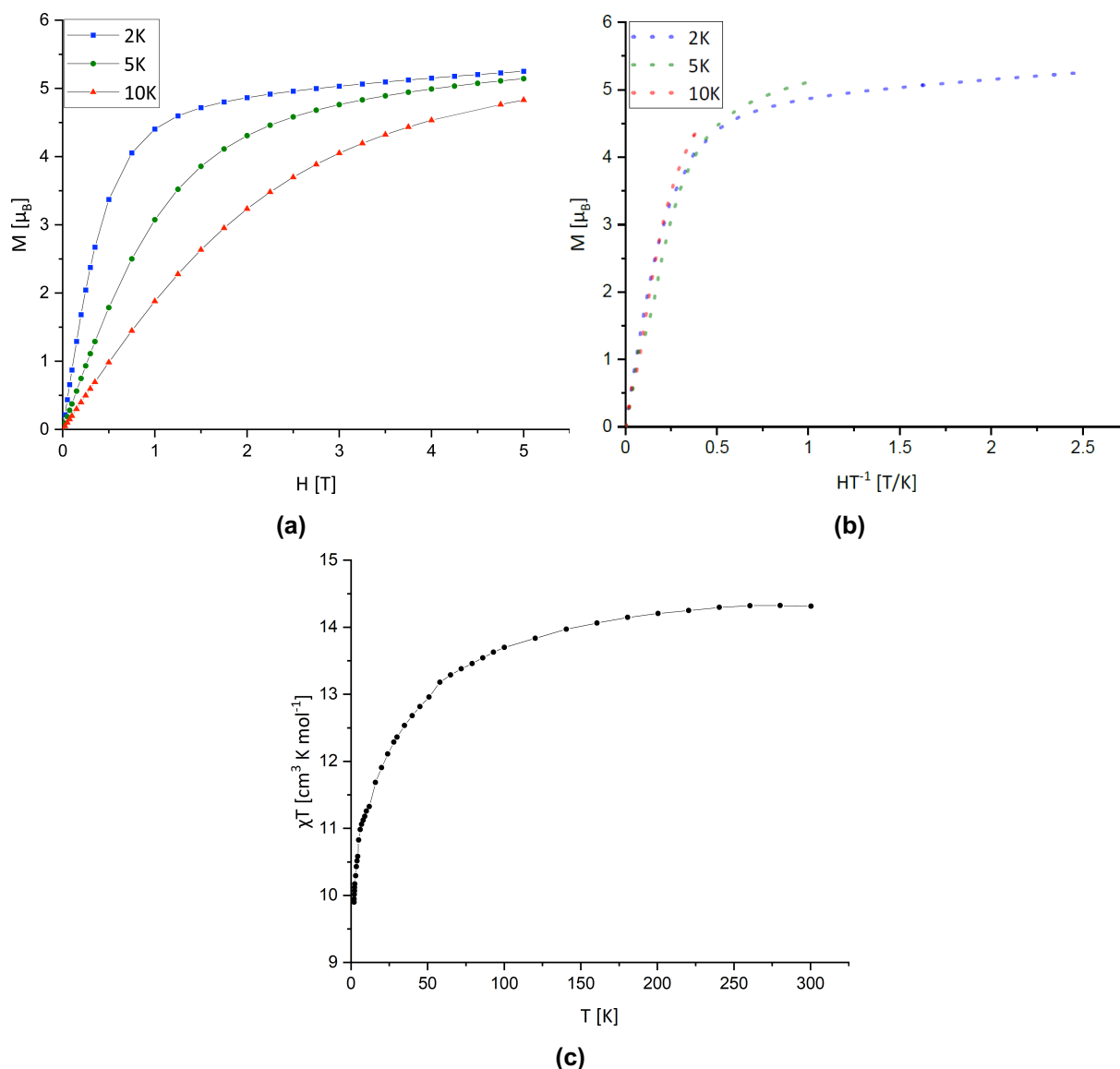
Figure 4.14: DC magnetic data of {DyL(NO$_3$)$_2$} **(2)**. **(a)** Magnetisation versus field. **(b)** Magnetisation versus field times inverse temperature. **(c)** χ times temperature versus temperature.

The direct current (DC) data shows the expected behaviour for a dysprosium single ion complex (Figure 4.14). In the isothermal magnetisation versus field graphs, a saturation value of marginally under 5 μ$_B$ is reached at 10 K and high fields as well as marginally above 5 μ$_B$ at 2 K and 5 K and high fields. This is lower than the calculated value of 10 μ$_B$ (J=15/2 and g=4/3) but matches the expected value of 5 μ$_B$ which is typically for powder samples obtained experimentally per dysprosium centre.[24,111-117] This value can vary incrementally or strongly with the crystal field dependent on the lanthanide ion.[117,118] In the magnetisation versus field times reciprocal temperature plot, there is an overlay of the isothermal curves at low fields in the margins of uncertainty. At about 0.25 T/K, the curves split. This shows the presence of anisotropy and/or low-lying excited states.

The $\chi T$ versus temperature plot shows a maximum value of 14.3 cm$^3$mol$^{-1}$K at high temperatures. This is slightly higher but still in very good agreement with the calculated value of 14.17 cm$^3$mol$^{-1}$K for a free dysprosium ion consistent with a $^6H_{15/2}$ ground state and g=4/3. The decrease of $\chi T$ towards lower temperatures is attributed to a thermal depopulation of m$_J$ sublevels or dipolar interactions.

In the alternating current (AC) measurements with applied field in phase and out of phase, susceptibility is strongly temperature dependent. Without applied field no signals can be observed shown in Figure 4.15. Depending on the applied field, two relaxation processes occur. If a weak field of between 500 and 4000 Oe is applied, there is an increase in the out of phase $\chi T$ versus frequency plot, which suggests maxima at higher frequencies than 1000 Hz. These start to vanish with an applied field of 1500 Oe and maxima at lower frequencies under 1 Hz appear. They have the highest intensity at a 4000 Oe DC field. So as the applied field is increased, the slower relaxation mode (i.e. the one seen at lower frequencies) is favoured while the faster relaxation mode (at higher frequencies) is suppressed. From this one can find an optimal field for further measurements chosen as 3000 Oe which was then used to create a plot (Figure 4.15 (b)). In the temperature dependent out of phase AC measurements at a 3000 Oe applied field, there is no frequency shift of the maxima with temperature. This suggests strong quantum tunnelling in the compound. This also seems to be the case for the higher frequency process although the maxima are at higher frequencies than in the frequency range of the measurement.

In order to compare this behaviour with that of the other compounds, SQUID measurements are still required. It would be interesting to see how well the electrostatic model works on these compounds for the above estimated anisotropy axes and strengths. However, compared to a ten coordinate dysprosium compound with two H$_2$dapp ligands in the literature, the properties in terms of slow magnetic relaxation are worse for {DyL(NO$_3$)$_2$} **(2)**. The ten coordinate compound neither can provide high symmetry nor a strong axial ligand field but still shows slow magnetic relaxation with 1200 Oe DC field up to 11 K.[101] Probably the better shielding of the metal ion by the two chelating pentadentate ligand is the reason for the better properties since spin-phonon coupling is quenched to some extent.
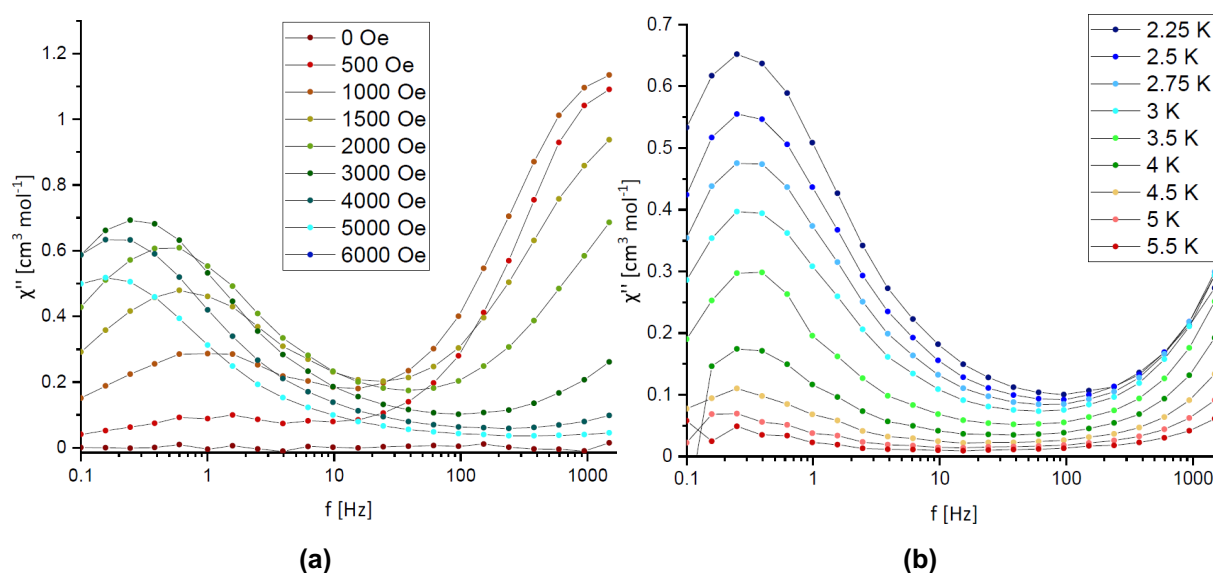
Figure 4.15: AC magnetic data of compound {DyL(NO$_3$)$_2$} **(2)**. **(a)** Field dependent χ'' versus frequency. **(b)** Temperature dependent χ'' versus frequency at 3000 Oe.

In the data collected for {DyL(NO$_3$)$_2$} **(2)** tunnelling processes have a big impact. These are not pictured by the electrostatic model, which was used to assess the anisotropy of the molecules since this rather refers to the height of the effective energy barrier and does not include the shortcuts by tunnelling processes. This means also observations of signs of these processes and a structural correlation would be intriguing. Moreover, possible influences of the small crystallographic differences on the magnetism between {DyL(NO$_3$)$_2$} **(2)** and {DyL(NO$_3$)$_2$} **(3)** would be a matter of interest. Therefore, the dysprosium complexes of {DyL(H$_2$O)$_4$} **(1)**, {DyL(NO$_3$)$_2$} **(3)** and {DyL(Ac)$_2$} **(4)** need to be investigated. Additionally, a closer look at the erbium derivative of {DyL(H$_2$O)$_4$} **(1)** could be interesting given the above discussed easy plane anisotropy.

### 4.1.2 Dysprosium-H$_2$dapp Complexes with Multiple Secondary Ligands

Under the right reaction conditions, a greater variety of mononuclear complexes with H$_2$dapp and dysprosium can be synthesised (Figure 4.16). This stepwise variation of the secondary ligands (aquo, nitrate and chloride), while keeping the primary H$_2$dapp ligand constant, allows a more detailed view on the structure-property relationship. Three different compounds were synthesised with water, nitrate and chloride ligands as secondary ligands according to the reaction scheme in Figure 4.17. As in subchapter 4.1.1, the general approach is a one-pot synthesis of the compounds. In some cases, although the same starting materials were used, different reaction and crystallisation conditions resulted in different products.

**(5)**



**(6)**



**(7)**
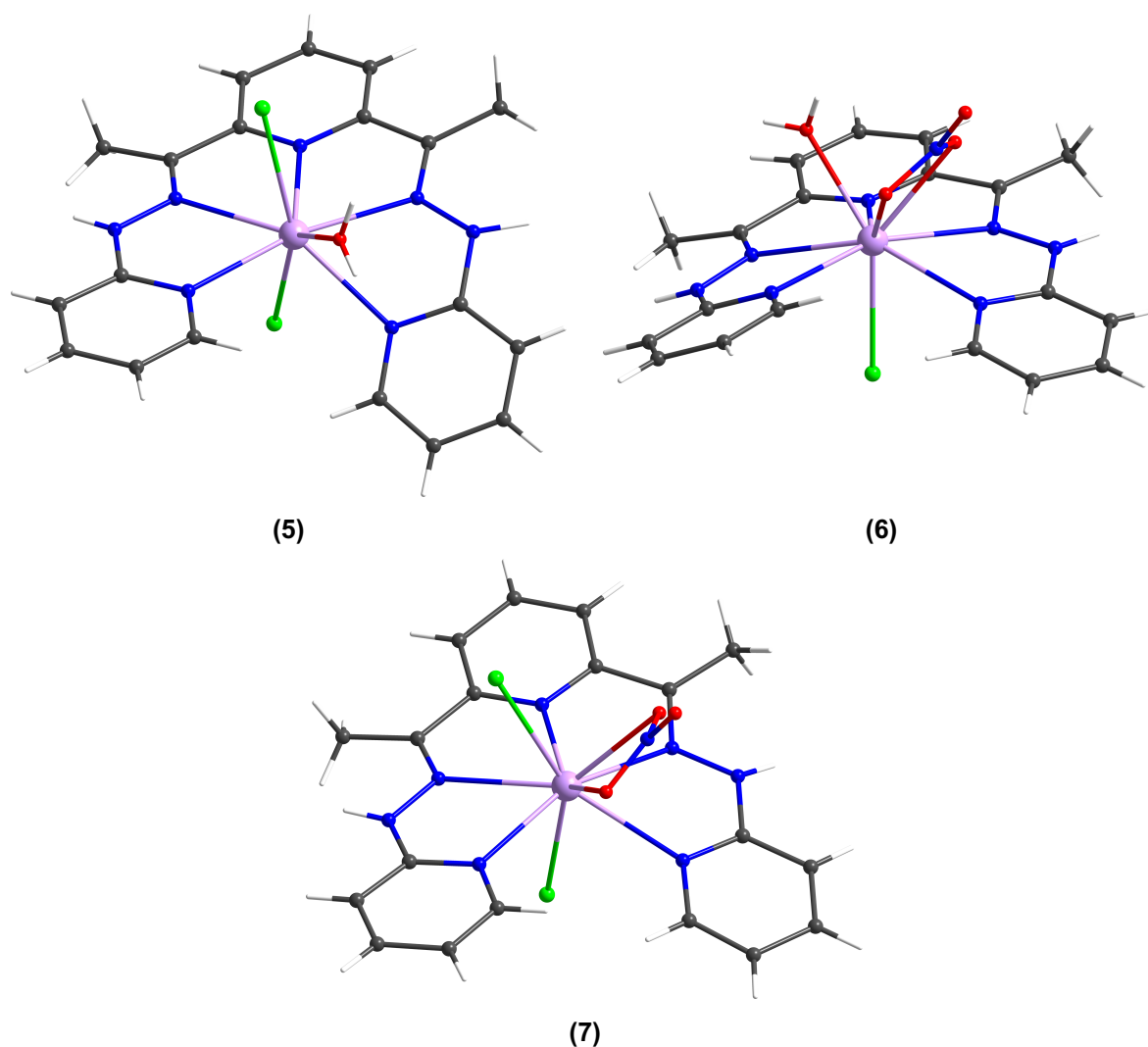
Figure 4.16: The three complexes {DyL(Cl)$_2$(H$_2$O)} **(5)**, {DyL(Cl)(H$_2$O)(NO$_3$)} **(6)** and {DyL(Cl)$_2$(NO$_3$)} **(7)** with multiple ligand types. Colour code: white = H; grey = C; blue = N; red = O; light green = Cl; lilac = Dy.
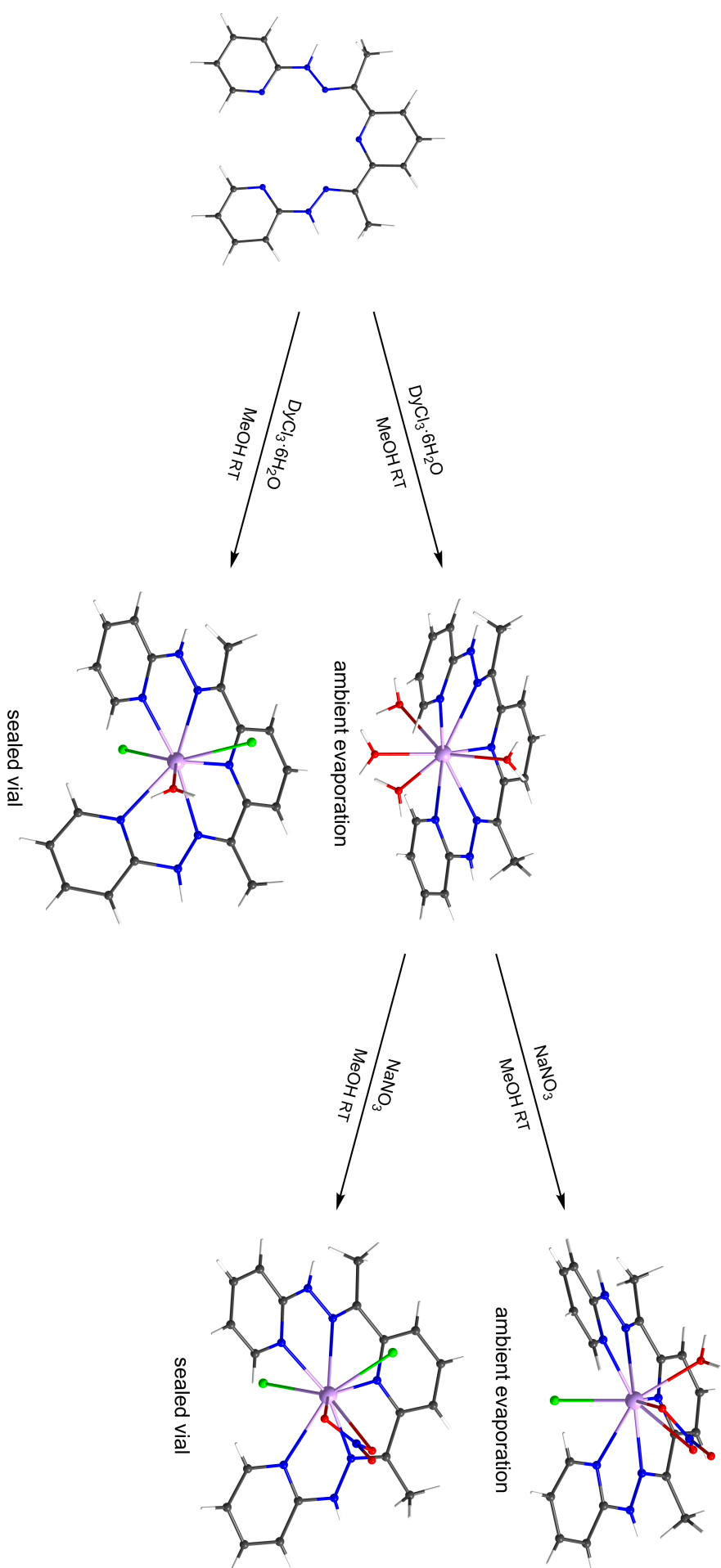
Figure 4.17: Reaction scheme for dysprosium complex synthesis of $[Dy(H_2dapp)(Cl)_2(H_2O)]Cl \cdot MeOH$ (5), $[Dy(H_2dapp)(NO_3)(Cl)(H_2O)]Cl \cdot 2MeOH$ (6) and $[Dy(H_2dapp)(NO_3)(Cl)_2] \cdot MeOH$ (7).

[Dy(H$_2$dapp)(Cl)$_2$(H$_2$O)]Cl·MeOH **(5)** is obtained with the same reaction mixture as {DyL(H$_2$O)$_4$} **(1)** directly from a methanolic H$_2$dapp solution with DyCl$_3$·6H$_2$O. In contrast to {DyL(H$_2$O)$_4$} **(1)**, the crystallisation needs to be conducted in a sealed vial. The formation of the crystalline product and the crystallisation speed can be significantly enhanced by heating of the reaction mixture under reflux for 15 minutes. [Dy(H$_2$dapp)(NO$_3$)(Cl)(H$_2$O)]Cl·2MeOH **(6)** and [Dy(H$_2$dapp)(NO$_3$)(Cl)$_2$]·MeOH **(7)** have the same reaction mixture. For both, a methanolic solution of H$_2$dapp and DyCl$_3$·6H$_2$O was stirred with the molar equivalent of sodium nitrate. If the vial is left sealed, crystalline {DyL(Cl)$_2$(NO$_3$)} **(7)** will be obtained rather than compound {DyL(Cl)(H$_2$O)(NO$_3$)} **(6)** after two days. The reaction mixture is left standing with a porous lid. Crystals of {DyL(Cl)$_2$(NO$_3$)} **(7)** appear on the bottom of the vial and crystals of {DyL(Cl)(H$_2$O)(NO$_3$)} **(6)** form on the walls of the vial and must be manually separated.

As with {DyL(H$_2$O)$_4$} **(1)**, {DyL(NO$_3$)$_2$} **(2)**, {DyL(NO$_3$)$_2$} **(3)** and {DyL(Ac)$_2$} **(4)**, the H$_2$dapp ligand shows helical distortion which can be quantified as before with the results shown in Table 4.3. It can be seen that for {DyL(Cl)(H$_2$O)(NO$_3$)} **(6)** and {DyL(Cl)$_2$(NO$_3$)} **(7)**, there is small contribution of folding of the molecule which is much less pronounced than in {DyL(H$_2$O)$_4$} **(1)**.

Table 4.3: Helical distortion values for {DyL(Cl)$_2$(H$_2$O)} **(5)**, {DyL(Cl)(H$_2$O)(NO$_3$)} **(6)** and {DyL(Cl)$_2$(NO$_3$)} **(7)**.

| Compound | $\alpha/°$ | $\beta/°$ | $\delta/°$ |
|:---:|:---:|:---:|:---:|
| **(5)** | -6.7 | -39.2 | **45.9** |
| **(6)** | 9.3 | -37.4 | **28.1** |
| **(7)** | 6.4 | -38.0 | **31.6** |

Compound {DyL(Cl)$_2$(H$_2$O)} **(5)** has the strongest helical distortion of the molecules within this section and shows a $\delta$ value of 45.9°. Nevertheless, it is not as pronounced as in {DyL(NO$_3$)$_2$} **(3)**. Intriguingly in this compound, the largest amount of distortion can be attributed to the deformation on N2 and N3 of the hydrazone of one arm of the ligand. This is visualised in Figure 4.18. As a result, Dy1 and the coordinating N3 to N7 atoms are all in a plane (depicted in yellow in Figure 4.18) while N1 is displaced out of that plane. The other two complexes of this subchapter {DyL(Cl)(H$_2$O)(NO$_3$)} **(6)** and {DyL(Cl)$_2$(NO$_3$)} **(7)** have similar distortion values. Complex {DyL(Cl)(H$_2$O)(NO$_3$)} **(6)** has a $\delta$ value of 28.1° and {DyL(Cl)$_2$(NO$_3$)} **(7)** has a $\delta$ value of 31.6°. These are lower than the ones found in {DyL(NO$_3$)$_2$} **(2)** and {DyL(Ac)$_2$} **(4)** but much higher than in {DyL(H$_2$O)$_4$} **(1)** where the ligand is folded rather than helical. The differences

between the distortion described as helical or folded are elaborated in detail in section 4.1.1. The distortion in {DyL(Cl)$_2$(NO$_3$)} **(7)** is slightly greater than in {DyL(Cl)(H$_2$O)(NO$_3$)} **(6)**. This time, the structures are too different to obtain a clear picture of correlations of the measured structures. However, it can be said that the variation in the $\delta$ value representing the helicity is high and that there is no simple correlation with the amount or size of the secondary ligands.
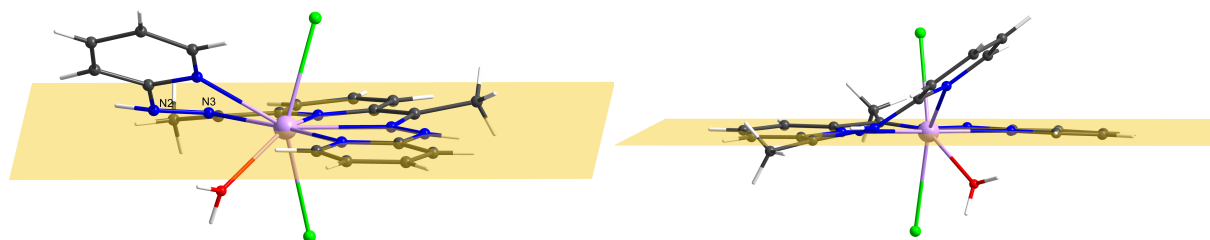


Figure 4.18: Helical distortion in {DyL(Cl)$_2$(H$_2$O)} **(5)**. Yellow: Shows the plane in which the dysprosium and the coordinating N3 to N7 are.

In all three molecular structures of the complexes {DyL(Cl)$_2$(H$_2$O)} **(5)**, {DyL(Cl)(H$_2$O)(NO$_3$)} **(6)** and {DyL(Cl)$_2$(NO$_3$)} **(7)**, dysprosium is the central ion which has one H$_2$dapp ligand and a chloride ligand in all structures. This chloride ligand is occupying one side relative to the chelate ligand. The other secondary ligands vary and occupy the other side. They can be an additional chloride ion, a water molecule or a nitrate ion. This is sketched in Figure 4.19. The remaining space for the secondary ligands can be easily seen in the space filling model (b).

**(a)**                                   **(b)**
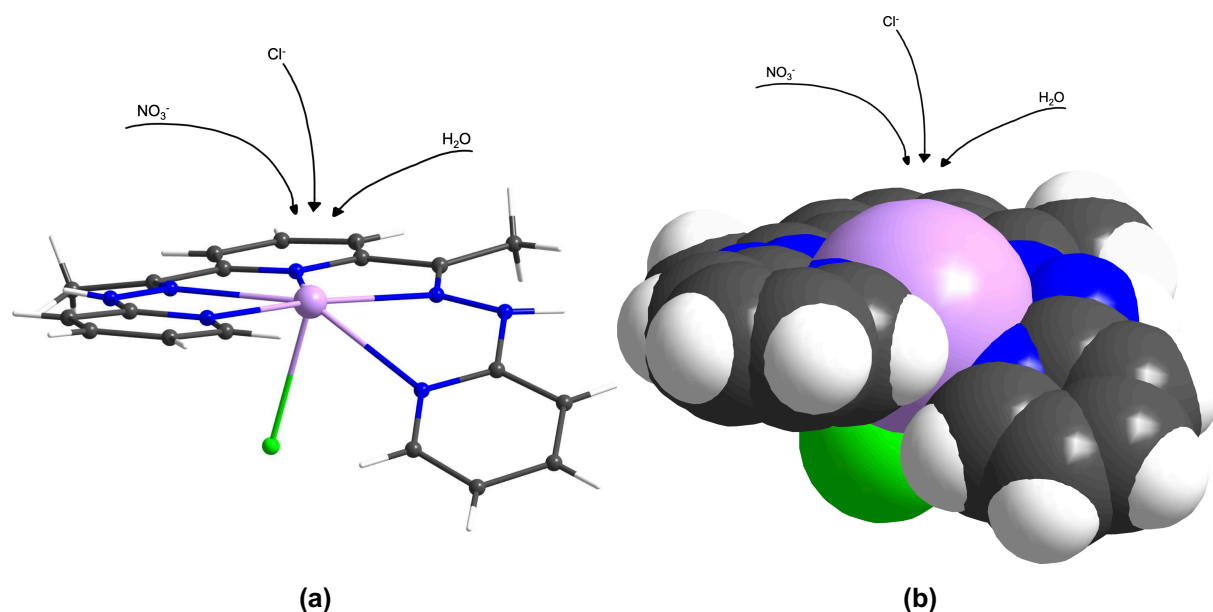
Figure 4.19: Scheme of the permanent ligand composition of the compounds $\{DyL(Cl)_2(H_2O)\}$ **(5)**, $\{DyL(Cl)(H_2O)(NO_3)\}$ **(6)** and $\{DyL(Cl)_2(NO_3)\}$ **(7)**. **(a)** Balls and sticks model with the variable ligands sketched above. **(b)** Space filling model.

Bond lengths and angles are listed in Table 4.4. As discussed for **(1)**-**(4)** in section 4.1.1 also in $\{DyL(Cl)_2(H_2O)\}$ **(5)**, $\{DyL(Cl)(H_2O)(NO_3)\}$ **(6)** and $\{DyL(Cl)_2(NO_3)\}$ **(7)**, the Dy-N bond lengths are between 2.4 and 2.5 Å, which falls within the scope of 54 % of the structures with Dy-N bond in the CSD. The values of the average bond length in subchapter 4.1.1 are similar to those for **(5)**-**(7)** with $\{DyL(Cl)_2(H_2O)\}$ **(5)** having the smallest (2.48 Å) and $\{DyL(Cl)_2(NO_3)\}$ **(7)** the largest Dy-N bonds average value (2.53 Å). Compound $\{DyL(Cl)(H_2O)(NO_3)\}$ **(6)** has an average value of 2.51 Å. The relation between bond lengths and distortion can be predicted given that there is a clear correlation between the helical distortion values and the average dysprosium-nitrogen bond lengths. As explained in the video in the digital appendix and as mentioned in section 4.1.1, the helical distortion allows for shorter Dy-N contacts. Before coordination, the pyridine groups of the ligand already have a close approach of the hydrogen shown from ChemDraw (section 2.1). The helical distortions allow the hydrogens to slide above and below each other. Despite the height difference induced by the loss of planarity, the resulting compression of the ligand leads to shorter Dy-N bonds. This inevitably poses the question whether the helical distortion causes the shorter Dy-N bonds or vice versa.

Table 4.4: Bond lengths and angles for compounds {DyL(Cl)$_2$(H$_2$O)} **(5)**, {DyL(Cl)(H$_2$O)(NO$_3$)} **(6)** and {DyL(Cl)$_2$(NO$_3$)} **(7)**.
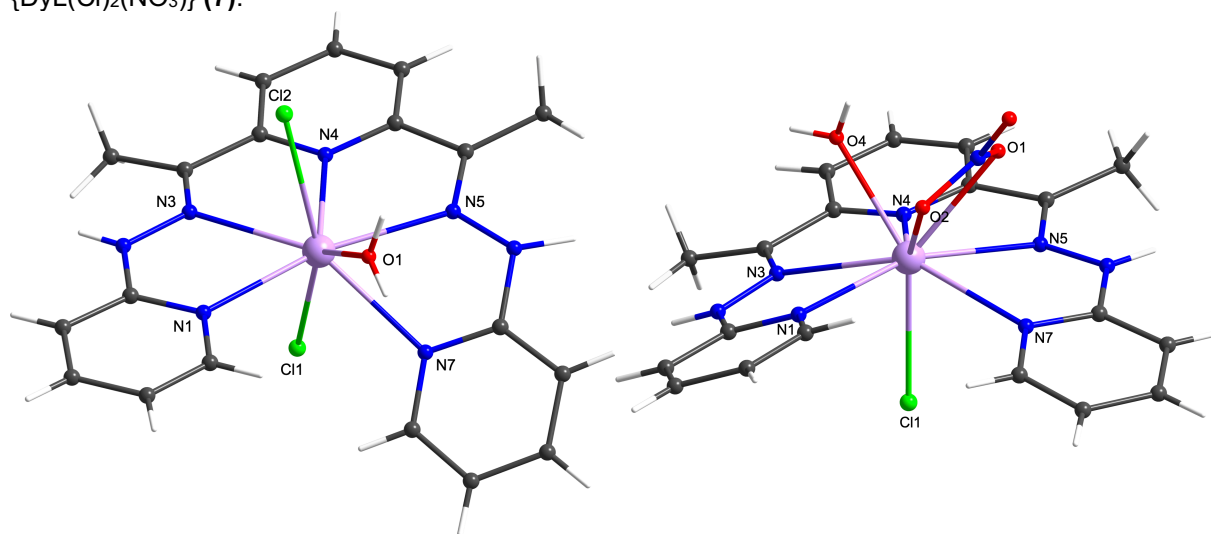


**(5)**

| Atom | Atom | Length/Å |
|------|------|----------|
| Dy1 | O1 | 2.372(2) |
| Dy1 | Cl1 | 2.6485(8) |
| Dy1 | Cl2 | 2.7134(8) |
| Dy1 | N1 | 2.456(2) |
| Dy1 | N3 | 2.496(2) |
| Dy1 | N4 | 2.452(2) |
| Dy1 | N5 | 2.468(3) |
| Dy1 | N7 | 2.508(3) |

| Atom | Atom | Atom | Angle/° |
|------|------|------|---------|
| N1 | Dy1 | N3 | 63.16(8) |
| N3 | Dy1 | N4 | 64.83(8) |
| N4 | Dy1 | N5 | 64.53(8) |
| N5 | Dy1 | N7 | 65.05(8) |
| N1 | Dy1 | N7 | 104.01(8) |
| O1 | Dy1 | Cl2 | 71.17(6) |
| O1 | Dy1 | Cl1 | 138.24(6) |
| Cl1 | Dy1 | Cl2 | 149.46(2) |

**(6)**

| Atom | Atom | Length/Å |
|------|------|----------|
| Dy1 | O1 | 2.4895(18) |
| Dy1 | O2 | 2.4764(18) |
| Dy1 | O4 | 2.360(2) |
| Dy1 | Cl1 | 2.6710(7) |
| Dy1 | N1 | 2.506(2) |
| Dy1 | N3 | 2.516(2) |
| Dy1 | N4 | 2.474(2) |
| Dy1 | N5 | 2.531(2) |
| Dy1 | N7 | 2.515(2) |

| Atom | Atom | Atom | Angle/° |
|------|------|------|---------|
| N1 | Dy1 | N3 | 64.33(7) |
| N3 | Dy1 | N4 | 63.86(7) |
| N4 | Dy1 | N5 | 63.05(7) |
| N5 | Dy1 | N7 | 63.60(7) |
| N1 | Dy1 | N7 | 99.91(7) |
| O1 | Dy1 | O4 | 71.76(7) |
| O2 | Dy1 | O4 | 74.92(7) |
| O1 | Dy1 | Cl1 | 142.85(5) |
| O2 | Dy1 | Cl1 | 134.31(5) |
| O4 | Dy1 | Cl1 | 141.92(5) |
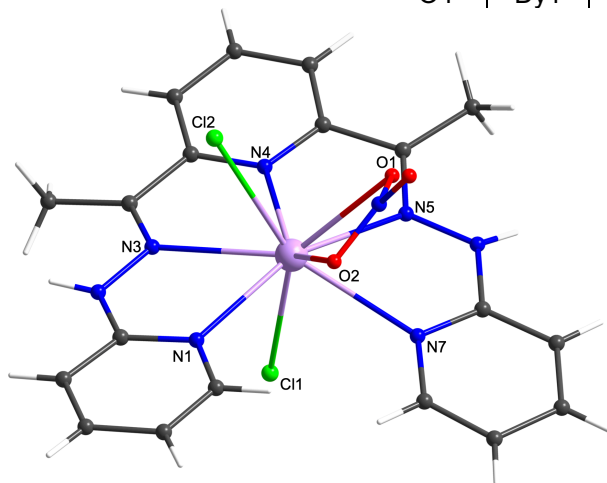
**(7)**

| Atom | Atom | Length/Å |
|------|------|----------|
| Dy1 | O1 | 2.492(3) |
| Dy1 | O2 | 2.507(3) |
| Dy1 | Cl1 | 2.6919(8) |
| Dy1 | Cl2 | 2.7367(8) |
| Dy1 | N1 | 2.503(3) |
| Dy1 | N3 | 2.525(3) |
| Dy1 | N4 | 2.507(3) |
| Dy1 | N5 | 2.530(3) |
| Dy1 | N7 | 2.573(3) |

| Atom | Atom | Atom | Angle/° |
|------|------|------|---------|
| N1 | Dy1 | N3 | 64.63(9) |
| N3 | Dy1 | N4 | 62.99(9) |
| N4 | Dy1 | N5 | 62.24(9) |
| N5 | Dy1 | N7 | 62.84(9) |
| N1 | Dy1 | N7 | 101.37(9) |
| O1 | Dy1 | Cl1 | 144.10(6) |
| O2 | Dy1 | Cl1 | 128.76(7) |
| O1 | Dy1 | Cl2 | 72.93(6) |
| O2 | Dy1 | Cl2 | 73.33(6) |
| Cl1 | Dy1 | Cl2 | 142.57(3) |

A plot of the $\delta$ values against the average Dy-N bond lengths reveals an almost linear dependence as shown in Figure 4.20. A shorter Dy-N bond comes along with a smaller $\delta$ value and vice versa. This corelation holds for all complexes with different ligands. For the molecular structures {DyL(NO$_3$)$_2$} **(2)** and {DyL(NO$_3$)$_2$} **(3)** with the same ligands on dysprosium, on the other hand, these findings are not true. While {DyL(NO$_3$)$_2$} **(2)** has a much smaller helical distortion ($\delta$=43.4°) than in {DyL(NO$_3$)$_2$} **(3)** ($\delta$=49.7°), the average Dy-N bond lengths are almost the same but even slightly larger for {DyL(NO$_3$)$_2$} **(3)**. This means for these two molecules, the dependence between $\delta$ values and average Dy-N bond lengths seems to be reversed.

In subchapter 4.1.1, it was discussed that the different packing of {DyL(NO$_3$)$_2$} **(2)** compared to {DyL(NO$_3$)$_2$} **(3)** caused this stronger helicity. Obviously, this does not have the same impact on the bond lengths, which almost stayed the same. This dependence suggests that shorter bond lengths lead to a stronger helicity while stronger helicity does not necessarily lead to shorter bond lengths.
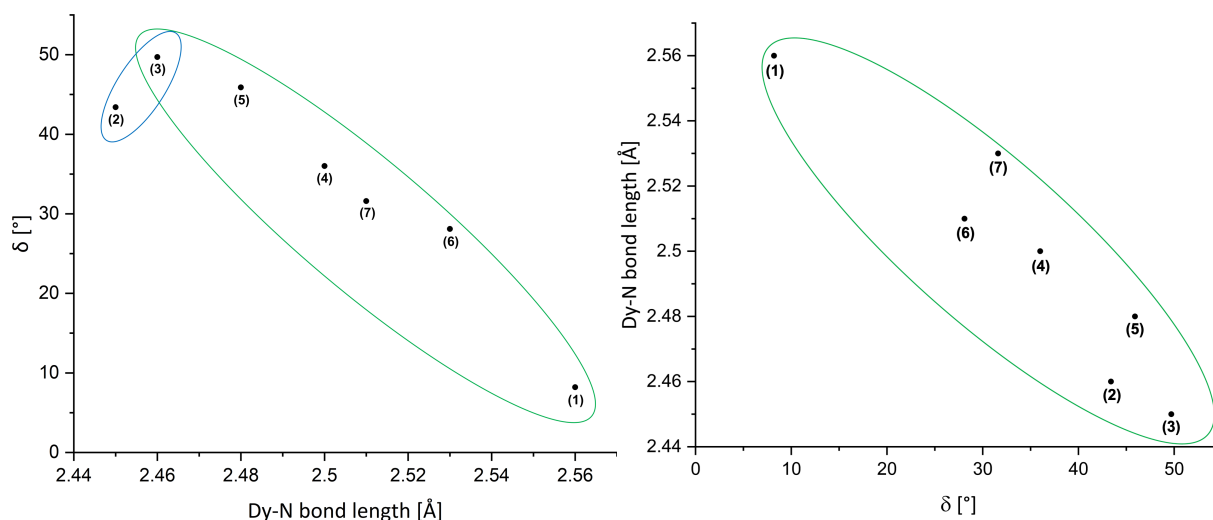
Figure 4.20: $\delta$ value versus average Dy-N bond lengths for compounds $\{DyL(H_2O)_4\}$ **(1)**, $\{DyL(NO_3)_2\}$ **(2)**, $\{DyL(NO_3)_2\}$ **(3)**, $\{DyL(Ac)_2\}$ **(4)**, $\{DyL(Cl)_2(H_2O)\}$ **(5)**, $\{DyL(Cl)(H_2O)(NO_3)\}$ **(6)** and $\{DyL(Cl)_2(NO_3)\}$ **(7)**.

It seems that the Dy-N bond length determines the helicity. While the influence of the lanthanide contraction on the coordination bond lengths is well studied, other influences on the coordination bonds of lanthanide complexes are not well understood.[119,120] From the findings here, there is no clear correlation to be made currently concerning the nature and charge of the secondary ligand. Therefore, mutual direct influences of the ligands do not seem to be the reason for the different bond lengths. Whilst the influence of the secondary ligands on the electronic structure of the lanthanide ion could impact the bond lengths, a large sample base needs to be studied before any definitive conclusions can be made. Nevertheless, a more detailed and computational supported analysis of additional similar structures would be needed to gain a clearer picture of the influences. Similar considerations have been proposed for 3d metal complexes.[121]

Within all the molecules discussed there is a large variation in the Dy-N bond lengths with no obvious pattern aside from Dy-N4 tending to be the shortest as it can be seen in Table 4.4.

The Dy-Cl1 bonds in $\{DyL(Cl)_2(H_2O)\}$ **(5)**, $\{DyL(Cl)(H_2O)(NO_3)\}$ **(6)** and $\{DyL(Cl)_2(NO_3)\}$ **(7)** increase from **(5)** to **(7)**. They are 2.65 Å in $\{DyL(Cl)_2(H_2O)\}$ **(5)**, 2.67 Å in $\{DyL(Cl)(H_2O)(NO_3)\}$ **(6)** and 2.69 Å in $\{DyL(Cl)_2(NO_3)\}$ **(7)**. In the complexes with an additional chloride ligand ($\{DyL(Cl)_2(H_2O)\}$ **(5)** and $\{DyL(Cl)_2(NO_3)\}$ **(7)**), the Dy-Cl2 bond is significantly longer than the Dy-Cl1 bond, which is most likely due to the fact that the space needs to be shared with the other secondary ligand. They are 2.71 Å in

{DyL(Cl)$_2$(H$_2$O)} **(5)** and 2.74 Å in {DyL(Cl)$_2$(NO$_3$)} **(7)**. It is a similar case in {DyL(H$_2$O)$_4$} **(1)** where the single H$_2$O has the shortest Dy-O bond.

The bond lengths between the dysprosium ion and the water molecules in {DyL(Cl)$_2$(H$_2$O)} **(5)** and {DyL(Cl)(H$_2$O)(NO$_3$)} **(6)** show the expected Dy-O bond length for water as already discussed in section 4.1.1. It is 2.37 Å in {DyL(Cl)$_2$(H$_2$O)} **(5)** and 2.36 Å in {DyL(Cl)(H$_2$O)(NO$_3$)} **(6)**. Other than in {DyL(NO$_3$)$_2$} **(2)** and {DyL(NO$_3$)$_2$} **(3)**, the bonds between the dysprosium ion and the nitrate oxygens are in the expected length range as listed in Table 4.4.

As was found for the complexes in section 4.1.1, the angles at the dysprosium ion subtended by two neighbouring nitrogens are constrained by the rigidity of the pentadentate H$_2$dapp ligand. The N-Dy-N angles which are coloured green in Figure 4.7, again correlate with the helical distortion. The smaller the helical distortion, the smaller the average N-Dy-N angle. This can be seen in Figure 4.21. Compound {DyL(Cl)$_2$(H$_2$O)} **(5)** shows the highest average angle (64.4°) followed by compound {DyL(Cl)(H$_2$O)(NO$_3$)} **(6)** showing an average angle of 63.7° and {DyL(Cl)$_2$(NO$_3$)} **(7)** having the smallest average angle of the three compounds (63.2°). These findings agree with the findings that were obtained in section 4.1.1. In agreement with this, the angle between the dysprosium and the terminal pyridine nitrogens, which is depicted yellow in Figure 4.7, also here compensates for all other distortions in the molecule and no clear correlation to helicity can be detected.
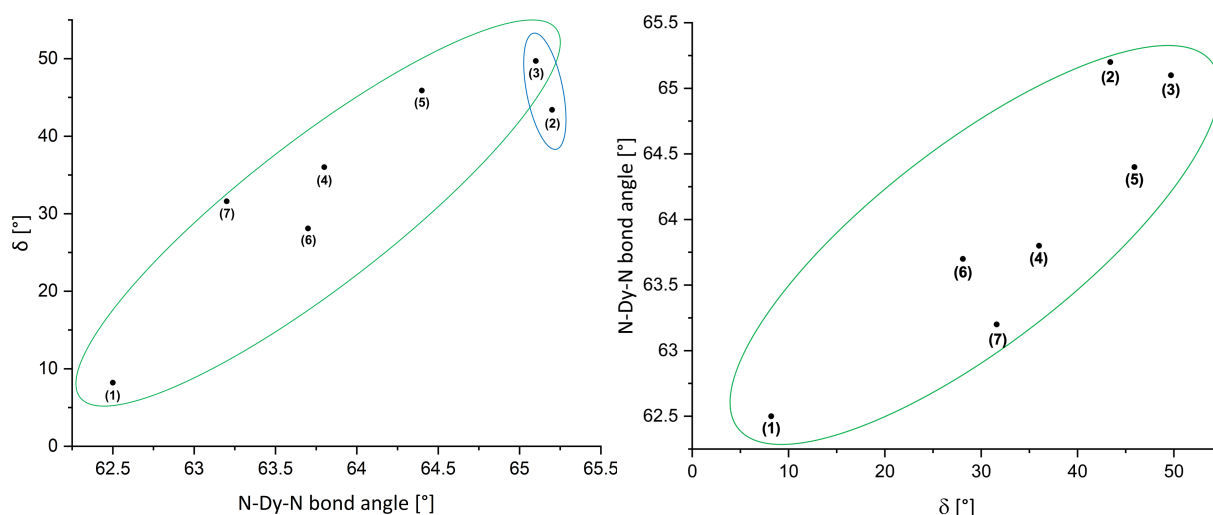


Figure 4.21: δ value versus N-Dy-N bond angles for compounds {DyL(H$_2$O)$_4$} **(1)**, {DyL(NO$_3$)$_2$} **(2)**, {DyL(NO$_3$)$_2$} **(3)**, {DyL(Ac)$_2$} **(4)**, {DyL(Cl)$_2$(H$_2$O)} **(5)**, {DyL(Cl)(H$_2$O)(NO$_3$)} **(6)** and {DyL(Cl)$_2$(NO$_3$)} **(7)**.

As a reference point, the Dy-Cl1 bond can be defined as an anchor vector in the three molecules {DyL(Cl)$_2$(H$_2$O)} **(5)**, {DyL(Cl)(H$_2$O)(NO$_3$)} **(6)** and {DyL(Cl)$_2$(NO$_3$)} **(7)**. To a

first approximation, the strongest influence on the anisotropy axis which is the easy axis for the alignment of the magnetic moment will be the relative position of the negatively polarised ligand atoms. Hence, the deviation angles of the other anionic ligands to this axis are shown in Figure 4.22.

For the nitrate and the acetate ligands, the centroid of the two coordinating oxygens is taken as the reference for calculating the angle. In Figure 4.22, it can be seen that the deviation angle for the other secondary ligands is the lowest for the Cl2 in $\{DyL(Cl)_2(H_2O)\}$ **(5)** (30.5°). The water ligand in this molecule has a deviation of the Dy-O bond of 41.8° from this anchor axis, which should ideally be 0°. This results in total to a rather axial alignment of the negative charges in this molecule which reflects in the minimal reversal energies calculated by MAGELLAN and will be discussed below. The Dy-O bond for the water deviates by an angle of 38.1° from the anchor axis. The deviation of the nitrate in $\{DyL(Cl)(H_2O)(NO_3)\}$ **(6)**, which corresponds to the chloride in $\{DyL(Cl)_2(H_2O)\}$ **(5)**, from the anchor axis is 33.8°. This means, the anionic nitrate ligand in $\{DyL(Cl)(H_2O)(NO_3)\}$ **(6)** has a larger deviation angle than the chloride ligand in $\{DyL(Cl)_2(H_2O)\}$ **(5)**. In $\{DyL(Cl)_2(NO_3)\}$ **(7)**, the deviations for nitrate and chloride are with 37.3° for the nitrate and 37.4° for the chloride of similar size. However, they are up to 10 % larger than for the anionic ligands in the other compounds.
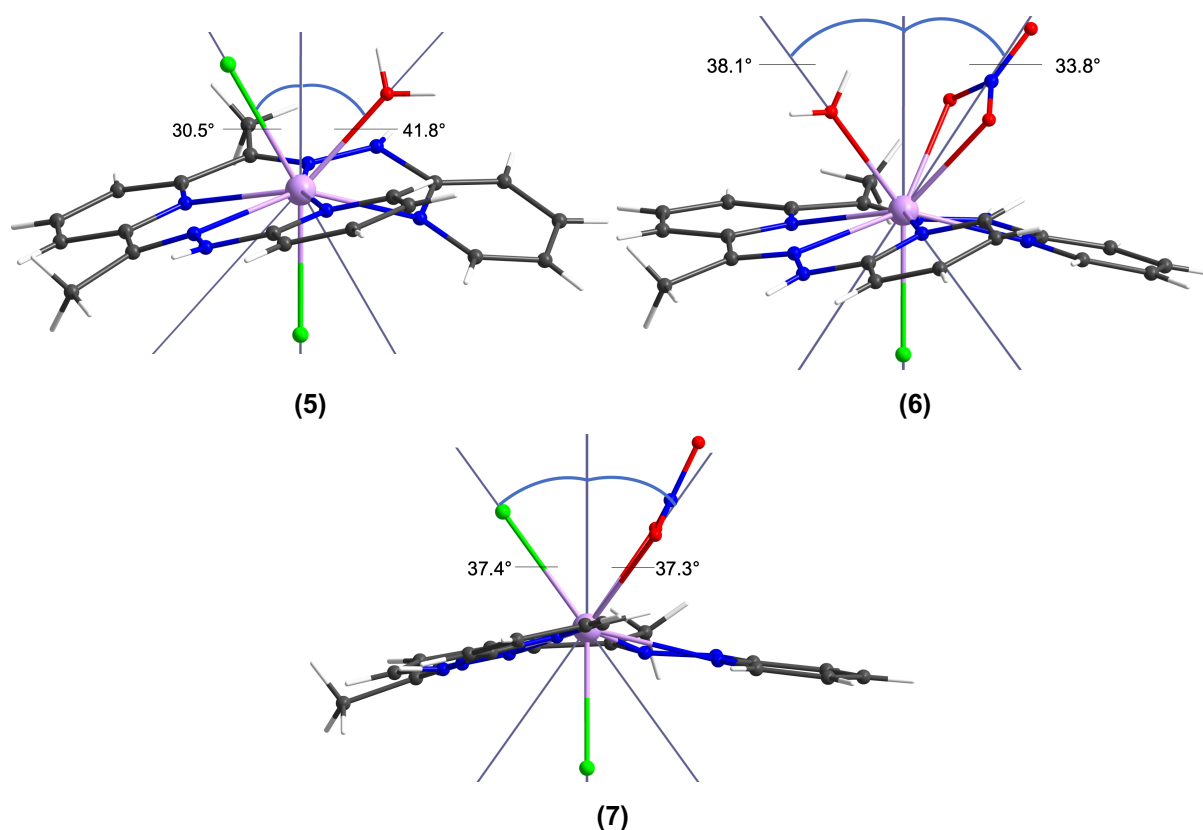
Figure 4.22: Angles between anchor axes and secondary ligands of {DyL(Cl)$_2$(H$_2$O)} **(5)**, {DyL(Cl)(H$_2$O)(NO$_3$)} **(6)** and {DyL(Cl)$_2$(NO$_3$)} **(7)**.

The three compounds presented in this section crystallise in the monoclinic space groups P2$_1$/n ({DyL(Cl)$_2$(H$_2$O)} **(5)** and {DyL(Cl)(H$_2$O)(NO$_3$)} **(6)**) and P2$_1$/c ({DyL(Cl)$_2$(NO$_3$)} **(7)**). As in subchapter 4.1.1 discussed, the centrosymmetric space groups make sense for the enantiomeric compounds in order to pack densely. The asymmetric units contain [Dy(H$_2$dapp)(Cl)$_2$(H$_2$O)]Cl·MeOH **(5)**, [Dy(H$_2$dapp)(Cl)(NO$_3$)(H$_2$O)]Cl·2MeOH **(6)** and [Dy(H$_2$dapp)(Cl)$_2$(NO$_3$)]·MeOH **(7)**.

a                                                    b

**(5)**

a                                        b

**(6)**

a                                                    c

**(7)**
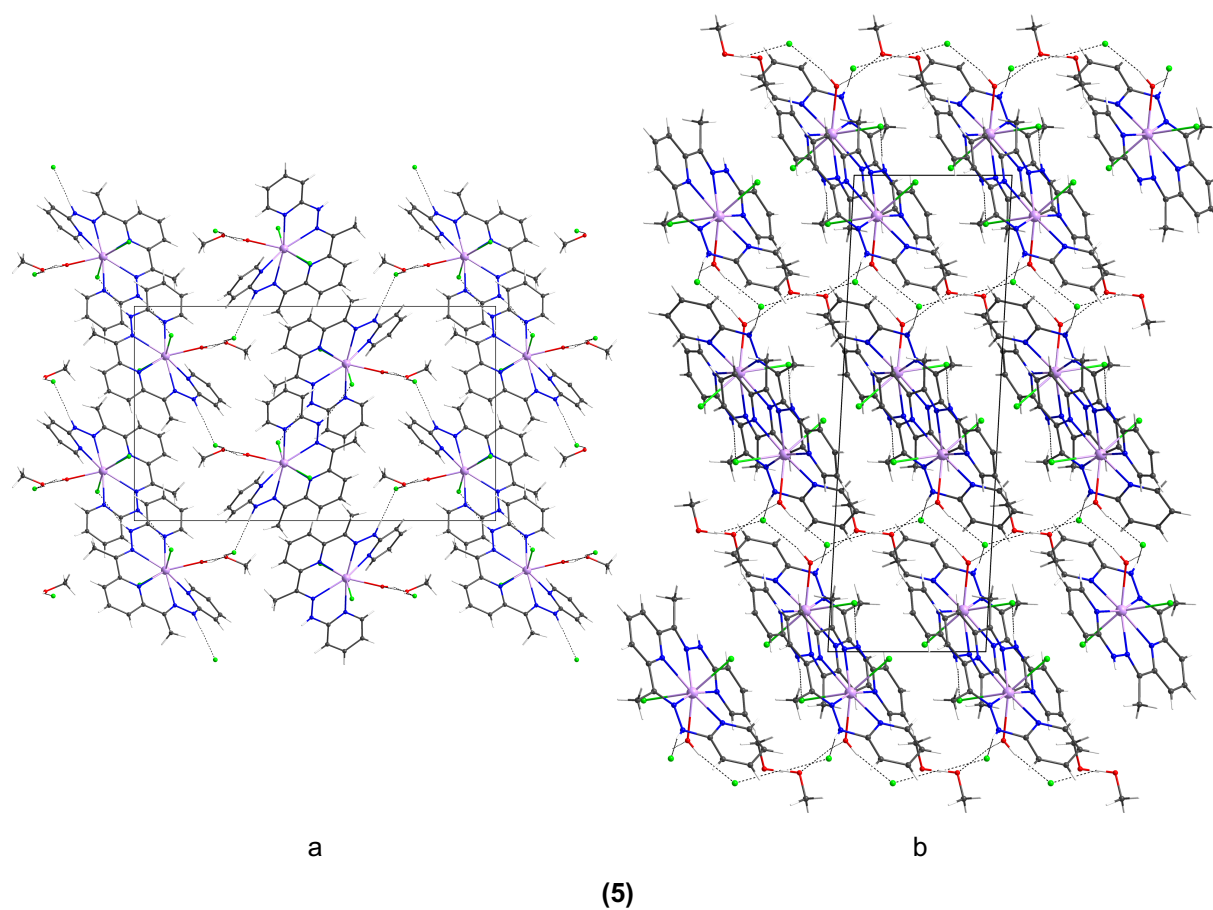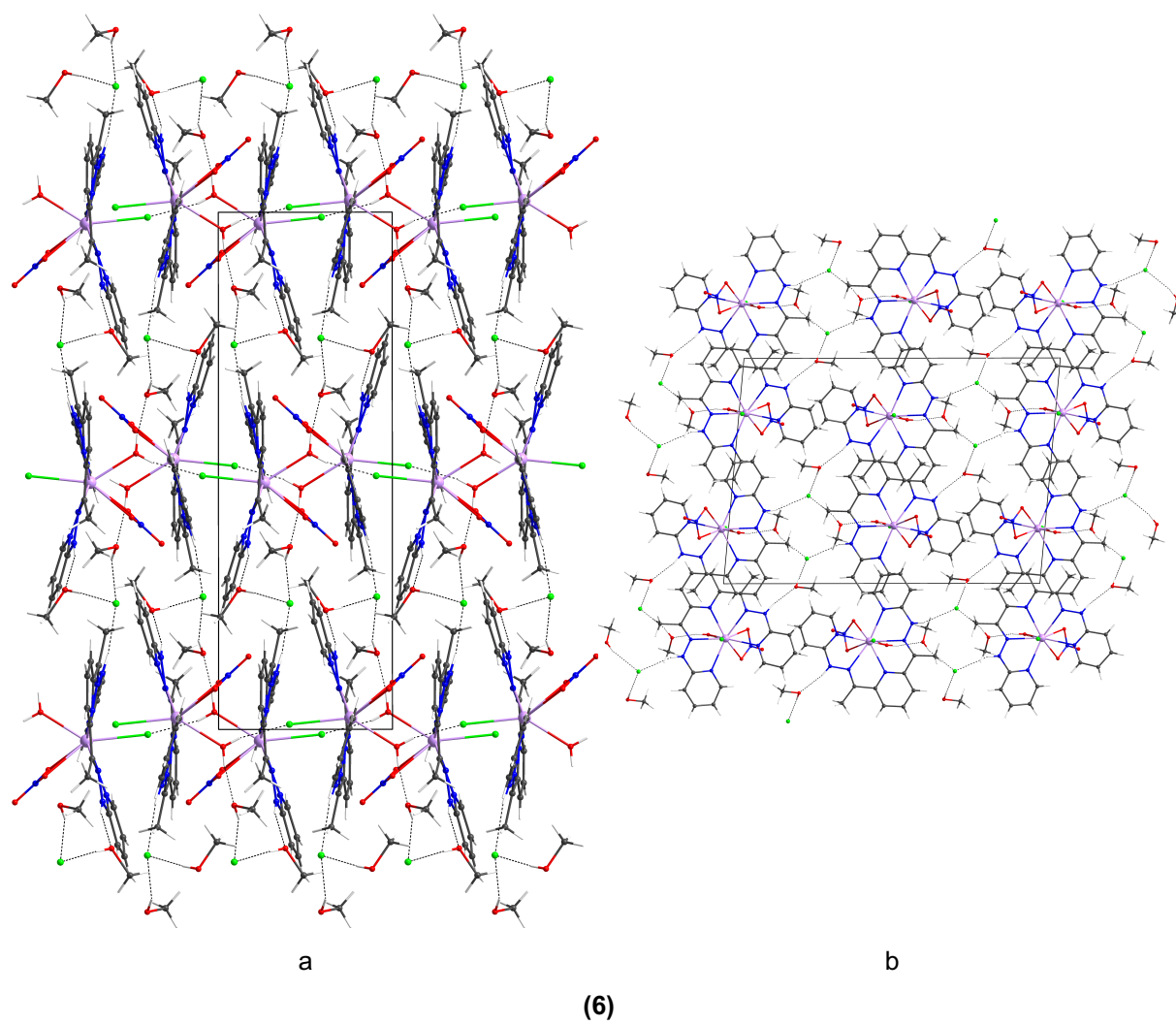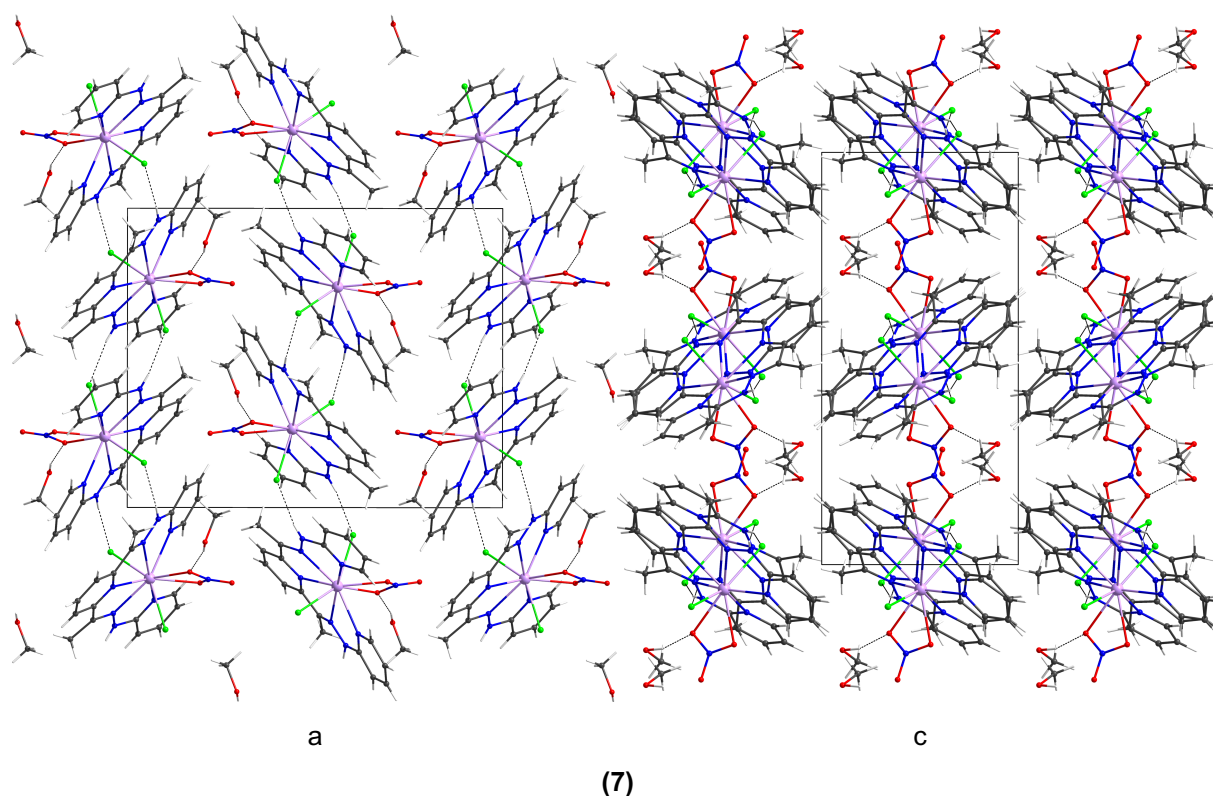
Figure 4.23: Crystal packing of {DyL(Cl)$_2$(H$_2$O)} **(5)**, {DyL(Cl)(H$_2$O)(NO$_3$)} **(6)** and {DyL(Cl)$_2$(NO$_3$)} **(7)** with viewing direction underneath.

The crystal packing of all structures is distinguished by hydrogen bonding (Figure 4.23). The anionic ligands function as hydrogen bond acceptors and the N-H groups as hydrogen bond donors. The lattice methanol and the lattice anions link the hydrogen bonds to the next neighbouring molecules. As the examples of {DyL(NO$_3$)$_2$} **(2)**, {DyL(NO$_3$)$_2$} **(3)** and {DyL(Ac)$_2$} **(4)** show, it can be expected that the strong hydrogen bonding may have an impact on the coordination sphere of the dysprosium ions.

As already discussed in section 4.1.1, the structures were designed for single molecular magnetic investigations and for the structure sensitive magnetic properties. A structure analysis by CShM with SHAPE 2.1 was conducted in this case as well.[107] Also here, the programme should not lead to misleading values for chemical interpretation since within these cases the coordination bonds are of similar magnitude. However in the investigated structures, there are differences within the bond lengths. Especially, the Dy-Cl bonds are longer than the other coordination bonds. Comparing the coordination polyhedra of the real complexes (coloured in pink) and the optimised polyhedra with the lowest deviation values (coloured blue to the right of each real complex) in Figure 4.24, it can be seen that the calculated polyhedra are reasonable.

| **(5)** | TDD | BTDR | SAPR |
| | 3.10 % | 3.61 % | 4.42 % |
| **(6)** | MFF | CSAPR | TCTPR |
| | 2.99 % | 3.75 % | 3.94 % |
| **(7)** | MFF | CSAPR | TCTPR |
| | 3.76 % | 4.01 % | 4.22 % |
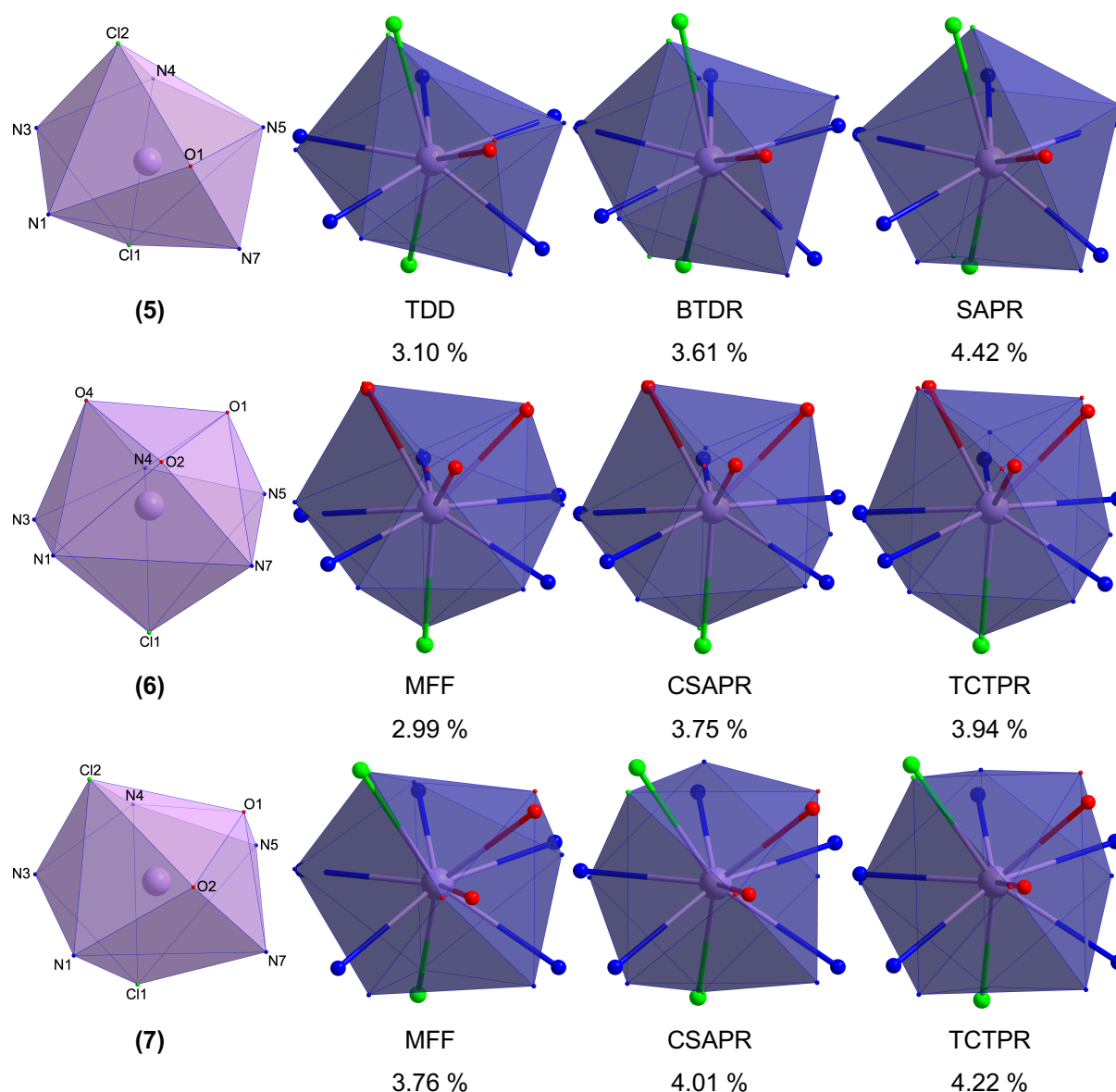
Figure 4.24: Lilac: coordination polyhedra of the complexes {DyL(Cl)$_2$(H$_2$O)} **(5)**, {DyL(Cl)(H$_2$O)(NO$_3$)} **(6)** and {DyL(Cl)$_2$(NO$_3$)} **(7)**. Blue: coordination polyhedra of the best fitting ideal structures, triangular dodecahedron (TDD), biaugmented trigonal prism (BTPR), square antiprism (SAPR), muffin structure type (MFF), spherical capped square antiprism (CSAPR), spherical capped trigonal prism (TCTPR) and the positions of the atoms in the original structure. Deviation values below ideal structures. The deviation values and the optimal polyhedra are obtained with SHAPE 2.1.[107]

All these polyhedra are of low symmetry as is often the case for lanthanide complexes, which was also found for the complexes in section 4.1.1.

The average deviation values are high compared to the ones for {DyL(H$_2$O)$_4$} **(1)**, {DyL(NO$_3$)$_2$} **(2)**, {DyL(NO$_3$)$_2$} **(3)** and {DyL(Ac)$_2$} **(4)**. For {DyL(Cl)(H$_2$O)(NO$_3$)} **(6)** and {DyL(Cl)$_2$(NO$_3$)} **(7)**, the ideal structures with the low symmetry muffin type (C$_s$ symmetry) have the lowest deviation value, which means the best agreement with the actual coordination sphere of the compounds. The deviation of {DyL(Cl)(H$_2$O)(NO$_3$)} **(6)** from this ideal structure is 2.99 % and the deviation of {DyL(Cl)$_2$(NO$_3$)} **(7)** from the muffin type is 3.76 %. For the sole eight coordinated dysprosium in {DyL(Cl)$_2$(H$_2$O)}

**(5)**, the best fitting ideal polyhedron is the triangular dodecahedron (TDD) geometry. The others are shown in Figure 4.24. The similarity of {DyL(Cl)(H$_2$O)(NO$_3$)} **(6)** and {DyL(Cl)$_2$(NO$_3$)} **(7)** can be anticipated because the difference between the structures is just the replacement of the water ligand by a chloride ligand. Although they are different in order, the three best fitting ideal geometries of the nine coordinate molecules {DyL(Cl)(H$_2$O)(NO$_3$)} **(6)** and {DyL(Cl)$_2$(NO$_3$)} **(7)** are the same structure types as in {DyL(H$_2$O)$_4$} **(1)**, {DyL(NO$_3$)$_2$} **(2)** and {DyL(NO$_3$)$_2$} **(3)**.

As discussed above, the low symmetry of the compounds leads to overparametrisation problems in computational approaches.[108,109] Therefore, the degrees of the anisotropy and the orientations of the Dy anisotropy axes for the compounds in this section were also estimated with a simple electrostatic model using the MAGELLAN software.[40] The use of MAGELLAN is known to give reliable results for single dysprosium ions as shown by *ab initio* calculations.[40] As in the case of the O1 in {DyL(H$_2$O)$_4$} **(1)**, the Dy-Cl anchor vectors are not coincident with the anisotropy axes found from MAGELLAN in the compounds {DyL(Cl)$_2$(H$_2$O)} **(5)**, {DyL(Cl)(H$_2$O)(NO$_3$)} **(6)** and {DyL(Cl)$_2$(NO$_3$)} **(7)**. The results are given in Figure 4.25.

**(5)**

980 cm$^{-1}$

**(6)**

810 cm$^{-1}$

**(7)**

920 cm$^{-1}$
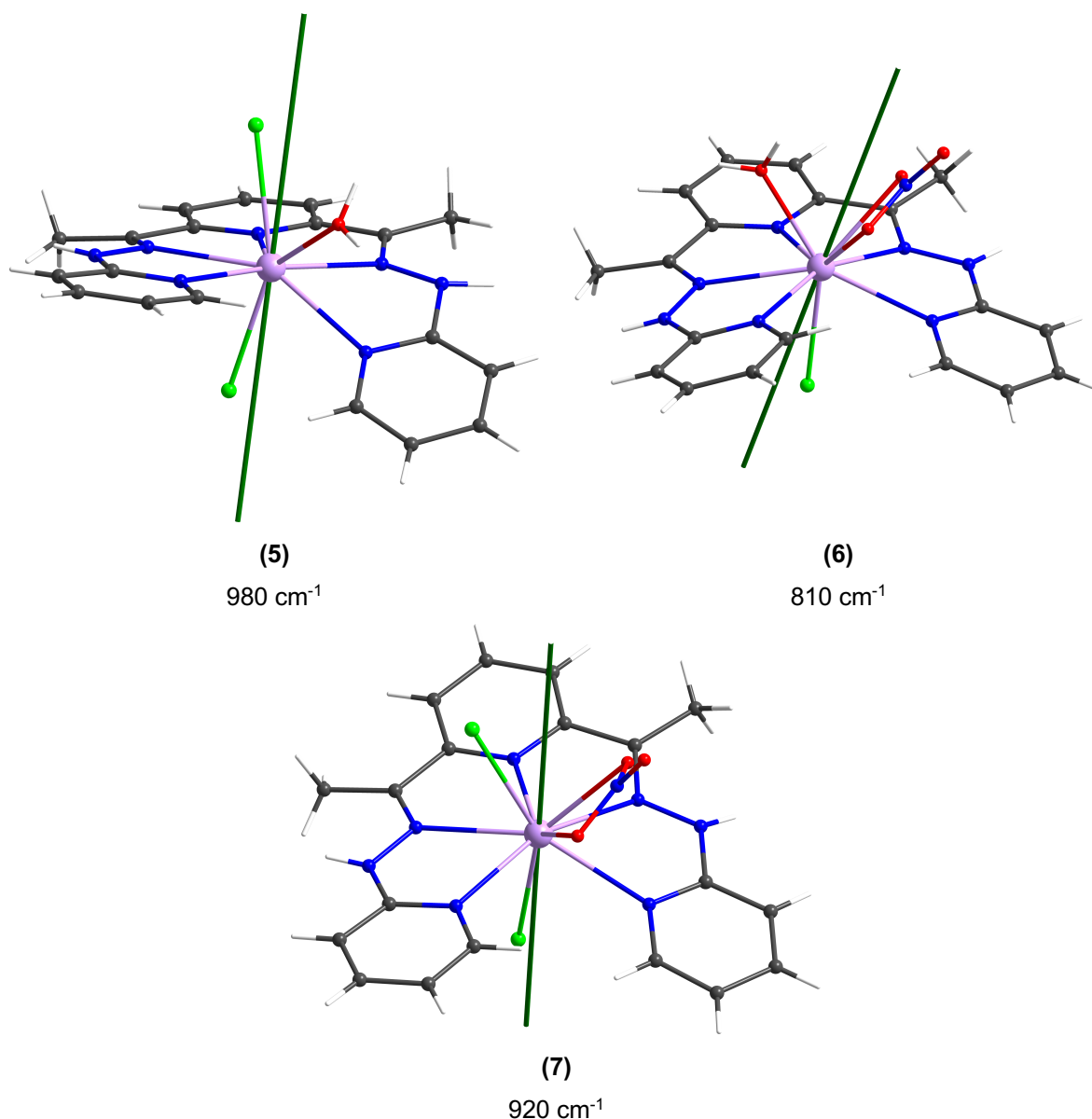
Figure 4.25: Molecules {DyL(Cl)$_2$(H$_2$O)} **(5)**, {DyL(Cl)(H$_2$O)(NO$_3$)} **(6)** and {DyL(Cl)$_2$(NO$_3$)} **(7)** with anisotropy axes and minimal reversal energies obtained from MAGELLAN.[40]

The figure shows the calculated anisotropy axes of each molecule in dark green and the estimated value for the minimal reversal energy below each picture of the molecules. It shows that the anisotropy of all three complexes is high and of similar magnitude in size. Compounds {DyL(Cl)$_2$(H$_2$O)} **(5)**, {DyL(Cl)(H$_2$O)(NO$_3$)} **(6)** and {DyL(Cl)$_2$(NO$_3$)} **(7)** present the opportunity to gage the relative influences of three secondary ligands. Compound {DyL(Cl)$_2$(H$_2$O)} **(5)** has two chlorides and one water, compound {DyL(Cl)(H$_2$O)(NO$_3$)} **(6)** has a chloride, a water and a nitrate and compound {DyL(Cl)$_2$(NO$_3$)} **(7)** has two chlorides and one nitrate. The reversal energies are in the order **(6)<(7)<(5)** (Figure 4.25) which probably reflects the relative negative charge distribution of the three secondary ligands. For compound

{DyL(Cl)(H$_2$O)(NO$_3$)} **(6)**, this lower relative energy compared to compound {DyL(Cl)$_2$(NO$_3$)} **(7)** reflects the fact that there is a water rather than a chloride ligand. On the other hand for compound {DyL(Cl)$_2$(H$_2$O)} **(5)**, the replacement of the nitrate secondary ligand of {DyL(Cl)$_2$(NO$_3$)} **(7)** by a water in {DyL(Cl)$_2$(H$_2$O)} **(5)** tips the balances to favour of a higher reversal energy. The software MAGELLAN calculates a value of 980 cm$^{-1}$ for the reversal energy in {DyL(Cl)$_2$(H$_2$O)} **(5)**. The complex with the three anionic ligands {DyL(Cl)$_2$(NO$_3$)} **(7)** has a smaller value of 920 cm$^{-1}$ for the reversal energy.

The deviation of the anisotropy axes to the anchor axes is similar in magnitude for all three compounds {DyL(Cl)$_2$(H$_2$O)} **(5)**, {DyL(Cl)(H$_2$O)(NO$_3$)} **(6)** and {DyL(Cl)$_2$(NO$_3$)} **(7)**. The angles between the anchor axes and the anisotropy axes are shown in Figure 4.26.
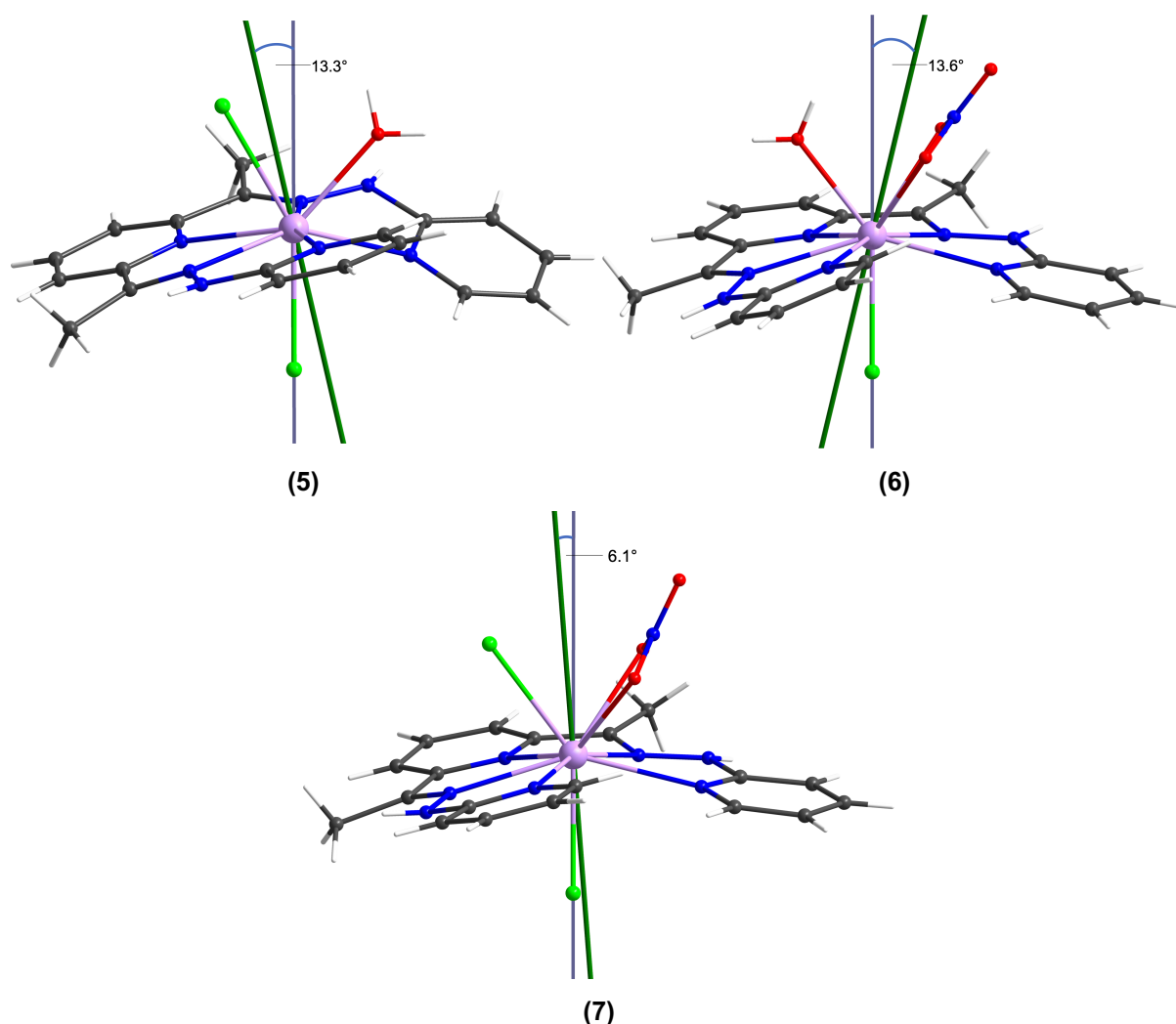


Figure 4.26: Angles between anchor axes and anisotropy axes of {DyL(Cl)$_2$(H$_2$O)} **(5)**, {DyL(Cl)(H$_2$O)(NO$_3$)} **(6)** and {DyL(Cl)$_2$(NO$_3$)} **(7)**.

Due to the monoclinic space groups of the crystal structures of the molecules of this section, the anisotropy axes of the molecules within the unit cell are not collinear unlike compounds **(1)-(4)** with their triclinic crystal structures. This can be an issue since the magnetisations might cancel each other to some extent and the magnetic field induced by the dysprosium in one molecule could act as a transverse field on an adjacent molecule enhancing quantum tunnelling. For $\{DyL(Cl)_2(NO_3)\}$ **(7)**, the deviation of the collinearity and thus, the angle between the anisotropy axes is 89.3°, which is almost 90° being the highest deviation it could go to. For $\{DyL(Cl)_2(H_2O)\}$ **(5)**, it is 50.6° and for $\{DyL(Cl)(H_2O)(NO_3)\}$ **(6)**, it is 39.5°. This means none of the anisotropy axes are very collinear. This is visualised in Figure 4.27.



**(5)**                                                                                                   **(6)**



**(7)**
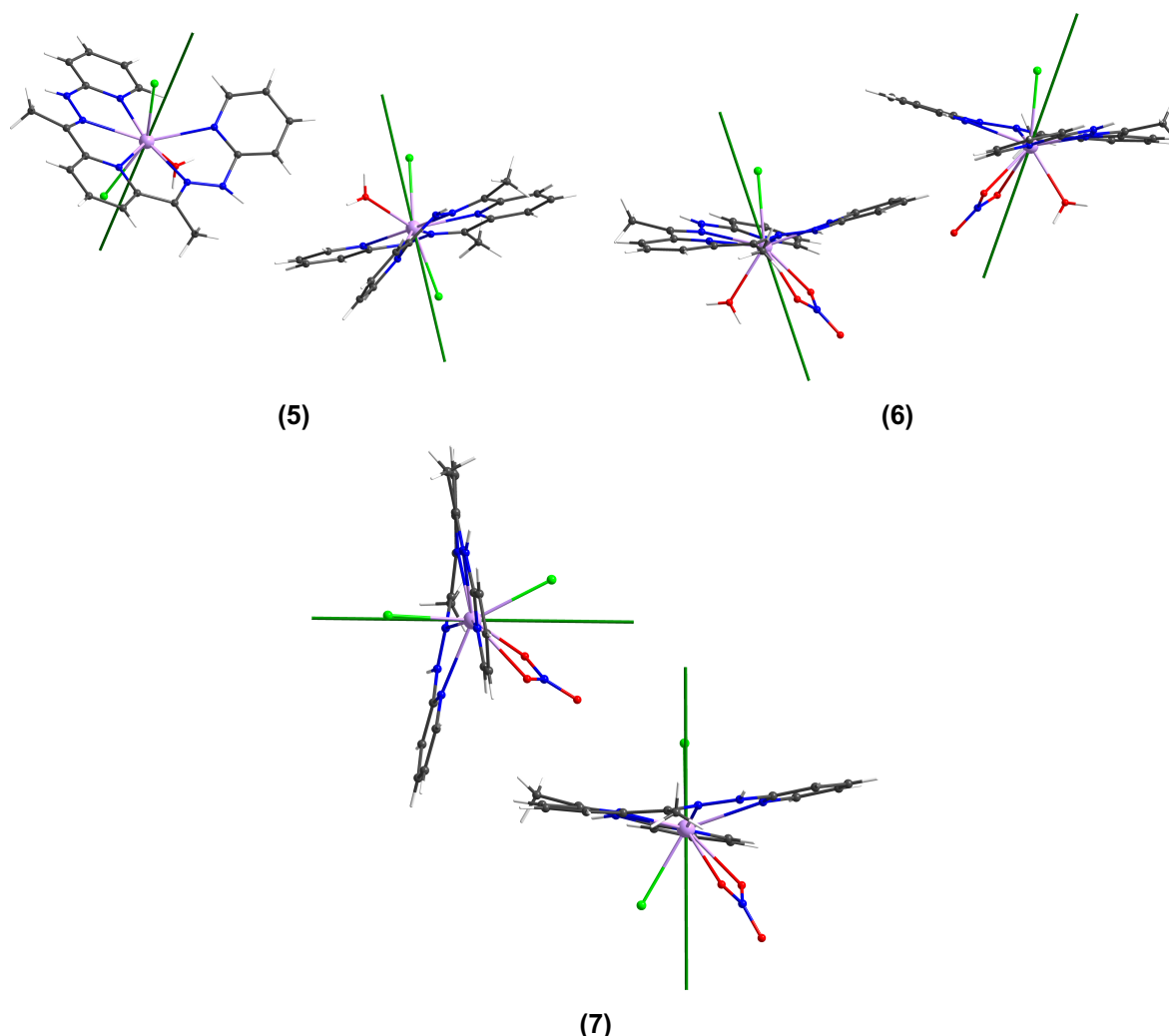
Figure 4.27: Relative direction of the anisotropy axes of the molecules $\{DyL(Cl)_2(H_2O)\}$ **(5)**, $\{DyL(Cl)(H_2O)(NO_3)\}$ **(6)** and $\{DyL(Cl)_2(NO_3)\}$ **(7)** in the crystal structure.

In order to have a better overview of the compounds and their specifications, all significant values are summarised in Table 4.5. In a plot of reversal energy versus $\delta$

(Figure 4.28), it can be seen that there is some dependence which fits for the compounds with the smallest $\delta$ well but with {DyL(Ac)$_2$} **(4)** being the highest point in the plot, the compounds with higher $\delta$ value seem to fit worse. It could be that {DyL(Ac)$_2$} **(4)** represents a close to a maximum value in the correlation. To make a final conclusion on this, more data points are needed.
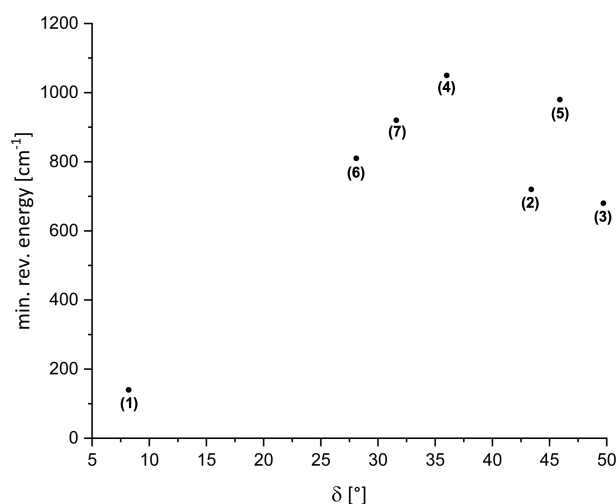


Figure 4.28: Reversal energies versus $\delta$ values for compounds {DyL(H$_2$O)$_4$} **(1)**, {DyL(NO$_3$)$_2$} **(2)**, {DyL(NO$_3$)$_2$} **(3)**, {DyL(Ac)$_2$} **(4)**, {DyL(Cl)$_2$(H$_2$O)} **(5)**, {DyL(Cl)(H$_2$O)(NO$_3$)} **(6)** and {DyL(Cl)$_2$(NO$_3$)} **(7)**.

Table 4.5: Summarised key figures for **(1)-(7)**.

| | {DyL(H$_2$O)$_4$} **(1)** | {DyL(NO$_3$)$_2$} **(2)** | {DyL(NO$_3$)$_2$} **(3)** | {DyL(Ac)$_2$} **(4)** | {DyL(Cl)$_2$(H$_2$O)} **(5)** | {DyL(Cl)(H$_2$O)(NO$_3$)} **(6)** | {DyL(Cl)$_2$(N$_2$O)$_3$} **(7)** |
|---|---|---|---|---|---|---|---|
| MAGELLAN anchor | 10.6° O1(H2O) | 6.7° O3O4(NO3) | 6.3° O3O4(NO3) | 5.9° O3O4(Ac) | 13.3° Cl1(Cl) | 13.6° Cl1(Cl) | 6.1° Cl1(Cl) |
| Lig. 1 anchor | 38.6° O2(H2O) | 6.5° O1O2(NO3) | 8.8° O1O2(NO3) | 13.5° O1O2(Ac) | 41.8° O1(H2O) | 33.9° O1O2(NO3) | 37.3° O1O2(NO3) |
| Lig. 2 anchor | 37.6° O3(H2O) | | | | 30.5° Cl2(Cl) | 38.1° O4(H2O) | 37.4° Cl2(Cl) |
| Lig. 3 anchor | 52.5° O4(H2O) | | | | | | |
| Lig. 1 anis | 43.7° O2(H2O) | 1.2° O1O2(NO3) | 2.7° O1O2(NO3) | 7.7° O1O2(Ac) | 54.4° O1(H2O) | 20.3° O1O2(NO3) | 40.2° O1O2(NO3) |
| Lig. 2 anis | 42.3° O3(H2O) | | | | 17.3° Cl2(Cl) | 51.5° O4(H2O) | 32.4° Cl2(Cl) |
| Lig. 3 anis | 41.9° O4(H2O) | | | | | | |
| δ value | 8.2 | 43.4 | 49.7 | 36.0 | 45.9 | 28.1 | 31.6 |
| Best shape | TCTPR 2.52 % | TCTPR 2.50 % | TCTPR 2.65 % | CCU 3.36 % | TDD 3.10 % | MFF 2.99 % | MFF 3.76 % |
| Min. rev. energies | 140 cm$^{-1}$ | 720 cm$^{-1}$ | 680 cm$^{-1}$ | 1050 cm$^{-1}$ | 980 cm$^{-1}$ | 810 cm$^{-1}$ | 920 cm$^{-1}$ |
| Average Dy-N | 2.56 Å | 2.46 Å | 2.45 Å | 2.50 Å | 2.48 Å | 2.51 Å | 2.53 Å |
| Average N-Dy-N | 62.5° | 65.2° | 65.1° | 63.8° | 64.4° | 63.7° | 63.2° |
| Angle between ligand planes | | 73.4° | 72.3° | 53.5° | | | |

### 4.1.3  Dysprosium-H$_2$dapp Dimeric Complexes

The design of the dysprosium-H$_2$dapp complexes presented in the sections above enables the exchange of ligands as already shown in subchapter 4.1.2. This is possible due to the chelating nature of the axial secondary ligands of the H$_2$dapp complex. Conditions can be changed to favour other secondary ligands on the dysprosium without losing the dysprosium-H$_2$dapp connectivity. Additionally, the derivative complexes can be crystallised rather easily due to the ability of effective hydrogen bonding. The strong bond between H$_2$dapp and dysprosium, as a result of the kinetic chelating effects, also allows the reaction with ligands that are rarely found in lanthanide compounds. In this section, examples of dysprosium-fluoride and

dysprosium-peroxide complexes are presented. These kinds of compounds are scarce because following the hard and soft acids and bases (HSAB) concept dysprosium ions in solution tend to form insoluble salts with fluoride and peroxide ions. Adding, for example, a fluoride source to a dysprosium chloride solution leads to the immediate formation and precipitation of dysprosium fluoride.[122] This white solid is inert to any other complexation under normal conditions. In some cases, it is possible to use hydrothermal reactions to overcome this problem.[123]

Only 29 examples[124-143] of lanthanide-peroxide complexes, disregarding the doubled isostructural compounds with different lanthanides, have been reported according to the CSD and only two of them have been magnetically investigated.[123,144] If only dysprosium compounds are taken into account, there are only four structures published.[145-148] For dysprosium fluoride compounds, there are only 16 dysprosium coordination compounds which have a fluoride ligand according to a research in the CSD.[122,123,144,149-156] Because of their scarcity, these compounds attract interest in the field of lanthanide coordination chemistry. Moreover, the short and strong bonds made by ligands such as peroxide or fluoride to $Dy^{3+}$ allow short contacts between lanthanides and other magnetic centres which leads to stronger coupling effects supressing quantum tunnelling. Additionally, the short lanthanide to anionic ligand distance allows negative charges close to the lanthanide which can increase the magnetic anisotropy.
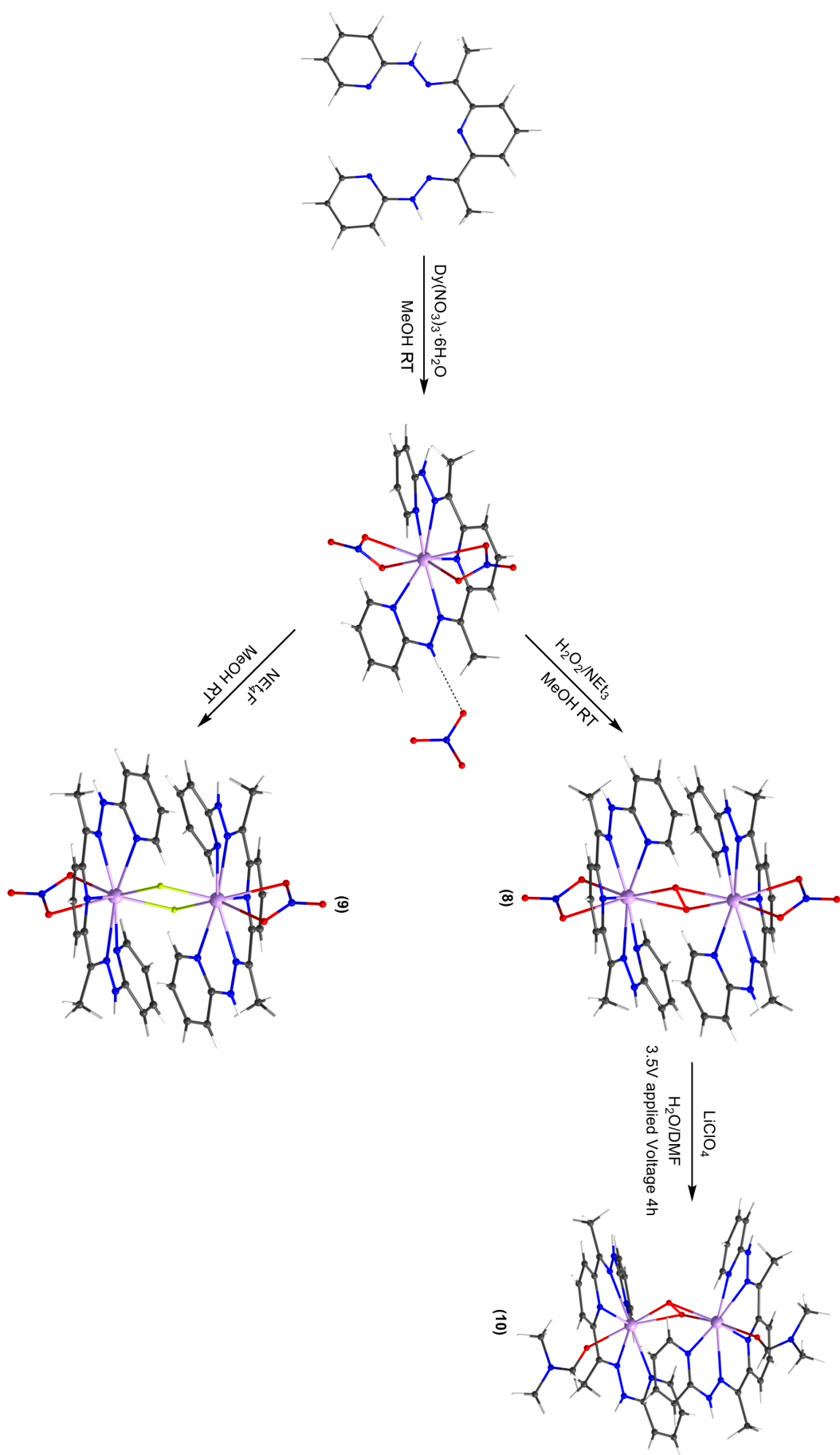
Figure 4.29: Reaction scheme for dysprosium complex synthesis of $[Dy_2(H_2dapp)_2(NO_3)2(O)_2](NO_3)_2$ **(8)**, $[Dy_2(H_2dapp)_2(NO_3)_2(F)_2](NO_3)_2 \cdot 4H_2O$ **(9)** and $[Dy_2(H_2dapp)_2(DMF)_2(O)_2](ClO_4)_4 \cdot 4H_2O$ **(10)**.

The synthesis of the compounds presented in this section is based on the synthesis of {DyL(NO$_3$)$_2$} **(2)**. Reaction solutions of {DyL(NO$_3$)$_2$} **(2)** were mixed with basic solutions of hydrogen peroxide or tetraethylammonium fluoride in order to form the dimers. The reaction scheme is depicted in Figure 4.29 giving an overview.



**(8)**                    **(9)**

**(10)**
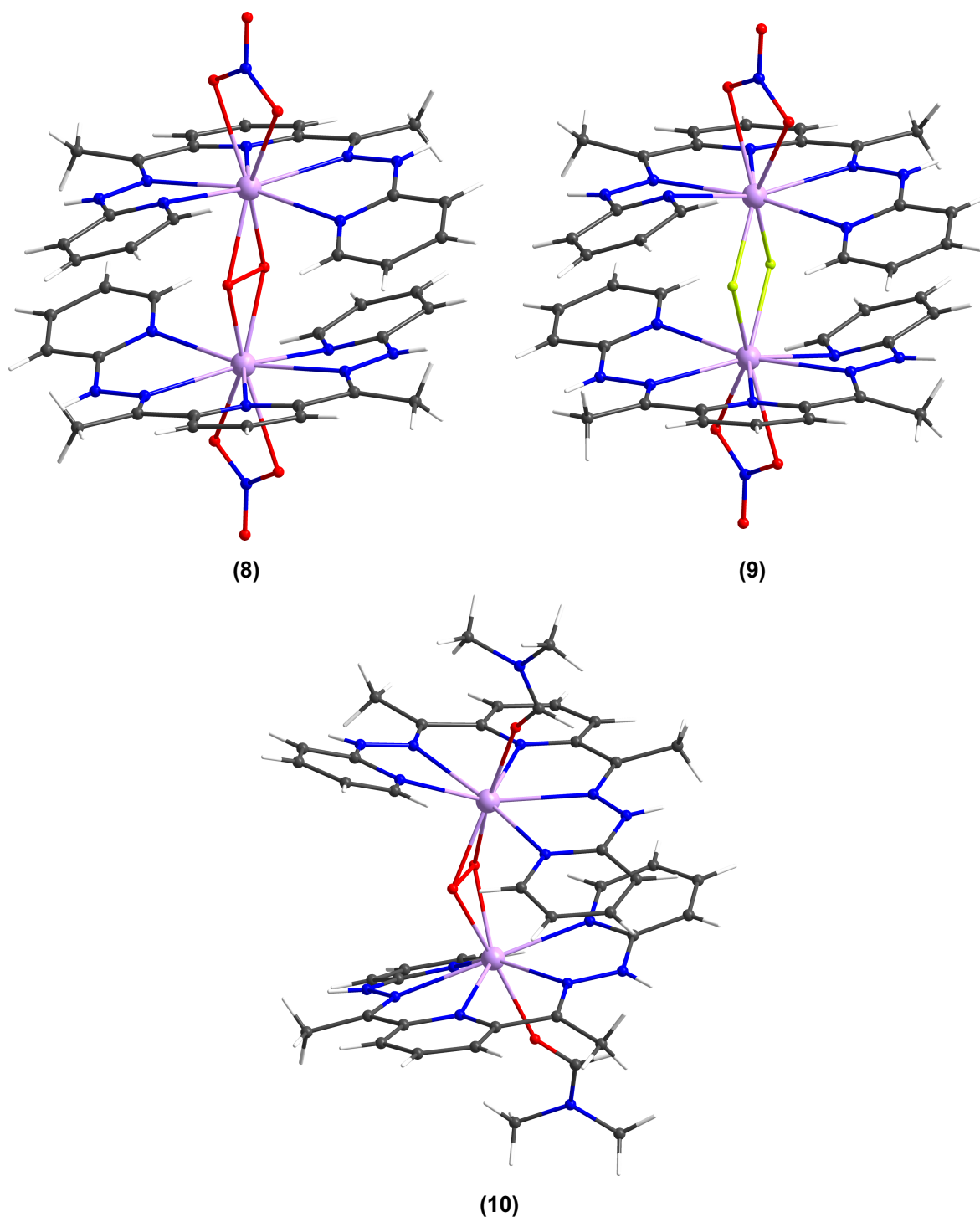
Figure 4.30: The three dimeric complexes {Dy$_2$L$_2$(O)$_2$(NO$_3$)$_2$} **(8)**, {Dy$_2$L$_2$(F)$_2$(NO$_3$)$_2$} **(9)** and {Dy$_2$L$_2$(O)$_2$(DMF)$_2$} **(10)**. Colour code: white = H; grey = C; blue = N; red = O; lime = F; lilac = Dy.

Given their structural similarity to hydroxide ions, the identity of the bridging fluoride ligands was confirmed by elemental analysis. All three compounds depicted in Figure 4.30 derive from [Dy(H$_2$dapp)(NO$_3$)$_2$]NO$_3$ **(2)** as the principal reaction mixture is the same. In the reaction scheme of Figure 4.29, the synthesis routes are shown. By adding the harder ligands, which are either fluoride or peroxide ions, the coupled dimeric and binuclear structures with terminal nitrate ligands can be obtained.

For the synthesis of [Dy$_2$(H$_2$dapp)$_2$(NO$_3$)$_2$(O)$_2$](NO$_3$)$_2$ **(8)**, a reaction mixture of {DyL(NO$_3$)$_2$} **(2)** is rapidly mixed with triethylamine (NEt$_3$) which prevents precipitation of {DyL(NO$_3$)$_2$} **(2)** and causes a strong colour shift from light orange to red. Then, H$_2$O$_2$ is added in small excess changing the colour back to orange. After one day, blade shaped orange-red crystals of {Dy$_2$L$_2$(O)$_2$(NO$_3$)$_2$} **(8)** grow. Crystals of {Dy$_2$L$_2$(O)$_2$(NO$_3$)$_2$} **(8)** with two different crystal structures in different space groups are obtained. This depends on whether the measurement was done immediately after precipitation which gives the structure ([Dy$_2$(H$_2$dapp)$_2$(NO$_3$)$_2$(O)$_2$](NO$_3$)$_2$·2MeOH) **(8a)** or if it was done when the crystals dried which gives the structure ([Dy$_2$(H$_2$dapp)$_2$(NO$_3$)$_2$(O)$_2$](NO$_3$)$_2$·4H$_2$O) **(8b)**. This is discussed in detail below.

The synthesis of [Dy$_2$(H$_2$dapp)$_2$(NO$_3$)$_2$(F)$_2$](NO$_3$)$_2$·4H$_2$O **(9)** used tetraethylammonium fluoride (NEt$_4$F) as a fluoride source. The orange reaction mixture of {DyL(NO$_3$)$_2$} **(2)** was treated with a stoichiometric amount of NEt$_4$F. After one day, blade shaped orange crystals are grown. These crystals are isomorphous to the hydrated form of the peroxide complex {Dy$_2$L$_2$(O)$_2$(NO$_3$)$_2$} **(8a)**. For this compound, the dried isostructural {Dy$_2$L$_2$(O)$_2$(NO$_3$)$_2$} **(8)** was found from the single crystal X-ray measurement. This will also be discussed in the following section of structure description. As a third compound, [Dy$_2$(H$_2$dapp)$_2$(DMF)$_2$(O)$_2$](ClO$_4$)$_4$·4H$_2$O **(10)** was synthesised during a cyclic voltametric experiment with LiClO$_4$ as electrolyte in DMF and water at a voltage of 3.5 V resulting in a few crystals after 4 h. So far, the compound could not be synthesised in a direct procedure. Possibly, the nitrate ligand, which stabilised the formation of the dimer, is not substitutable for the formation of the dimeric compounds. Also, synthetic attempts starting with the dimer {Dy$_2$L$_2$(O)$_2$(NO$_3$)$_2$} **(8)** in a mixture of DMF and water with an excess of LiClO$_4$ did not lead to crystalline product of {Dy$_2$L$_2$(O)$_2$(DMF)$_2$} **(10)**. Currently it is not known whether the applied voltage plays any role.

For these molecules, the consideration of the helicity gives some interesting perspectives. As already briefly mentioned in section 4.1.2, the helicity of the ligands also gives rise to their chirality. This means, the helical deformation around a given Dy

can either be right- or left-handed. This is shown in the video animation in the digital appendix. For the dimeric and binuclear complexes, this can mean that they are either composed of only right-handed or only left-handed helically distorted ligands at both dysprosium centres or that they are a meso compound composed of a left-handed and a right-handed helically distorted ligand. The molecular structures of $\{Dy_2L_2(O)_2(NO_3)_2\}$ **(8)**, $\{Dy_2L_2(F)_2(NO_3)_2\}$ **(9)** and $\{Dy_2L_2(O)_2(DMF)_2\}$ **(10)** show that the homo as well as the meso compounds are formed. While $\{Dy_2L_2(O)_2(NO_3)_2\}$ **(8)** and $\{Dy_2L_2(F)_2(NO_3)_2\}$ **(9)** have molecular structures in the meso form, $\{Dy_2L_2(O)_2(DMF)_2\}$ **(10)** has an isomeric form with $\Delta,\Delta$ and $\Lambda,\Lambda$ enantiomers. The helicities of $\{Dy_2L_2(O)_2(NO_3)_2\}$ **(8)** and $\{Dy_2L_2(O)_2(DMF)_2\}$ **(10)** are described with arrows in Figure 4.31. It can be seen that $\{Dy_2L_2(O)_2(NO_3)_2\}$ **(8)** consists of one (the upper) dysprosium centre with $\Delta$ and one (the lower) with a $\Lambda$ coordinated H$_2$dapp ligand. In the right picture, on the other hand, compound $\{Dy_2L_2(O)_2(DMF)_2\}$ **(10)** shows $\Delta,\Delta$-configuration. For the compounds, this means that either the chirality of a ligand can change in solution or the dimeric structures decompose to some extend in solution not only losing the nitrate ligand but also detaching one of the monomeric units. It is possible that the handedness of the helix inverts easily as is the case for amines in aqueous solution or if this can be inhibited to some extent through the strong chelation to the metal centre and leading to a high enough energy barrier to the inversion of handedness.[157,158] Either way, this is an intriguing detail to explore in the field of coordination dynamics in solution but beyond the scope of this thesis. In the solid state the crystal packing finally fixes the handedness.

(8)　　　　　　　　　　　　　　(10)
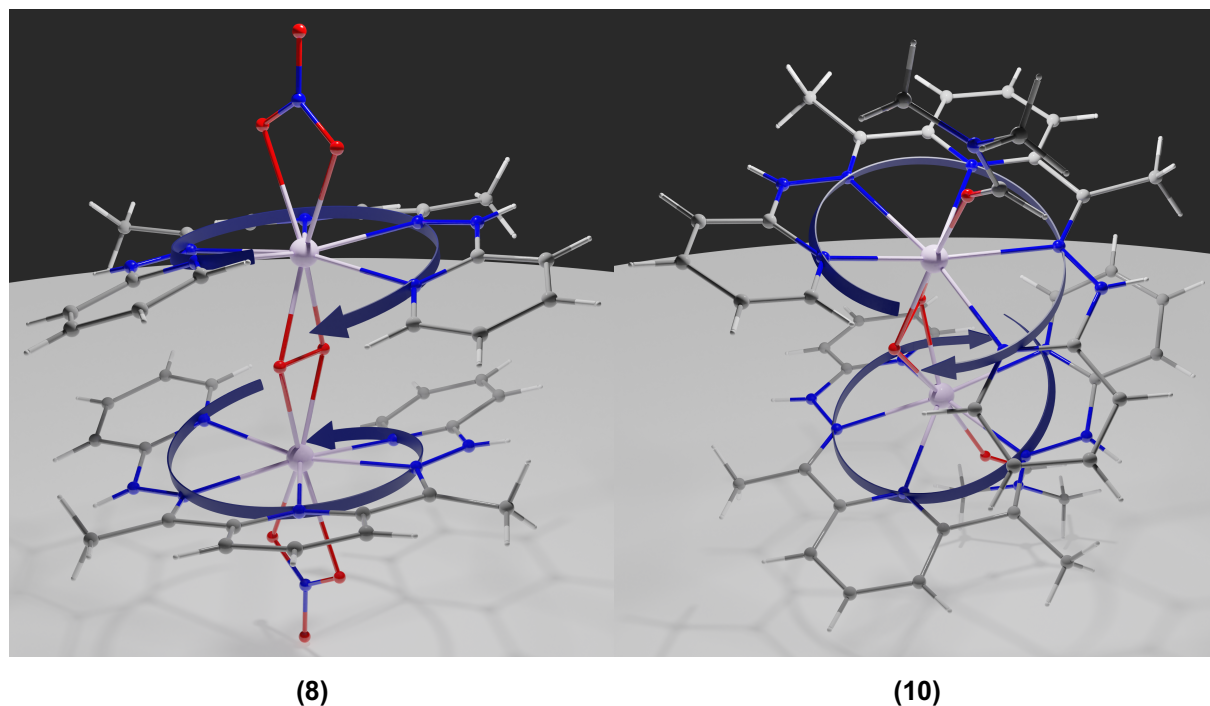
Figure 4.31: Helical distortion of $\{Dy_2L_2(O)_2(NO_3)_2\}$ **(8)** in meso form and $\{Dy_2L_2(O)_2(DMF)_2\}$ **(10)** in $\Delta,\Delta$-configuration.

The amount of helical distortion in the complexes as explained in the previous sections (4.1.1 and 4.1.2) is described by the $\delta$ value. The resulting angles are listed in Table 4.6. For $\{Dy_2L_2(O)_2(NO_3)_2\}$ **(8a)** and $\{Dy_2L_2(F)_2(NO_3)_2\}$ **(9)**, the angles are almost the same. Compound $\{Dy_2L_2(O)_2(NO_3)_2\}$ **(8a)** shows a $\delta$ value of 24.3° and compound $\{Dy_2L_2(F)_2(NO_3)_2\}$ **(9)** shows a value of 25.0°. Intriguingly, compound $\{Dy_2L_2(O)_2(NO_3)_2\}$ **(8b)** which is isomorphous to $\{Dy_2L_2(F)_2(NO_3)_2\}$ **(9)** shows much smaller distortion values of 21.3° and 20.1° for the top half and the bottom half coordination of $H_2$dapp. These values are comparatively small compared to the $\delta$ values of the compounds in section 4.1.1 and section 4.1.2. The small variations in the distortion values could, as in the example of $\{DyL(NO_3)_2\}$ **(2)** and $\{DyL(NO_3)_2\}$ **(3)**, originate from steric effects. However, in the case of the dimers and binuclear compounds this distortion is intermolecular in origin as can be seen from the crystal packing (Figure 4.35). Compound $\{Dy_2L_2(O)_2(DMF)_2\}$ **(10)**, on the other hand, has a stronger distortion and exhibits a $\delta$ value of 36.7°, which is an intermediate value compared to the structures described so far. This bigger value is possibly a result of the folding of the O-Dy-O axes which will be discussed below in detail. In compounds $\{Dy_2L_2(F)_2(NO_3)_2\}$ **(9)** and $\{Dy_2L_2(O)_2(DMF)_2\}$ **(10)**, some folding distortion in the ligands can be detected having the different sign for the $\alpha$ and $\beta$ angle (Table 4.6) as it can be observed in $\{DyL(H_2O)_4\}$

**(1)** to a strong and in $\{DyL(Cl)(H_2O)(NO_3)\}$ **(6)** and $\{DyL(Cl)_2(NO_3)\}$ **(7)** to a smaller extent.

Table 4.6: Helical distortion values for $\{Dy_2L_2(O)_2(NO_3)_2\}$ **(8a)**, $\{Dy_2L_2(O)_2(NO_3)_2\}$ **(8b)**, $\{Dy_2L_2(F)_2(NO_3)_2\}$ **(9)** and $\{Dy_2L_2(O)_2(DMF)_2\}$ **(10)**.

| Compound | Dy centre | $\alpha/°$ | $\beta/°$ | $\delta/°$ |
|---|---|---|---|---|
| **(8a)** | | -20.2 | -4.1 | **24.3** |
| **(8b)** | top half | -12.3 | -9.0 | **21.3** |
| | bottom half | 0.1 | 20.0 | **20.1** |
| **(9)** | top half | -28.2 | 3.4 | **25.0** |
| | bottom half | -0.6 | 25.1 | **24.5** |
| **(10)** | | -40.7 | 4.1 | **36.7** |

All three molecules are composed of two dysprosium centres each with an $H_2$dapp ligand bridged by either a peroxide, which is the case in $\{Dy_2L_2(O)_2(NO_3)_2\}$ **(8)** and $\{Dy_2L_2(O)_2(DMF)_2\}$ **(10)**, or two fluoride ions as in $\{Dy_2L_2(F)_2(NO_3)_2\}$ **(9)**. In $\{Dy_2L_2(O)_2(NO_3)_2\}$ **(8)** and in $\{Dy_2L_2(F)_2(NO_3)_2\}$ **(9)** the bridging atoms and the dysprosium centres are in a plane. In $\{Dy_2L_2(O)_2(DMF)_2\}$ **(10)** each dysprosium centre and the peroxide bridge are in different planes forming a dihedral angle of 37.3°.

In $\{Dy_2L_2(O)_2(NO_3)_2\}$ **(8)** and $\{Dy_2L_2(F)_2(NO_3)_2\}$ **(9)**, nitrate ions function as bidentate capping ligands while in $\{Dy_2L_2(O)_2(DMF)_2\}$ **(10)**, DMF coordinates with its oxygen as a capping ligand. Whilst the molecules $\{Dy_2L_2(O)_2(NO_3)_2\}$ **(8)** and $\{Dy_2L_2(F)_2(NO_3)_2\}$ **(9)** have inversion centres between the dysprosium ions which relate them and their coordination sphere into each other, $\{Dy_2L_2(O)_2(DMF)_2\}$ **(10)** has a rotational $C_2$ axis going through the mid-point of the peroxide bond and perpendicular to it. The molecule in $\{Dy_2L_2(F)_2(NO_3)_2\}$ **(9)** is essentially centrosymmetric, but this is not crystallographically imposed. The symmetries in the dimeric compounds also explain the different $\Delta$- and $\Lambda$-configurations. Obviously, only certain symmetry operations in a molecule can lead to homo isomeric or meso forms. While an inversion centre changes $\Delta$ to $\Lambda$ and vice versa, rotation keeps the isomeric configuration.

All coordination bond lengths and angles for $\{Dy_2L_2(O)_2(NO_3)_2\}$ **(8)**, $\{Dy_2L_2(F)_2(NO_3)_2\}$ **(9)** and $\{Dy_2L_2(O)_2(DMF)_2\}$ **(10)** are depicted in Table 4.7. Compound $\{Dy_2L_2(O)_2(NO_3)_2\}$ **(8)** crystallises in two different space groups. Therefore, values for the triclinic space group $\{Dy_2L_2(O)_2(NO_3)_2\}$ **(8a)** and the monoclinic space group $\{Dy_2L_2(O)_2(NO_3)_2\}$ **(8b)** are listed. The Dy-N bond lengths fit the expectations discussed in the subchapters above. The average value of the Dy-N bonds is 2.49 Å for $\{Dy_2L_2(O)_2(NO_3)_2\}$ **(8a)**, 2.50 Å for both dysprosium centres in $\{Dy_2L_2(O)_2(NO_3)_2\}$ **(8b)**, 2.51 Å for both dysprosium centres in $\{Dy_2L_2(F)_2(NO_3)_2\}$ **(9)** and 2.49 Å for

{$Dy_2L_2(O)_2(DMF)_2$} **(10)**. These values are very similar to each other. Other than for the molecules of section 4.1.1 and section 4.1.2, no correlation between the Dy-N bond lengths and helicity can be found fitting to the results of the first two subchapters. This is not at all surprising since the two $H_2$dapp ligands in all of the molecules have the shortest contacts of the magnitude of van der Waals radii of two carbon atoms (3.40 Å).[159] These are 3.45 Å in {$Dy_2L_2(O)_2(NO_3)_2$} **(8a)** and {$Dy_2L_2(O)_2(NO_3)_2$} **(8b)**, 3.33 Å in {$Dy_2L_2(F)_2(NO_3)_2$} **(9)** and also 3.33 Å in {$Dy_2L_2(O)_2(DMF)_2$} **(10)**. This means, the bond forces of the bridging ligands pull the dysprosium ions so close together that the chelating ligands start interacting with each other. This steric pressure inhibits strong helical distortion. The distance between the dysprosium ions in the complexes is also smaller than the van der Waals radii of two dysprosium ions (5.74 Å).[159] It is 4.15 Å in {$Dy_2L_2(O)_2(NO_3)_2$} **(8a)** and {$Dy_2L_2(O)_2(NO_3)_2$} **(8b)**, 4.00 Å in {$Dy_2L_2(F)_2(NO_3)_2$} **(9)** and 3.71 Å in {$Dy_2L_2(O)_2(DMF)_2$} **(10)** which means in {$Dy_2L_2(F)_2(NO_3)_2$} **(9)**, the distance is even shorter than the covalent radii of two dysprosium ions (3.84 Å).[160] It should be anticipated that these short distances have considerable effects on the properties of the molecules as lanthanide-lanthanide interactions occur. Although they were found to be small in other cases, the dimeric and binuclear molecules in this subchapter have shorter Dy-Dy distances and the influence of their special bridging ligands is not well studied to date.[161]

Table 4.7: Bond lengths and angles for {$Dy_2L_2(O)_2(NO_3)_2$} **(8a)**, {$Dy_2L_2(O)_2(NO_3)_2$} **(8b)**, {$Dy_2L_2(F)_2(NO_3)_2$} **(9)** and {$Dy_2L_2(O)_2(DMF)_2$} **(10)**.
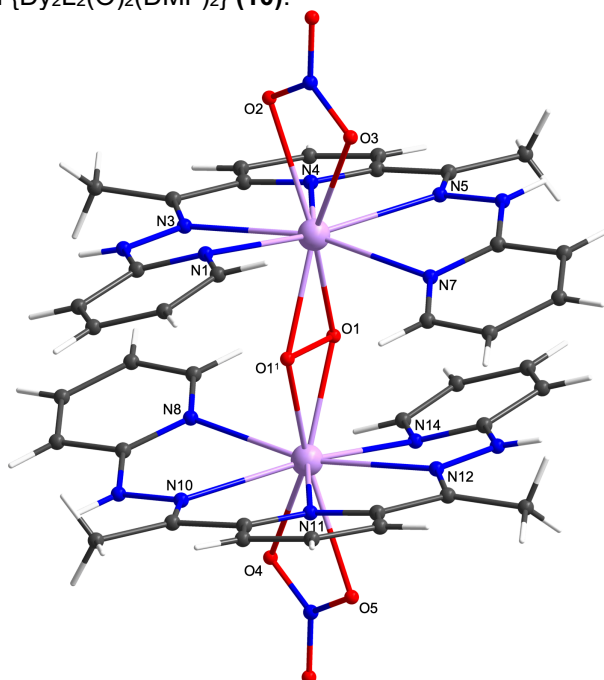
**(8a)**

| Atom | Atom | Length/Å |
|------|------|----------|
| Dy1 | O1[1] | 2.2082(19) |
| Dy1 | O1 | 2.2206(19) |
| Dy1 | O2 | 2.511(2) |
| Dy1 | O3 | 2.468(2) |
| Dy1 | N1 | 2.484(2) |
| Dy1 | N3 | 2.474(2) |
| Dy1 | N4 | 2.470(2) |
| Dy1 | N5 | 2.482(2) |
| Dy1 | N7 | 2.529(2) |
| O1 | O1[1] | 1.543(3) |
| Dy1 | Dy1[1] | 4.1513(5) |

**(8b)**

| Atom | Atom | Length/Å |
|------|------|----------|
| Dy1 | O1 | 2.342(16) |
| Dy1 | O2 | 2.312(18) |
| Dy1 | O3 | 2.504(19) |
| Dy1 | O4 | 2.474(17) |
| Dy1 | N1 | 2.49(2) |
| Dy1 | N3 | 2.47(2) |
| Dy1 | N4 | 2.50(2) |
| Dy1 | N5 | 2.48(2) |
| Dy1 | N7 | 2.54(2) |
| Dy2 | O1 | 2.109(17) |
| Dy2 | O2 | 2.13(2) |
| Dy2 | O6 | 2.41(2) |
| Dy2 | O7 | 2.512(18) |
| Dy2 | N8 | 2.48(2) |
| Dy2 | N10 | 2.52(2) |
| Dy2 | N11 | 2.47(2) |
| Dy2 | N12 | 2.49(2) |
| Dy2 | N14 | 2.52(3) |
| O1 | O2 | 1.61(2) |
| Dy1 | Dy2 | 4.1451(24) |

| Atom | Atom | Atom | Angle/° |
|------|------|------|---------|
| O1[1] | Dy1 | O2 | 149.78(7) |
| O1 | Dy1 | O2 | 147.95(7) |
| O1[1] | Dy1 | O3 | 137.78(7) |
| O1 | Dy1 | O3 | 154.81(7) |
| N1 | Dy1 | N3 | 64.97(7) |
| N3 | Dy1 | N4 | 65.01(7) |
| N4 | Dy1 | N5 | 64.42(7) |
| N5 | Dy1 | N7 | 64.44(7) |
| N1 | Dy1 | N7 | 103.71(7) |

| Atom | Atom | Atom | Angle/° |
|------|------|------|---------|
| O1 | Dy1 | O3 | 149.8(7) |
| O1 | Dy1 | O4 | 134.7(6) |
| O2 | Dy1 | O3 | 153.8(7) |
| O2 | Dy1 | O4 | 150.5(7) |
| N1 | Dy1 | N3 | 64.9(8) |
| N3 | Dy1 | N4 | 64.3(8) |
| N4 | Dy1 | N5 | 64.4(7) |
| N5 | Dy1 | N7 | 64.4(8) |
| N1 | Dy1 | N7 | 103.8(8) |
| O1 | Dy2 | O6 | 150.8(7) |
| O1 | Dy2 | O7 | 151.1(6) |
| O2 | Dy2 | O6 | 134.8(7) |
| O2 | Dy2 | O7 | 146.9(7) |
| N8 | Dy2 | N10 | 63.9(8) |
| N10 | Dy2 | N11 | 63.9(7) |
| N11 | Dy2 | N12 | 64.5(8) |
| N12 | Dy2 | N14 | 64.1(8) |
| N8 | Dy2 | N14 | 105.7(8) |

**(9)**
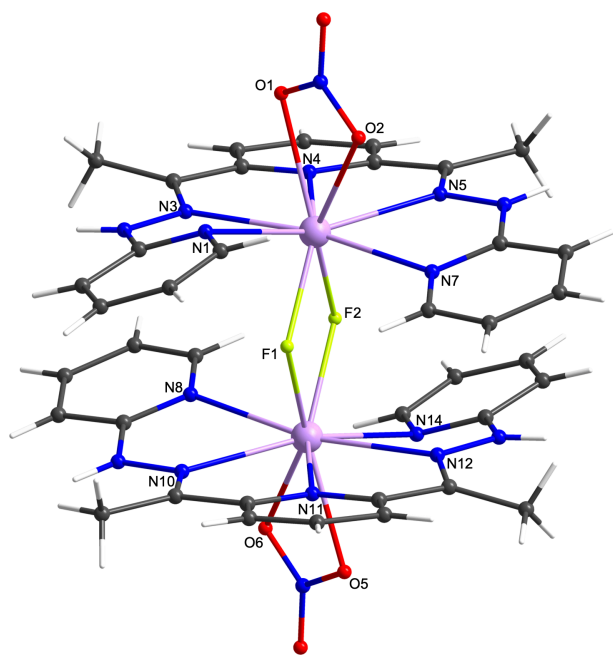
| Atom | Atom | Length/Å |
|------|------|----------|
| Dy1 | F1 | 2.204(6) |
| Dy1 | F2 | 2.187(6) |
| Dy1 | O1 | 2.521(8) |
| Dy1 | O2 | 2.483(8) |
| Dy1 | N1 | 2.539(12) |
| Dy1 | N3 | 2.483(11) |
| Dy1 | N4 | 2.492(10) |
| Dy1 | N5 | 2.505(11) |
| Dy1 | N7 | 2.517(12) |
| Dy2 | F1 | 2.254(6) |
| Dy2 | F2 | 2.260(6) |
| Dy2 | O4 | 2.415(8) |
| Dy2 | O5 | 2.472(8) |
| Dy2 | N8 | 2.511(12) |
| Dy2 | N10 | 2.499(12) |
| Dy2 | N11 | 2.479(10) |
| Dy2 | N12 | 2.511(12) |
| Dy2 | N14 | 2.525(12) |
| F1 | F2 | 2.4647(87) |
| Dy1 | Dy2 | 3.7085(10) |

| Atom | Atom | Atom | Angle/° |
|------|------|------|---------|
| F2 | Dy2 | O4 | 117.8(2) |
| F2 | Dy2 | O5 | 143.6(3) |
| N1 | Dy1 | N3 | 63.2(4) |
| N3 | Dy1 | N4 | 64.1(4) |
| N4 | Dy1 | N5 | 64.1(4) |
| N5 | Dy1 | N7 | 63.7(4) |
| N1 | Dy1 | N7 | 107.0(4) |
| N8 | Dy2 | N10 | 63.6(4) |
| N10 | Dy2 | N11 | 64.2(4) |
| N11 | Dy2 | N12 | 63.9(4) |
| N12 | Dy2 | N14 | 63.7(4) |
| N8 | Dy2 | N14 | 107.3(4) |
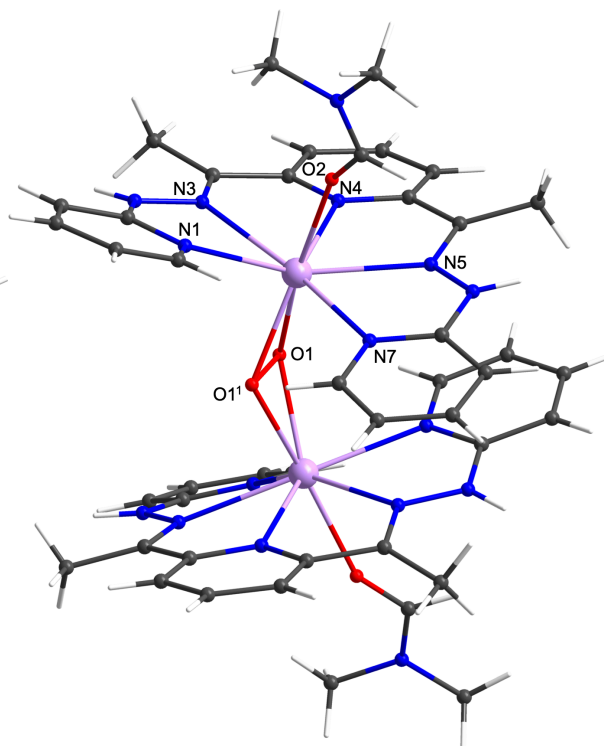
**(10)**

| Atom | Atom | Length/Å |
|------|------|----------|
| Dy1 | O1 | 2.256(2) |
| Dy1 | O1[1] | 2.242(2) |
| Dy1 | O2 | 2.274(2) |
| Dy1 | N1 | 2.508(3) |
| Dy1 | N3 | 2.486(3) |
| Dy1 | N4 | 2.457(3) |
| Dy1 | N5 | 2.500(3) |
| Dy1 | N7 | 2.482(3) |
| O1 | O1[1] | 1.557(5) |
| Dy1 | Dy1[1] | 3.9985(3) |

| Atom | Atom | Atom | Angle/° |
|------|------|------|---------|
| O1 | Dy1 | O2 | 167.29(9) |
| O1[1] | Dy1 | O2 | 151.37(10) |
| N1 | Dy1 | N3 | 64.22(9) |
| N3 | Dy1 | N4 | 64.01(9) |
| N4 | Dy1 | N5 | 64.42(9) |
| N5 | Dy1 | N7 | 64.66(9) |
| N1 | Dy1 | N7 | 101.06(9) |

The peroxide bond in $\{Dy_2L_2(O)_2(NO_3)_2\}$ **(8a)** has a length of 1.54 Å which is 0.09 Å longer than in hydrogen peroxide (1.45 Å) and 0.07 Å longer than the approximately 1.47 Å in the alkaline and alkaline earth metal peroxides.[162-164] Compared to the four dysprosium compounds with peroxide ligands, it is in good agreement but 0.02 Å longer than the average value showing the longest peroxide bond length reported for such a compound. The average value for all 38 reported structures of lanthanide compounds with peroxide ligands is 1.50 Å. As in the compounds of section 4.1.1, the nitrates are unsymmetrically bidentate bound to the lanthanide ions as it is the case in the monomers described in subchapter 4.1.2 and as it is reported to be a standard coordination mode for lanthanide complexes.[105] The shorter Dy-O bond is again above the yellow arc of Figure 4.7. For the oxygen-oxygen bonds in $\{Dy_2L_2(O)_2(NO_3)_2\}$ **(8b)** and $\{Dy_2L_2(O)_2(DMF)_2\}$ **(10)**, even bigger values were found. They are 1.56 Å for $\{Dy_2L_2(O)_2(DMF)_2\}$ **(10)** and 1.61 Å for $\{Dy_2L_2(O)_2(NO_3)_2\}$ **(8b)**. In the dimeric and binuclear molecules $\{Dy_2L_2(O)_2(NO_3)_2\}$ **(8a)**, $\{Dy_2L_2(O)_2(NO_3)_2\}$ **(8b)** and $\{Dy_2L_2(F)_2(NO_3)_2\}$ **(9)** due to the inversion centre in the middle of the bridging bond, the coordination axes of the nitrates are coparallel. The coordination axis of a nitrate can be defined as the line between dysprosium and the nitrate's centre of charge which is the nitrogen. The average Dy-O bond length with the oxygens of the nitrates is 2.49 Å in $\{Dy_2L_2(O)_2(NO_3)_2\}$ **(8a)**, 2.48 Å in $\{Dy_2L_2(O)_2(NO_3)_2\}$ **(8b)** and 2.47 Å in $\{Dy_2L_2(F)_2(NO_3)_2\}$ **(9)** and therefore significantly longer than in the monomeric complexes $\{DyL(NO_3)_2\}$ **(2)** and $\{DyL(NO_3)_2\}$ **(3)**. In contrast to this, the Dy-O bond with the DMF oxygen in $\{Dy_2L_2(O)_2(DMF)_2\}$ **(10)** is much shorter. It shows a value of only 2.26 Å which is about the same size as the Dy-O bonds with the peroxide ions in $\{Dy_2L_2(O)_2(NO_3)_2\}$ **(8a)**, $\{Dy_2L_2(O)_2(NO_3)_2\}$ **(8b)** and $\{Dy_2L_2(O)_2(DMF)_2\}$ **(10)**. The average dysprosium-peroxide bond length in $\{Dy_2L_2(O)_2(NO_3)_2\}$ **(8a)** is 2.21 Å. In $\{Dy_2L_2(O)_2(NO_3)_2\}$ **(8b),** it is 2.22 Å and in $\{Dy_2L_2(O)_2(DMF)_2\}$ **(10)**, it is 2.26 Å. The average Dy-O bond length in the complexes reported in literature is longer and shows a value of 2.33 Å. For the Dy-F bonds in $\{Dy_2L_2(F)_2(NO_3)_2\}$ **(9)**, values of similar size can be found. In average, the Dy-F bonds show a length of 2.23 Å. The much shorter Dy-Dy distance in $\{Dy_2L_2(F)_2(NO_3)_2\}$ **(9)** compared to the other binuclear and dimeric compounds results from the fact that the F-F distance is much longer than the peroxide bond. Furthermore, the more acute angle for Dy-F-Dy compared to the Dy-O-Dy in the rhombic shaped bridging connection leads to a contraction of the dysprosium-dysprosium distance as highlighted in Figure 4.32.

**(8a)**

**(8b)**

**(9)**

**(10)**
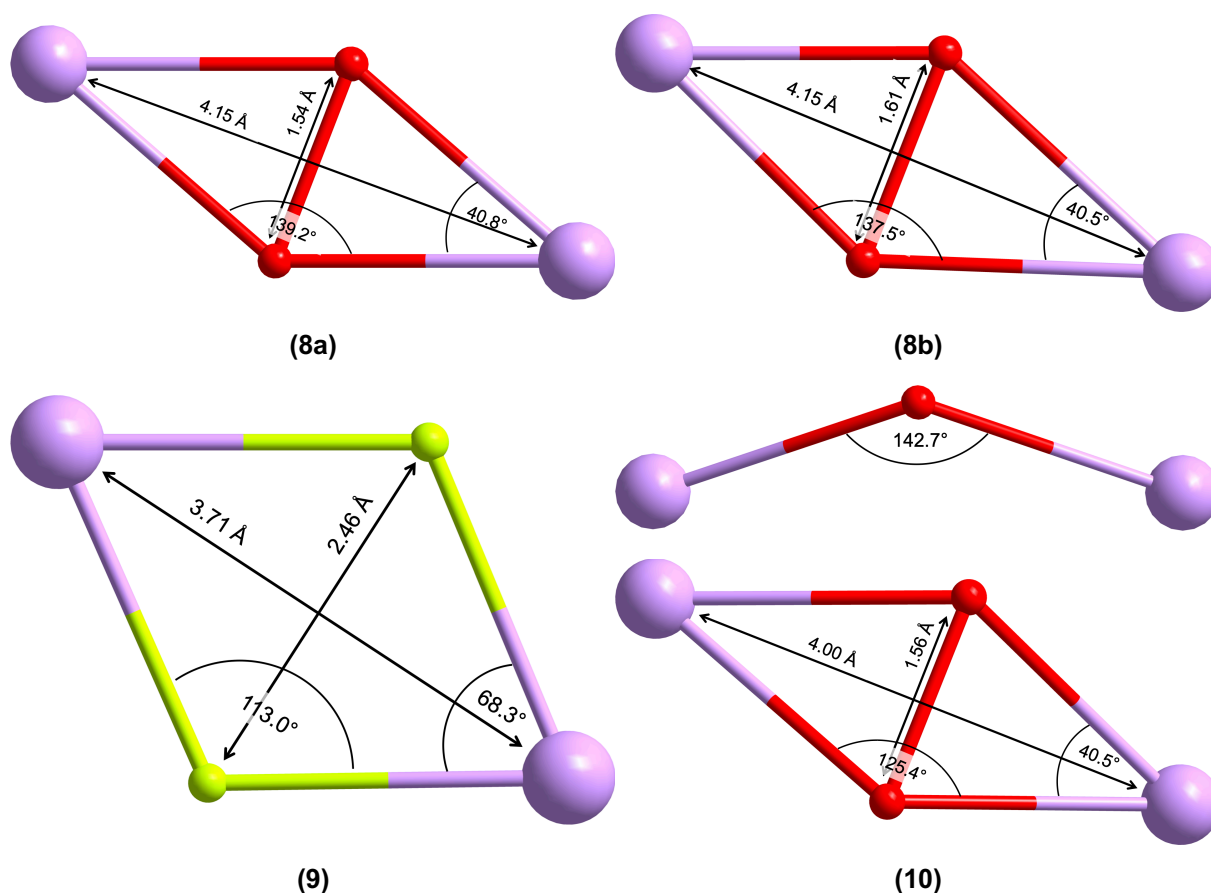
Figure 4.32: Angles and lengths in the bridging structure motif in the binuclear and dimeric compounds $\{Dy_2L_2(O)_2(NO_3)_2\}$ **(8a)**, $\{Dy_2L_2(O)_2(NO_3)_2\}$ **(8b)**, $\{Dy_2L_2(F)_2(NO_3)_2\}$ **(9)** and $\{Dy_2L_2(O)_2(DMF)_2\}$ **(10)**.

The N-Dy-N angles are of similar size as in the complexes presented above. The average angle of the angles between dysprosium and two next neighbouring nitrogens of the complex is 64.7° for $\{Dy_2L_2(O)_2(NO_3)_2\}$ **(8a)**, 64.5° and 64.1° for the top respectively bottom half of $\{Dy_2L_2(O)_2(NO_3)_2\}$ **(8b)**, 63.8° respectively 63.9° for the top and bottom half of $\{Dy_2L_2(F)_2(NO_3)_2\}$ **(9)** and 64.3° for $\{Dy_2L_2(O)_2(DMF)_2\}$ **(10)**, which are medium values compared to the average angles in **(1)**-**(7)**. Also here, a correlation with the helicity could not be found due to the reasons mentioned above. From the relative angles between the capping ligand, the dysprosium and the bridging ligand, one can see that the relative coordination is unsymmetrical as it is the case for the two capping ligands in **(2)**-**(4)**. As it can be seen in Figure 4.32, the angle between the bent off dysprosium centres in $\{Dy_2L_2(O)_2(DMF)_2\}$ **(10)** is 142.7°. This bent off structure feature looks counter intuitive on the first impression but a closer look reveals the dense packing in the crystal structure which is discussed below. The monodentate DMF capping ligand does not occupy as much space as the nitrate capping ligands for example do. This open coordination space on the lanthanide, however, is energetically unfavourable but lack of suitable co ligands means that as in $\{DyL(H_2O)_4\}$ **(1)**, which

only has one water ligand on one side relative to the $H_2$dapp ligand, the pentadentate ligand folds in order to get a better distribution of the ligands. Whilst helical distortion is very helpful in avoiding the short hydrogen-hydrogen distance discussed above, it is not very useful to reduce the ligand sphere selectively above or below the $H_2$dapp. This folding distortion, on the other hand, can serve that very well as can be seen in a space filling model (Figure 4.33 (a)). Nevertheless, the folded ligands do not pack very well when they are inverted which the helically distorted ligands do. To allow a dense and energetically sensible packing, the molecule needs to bend and open enough space for the pyridine ring of a neighbouring molecule. This can be seen in Figure 4.33 (b).



**(a)**                                               **(b)**
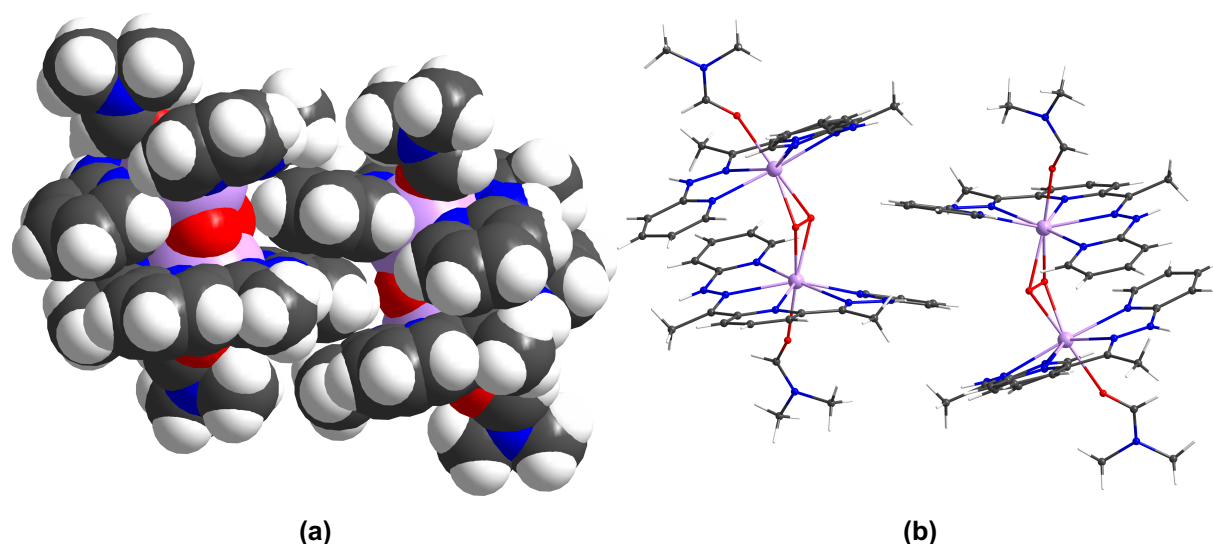
Figure 4.33: **(a)** Space filling model of $\{Dy_2L_2(O)_2(DMF)_2\}$ **(10)** showing the mesh of two dimeric molecules. **(b)** Same scene in the balls and sticks scheme.

The molecular symmetry also influences the space group of the systems. Compound $\{Dy_2L_2(O)_2(DMF)_2\}$ **(10)** crystallises in C2/c where the rotational symmetry reflects in the rotation axis of the space group. For compound $\{Dy_2L_2(O)_2(NO_3)_2\}$ **(8)**, two different space groups can be found, the triclinic $P\bar{1}$ $\{Dy_2L_2(O)_2(NO_3)_2\}$ **(8a)** and the monoclinic $P2_1$ $\{Dy_2L_2(O)_2(NO_3)_2\}$ **(8b)**. From the reaction mixture, $\{Dy_2L_2(O)_2(NO_3)_2\}$ **(8)** crystallises in the triclinic space group with methanol in the crystal lattice. The monoclinic space group will be obtained if the crystals are left at air for some time. Nevertheless, this also leads to the loss of methanol and exchange by water in air which impacts the quality of the crystals negatively. Therefore, the X-ray dataset obtained for $\{Dy_2L_2(O)_2(NO_3)_2\}$ **(8b)** is worse than for $\{Dy_2L_2(O)_2(NO_3)_2\}$ **(8a)**. Owing to this exchange of solvent molecules, the unit cell transforms crystallographically with

$\begin{pmatrix} -1 & 0 & 0 \\ -\frac{1}{2} & -\frac{1}{2} & -1 \\ 0 & -1 & 0 \end{pmatrix}$. This is shown in Figure 4.34. The fluoride binuclear compound {Dy$_2$L$_2$(F)$_2$(NO$_3$)$_2$} **(9)** is isostructural to {Dy$_2$L$_2$(O)$_2$(NO$_3$)$_2$} **(8b)** according to the matrix having the same space group P2$_1$ with the same packing. This and the packing of all crystal structures can be seen in Figure 4.35. The asymmetric units of the structures contain [Dy(H$_2$dapp)(NO$_3$)(O)](NO$_3$)·MeOH in compound {Dy$_2$L$_2$(O)$_2$(NO$_3$)$_2$} **(8a)**, [Dy$_2$(H$_2$dapp)$_2$(NO$_3$)$_2$(O)$_2$](NO$_3$)$_2$·4H$_2$O in compound {Dy$_2$L$_2$(O)$_2$(NO$_3$)$_2$} **(8b)**, [Dy$_2$(H$_2$dapp)$_2$(NO$_3$)$_2$(F)$_2$](NO$_3$)$_2$·4H$_2$O in compound {Dy$_2$L$_2$(F)$_2$(NO$_3$)$_2$} **(9)** and [Dy(H$_2$dapp)(DMF)(O)](ClO$_4$)$_2$·2H$_2$O in compound {Dy$_2$L$_2$(O)$_2$(DMF)$_2$} **(10)**. In the pictures of the crystal packing (Figure 4.35), it can be seen that the hydrogen bonding is not as pronounced as in the crystal structures presented in the previous chapter.



**(8a)**          **(8b)**
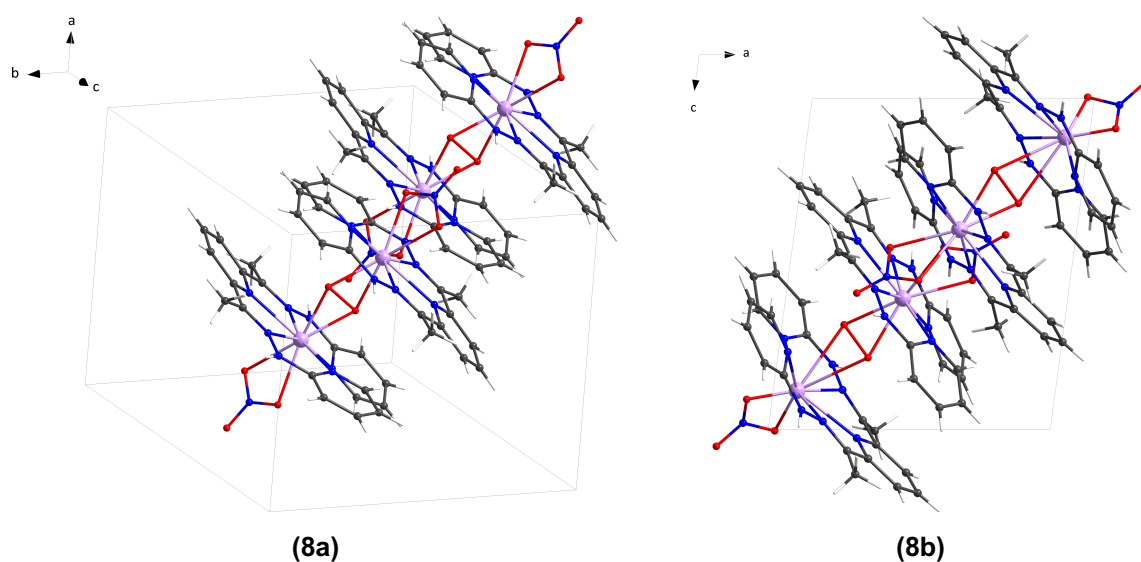
Figure 4.34: Packing diagrams for {Dy$_2$L$_2$(O)$_2$(NO$_3$)$_2$} **(8a)** and {Dy$_2$L$_2$(O)$_2$(NO$_3$)$_2$} **(8b)** with viewing directions chosen to show the crystallographic relation of the crystal structures.



b          c

**(8a)**

b                                                    c

**(8b)**



a                                                    c

**(9)**

b c

**(10)**
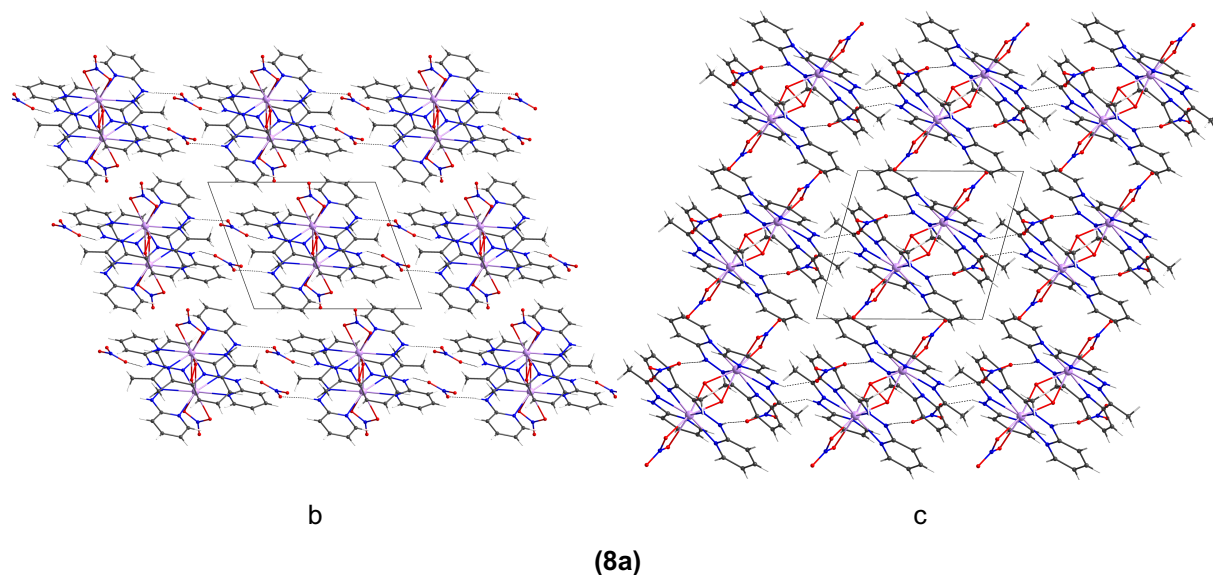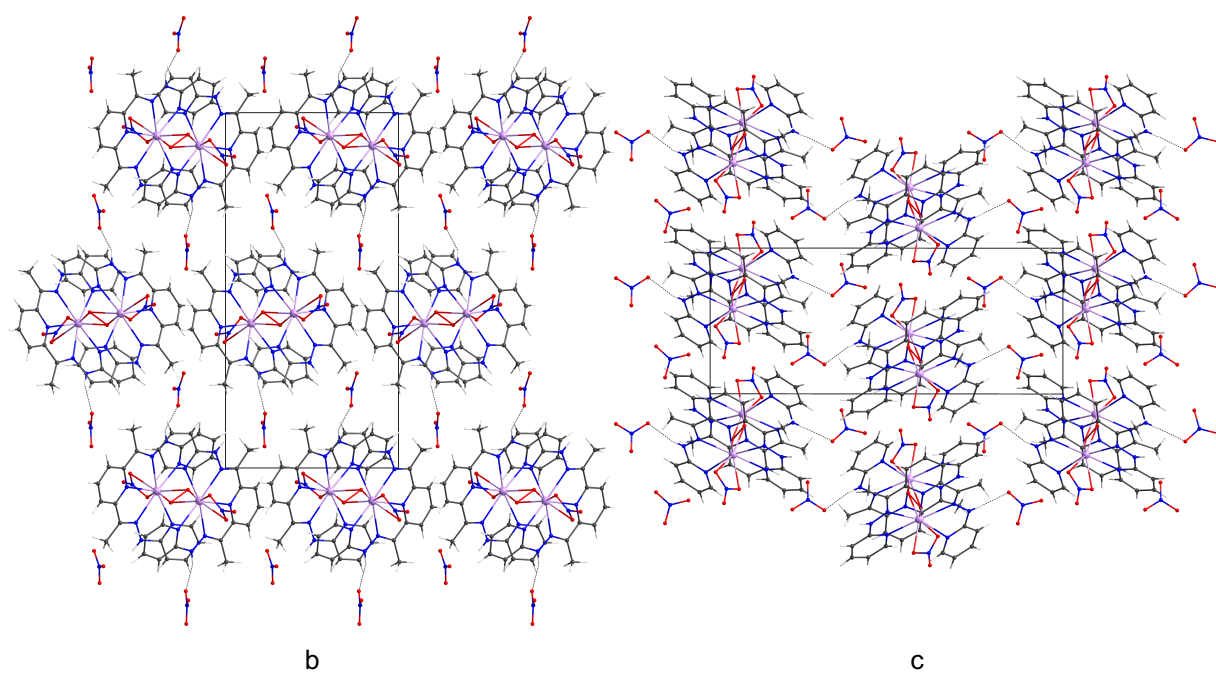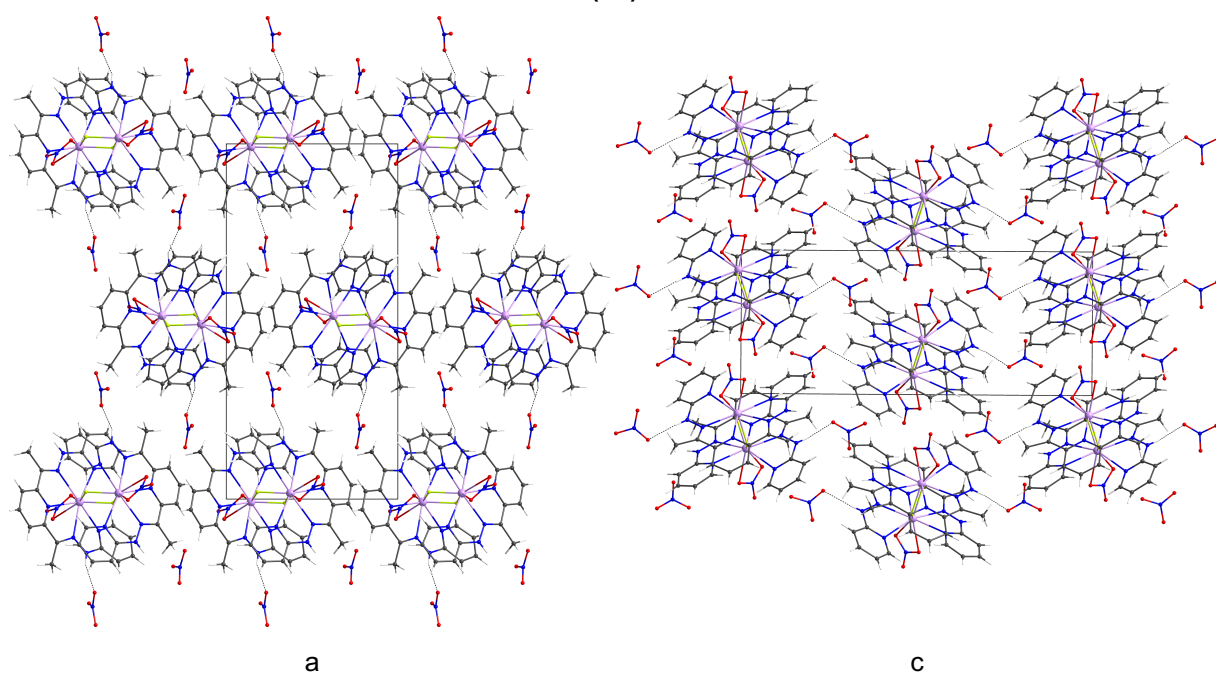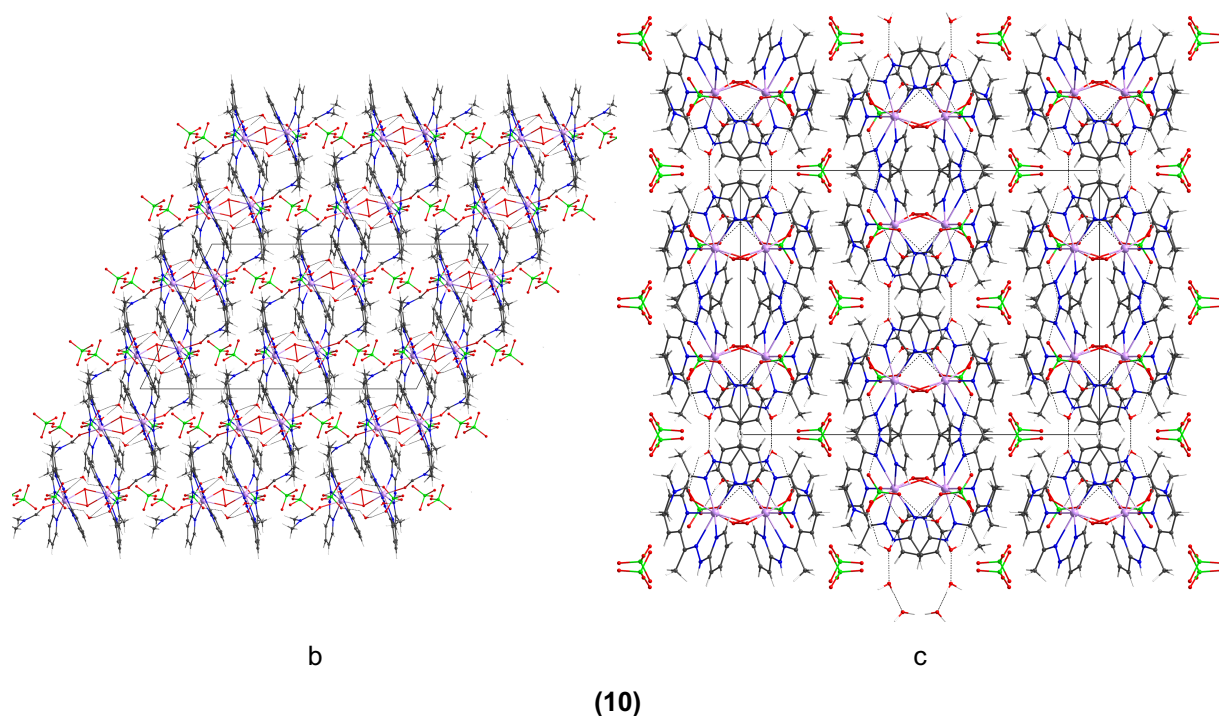
Figure 4.35: Crystal packing of $\{Dy_2L_2(O)_2(NO_3)_2\}$ **(8a)**, $\{Dy_2L_2(O)_2(NO_3)_2\}$ **(8b)**, $\{Dy_2L_2(F)_2(NO_3)_2\}$ **(9)** and $\{Dy_2L_2(O)_2(DMF)_2\}$ **(10)** with viewing direction underneath.

Also for these molecules, a structure analysis by CShM with SHAPE 2.1 was conducted.[107] Although the results of the program can be misleading for chemical interpretation, here due to the fact that the bond lengths are of comparable magnitude comparisons between the found idealised coordination geometries can prove helpful. As for the coordination spheres in section 4.1.2, there are bonds that differ from the average which are the shorter dysprosium-peroxide bonds and the dysprosium-fluoride bonds but not so much that they significantly influence the outcome. This can be seen in the comparison of the coordination polyhedra of the real complexes (coloured in lilac) and the optimised polyhedra with the lowest deviation values (coloured in indigo to the right of each real complex) in Figure 4.36.

All coordination polyhedral are low in symmetry as it is usually the case for lanthanide complexes and as it was measured for the complexes in sections 4.1.1 and 4.1.2. For $\{Dy_2L_2(O)_2(NO_3)_2\}$ **(8b)** and $\{Dy_2L_2(F)_2(NO_3)_2\}$ **(9)**, the top half (th) and the bottom half (bh) have to be regarded separately.

The average deviation values of $\{Dy_2L_2(F)_2(NO_3)_2\}$ **(9th)** and $\{Dy_2L_2(F)_2(NO_3)_2\}$ **(9bh)** are similar compared to the ones of $\{DyL(Cl)_2(H_2O)\}$ **(5)**, $\{DyL(Cl)(H_2O)(NO_3)\}$ **(6)** and $\{DyL(Cl)_2(NO_3)\}$ **(7)**. The ones of $\{Dy_2L_2(O)_2(NO_3)_2\}$ **(8a)**, $\{Dy_2L_2(O)_2(NO_3)_2\}$ **(8bth)** and $\{Dy_2L_2(O)_2(NO_3)_2\}$ **(8bbh)** are a bit higher. For $\{Dy_2L_2(O)_2(DMF)_2\}$ **(10)**, much higher minimal deviation values bigger than 6 % were found. All nitrate capped peroxide

structures ($\{Dy_2L_2(O)_2(NO_3)_2\}$ **(8a)**, $\{Dy_2L_2(O)_2(NO_3)_2\}$ **(8bth)** and $\{Dy_2L_2(O)_2(NO_3)_2\}$ **(8bbh)**) show coordination spheres with the best agreement with the spherical tricapped trigonal prism (TCTPR) with $D_{3h}$ symmetry. The deviation values are 4.13 % for $\{Dy_2L_2(O)_2(NO_3)_2\}$ **(8a)**, 4.27 % for $\{Dy_2L_2(O)_2(NO_3)_2\}$ **(8bth)** and 3.94 % for $\{Dy_2L_2(O)_2(NO_3)_2\}$ **(8bbh)**. In compound $\{Dy_2L_2(F)_2(NO_3)_2\}$ **(9)**, the ideal structures with the muffin type (MFF) with $C_s$ symmetry have the lowest deviation value and the best agreement with the actual coordination sphere of the compounds. The deviation of $\{Dy_2L_2(F)_2(NO_3)_2\}$ **(9th)** from this ideal structure is 3.34 % and the deviation of $\{Dy_2L_2(F)_2(NO_3)_2\}$ **(9bh)** from the MFF is 3.24 %. The muffin type is the second best for the structures of $\{Dy_2L_2(O)_2(NO_3)_2\}$ **(8)**. They show values of 4.55 % in $\{Dy_2L_2(O)_2(NO_3)_2\}$ **(8a)**, 4.98 % in $\{Dy_2L_2(O)_2(NO_3)_2\}$ **(8bth)** and 4.69 % in $\{Dy_2L_2(O)_2(NO_3)_2\}$ **(8bbh)**. Since only the first two positions are swapped in $\{Dy_2L_2(F)_2(NO_3)_2\}$ **(9)** compared to $\{Dy_2L_2(O)_2(NO_3)_2\}$ **(8)**, TCTPR is the second-best fitting for $\{Dy_2L_2(F)_2(NO_3)_2\}$ **(9th)** and $\{Dy_2L_2(F)_2(NO_3)_2\}$ **(9bh)**. The deviation values are very similar to those of MFF. They are 3.34 % and 3.29 % for $\{Dy_2L_2(F)_2(NO_3)_2\}$ **(9th)** and $\{Dy_2L_2(F)_2(NO_3)_2\}$ **(9bh)**, respectively. The third best fitting structure type for all five coordination polyhedra of $\{Dy_2L_2(O)_2(NO_3)_2\}$ **(8)** and $\{Dy_2L_2(F)_2(NO_3)_2\}$ **(9)** is the spherical capped square antiprism (CSAPR) with $C_{4v}$ symmetry. Their deviation values are 4.81 % for $\{Dy_2L_2(O)_2(NO_3)_2\}$ **(8a)**, 5.12 % for $\{Dy_2L_2(O)_2(NO_3)_2\}$ **(8bth)**, 4.74 % for $\{Dy_2L_2(O)_2(NO_3)_2\}$ **(8bbh)**, 3.49 % for $\{Dy_2L_2(F)_2(NO_3)_2\}$ **(9th)** and 3.51% for $\{Dy_2L_2(F)_2(NO_3)_2\}$ **(9bh)**. Compound $\{Dy_2L_2(O)_2(DMF)_2\}$ **(10)** has a coordination sphere on its dysprosium ions of only 7 ligating atoms as in $\{DyL(Cl)_2(H_2O)\}$ **(5)**. Therefore, the optimised structures are different for this compound. The best suitable ideal structure is the triangular dodecahedron (TDD) with $D_{2d}$ symmetry as it is the case in $\{DyL(Cl)_2(H_2O)\}$ **(5)**. The deviation value, however, is much higher with 6.19 %. The second and the third best fitting structure type are the square antiprism (SAPR) with $D_{4d}$ symmetry showing a deviation value of 6.68 % and the biaugmented trigonal prism (BTPR) with $C_{2v}$ symmetry showing a value of 6.72 %. The order of the second and the third best fitting structure type are the other way around in $\{DyL(Cl)_2(H_2O)\}$ **(5)**. These values are the highest obtained for all investigated structures with $H_2$dapp ligand. Chemically interpreted, this means the coordination spheres in $\{Dy_2L_2(O)_2(DMF)_2\}$ **(10)** cannot be related to any symmetry and need to be considered as completely unsymmetrical.

**(8a)**  TCTPR  MFF  CSAPR
4.13 %  4.55 %  4.81 %

**(8bth)**  TCTPR  MFF  CSAPR
4.27 %  4.98 %  5.12 %

**(8bbh)**  TCTPR  MFF  CSAPR
3.94 %  4.69 %  4.74 %

**(9th)**  MFF  TCTPR  CSAPR
3.34 %  3.34 %  3.49 %
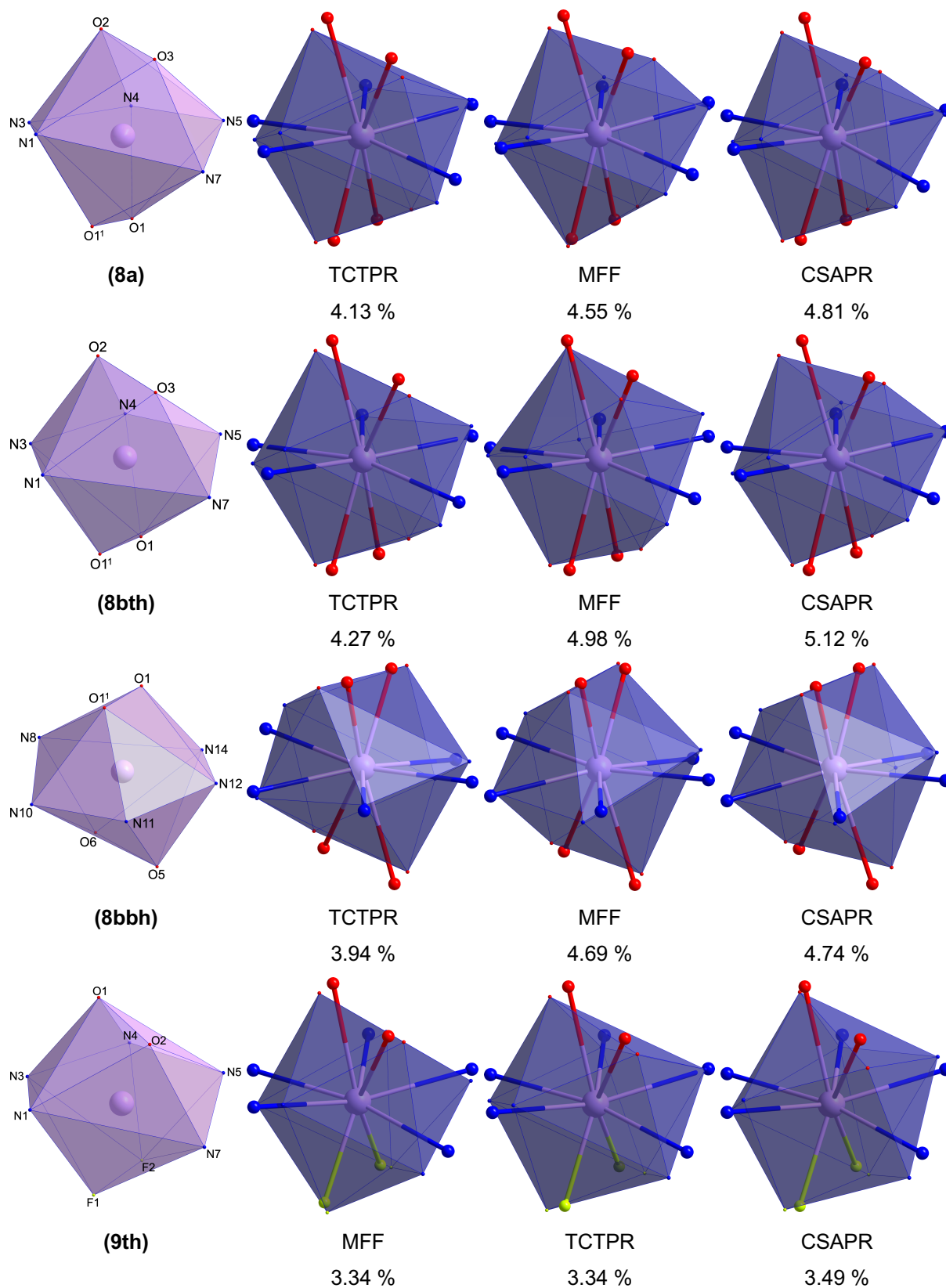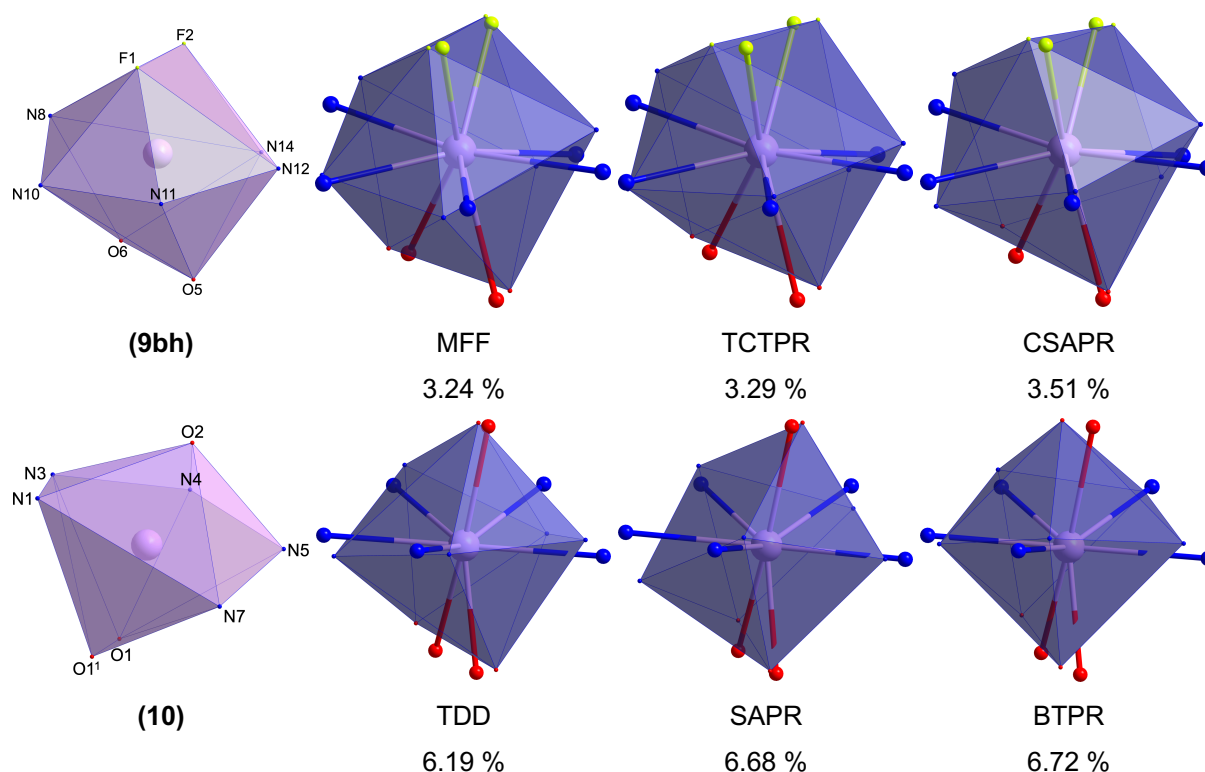
Figure 4.36: Lilac: coordination polyhedra of the complexes {Dy$_2$L$_2$(O)$_2$(NO$_3$)$_2$} **(8a)**, {Dy$_2$L$_2$(O)$_2$(NO$_3$)$_2$} **(8bth)**, {Dy$_2$L$_2$(O)$_2$(NO$_3$)$_2$} **(8bbh)**, {Dy$_2$L$_2$(F)$_2$(NO$_3$)$_2$} **(9th)**, {Dy$_2$L$_2$(F)$_2$(NO$_3$)$_2$} **(9bh)** and {Dy$_2$L$_2$(O)$_2$(DMF)$_2$} **(10)**. Blue: coordination polyhedra of the best fitting ideal structures, muffin structure type (MFF), spherical capped trigonal prism (TCTPR), spherical capped square antiprism (CSAPR), triangular dodecahedron (TDD), square antiprism (SAPR), biaugmented trigonal prism (BTPR) and the positions of the atoms in the original structure. Deviation values below ideal structures. The deviation values and the optimal polyhedra are obtained with SHAPE 2.1.[107]

For the same reasons discussed above, the compounds in this section were investigated with aid of the MAGELLAN software in order to obtain estimations for the anisotropy axes and the strengths of anisotropy in form of minimal reversal energy values.[40] The calculated anisotropy axes by the electrostatic model and the size of the minimal reversal energy are depicted in Figure 4.37.

As expected and seen in the other molecules above, the H$_2$dapp ligands form the hard plane and the easy axis goes through the capping ligand and the peroxide bond or the middle of the distance between the two fluorides in {Dy$_2$L$_2$(F)$_2$(NO$_3$)$_2$} **(9)**, respectively. This leads to a symmetry conditioned coparallel axis which is also almost collinear in {Dy$_2$L$_2$(O)$_2$(NO$_3$)$_2$} **(8a)** as it has a triclinic space group with an inversion centre in the peroxide bond and a non-coparallel axis in {Dy$_2$L$_2$(O)$_2$(DMF)$_2$} **(10)** as the rotation symmetry element of the monoclinic space group is between the dysprosium centres. For the dysprosium centres of {Dy$_2$L$_2$(O)$_2$(NO$_3$)$_2$} **(8b)** and {Dy$_2$L$_2$(F)$_2$(NO$_3$)$_2$} **(9)**, there is a very small deviation of the two vectors of the anisotropy axes in the top half and bottom half. Additionally, due to the monoclinic space group there is a symmetry

conditioned tilted second molecule in the unit cell causing more strongly deviating nonparallel anisotropy axes.
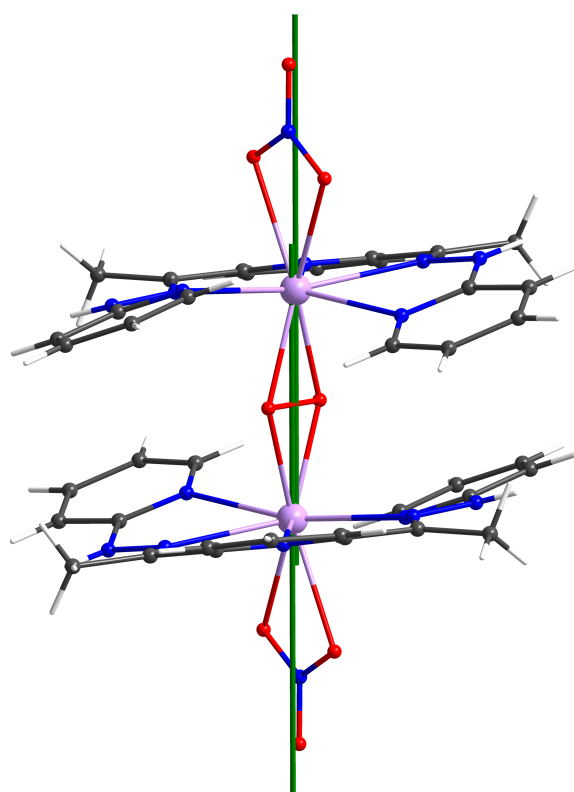


**(8a)**
1700 cm$^{-1}$                    **(8b)**
                                  1620 cm$^{-1}$

**(9)**

620 cm$^{-1}$

**(10)**
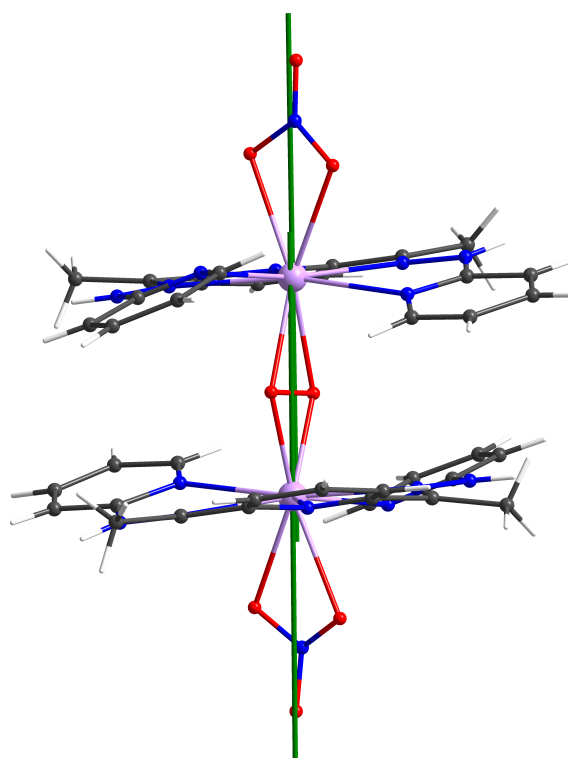
1140 cm$^{-1}$
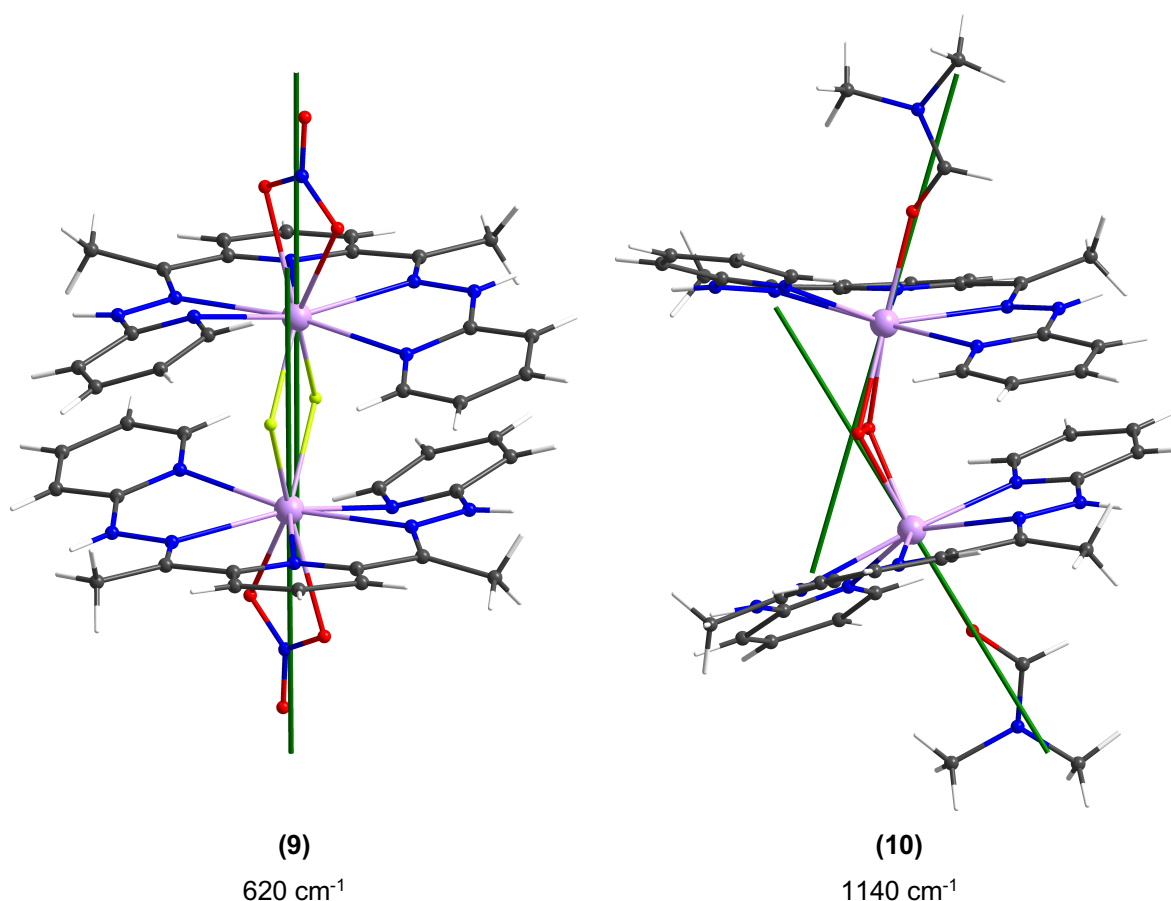
Figure 4.37: Molecules {$Dy_2L_2(O)_2(NO_3)_2$} **(8a)**, {$Dy_2L_2(O)_2(NO_3)_2$} **(8b)**, {$Dy_2L_2(F)_2(NO_3)_2$} **(9)** and {$Dy_2L_2(O)_2(DMF)_2$} **(10)** with anisotropy axis and minimal reversal energies obtained from MAGELLAN.[40]

Strong anisotropy was found in all binuclear and dimeric complexes. The minimal reversal energies found in the complexes are 1700 cm$^{-1}$ in {$Dy_2L_2(O)_2(NO_3)_2$} **(8a)**, as expected approximately the same in {$Dy_2L_2(O)_2(NO_3)_2$} **(8b)** showing a value of 1620 cm$^{-1}$, 620 cm$^{-1}$ in {$Dy_2L_2(F)_2(NO_3)_2$} **(9)** and 1140 cm$^{-1}$ in {$Dy_2L_2(O)_2(DMF)_2$} **(10)**. In view of the fact that the computation base is an electrostatic model, it can be anticipated that the value received for compound {$Dy_2L_2(O)_2(DMF)_2$} **(10)** is not accurate. For the calculation, DMF was regarded as neutral at the oxygen which is not representing the charge density very well because of the molecule's resonance structure. Indeed, it can be calculated with the "Extended Huckel" extension in Chem3D that the charge density on the coordinating oxygen is -0.8.[104] Taking the calculations of the electron density in the DMF molecule into account, a minimal reversal energy of 1820 cm$^{-1}$ can be found. This is the highest value for all the compounds investigated in this subchapter. Intriguingly, the difference in the calculated minimal reversal energy values is very high between the peroxide and the fluoride coupled binuclear molecules. The minimal reversal energy of the peroxide coupled

isostructural complexes is over 2.5 times higher than the fluoride coupled version. This is most probably due to the more acute O1-Dy-O1' angle in $\{Dy_2L_2(O)_2(NO_3)_2\}$ **(8)** compared to the F1-Dy-F1 angle in $\{Dy_2L_2(F)_2(NO_3)_2\}$ **(9)** as shown in Figure 4.32 and the therefore shorter distance between the two 3+ charged dysprosium cores. This results from the negatively charged fluoride ions being further from the Dy-Dy axis. The influence of this finding on the spatial alignment of the anisotropy axis of $\{Dy_2L_2(F)_2(NO_3)_2\}$ **(9)** does not seem to be large as can be seen in Figure 4.37. Between the anisotropy axes of the inversion symmetry related dysprosium centres, there is a deviation angle of 19.8° in $\{Dy_2L_2(O)_2(NO_3)_2\}$ **(8)** and 20.9° in $\{Dy_2L_2(F)_2(NO_3)_2\}$ **(9)**. The tilting of the molecule is shown in Figure 4.38. In $\{Dy_2L_2(O)_2(DMF)_2\}$ **(10)**, the angle between the anisotropy axis in the bent molecule is 47.9°.



**(8b)**                    **(9)**
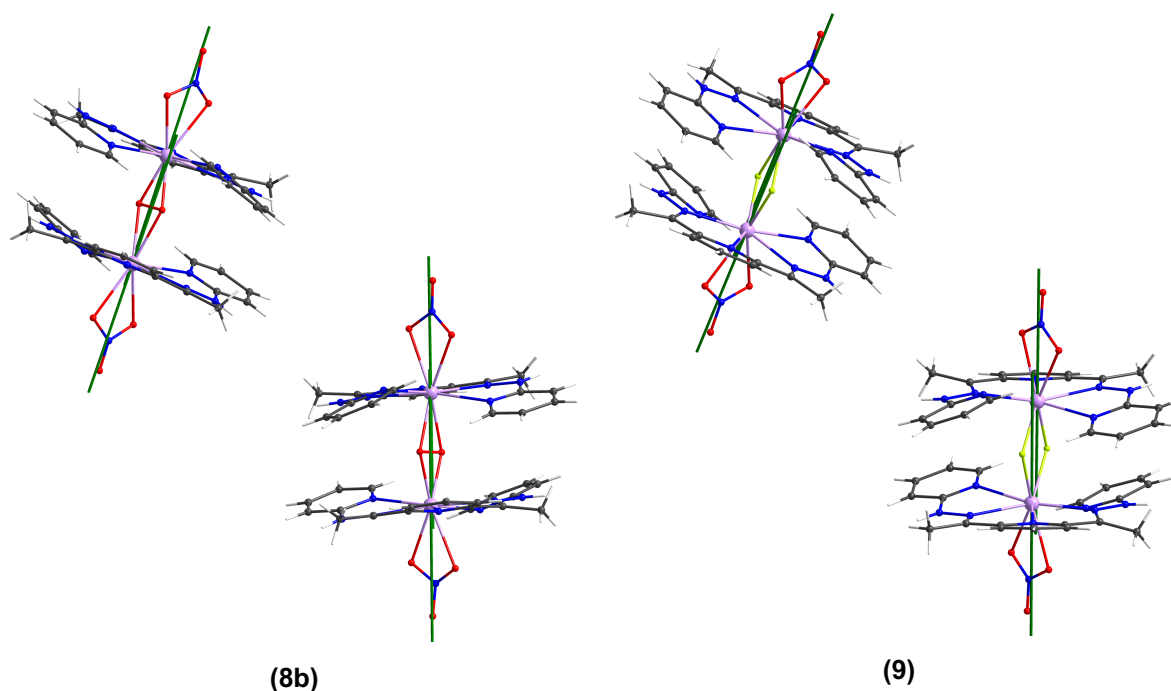
Figure 4.38: Spatial alignment of the anisotropy axes in $\{Dy_2L_2(O)_2(NO_3)_2\}$ **(8b)** and $\{Dy_2L_2(F)_2(NO_3)_2\}$ **(9)**.

These small but important structural differences between $\{Dy_2L_2(O)_2(NO_3)_2\}$ **(8)** and $\{Dy_2L_2(F)_2(NO_3)_2\}$ **(9)** also appear in the magnetic properties of the compounds. It needs to be considered that the magnetic measurements performed at Københavns Universitet (University of Copenhagen) conducted in the group of Prof. Jesper Bendix were on dry microcrystalline powder samples of $\{Dy_2L_2(O)_2(NO_3)_2\}$ **(8)** and $\{Dy_2L_2(F)_2(NO_3)_2\}$ **(9)** meaning that it was $\{Dy_2L_2(O)_2(NO_3)_2\}$ **(8b)** that was measured. Whilst for $\{Dy_2L_2(O)_2(NO_3)_2\}$ **(8b)** and $\{Dy_2L_2(F)_2(NO_3)_2\}$ **(9)** the high temperature

values of $\chi_M T$ are close to that expected for two free $Dy^{3+}$ ions with $^6H_{15/2}$ ground state and a g value of 4/3, the low temperature behaviour differs significantly. The $\chi_M T$ versus temperature plots are shown in Figure 4.39. The high temperature value is 27.60 $cm^3mol^{-1}K$ in {$Dy_2L_2(O)_2(NO_3)_2$} **(8b)** and 28.06 $cm^3mol^{-1}K$ in {$Dy_2L_2(F)_2(NO_3)_2$} **(9)**, which is lower than the expected value of 28.35 $cm^3mol^{-1}K$.
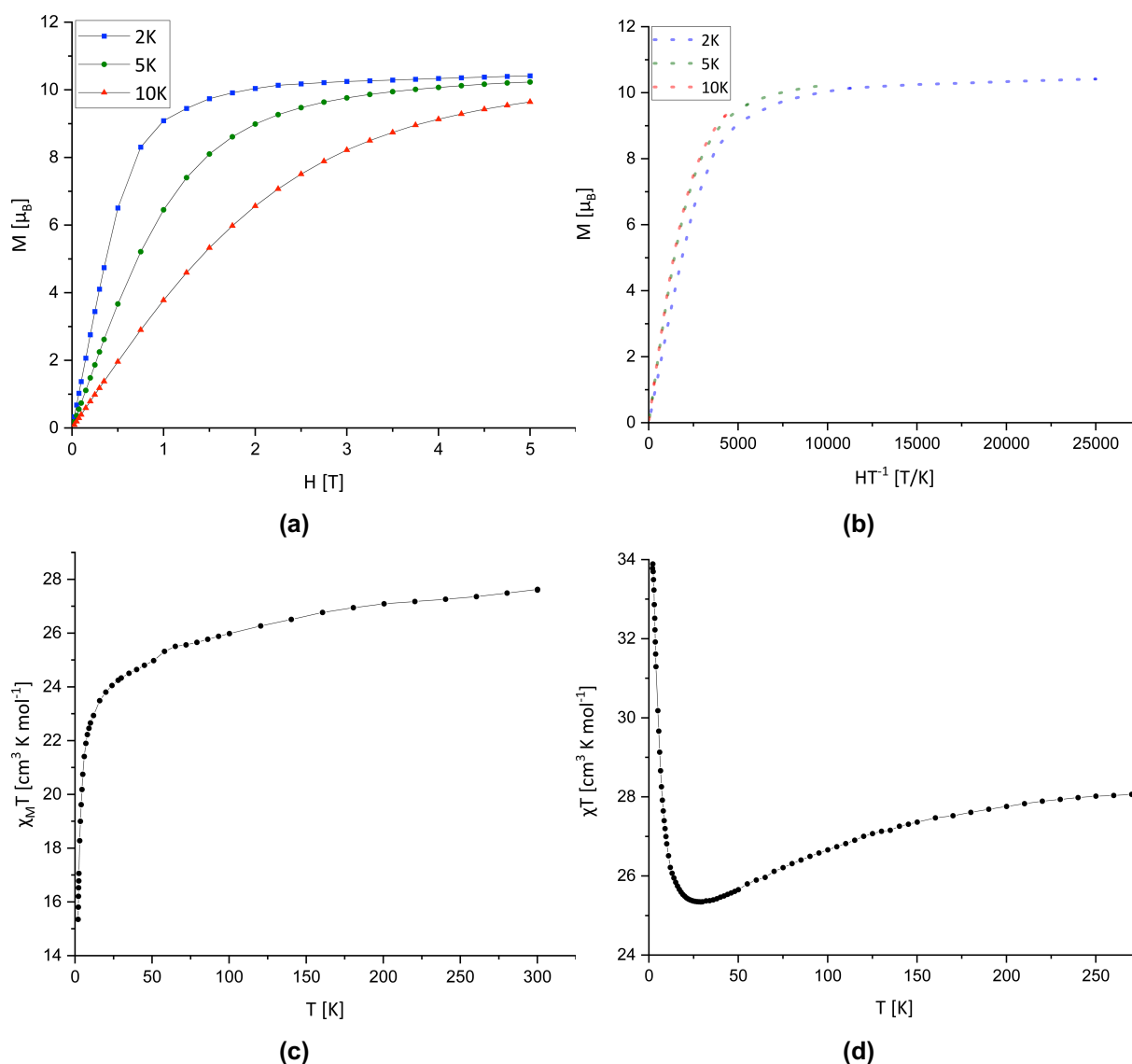


Figure 4.39: DC magnetic data of {$Dy_2L_2(O)_2(NO_3)_2$} **(8)**. **(a)** Magnetisation versus field. **(b)** Magnetisation versus field times inverse temperature. **(c)** $\chi_M T$ versus temperature plot. DC magnetic data of {$Dy_2L_2(F)_2(NO_3)_2$} **(9)**. **(d)** $\chi_M T$ versus temperature plot.

In the low temperature regime, compound {$Dy_2L_2(O)_2(NO_3)_2$} **(8b)** shows a decrease to 28 K and 24.25 $cm^3mol^{-1}K$ likely due to antiferromagnetic coupling and/or thermal depopulation of the $m_J$ levels. In the $\chi_M T$ versus temperature plot of {$Dy_2L_2(F)_2(NO_3)_2$} **(9)**, it can be seen that there is also a depopulation of $m_J$ levels and/or dipolar interactions causing a decrease towards lower temperatures. However at 29 K and

25.35 $cm^3mol^{-1}K$, a minimum is reached from which the $\chi_M T$ increases up to 33.89 $cm^3mol^{-1}K$ at 2.2 K. This indicates ferromagnetic coupling in the fluoride coupled compound. This is consistent with the findings for the two dysprosium structures with the same fluoride bridging motif that can be found in the literature.[123,144] The dramatic switch towards ferromagnetic coupling by replacing the peroxide bridging ligand by two fluoride bridging ligands is noteworthy.

For compound $\{Dy_2L_2(O)_2(NO_3)_2\}$ **(8b)**, direct current isothermal magnetisation versus field data was collected which shows the expected behaviour for two dysprosium ions. As can be seen in Figure 4.39, the saturation value at high fields, which is a little below 10 $\mu_B$ at 10 K and a little above 10 $\mu_B$ at 2 K and 5 K, is lower than the calculated value of 20 $\mu_B$ (J=15/2 and g=4/3) for two free dysprosium ions but typical for the experimental value in dysprosium complexes.[24,111-117] In the M versus H/T plot (Figure 4.39 (b)) it can be seen that the system shows anisotropy and/or low lying excited states because the curves do not overlay and split for 2 K and 5 K already at very low fields.

Whilst compound $\{Dy_2L_2(F)_2(NO_3)_2\}$ **(9)** does not show slow magnetic relaxation, neither without nor with applied DC field, compound $\{Dy_2L_2(O)_2(NO_3)_2\}$ **(8b)** shows SMM behaviour without applied field. In the plots in Figure 4.40, it can be seen that there can be maxima found in the out of phase susceptibility measurements up to 10 K and 1000 Hz with 0 Oe DC field and with 3000 Oe DC field. From the difference in the shift of maxima with the frequency, it can also be anticipated that there are tunnelling processes present when no DC field is applied and they are dominant at 5 K and below. If a DC field of 3000 Oe is applied, it can be seen in Figure 4.40 (b) that the tunnelling processes become less important and temperature dependent processes overweigh.
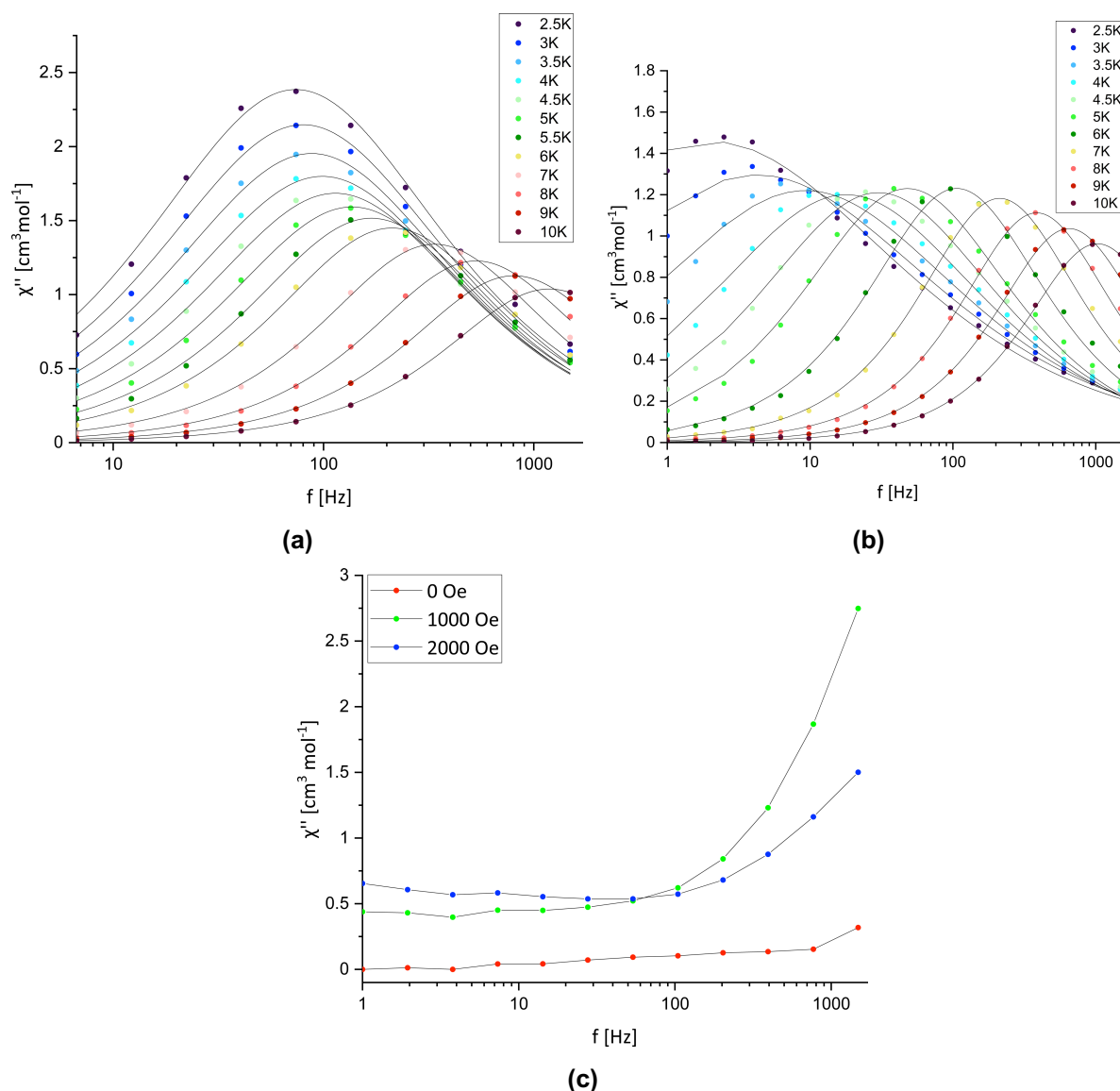
Figure 4.40: AC magnetic data of compound {Dy$_2$L$_2$(O)$_2$(NO$_3$)$_2$} **(8)**. **(a)** Temperature dependent χ'' versus frequency at 0 Oe applied DC field. **(b)** Temperature dependent χ'' versus frequency at 3000 Oe. AC magnetic data for compound {Dy$_2$L$_2$(F)$_2$(NO$_3$)$_2$} **(9)**. **(c)** Field dependent χ'' versus frequency.

The magnetic out of phase susceptibility data, which are the coloured dots in Figure 4.40, was fitted simultaneously with the corresponding in phase susceptibility data by a Debye function in the way described in the theory part of the thesis in section 2.3. The fitted curves are depicted as black lines in Figure 4.40 (a) and (b). Also, the rest of the procedure to assess the data is described in section 2.3 in the theory part. Hence from these curves, Arrhenius plots were obtained and were fitted using the general formula for the relaxation time. The Arrhenius plots are depicted in Figure 4.41. For the fitting, a simpler general function, in which the tunnelling processes are condensed to a factor B, was used in contrast to the one discussed in section 2.3 with equation (15).

$$\tau^{-1} = B + AT + CT^n + \tau_0^{-1} \cdot e^{\frac{U_{eff}}{T}} \tag{15}$$

Where B takes care of quantum tunnelling (QT), AT is for the direct processes (Dir), $CT^n$ for Raman processes (Rm) and $\tau_0^{-1} \cdot \exp(U_{eff}/T)$ for the Orbach process (Or).[11,43,51,53-56] There are so many parameters that it leads to overparameterisation for many data sets. In order to obtain meaningful data from the fitting, it was conducted not only with the complete function but also with some of the terms eliminated by setting the parameters to zero. The quality of the fitting then was assessed by goodness of fit testing and the comparison of the error values for the obtained parameter values. The results are shown in Table 4.8.

Table 4.8: Fitting of the zero field field AC data of compound {Dy$_2$L$_2$(O)$_2$(NO$_3$)$_2$} **(8)** with different terms of equation (15) (Or=Orbach, Rm=Raman, Qt=quantum tunnelling, Dir=direct processes).

| Model | Or+Rm+Qt+Dir | Or+Rm+Qt |
|---|---|---|
| Equation | $\tau_0^{-1} \cdot e^{-U_{eff}/T} + C \cdot T^n + B + A \cdot T$ | $\tau_0^{-1} \cdot e^{-U_{eff}/T} + C \cdot T^n + B$ |
| A | 72.04999 ± 6.26042 | 0 ± 0 |
| B | 281.02956 ± 16.43574 | 445.96456 ± 7.16718 |
| C | 0.0077 ± 0.00977 | 0.74956 ± 0.15005 |
| n | 5.54875 ± 0.45185 | 3.8883 ± 0.10402 |
| $\tau_0$ | 1.15669E-5 ± 1.97781E-6 | 1.71771E-5 ± 1.09097E-5 |
| $U_{eff}$ | 31.50356 ± 0.46461 | 38.93394 ± 4.08375 |
| Reduced $\chi^2$ | 7.25563 | 45.65686 |
| $R^2$ | 1 | 0.99999 |
| Adj. $R^2$ | 1 | 0.99999 |
| Model | Or+Rm | Or+Qt+Dir |
| Equation | $\tau_0^{-1} \cdot e^{-U_{eff}/T} + C \cdot T^n$ | $\tau_0^{-1} \cdot e^{-U_{eff}/T} + B + A \cdot T$ |
| A | 0 ± 0 | 133.56108 ± 15.13359 |
| B | 0 ± 0 | 97.83783 ± 57.87864 |
| C | 0.84937 ± 0.06589 | 0 ± 0 |
| n | 3.9165 ± 0.03296 | 0 ± 0 |
| $\tau_0$ | 0.00243 ± 8.56861E-5 | 2.911E-6 ± 2.24127E-7 |
| $U_{eff}$ | 2.03683E-14 ± 0.02462 | 40.52181 ± 0.88346 |
| Reduced $\chi^2$ | 622.94938 | 991.67992 |
| $R^2$ | 0.99991 | 0.99985 |
| Adj. $R^2$ | 0.99987 | 0.9998 |

---

(15): General formula for the relaxation time with possible relaxation processes, B for quantum tunnelling (Qt), AT for direct processes (Dir), $CT^n$ for Raman processes (Rm) and $\tau_0^{-1} \cdot \exp(U_{eff}/T)$ for the Orbach process (Or).
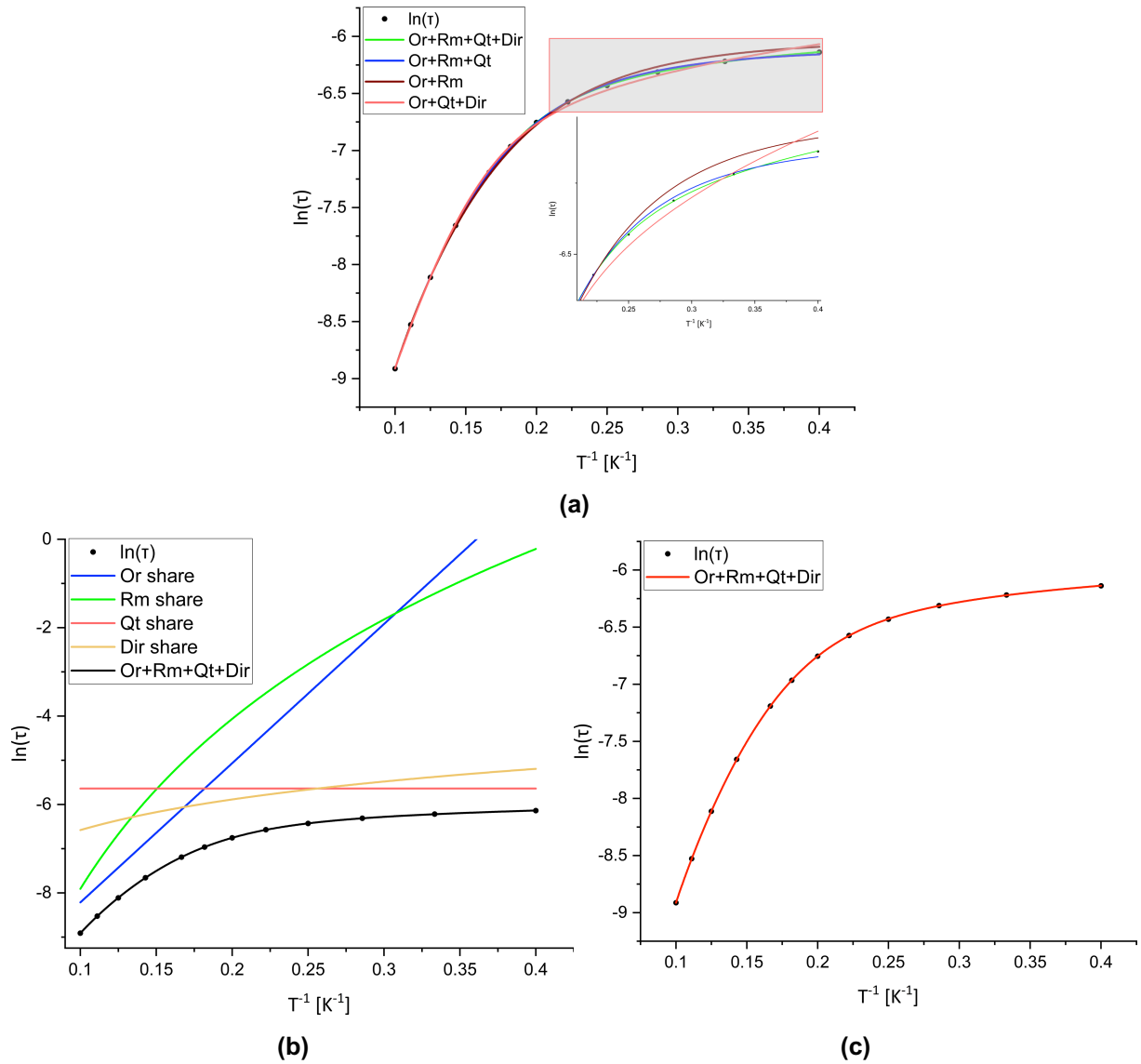
Figure 4.41: Arrhenius plots for the out of phase susceptibility data with zero DC field of compound {Dy$_2$L$_2$(O)$_2$(NO$_3$)$_2$} (8). **(a)** Data fitted with an equation for the relaxation times with the terms displayed in the legend for each curve. The cutout shows the deviations from the data at low temperatures. **(b)** Optimised fit of the data with plots for each term of the fitting curve. **(c)** Optimised fit of the data of {Dy$_2$L$_2$(O)$_2$(NO$_3$)$_2$} (8) in the Arrhenius plot.

It can be seen that for the AC data of the measurement with no applied DC field, the Orbach, the Raman and the quantum tunnelling term are certainly needed. If one of them is set to zero, the quality of the fitting decreases significantly as it can be seen in the increase of the $\chi^2$ and the bigger error values of the fit parameters in the results. A value of close to but above 1 for the $\chi^2$ is indicating a good fitting result. The additional use of the term for the direct process improves the quality of the fit and it was decided that the fitting with the full equation makes most sense. However, the negative impact on the results by leaving the direct process out is not as big as by setting other terms to zero. Setting the Orbach part to zero leads to divergence of the fitting routine. This is why it is not shown as a result. All fitting attempts for the AC data of the measurement

with no applied DC field are plotted in Figure 4.41 (a). In the enlarged cut-out, it can be seen that the fitting result of the equation incorporating all terms is the best and that setting the direct process term to zero is still ok from the optical perception. The plots with the Raman process set to zero or both the direct and the quantum tunnelling set to zero do not provide good fitting results as it already can be seen in the picture. The optimised fitting curve can be seen as red line in Figure 4.41 (c). In Figure 4.41 (b), the terms for each process are plotted separately next to the fit curve. It can be seen that for higher temperatures the Orbach dependence is dominant whilst in the middle part of the curve the Raman process is dominant and for low temperatures the quantum tunnelling and the direct processes are dominant. This is according to the evaluation of the zero DC field out of phase AC signals above. For the 3000 Oe DC field out of phase signals, the consideration is that the quantum tunnelling is blocked due to the applied DC field. This is supported by the fitting of the plot using the full equation. Although the terms for the direct process and the quantum tunnelling are not set to zero, the resulting values for the parameters of these terms are effectively zero, which can be seen in Table 4.9. Setting these two parameters (A and B) to zero leads to a better goodness of fit and lower error values. This means, there are no quantum tunnelling and direct processes present in the 3000 Oe applied field AC measurements.
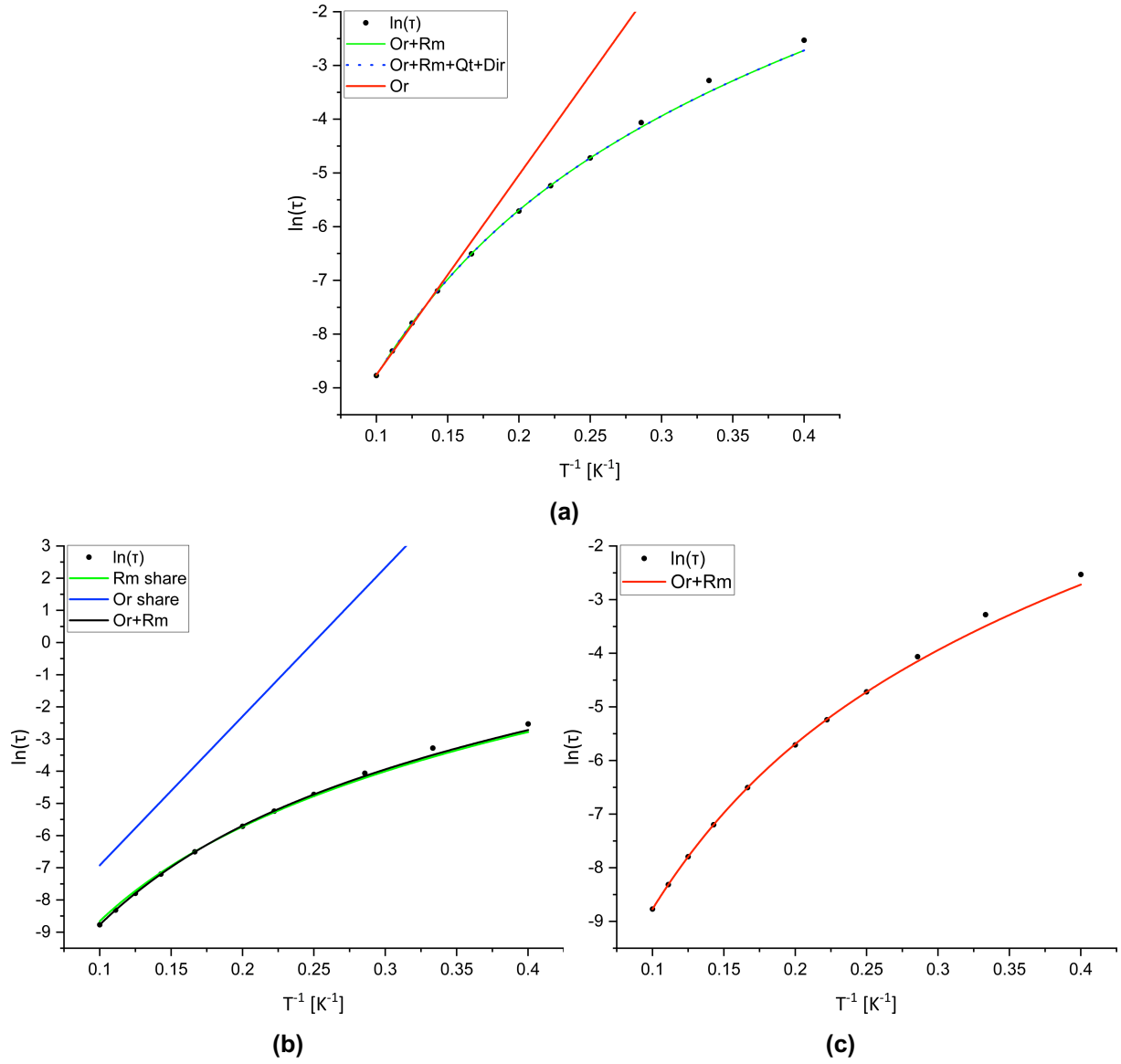
Figure 4.42: Arrhenius plots for the out of phase susceptibility data of compound {$Dy_2L_2(O)_2(NO_3)_2$} **(8)** with applied 3000 Oe DC field. **(a)** Data fitted with an equation for the relaxation times with the terms displayed in the legend for each curve. **(b)** Optimised fit of the data with plots for each term of the fitting curve. **(c)** Optimised fit of the data of {$Dy_2L_2(O)_2(NO_3)_2$} **(8)** in the Arrhenius plot.

Table 4.9: Fitting of the 3000 Oe DC field AC data of compound {$Dy_2L_2(O)_2(NO_3)_2$} **(8)** with different terms of equation (15) (Or=Orbach, Rm=Raman, Qt=quantum tunnelling, Dir=direct processes).

| Model | Or+Rm+Qt+Dir | Or+Rm |
|---|---|---|
| Equation | $\tau_0^{-1}\cdot e^{-U_{eff}/T}+C\cdot T^n+B+A\cdot T$ | $\tau_0^{-1}\cdot e^{-U_{eff}/T}+C\cdot T^n$ |
| A | 3.88722E-16 ± 0 | 0 ± 0 |
| B | 1.51417E-15 ± 0 | 0 ± 0 |
| C | 0.31128 ± 0.03333 | 0.31112 ± 0.02815 |
| n | 4.2413 ± 0.06418 | 4.24162 ± 0.05422 |
| $\tau_0$ | 9.61685E-6 ± 4.01766E-6 | 9.63546E-6 ± 3.4071E-6 |
| $U_{eff}$ | 46.27113 ± 1.97116 | 46.26298 ± 1.66942 |
| Reduced $\chi^2$ | 22.16523 | 15.83216 |
| $R^2$ | 1 | 1 |
| Adj. $R^2$ | 0.99999 | 1 |

| Model | Or |
|---|---|
| Equation | $\tau_0^{-1} \cdot e^{-U_{eff}/T}$ |
| A | $0 \pm 0$ |
| B | $0 \pm 0$ |
| C | $0 \pm 0$ |
| n | $0 \pm 0$ |
| $\tau_0$ | 3.81095E-6 ± 4.92284E-7 |
| $U_{eff}$ | 37.20677 ± 1.21032 |
| Reduced $\chi^2$ | 10836.96117 |
| $R^2$ | 0.99779 |
| Adj. $R^2$ | 0.99754 |

The additional cancelling of the Orbach term leads to divergence in the fitting procedure and is therefore not shown in Figure 4.42. Setting additionally the Raman term to zero, on the other hand, leads to large degradation of goodness of the fit indicators. This can be anticipated since the Orbach term is a straight line in the $\ln(\tau)$ versus 1/T Arrhenius plot while the distribution of the measured data is far from linear. All three fits are depicted in Figure 4.42 (a) showing that fitting by the full equation gives the same result as fitting only with Orbach and Raman terms. Additionally, it can be seen that the single Orbach term is not suited for fitting of the data. The best fit with Orbach and Raman is shown in Figure 4.42 (c) and the contributions of the Orbach and Raman terms are shown in Figure 4.42 (b). This plot also shows that the data is strongly Raman dependent over the complete treated temperature range. The Raman exponents are typical for lanthanide SMMs and SIMs, respectively.[165] Raman dominated relaxation processes are reported to be usual for lanthanide complexes which show single molecule magnetic behaviour and have sufficient blocking of the quantum tunnelling.[51] In this paper of Chilton, Winpenny et al., it is also discussed that the presence of an equatorial ligand is unfavourable for supressing the Raman processes which seems to be the critical factor for higher blocking temperatures as the authors suggest. They also point out that there were no systematic studies on a system with equatorially bound ligands and deliberate variations to "identify a clear dependence on the effect of specific ligands or on coordination geometry".[51] The deliberate variations and the detailed description of the structures of the monomers and dimers or binuclear compounds, respectively, will allow for this.

In order to provide more information about the influence of the beneficial coupling in the peroxide complex $\{Dy_2L_2(O)_2(NO_3)_2\}$ **(8)**, the dysprosium compound and its terbium and erbium derivatives were investigated together with the collaboration partners Mauro Perfetti, PhD and Niels Bonde at the Institute Laue-Langevin in Grenoble by

inelastic neutron scattering. The results are not fully evaluated but as the picture below shows only for erbium and terbium signals could be detected.
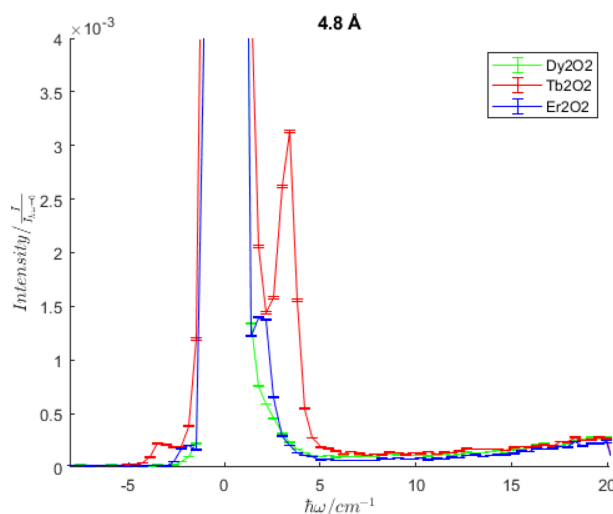


Figure 4.43: Results from inelastic neutron scattering comparison of the disprosium, terbium and erbium derivatives of $\{Dy_2L_2(O)_2(NO_3)_2\}$ **(8)**.

Considering the magnetic measurements that were conducted on the compounds of this subchapter and compound $\{DyL(NO_3)_2\}$ **(2)**, it is shown how small structural changes have a large effect on the magnetic properties. This can be examined from different viewpoints. From the perspective of coupling, it is shown that it can have good and bad influence on slow magnetic relaxation. Whilst the monomer $\{DyL(NO_3)_2\}$ **(2)** only shows slow relaxation in the AC measurements with applied DC field and also then exhibits two relaxation processes, there cannot be any slow relaxation found in the fluoride coupled $\{Dy_2L_2(F)_2(NO_3)_2\}$ **(9)**. In $\{Dy_2L_2(O)_2(NO_3)_2\}$ **(8)**, on the other hand, the peroxide bridge leads to zero field SMM behaviour. The nature of coupling could be the key factor in explaining the vast differences in the magnetic properties of the compounds. Along with considerations about exchange coupling via the ligand, dipolar and Ising interactions, which should be strong for the peroxide coupled dimer, need to be considered because of the short distance between the dysprosium centres and the short Dy-O bond lengths.[85,86] Usually, ferromagnetic coupling has a negative impact on slow relaxation. However, this is not the case for similarly fluoride coupled compounds.[123,144] In the referenced examples these lead to slow relaxation instead of quenching it. Probably this behaviour is different in compound $\{Dy_2L_2(F)_2(NO_3)_2\}$ **(9)** because the anisotropy axes point along the Dy-Dy vector while for the two molecules in the literature they are perpendicular to this vector. It can also be examined from the anisotropy and structural view. This perspective spotlights the differences in the

minimal reversal energies, which change significantly with only small structural changes.

It would be interesting to investigate whether selective oxidation to a superoxide could provide stronger coupling due to its radical character. To this end, cyclic voltametric measurements were conducted on compound $\{Dy_2L_2(O)_2(NO_3)_2\}$ **(8)**. There have not been many cyclic voltametric studies found on lanthanides and especially lanthanide complexes. It was decided to use a 0.05 M solution of $LiClO_4$ in DMF in the range of -1.5 to 3.5 V against an Ag/AgCl electrode with a sweep rate of 50 mV/s. This was done to allow measurements in a range as large as possible given the scarcity on similar measurements in the literature. It can be seen in Figure 4.44 (a) that there can be signals found at 0.7 to 1 V that match an expected voltage for the oxidation of peroxide. It can also be seen that there is a reduction signal appearing at -1.5 V which is a high value for nitrate reduction. Since it is the only significantly different reduction signal for the $Dy(NO_3)_3$ containing electrolyte solution compared to the pure electrolyte solution, it could possibly be that this is the signal corresponding to nitrate reduction. Dr. Claudia Bizzari collected the spectro-electrochemical data on the compound which is shown in Figure 4.44 (b). When a voltage in the range 0.7 to 1.0 V was applied, corresponding to the signal assigned to the peroxide reduction, an increase in the UV-vis absorbance at 265 nm was observed together with a decrease in the absorbance at 340 nm. With higher voltages, the 340 nm peak decreases more rapidly but the peak at 265 nm does not appear to increase.
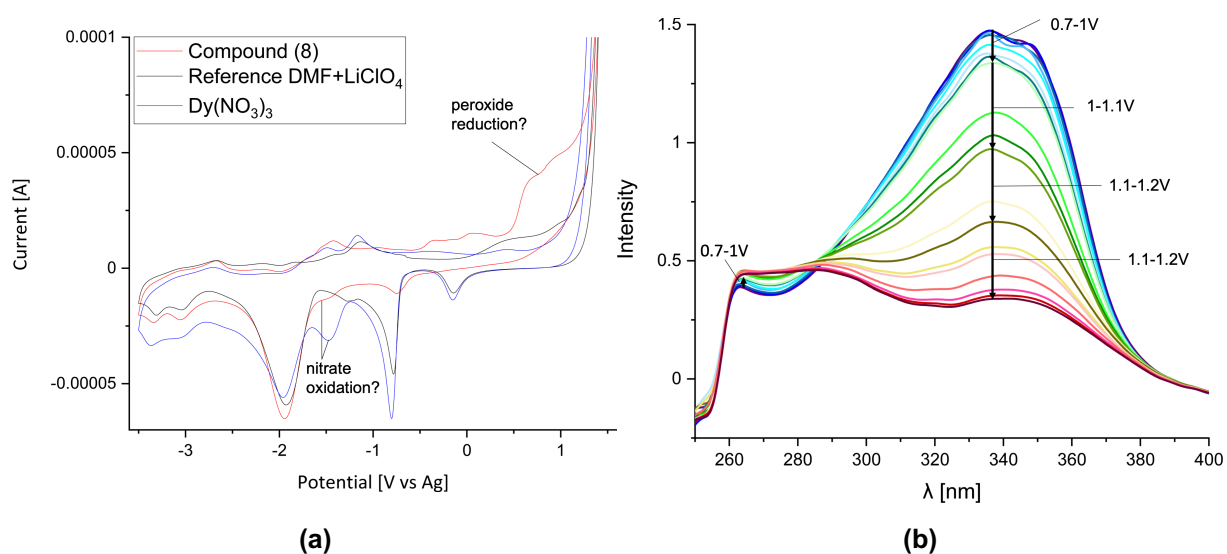


Figure 4.44: **(a)** Cyclic voltametric measurments on the peroxide compound $\{Dy_2L_2(O)_2(NO_3)_2\}$ **(8)**, reference measurement with 0.05 M $LiClO_4$ electrolyte solution and $Dy(NO_3)_3$ in reference solution. **(b)** Spectroelectrochemical measurements on $\{Dy_2L_2(O)_2(NO_3)_2\}$ **(8)**.

Given these results it was planned to have resonance Raman spectra collected by another collaborator, Dr. Maurice van Gastel. However, the compound showed such strong fluorescence it was not possible to get any evidence for the formation of superoxide by electrochemical oxidation.

In order to provide a more detailed picture on how deliberate and small structural changes have an impact on the magnetic properties, the magnetic measurements for the other compounds are still to be conducted. The bent coupling mode and the DMF ligands in {Dy$_2$L$_2$(O)$_2$(DMF)$_2$} **(10)** are unusual structural features in already unusual compounds. Therefore, magnetic data on this compound will probably reveal some new aspects of the magnetism in small lanthanide complexes. However, the electrochemical synthesis route has to be optimised or a new synthesis route must be established in order to have high enough yield to investigate the compound properly. A further step should be attempting to vary the bridging motif, which can be for example done by the use of hydroxide ions instead of peroxide or fluoride ions and other structural variations such as other capping ligands or deliberate changes in the helicity. Targeting these will provide an even better test bed for investigating influences on single ion and small single molecule magnetic properties.

### 4.1.4  Conclusions

In this chapter, a test bed system designed for magnetic investigations on single lanthanide ion complexes is introduced which allows for deliberate and small variations. It was discussed that a test bed system like this was missed in the field of molecular magnetism.[51] The system consists of a dysprosium as central ion and the literature known H$_2$dapp ligand shown in Figure 4.1 with a variation in the secondary ligands.[98,100]

In a second step, the structural factors of the mononuclear compounds were analysed using continuous shape measurements on all dysprosium coordination spheres. This revealed low symmetry for all coordination spheres and gave the best agreement for different optimised geometries. This emphasises the variability of the system. To investigate the effects of the observed helical distortion of the H$_2$dapp ligands, a dihedral angle $\delta$ was defined in section 4.1.1 to quantify this distortion, and this correlated to the average bond lengths between dysprosium as the central ion and the coordinating nitrogen atoms of the H$_2$dapp ligand. It also showed a correlation to the angles of Dy with two of these nitrogen atoms. This correlation was broken by the exchange of the counter ion from nitrate in {DyL(NO$_3$)$_2$} **(2)** to chloride in {DyL(NO$_3$)$_2$}

**(3)** which only affected the helicity due to denser packing but did not significantly change the average Dy-N bond lengths or the average N-Dy-N angles. From this, it can be concluded that bond lengths and angles are also influenced by other effects than relative ligand position and packing. For the dysprosium centres, anisotropy axes and minimal reversal energies were calculated with MAGELLAN. In all cases, the neutral pentadentate ligand was confirmed to define the magnetic hard plane of the complexes with the anisotropy axes oriented towards the axial secondary ligands as had been expected. The deliberate changes of the secondary ligand affected the anisotropy axes. The anionic ligands close to the vertical axis revealed a positive effect on the calculated minimal reversal energy.

The minimal reversal energies were shown to have no straightforward correlation with the $\delta$ value as a measure of distortion. However, it becomes clear that when nitrate secondary ligands are present, the correlation breaks down. A trend was detected suggesting there is an optimal amount of helicity for the systems in terms of increase of the reversal energy.

As a third step, the monomeric systems were coupled via bridging ligands that are rarely used with lanthanide ions. Peroxide and fluoride ligands are usually considered "difficult" in lanthanide chemistry, but with careful choice of reaction conditions dinuclear complexes with fluorido and peroxido bridges could be synthesised and structurally characterised. The helical distortion of the $H_2$dapp ligand induces a chirality in the Dy($H_2$dapp) moieties. The dinuclear complexes could be obtained either as the meso or enantiopure forms.

The magnetic properties of the coupled binuclear complexes $\{Dy_2L_2(O)_2(NO_3)_2\}$ **(8)** and $\{Dy_2L_2(F)_2(NO_3)_2\}$ **(9)** were compared with the properties of the mononuclear compound $\{DyL(NO_3)_2\}$ **(2)**. This revealed that the coupling could have positive as well as negative effects on the relaxation behaviour of lanthanide ions. A comparison with the only two dysprosium structures in the literature with the same fluoride coupling motif showed that the resulting effect might not be easy to predict since the fluoride coupling enhances the relaxation properties in the literature examples. It was concluded that the direction of the anisotropy axes relative to the Dy-Dy vector is an important factor.

The results of the magnetic measurements on $\{DyL(NO_3)_2\}$ **(2)** were compared with the results for a dysprosium complex with two $H_2$dapp ligands on the lanthanide ion. This showed that the approach to stabilise the oblate shaped ground state of dysprosium

does not necessarily lead to better magnetic properties. Attempts to oxidise the peroxide to a superoxide electrochemically gave inconclusive results.

Future work will include further investigation of the effect of the anions on the reversal energy barrier. Similarly, study of a greater variety of binuclear complexes with other bridging ligand(s) between the Dy(H$_2$dapp) moieties would lead to a better understanding of the system.

## 4.2 Towards High Symmetry Compounds

As already broadly discussed, high symmetry compounds should lead to better SMM performance. The unhelpful mixing of states can be suppressed by applying the right symmetry which reduces quantum tunnelling and enables accurate *ab initio* calculations giving better understanding of relaxation and the structural aspects that need to be adjusted for enhanced magnetic properties. Phosphine oxide ligands are known to give rise to higher axial symmetries and strong ligand fields since they coordinate almost linearly, saturate a lot of space of the ligand sphere depending on their substituents and have a high effective negative charge on the coordinating oxygen.[69,79,80,166-168]

It could be said that the $[Dy(OPCy_3)_2(H_2O)_5]^{3+}$ complexes, like the bis-phthalocyanine complexes before them, repeated the history of the famous $Mn_{12}$ cluster, since all were synthesised and structurally characterised years before they were first studied magnetically. It seems hard to believe that these complexes with their serendipitous syntheses and untargeted structures should be among the best SMMs. Nevertheless, these examples elucidate the necessity of basic research and report of results which do not have an immediate impact. As a consequence, all of these systems have been used as "drosophilas of single molecule magnetism" as Rashmi Bagai and George Christou described $Mn_{12}$.[7] What this implies is by reducing complexity of a system sufficiently it becomes possible to make general predictions from experimental results through the reduction of interfering parameters. Thus, new measurement techniques can be applied to these kinds of testbed systems.

In this chapter, we move from low symmetry mononuclear lanthanide SMMs to those of high symmetry. First, new aspects of $[Ln(OPCy_3)_2(H_2O)_5]Br_3$ will be considered, and then new high symmetry dysprosium single ion complexes are presented.

### 4.2.1 Lanthanide Complexes with Phosphine Oxide Ligands

In the magnetic measurements of the complexes in the sections 4.1.1 and 4.1.3, it can be seen that positioning of negatively charged ligands close to the axial position and neutral ligands in the equatorial as proposed by Rinehart and Long does not necessarily lead to impressive slow relaxation of the magnetic moment.[16] Their approach may well lead to a better separation between a ground state with high $m_J$ and the excited states, but this does not help if the relaxation does not go over the energy barrier but through it. These shortcuts are mainly tunnelling and Raman processes.[63]

The significance of tunnelling processes became better understood in the last decade of research on lanthanide SIMs. It is now well known that they can be quenched by applied DC fields, by strong magnetic coupling between Ln centres, or by certain symmetries.[11,52] However, Raman processes are still neither well investigated nor well understood, but as discussed at the end of section 4.1.3, might be the key factor to understand how to obtain high temperature SIMs and SMMs.[51]

Raman processes, in common with tunnelling and Orbach processes, are fuelled by the energy of phonons.[169,170] Moreover, the original estimates of the parameters for relaxation via Raman processes in simple inorganic salts stem from considerations about their phonon modes.[43,51] As a consequence, understanding and reducing the supply of such phonon modes would pave the way to high temperature SMMs. This was considered for long in the literature.[11] However to date, not much research has been conducted on it. Recently, there has been a strong drive in the field emphasising spin-phonon coupling as a key factor to investigate in order to be able to increase the blocking temperature in SIMs and SMMs.[63-65]

For this reason, it was proposed to use the novel technique of nuclear resonance vibrational spectroscopy (NRVS) to investigate spin-phonon coupling modes involving significant ligand displacement relative to a metal centre. These lead to the modulation of the ligand field. In collaboration with Dr. Lena Scherthan and Prof. Dr. Volker Schünemann it was decided to use $[^{161}Dy(OPCy_3)_2(H_2O)_5]Br_3 \cdot 2EtOH \cdot 2H_2O$ (Figure 4.45).[171] This compound has the advantage of quenched zero field quantum tunnelling and a high blocking temperature because of the approximate pentagonal bipyramidal $D_{5h}$ symmetry in the first and second coordination sphere.[69,79] The isotopically enriched $^{161}Dy$ compound was used in order to optimise the observed intensity.

**(11)**
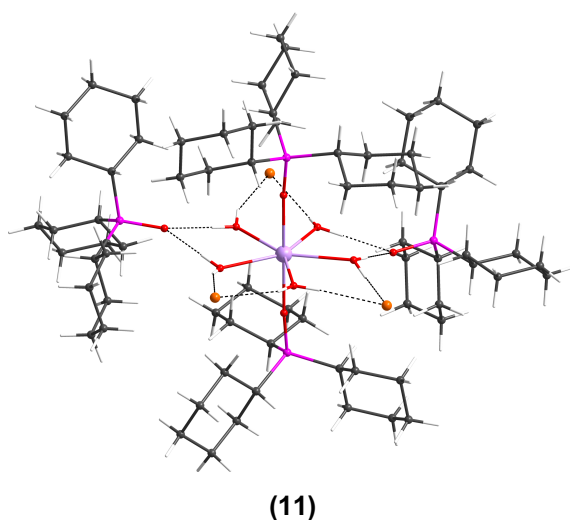
Figure 4.45: Molecular structure of [Dy(OP(Cy)$_3$)$_2$(H$_2$O)$_5$]Br$_3$·2EtOH·2H$_2$O **(11)** which is isostructural to [Gd(OP(Cy)$_3$)$_2$(H$_2$O)$_5$]Br$_3$·2EtOH·2H$_2$O. Colour code: white = H; grey = C; pink = P; orange = Br; lilac = Dy.

For this reason, isotopically enriched $^{161}$Dy$_2$O$_3$ was used as starting material, which is scarce and expensive. Therefore, the literature synthesis was first optimised using standard dysprosium oxide. For the literature synthesis lanthanide bromide is used. The first challenge was to convert lanthanide oxide to lanthanide bromide. However, water insoluble Ln$_2$O$_3$ does not transform easily into the bromide salt directly. For that reason, the $^{161}$Dy$_2$O$_3$ was dissolved in HCl$_{aq}$ and precipitated as hydroxide by adding a sodium hydroxide solution. The white solid was then transformed to the $^{161}$DyBr$_3$ with three equivalents of HBr$_{aq}$ and moderate heating. The complexation was directly conducted with the aqueous $^{161}$DyBr$_3$ solution in quantitative yield.

From the experiments on the compound, the partial density of states for the vibrations involving motion of the $^{161}$Dy atom could be extracted. This is not trivial as for most methods like Raman or IR spectroscopy, the selection rules are rather restrictive which is not the case with the NRVS method. However, it could be shown that this new technique is a good tool for the investigation of spin-phonon coupling, which could also be applied to other systems.

The pentagonal bipyramidal compound [Dy(OPCy$_3$)$_2$(H$_2$O)$_5$]Br$_3$·2EtOH·2H$_2$O, which was used for the measurement, was fully investigated with dysprosium as metal ion.[69] However, magnetic measurements were not reported for all the lanthanide analogues. The Gd$^{3+}$ cation is usually considered as magnetically isotropic so that no SMM behaviour would be expected. As it turned out, although the energy differences between the m$_J$ states is small, a weak rate of transition between them or the anisotropy stemming from ligand imposed orbital non-degeneracy of the $^8$S$_{7/2}$ ground

term and indeed there are six examples of gadolinium SMMs in the literature.[172-177] The high symmetry and the strong axial ligand field suggested that it might be possible to observe slow relaxation for the gadolinium compound of the $[Ln(OPCy_3)_2(H_2O)_5]Br_3$ series.[177]

Attempts in the literature to synthesise $[Gd(OPCy_3)_2(H_2O)_5]Br_3$ resulted in an octahedral compound with three bromides and three phosphine oxide ligands on the gadolinium.[79] Therefore, an optimised synthesis had to be used.[69] A 1:4 water-ethanol solvent mixture was used, and the mixture was heated and filtered while hot. This modified synthesis led to the correct molecular product, although it was obtained as a mixture of the two crystal phases reported for the Dy analogue with and without lattice solvent.[69,79] The powder pattern with the calculated patterns of both is shown in Figure 4.46.
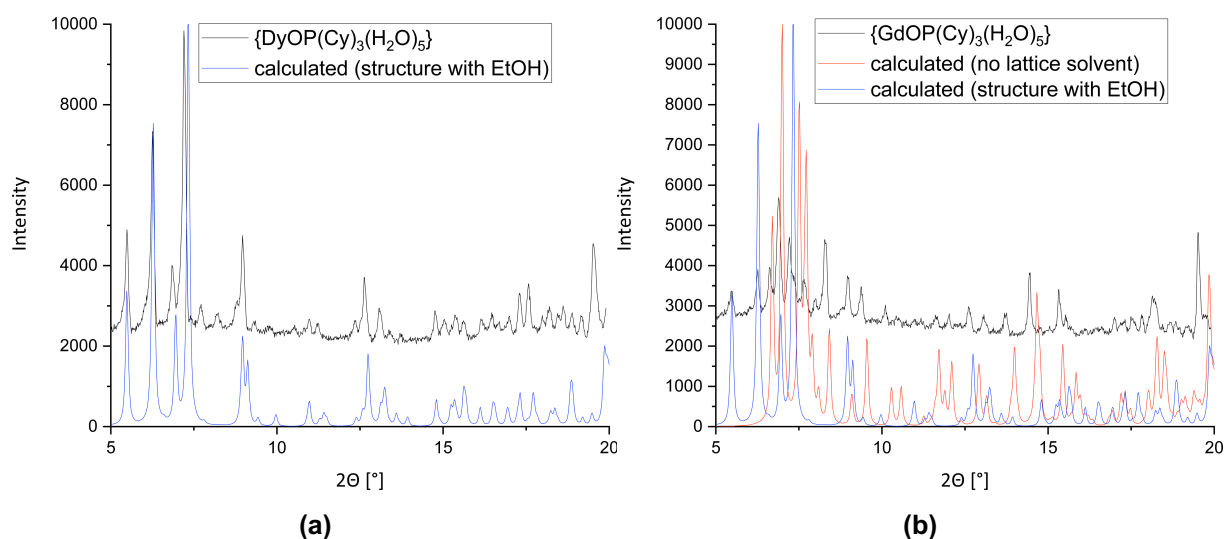


Figure 4.46: X-ray powder patterns of **(a)** {$^{161}$Dy(OP(Cy)$_3$)$_2$(H$_2$O)$_5$} and **(b)** {Gd(OP(Cy)$_3$)$_2$(H$_2$O)$_5$} **(11)**. The dysprosium compound shows phase purity of the crystal structure with ethanol as lattice solvent.[69] The gadolinium gave a mixed crystalline product of two phases for the crystal structures with ethanol lattice solvent and solvent free lattice.[79]

The results of the magnetic measurements on the gadolinium analogue of $[Dy(OP(Cy)_3)_2(H_2O)_5]Br_3$ compound {Gd(OP(Cy)$_3$)$_2$(H$_2$O)$_5$} **(11)** (Figure 4.45) indeed showed slow relaxation of the magnetisation as can be seen in Figure 4.47 (b). The data were fitted as described in subchapter 2.3 with two relaxation processes.

It can be seen in Figure 4.47 (a) that the $\chi_M T$ versus temperature plot shows the expected Curie paramagnetism. The $\chi_M T$ value remains close to the expected 7.88 $cm^3 mol^{-1} K$ for a gadolinium ion with S=7/2 and g=2. In the out of phase AC susceptibility maxima can only be observed with applied DC field. With a field of 2000

Oe slow relaxation can be seen up to 4 K. The simultaneous fitting of the in phase and out of phase data is shown as black lines in Figure 4.47 (b). The measured data points are the coloured dots. From the maxima in the fitting curves, the relaxation times at the measured temperatures are extracted and plotted as $\ln(\tau)$ versus $T^{-1}$. Due to the limited temperature range over which maxima in the out of phase signals were observed, the plot is not of high precision. However, it seems to be linear indicating the presence of an Orbach process. Although the points indicate only an Arrhenius type behaviour it is not possible to get a single satisfactory fitting. It is known for other gadolinium SMMs that the Orbach processes are the dominant ones because the energy states are close to each other.[177] Therefore, a regression line was drawn to at least extract the parameters for the Orbach process at high temperatures (Figure 4.47 (c)). These were found to be 5 K and $2.21 \cdot 10^{-5}$ s.

In order to investigate the chemistry with phosphine oxide ligands before using the expensive $^{161}Dy_2O_3$ in synthesis and in order to improve the synthesis to not waste starting material, syntheses with phosphine oxide ligands were conducted in different media and with different proportions. In these experiments, two new octahedral compounds were synthesised using the original triscyclhexylphosphine oxide for compound $\{Dy(OP(Cy)_3)_3(Br)_3\}$ **(12)** with the composition of $[Dy(OP(Cy)_3)_3(Br)_3]$ and $\{Dy(OP(Cy)_2(Ph))_4(Br)_2\}$ **(13)** with the composition of $[Dy(OP(Cy)_2(Ph))_4(Br)_2]Br$. For the synthesis of $\{Dy(OP(Cy)_2(Ph))_4(Br)_2\}$ **(13)** the related $OP(Ph)(Cy)_2$ ligand was used, in which one of the cyclohexyl rings in the original ligand has been replaced by a planar phenyl group. These compounds, with their unusual octahedral coordination geometry shown in Figure 4.48, are structurally similar to complexes in the literature[178,179] but these mostly involve the lighter lanthanides and no dysprosium analogue has previously been reported. In the reference[79], it was discussed that the smaller lanthanide ions form the pentagonal bipyramidal complexes shown above (Figure 4.45). However, the work presented here shows that with the right synthetic route for the other small lanthanide ions the octahedral complexes can also be obtained.

**(a)**



**(b)**



**(c)**
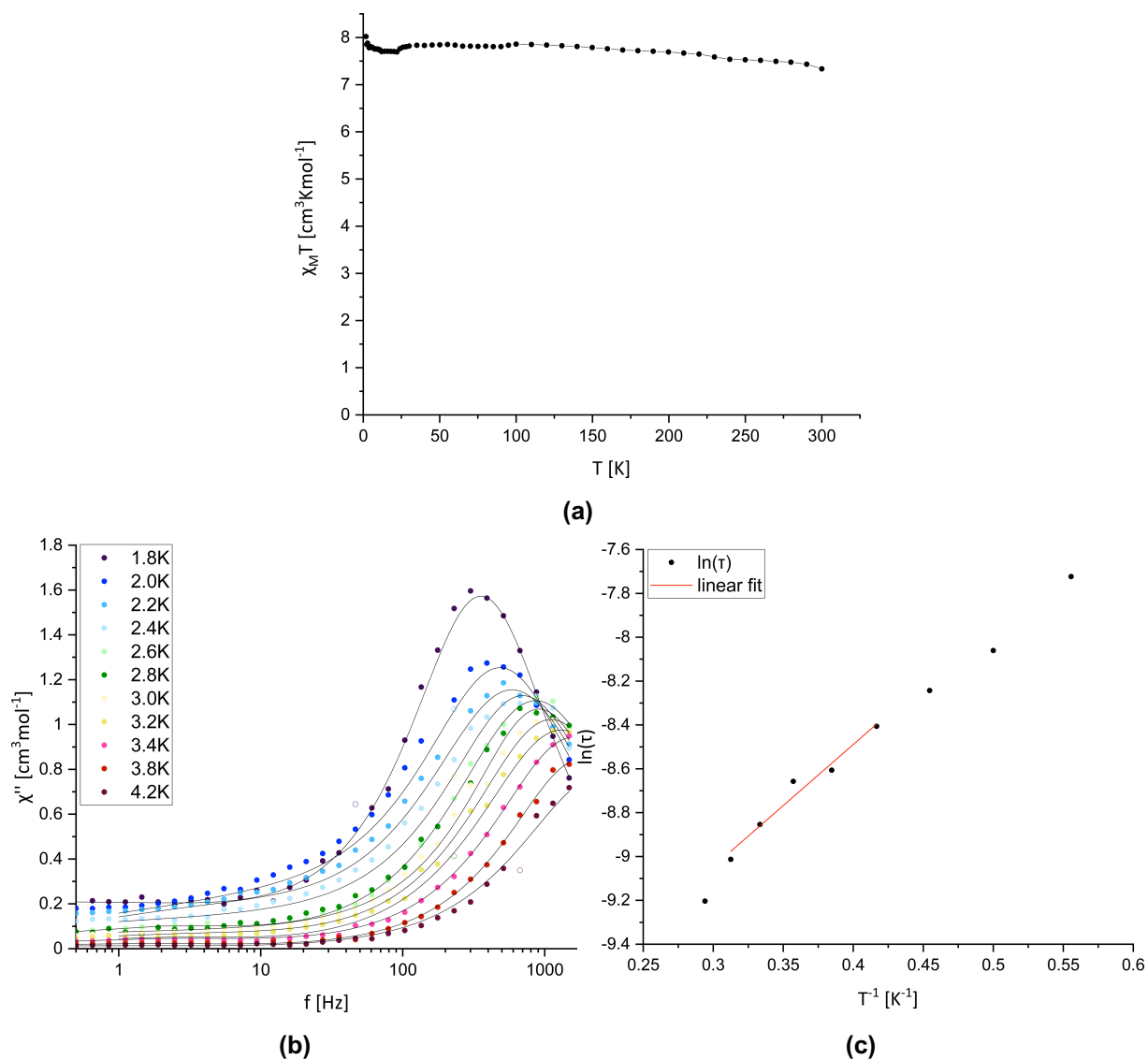
Figure 4.47: Magnetic data of {Gd(OP(Cy)$_3$)$_2$(H$_2$O)$_5$} **(11)**. DC **(a)** $\chi_M$T versus temperature plot. AC **(b)** Temperature dependent $\chi''$ versus frequency at 2000 Oe. **(c)** Arrhenius plots for the out of phase susceptibility data with 2000 Oe DC field of compound {Gd(OP(Cy)$_3$)$_2$(H$_2$O)$_5$} **(11)**.

**(12)**              **(13)**
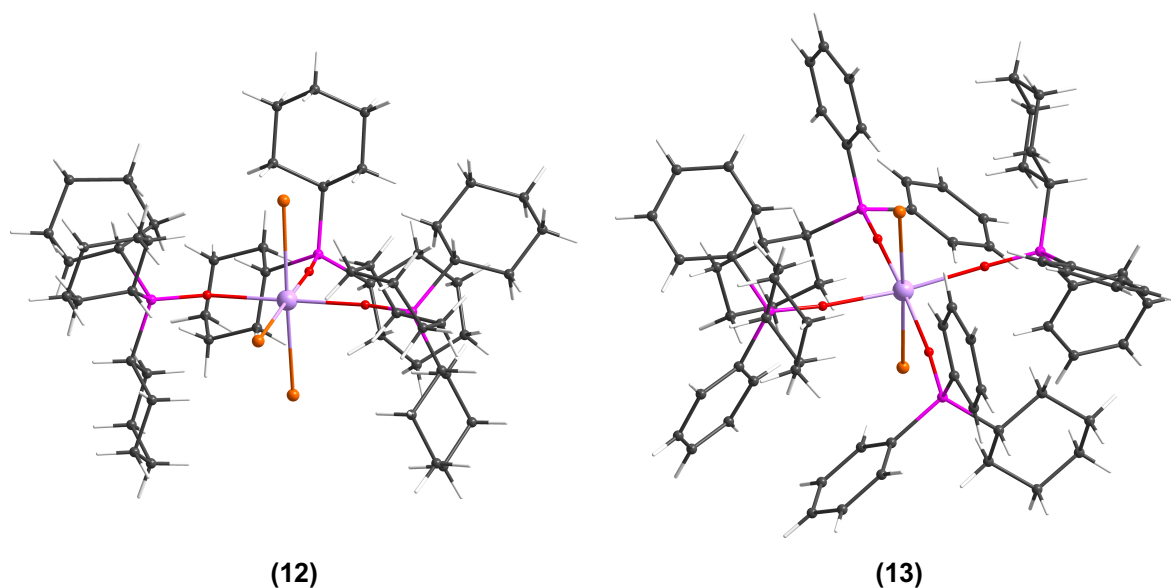
Figure 4.48: The two mononuclear octahedral complexes {Dy(OP(Cy)$_3$)$_3$(Br)$_3$} **(12)** and {Dy(OP(Cy)$_2$(Ph))$_4$(Br)$_2$} **(13)**. Colour code: white = H; grey = C; pink = P; orange = Br; lilac = Dy.

Compound {Dy(OP(Cy)$_3$)$_3$(Br)$_3$} **(12)** and compound {Dy(OP(Cy)$_2$(Ph))$_4$(Br)$_2$} **(13)** were both synthesised in a methanolic solution in a 4:1 ligand to dysprosium ratio with DyBr·6H$_2$O as dysprosium source. For compound {Dy(OP(Cy)$_3$)$_3$(Br)$_3$} **(12)**, tris-cyclohexylphosphine oxide was used as ligand and for compound {Dy(OP(Cy)$_3$)$_4$(Br)$_2$} **(13)**, dicyclohexyl(phenyl)phosphine oxide was used. Whilst the reaction mixture for {Dy(OP(Cy)$_3$)$_3$(Br)$_3$} **(12)** was left under ambient conditions, the reaction mixture for {Dy(OP(Cy)$_2$(Ph))$_4$(Br)$_2$} **(13)** was heated to 80 °C and filtered. In both cases, big octahedral crystals grew after one day. Bond lengths and angles about the central Dy for **(12)** and **(13)** are listed in Table 4.10.

Table 4.10: Bond lengths and angles for compounds {Dy(OP(Cy)$_3$)$_3$(Br)$_3$} **(12)** and {Dy(OP(Cy)$_2$(Ph))$_4$(Br)$_2$} **(13)**.
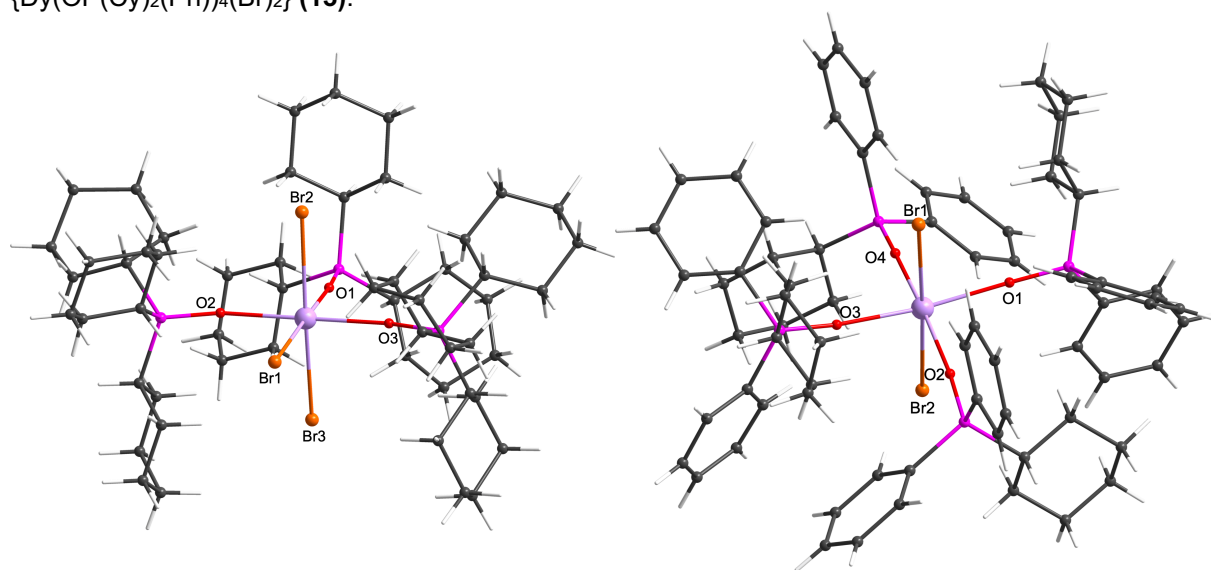


| | **(12)** | | | | **(13)** | |
|---|---|---|---|---|---|---|
| Atom | Atom | Length/Å | | Atom | Atom | Length/Å |
| Dy1 | Br1 | 2.8401(5) | | Dy1 | Br1 | 2.8304(2) |
| Dy1 | Br2 | 2.8183(6) | | Dy1 | Br2 | 2.8258(2) |
| Dy1 | Br3 | 2.8075(6) | | Dy1 | O1 | 2.2468(13) |
| Dy1 | O1 | 2.257(3) | | Dy1 | O2 | 2.2315(14) |
| Dy1 | O2 | 2.224(3) | | Dy1 | O3 | 2.2492(14) |
| Dy1 | O3 | 2.218(3) | | Dy1 | O4 | 2.2445(14) |
| Atom | Atom | Atom | Angle/° | Atom | Atom | Atom | Angle/° |

| Atom | Atom | Atom | Angle/° | Atom | Atom | Atom | Angle/° |
|---|---|---|---|---|---|---|---|
| Br1 | Dy1 | Br2 | 95.30(2) | Br1 | Dy1 | Br2 | 177.655(8) |
| Br1 | Dy1 | Br3 | 91.18(2) | Br1 | Dy1 | O1 | 85.21(4) |
| Br1 | Dy1 | O1 | 177.13(9) | Br1 | Dy1 | O2 | 96.28(4) |
| Br1 | Dy1 | O2 | 87.99(8) | Br1 | Dy1 | O3 | 84.28(4) |
| Br1 | Dy1 | O3 | 88.23(9) | Br1 | Dy1 | O4 | 93.51(4) |
| Br2 | Dy1 | Br3 | 173.501(18) | Br2 | Dy1 | O1 | 96.43(4) |
| Br2 | Dy1 | O1 | 87.45(9) | Br2 | Dy1 | O2 | 85.43(4) |
| Br2 | Dy1 | O2 | 88.87(9) | Br2 | Dy1 | O3 | 94.17(4) |
| Br2 | Dy1 | O3 | 89.59(9) | Br2 | Dy1 | O4 | 84.78(4) |
| Br3 | Dy1 | O1 | 86.06(9) | O1 | Dy1 | O2 | 89.68(5) |
| Br3 | Dy1 | O2 | 90.94(9) | O1 | Dy1 | O3 | 169.05(5) |
| Br3 | Dy1 | O3 | 91.04(9) | O1 | Dy1 | O4 | 91.17(5) |
| O1 | Dy1 | O2 | 91.25(12) | O2 | Dy1 | O3 | 88.41(6) |
| O1 | Dy1 | O3 | 92.62(12) | O2 | Dy1 | O4 | 170.21(5) |
| O2 | Dy1 | O3 | 175.77(12) | O3 | Dy1 | O4 | 92.54(6) |

The crystal structures are shown in Figure 4.49. Compound {Dy(OP(Cy)$_3$)$_3$(Br)$_3$} **(12)** crystallises in the orthorhombic space group Pca2$_1$ as [Dy(OP(Cy)$_3$)$_3$(Br)$_3$] in the asymmetric unit whilst {Dy(OP(Cy)$_2$(Ph))$_4$(Br)$_2$} **(13)** crystallises in triclinic P$\bar{1}$ as [Dy(OP(Cy)$_2$(Ph))$_4$(Br)$_2$]Br·3MeOH.
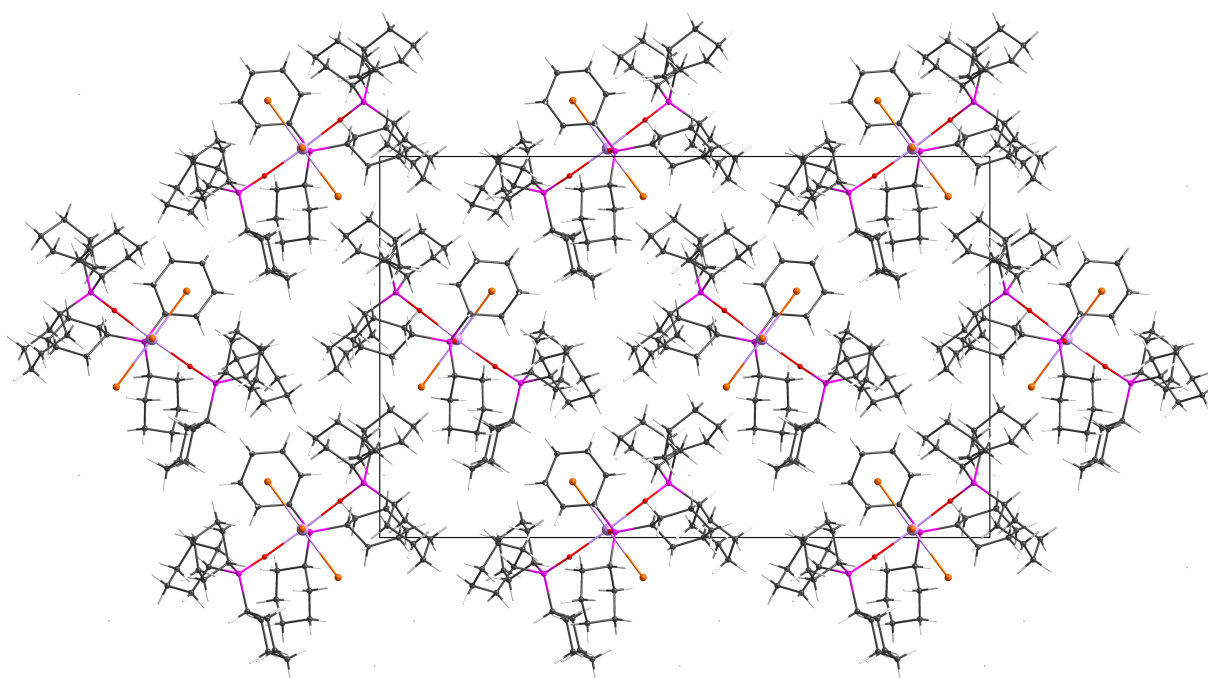
**(12)**
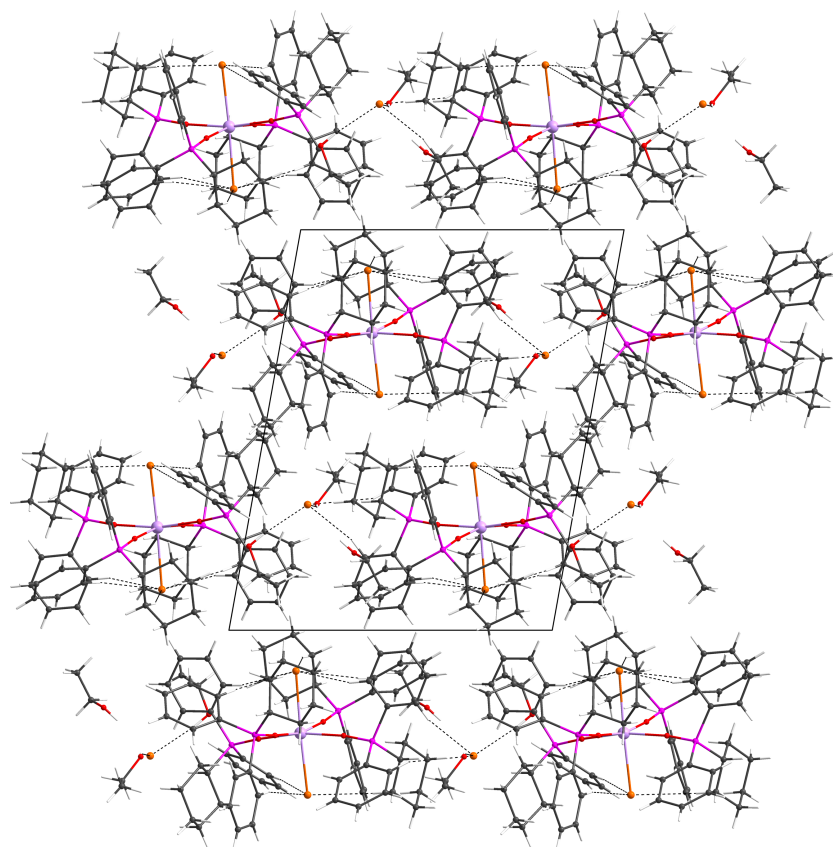


**(13)**

Figure 4.49: Crystal packing of {Dy(OP(Cy)$_3$)$_3$(Br)$_3$} **(12)** and {Dy(OP(Cy)$_2$(Ph))$_4$(Br)$_2$} **(13)** in viewing direction b.

For {Dy(OP(Cy)$_3$)$_3$(Br)$_3$} **(12)** and {Dy(OP(Cy)$_2$(Ph))$_4$(Br)$_2$} **(13)**, CShM were done on the molecules with SHAPE 2.1.[107] It can be seen that the coordination spheres on the dysprosium ions in both compounds are close to octahedral as expected (Figure 4.50).

This coordination geometry on the lanthanide ion should enable strong mixing of states and therefore enhance quantum tunnelling.



**(12)**      OC      **(13)**      OC

1.46 %      1.78 %
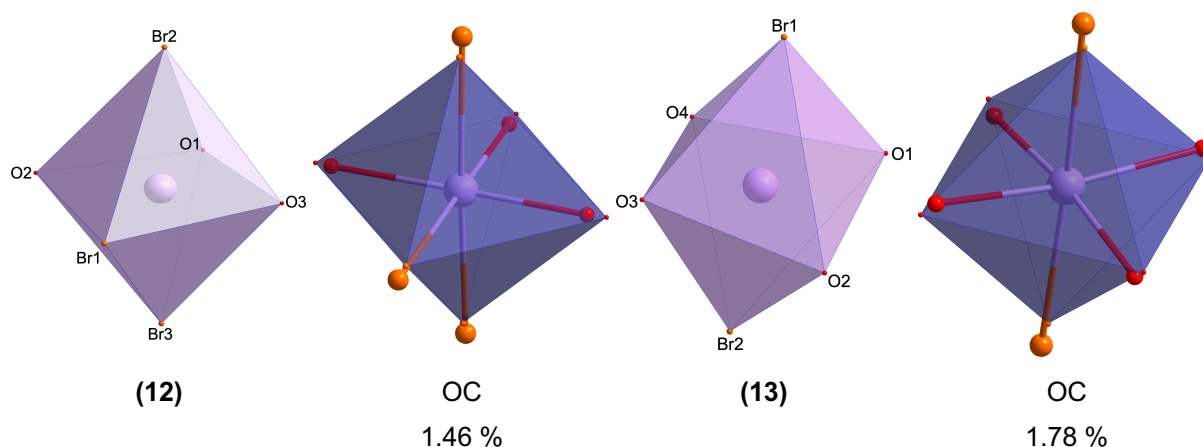
Figure 4.50: Lilac: Coordination polyhedra of the complexes {Dy(OP(Cy)$_3$)$_3$(Br)$_3$} **(12)** and {Dy(OP(Cy)$_2$(Ph))$_4$(Br)$_2$} **(13)**. Blue: Coordination polyhedra of the best fitting ideal structures, octahedra in both cases (OC), with the positions of the atoms in the original structure. Deviation values below ideal structures. The deviation values and the optimal polyhedra are obtained with SHAPE 2.1.[107]

Analysis with MAGELLAN was conducted on the molecules. This applies an electrostatic model in order to calculate the directions of the anisotropy axes and the minimal reversal energies for dysprosium complexes (Figure 4.51).[40] This reveals minimal reversal energies of 550 cm$^{-1}$ for {Dy(OP(Cy)$_3$)$_3$(Br)$_3$} **(12)** and 1060 cm$^{-1}$ for {Dy(OP(Cy)$_2$(Ph))$_4$(Br)$_2$} **(13)**. However, such calculations will depend critically on the charges assigned to the bromide ligands and to the phosphine oxide oxygens. The above results were obtained assigning charges of -1 to the bromides and assuming the oxygens were uncharged. But in a recent paper on lanthanide complexes with phosphine oxide ligands, the charge distributions on the ligating atoms was calculated by Loprop which showed a charge of -1.10 on the phosphine oxide oxygen and only -0.85 on the bromine one.[168] Therefore, the calculations with MAGELLAN were repeated using these reported charges.[40,168] As might be expected, with a larger negative charge on the oxygens than on the bromides, the results now show a close to 90° deviation for the anisotropy axes and higher values for the minimal reversal energies still having a higher value for {Dy(OP(Cy)$_2$(Ph))$_4$(Br)$_2$} **(13)** compared to {Dy(OP(Cy)$_3$)$_3$(Br)$_3$} **(12)**. This is shown in Figure 4.52. It has not yet proved possible to make magnetic measurements on {Dy(OP(Cy)$_3$)$_3$(Br)$_3$} **(12)** and {Dy(OP(Cy)$_2$(Ph))$_4$(Br)$_2$} **(13)**. However, such measurements have been reported for similar octahedral complexes with iodide ligands.[167,168] Apart from the different halide ligands and slight changes in the organic residues on the phosphine oxides, the

structures are similar to {Dy(OP(Cy)$_3$)$_3$(Br)$_3$} **(12)** and {Dy(OP(Cy)$_2$(Ph))$_4$(Br)$_2$} **(13)**. In these investigations, no out of phase AC signals were found for the iodide analogue [Dy(OP(Ph)$_3$)$_4$(I)$_2$] of {Dy(OP(Cy)$_2$(Ph))$_4$(Br)$_2$} **(13)**. Surprisingly, slow magnetic relaxation was detectable up to 20 K without applied DC field for the iodide analogue [Dy(OP(Cy)$_3$)$_3$(I)$_3$] of {Dy(OP(Cy)$_3$)$_3$(Br)$_3$} **(12)**. Neither of these findings can be expected from the initial calculations of SHAPE and MAGELLAN. From this example, it can be seen that there are limits with the software used in rationalising the structural effects on the magnetism of the molecule. These limits could possibly result from the effective shielding from spin-phonon coupling by the ligands. If the lattice energy for spin reversal is not transfered to the spin carrier, there is insufficient energy for relaxation and therefore mixing of states and symmetry matter less.

Whatever the reasons for ambiguous results from these calculations are, this example shows that first of all magnetism in lanthanide compounds has so many parameters influencing the magnetic properties. This makes it difficult to propose structure property correlations. Therefore, it is worth measuring compounds that may not look promising at first glance. Second, this example should teach that results of these "low cost" calculations need to be treated carefully. Finally, a proper means of assigning charge density needs to be discovered.



**(12)**

550 cm$^{-1}$

**(13)**

1060 cm$^{-1}$
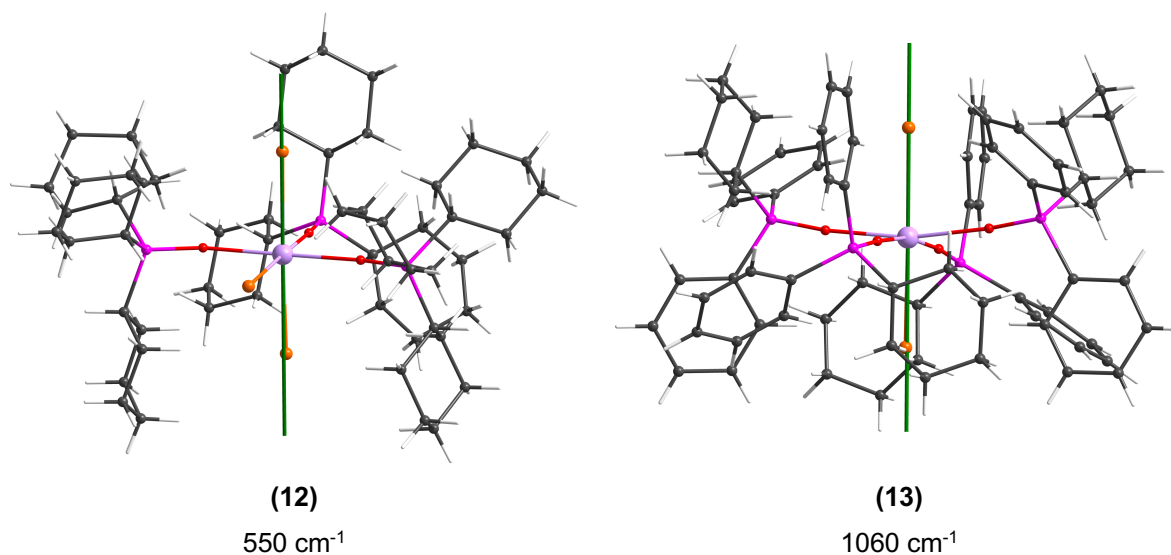
Figure 4.51: Molecules {Dy(OP(Cy)$_3$)$_3$(Br)$_3$} **(12)** and {Dy(OP(Cy)$_2$(Ph))$_4$(Br)$_2$} **(13)** with anisotropy axes and minimal reversal energies obtained from MAGELLAN.[40] The calculations are based on estimated charges based on the valence bond theory (Br as -1 and O as neutral).

**(12)**                    **(13)**

1040 cm$^{-1}$              1370 cm$^{-1}$
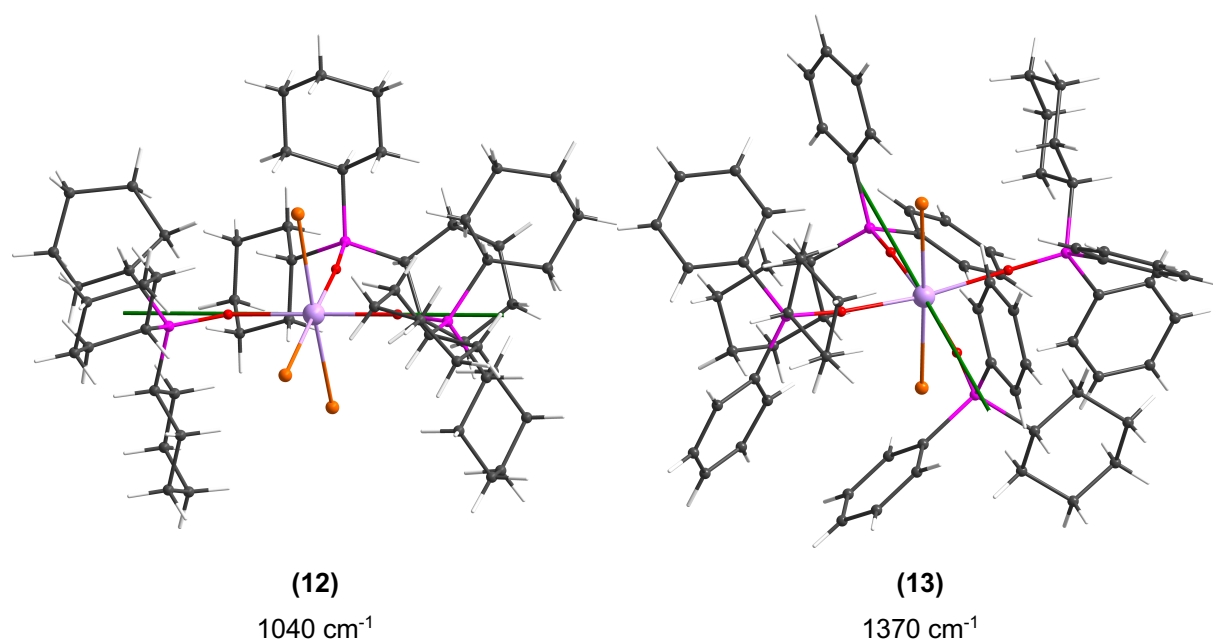
Figure 4.52: Molecules {Dy(OP(Cy)$_3$)$_3$(Br)$_3$} **(12)** and {Dy(OP(Cy)$_2$(Ph))$_4$(Br)$_2$} **(13)** with anisotropy axes and minimal reversal energies obtained from MAGELLAN.[40] using calculated charges from the Loprop calculations by Dunbar et al.[168]

## 4.2.2 Conclusions

An optimised synthesis was developed for a compound known from the literature. This was in order to use isotopically pure $^{161}$Dy$_2$O$_3$ to target a sufficient amount of this compound for a novel NRVS study. The Gd analougue showed SIM properties which were modelled using ab initio calculations.[69,79] It can be concluded that for this rare example of a gadolinium SMM, the combination of high symmetry and strong axiality gives rise to the observed slow relaxation. It is also shown that the main relaxation pathway in the compound is an Orbach process. In the section above, two new compounds related to compounds from the literature were presented. For the two new structures {Dy(OP(Cy)$_3$)$_3$(Br)$_3$} **(12)** and {Dy(OP(Cy)$_2$(Ph))$_4$(Br)$_2$} **(13)**, it has been shown that the investigations on the coordination geometry and the MAGELLAN calculations can give misleading ideas on the magnetic properties if a "conventional" set of charges on the ligands atoms is assumed. This is particularly true for neutral ligand atoms that are highly polarised (such as phosphine oxides) or for soft ligands (such as bromides or iodides) that favour covalent rather than electrostatic bonding. Therefore, it was proposed to carefully consider electronic charge distributions, not to overestimate the validity of calculations and, if in doubt, measure the magnetic properties.

# 5 EXPERIMENTAL DETAILS

The single crystal XRD measurements were performed on an IPSD II and a STADIVARI by STOE using Mo-K$\alpha$ I = 0,71073 Å, a STADIVARI (Ga-K$\alpha$, λ = 1.34143 Å, detector: Dectris Eiger2 R 4M (detector type: HPC)) (STOE) and Supernova (Mo-K$\alpha$, λ = 0.71073 Å; Cu-K$\alpha$, λ = 1.5405 Å, detector: Dectris Pilatus R 200K (detector: HPA)) (Rigaku).

The structures were solved using OLEX2 and ShelXT program and refined with the ShelXT software package.[180,181] Figures were produced using Diamond 4.5.2.

Powder X-ray diffraction measurements were performed on a STOE STADI-P diffractometer using Cu-K$\alpha$ I = 1,5405 Å radiation. The data was processed using the Origin software and simulated powder patters were produced using Mercury 3.7.

The IR measurements were performed on a Bruker Alpha Platinum ATR Diamond.

Magnetic measurements were conducted on a Quantum Design MPMS-XL SQUID magnetometer with a 5 T DC magnet and one with 7 T DC magnet. The samples were immobilised in eicosan and the data were corrected by the diamagnetic contributions of the sample holder.

The INS data were collected at Institute Laue-Langevin, Grenoble, France, using the direct geometry cold and thermal neutron time-of-flight instruments IN5

The elemental analysis was conducted with a device from Perkin Elmer (Vario El).

# 6 SYNTHESIS

## 6.1 [Dy(H₂dapp)(H₂O)₄]Cl₃·5H₂O

88 mg (0.81 mmol) 2-hydrazinopyridine and 65 mg 2,6-diacetylpyridine (0.4 mmol) are dissolved in 15 ml of methanol and stirred vigorously giving a clear and pale yellow solution. A suspension of 151 mg (0.4 mmol) $DyCl_3·6H_2O$ and 5 ml of methanol is prepared separately and the two mixtures are combined yielding a clear but deeply coloured yellow solution. The solution is heated under reflux and stirred for 15 min. Evaporation of the solvent to 1 ml of liquid within one day yields in block shaped single crystals and powder of [Dy(H₂dapp)(H₂O)₄]Cl₃·5H₂O. Elemental calc. (C, H, N) 29.39 %, 4.8 %, 12.63 %. Found 33.64 %, 3.34 %, 13.24 %. IR / cm$^{-1}$: 3066 (b,m) 1617 (s) 1252 (m) 1487 (s) 1422 (s) 1278 (s) 1249 (s) 1190 (s) 1157 (s) 1089 (s) 1000 (s) 780 (s) 529 (s,b) 486 (s,b)

## 6.2 [Dy(H₂dapp)(NO₃)₂]NO₃

88 mg (0.81 mmol) 2-hydrazinopyridine and 65 mg 2,6-diacetylpyridine (0.4 mmol) are dissolved in 15 ml of methanol and stirred vigorously giving a clear and pale yellow solution. A suspension of 181 mg (0.4 mmol) $Dy(NO_3)_3·6H_2O$ and 5 ml of methanol is prepared separately and the two mixtures are combined yielding a clear but deeply coloured orange solution. The reaction mixture is heated under reflux and stirred until a precipitate forms. The slurry is filtered and the solid powder is washed with ethanol yielding [Dy(H₂dapp)(NO₃)₂]NO₃. Trapezoid orange single crystals suitable for single crystal X-ray measurements are obtained by slow evaporation of the filtrate. Elemental calc. (C, H, N) 32.89 %, 2.75 %, 20.19 %. Found 32.41 %, 2.21 %, 18.98 %. IR / cm$^{-1}$ 1619 (m) 1516 (m) 1485 (m) 1422(w) 1387 (w) 1321 (w) 1266 (s) 1192 (w) 1155 (w) 1091 (w) 1020 (w) 1003 (w) 816 (w) 780 (m) 742 (m) 488 (w) 418 (w)

## 6.3 [DyL(NO₃)₂]Cl₀.₉₂ (NO₃)₀.₀₈

88 mg (0.81 mmol) 2-hydrazinopyridine and 65 mg 2,6-diacetylpyridine (0.4 mmol) are dissolved in 15 ml of methanol and stirred vigorously giving a clear and pale yellow solution. A suspension of 100 mg (0.27 mmol) $DyCl_3·6H_2O$, 60 mg (0.13 mmol) $Dy(NO_3)_3·6H_2O$ and 5 ml of methanol is prepared separately and the two mixtures are combined yielding a clear but deeply coloured orange solution. The reaction mixture is

heated for 10 minutes at 80 °C and orange crystals of $[DyL(NO_3)_2]Cl_{0.92}(NO_3)_{0.08}$ are obtained suitable for single crystal X-ray measurements after leaving it for two days in a vial with porous lid. Elemental calc. (C, H, N) 34.09 %, 2.86 %, 19.00 %. Found 33.62 %, 2.86 %, 15.94 %. IR / cm$^{-1}$ 1619 (m) 1512 (m) 1483 (s) 1426 (s) 1276 (s) 1241 (m) 1192 (m) 1157 (m) 1094 (m) 1017 (s) 810 (m) 778 (s) 741 (s) 638 (s) 587 (m) 535 (m) 486 (m) 416 (m)

## 6.4 $[Dy(H_2dapp)Cl_2(H_2O)]Cl·MeOH·H_2O$

88 mg (0.81 mmol) 2-hydrazinopyridine and 65 mg 2,6-diacetylpyridine (0.4 mmol) are dissolved in 15 ml of methanol and stirred vigorously giving a clear and pale yellow solution. A suspension of 151 mg (0.4 mmol) $DyCl_3·6H_2O$ and 5 ml of methanol is prepared separately and the two mixtures are combined yielding a clear but deeply coloured yellow solution. The solution is heated under reflux and stirring for 15 min. Slow evaporation leads to crystals of $[DyLCl_2(H_2O)]Cl·MeOH·H_2O$. Elemental calc. (C, H, N) 36.16 %, 3.79 %, 14.76 %. Found 34.25 %, 3.49 %, 13.67 %. IR / cm$^{-1}$ 2920 (w,b) 1615 (m) 1524 (m) 1490 (m) 1446 (s) 1414 (s) 1274 (m) 1245 (m) 1155 (m) 1093 (m) 1000 (m) 931 (w) 773 (s) 673 (s) 488 (m) 416 (m)

## 6.5 $[Dy(H_2dapp)(NO_3)Cl(H_2O)]Cl·2MeOH$

88 mg (0.81 mmol) 2-hydrazinopyridine and 65 mg 2,6-diacetylpyridine (0.4 mmol) are dissolved in 15 ml of methanol and stirred vigorously giving a clear and pale yellow solution. A suspension of 151 mg (0.4 mmol) $DyCl_3·6H_2O$ and 5 ml of methanol is prepared separately and the two mixtures are combined yielding a clear but deeply coloured yellow solution. 34 mg of $NaNO_3$ (0.4 mmol) is added and the solution is stirred for 10 min until it is completely homogenous. Yellow single crystals of $[Dy(H_2dapp)(NO_3)Cl(H_2O)]Cl·2MeOH$ form after evaporation to about 15 ml after one day accompanied with dark orange to red crystals of $[Dy(H_2dapp)(NO_3)Cl_2]·MeOH$. The products are separated by hand. Elemental calc. (C, H, N) 34.89 %, 4.04 %, 15.50 %. Found 33.02 %, 3.53 %, 15.60 %. IR / cm$^{-1}$ 3351 (s,b) 3023 (s,b) 1621 (s) 1494 (s) 1455 (s) 1334 (s) 1292 (m) 1247 (s) 1190 (s) 1157 (s) 1095 (s) 999 (m) 913 (w) 866 (w) 810 (m) 779 (s) 619 (w) 525 (s) 484 (s)

## 6.6 [Dy(H$_2$dapp)(NO$_3$)Cl$_2$]·MeOH

88 mg (0.81 mmol) 2-hydrazinopyridine and 65 mg 2,6-diacetylpyridine (0.4 mmol) are dissolved in 15 ml of methanol and stirred vigorously giving a clear and pale yellow solution. A suspension of 151 mg (0.4 mmol) DyCl$_3$·6H$_2$O and 5 ml of methanol is prepared separately and the two mixtures are combined yielding a clear but deeply coloured yellow solution. 34 mg of NaNO$_3$ (0.4 mmol) is added and the solution is stirred for 10 min until it is completely homogenous. Dark orange to red single crystals of [Dy(H$_2$dapp)(NO$_3$)Cl$_2$]·MeOH are obtained by leaving the closed vial stand for two days. Elemental calc. (C, H, N) 35.70 %, 3.45 %, 16.66 %. Found 31.52 %, 2.66 %, 17.82 %. IR / cm$^{-1}$ 3084 (w,b) 1619 (m) 1483 (s) 1453 (s) 1400 (m) 1272 (s) 1194 (m) 1161 (m) 1091 (m) 1022 (m) 911 (w) 814 (m) 773 (s) 742 (s) 589 (m) 488 (s) 412 (s)

## 6.7 [Dy(H$_2$dapp)(Ac)$_2$]Cl

88 mg (0.81 mmol) 2-hydrazinopyridine and 65 mg 2,6-diacetylpyridine (0.4 mmol) are dissolved in 15 ml of methanol and stirred vigorously giving a clear and pale yellow solution. A suspension of 100 mg (0.27 mmol) DyCl$_3$·6H$_2$O, 60 mg (0.13 mmol) Dy(Ac)$_3$·6H$_2$O and 5 ml of methanol is prepared separately and the two mixtures are combined yielding a clear but deeply coloured orange solution. The reaction mixture is heated for 10 minutes at 80 °C and orange crystals of [Dy(H$_2$dapp)(Ac)$_2$]Cl are obtained suitable for single crystal X-ray measurements after leaving it for two days in a vial with porous lid. Elemental calc. (C, H, N) 41.76 %, 3.81 %, 14.82 %. Found 39.99 %, 3.28 %, 13.41 %. IR / cm$^{-1}$ 2930 (w,b) 1613 (m) 1522 (m) 1424 (s) 1274 (m) 1155 (s) 1093 (m) 1003 (m) 931 (w) 880 (w) 773 (s) 671 (s) 486 (m) 416 (m)

## 6.8 [Dy$_2$(H$_2$dapp)$_2$(NO$_3$)$_2$O$_2$](NO$_3$)$_2$

88 mg (0.81 mmol) 2-hydrazinopyridine and 65 mg 2,6-diacetylpyridine (0.4 mmol) are dissolved in 15 ml of methanol and stirred vigorously giving a clear and pale yellow solution. A suspension of 181 mg (0.4 mmol) Dy(NO$_3$)$_3$·6H$_2$O and 5 ml of methanol is prepared separately and the two mixtures are combined yielding a clear but deeply coloured orange solution. Subsequently, 40 mg (0.4 mmol) of NEt$_3$ is added causing a drastic colour change to deep red. 80 mg of a 30 % aqueous H$_2$O$_2$ solution is added giving a strongly yellow coloured solution. This is left over night in a closed vial giving axe blade shaped orange to red single crystals of [Dy$_2$(H$_2$dapp)$_2$(NO$_3$)$_2$O$_2$](NO$_3$)$_2$. Elemental calc. (C, H, N) 33.30 %, 3.31 %, 18.43 %. Found 33.88 %, 2.82 %, 17.32

%. IR / cm$^{-1}$ 3242 (w,b) 2984 (w,b) 1613 (m) 1485 (s) 1381 (m) 1321 (s) 1276 (s) 1243 (m) 1186 (m) 1155 (m) 1089 (m) 1028 (m) 1003 (m) 905 (w) 810 (m) 775 (m) 738 (m) 634 (m) 486 (s) 414 (s)

## 6.9  [Dy$_2$(H$_2$dapp)$_2$(NO$_3$)$_2$F$_2$](NO$_3$)$_2$

88 mg (0.81 mmol) 2-hydrazinopyridine and 65 mg 2,6-diacetylpyridine (0.4 mmol) are dissolved in 15 ml of methanol and stirred vigorously giving a clear and pale yellow solution. A suspension of 181 mg (0.4 mmol) Dy(NO$_3$)$_3$·6H$_2$O and 5 ml of methanol is prepared separately and the two mixtures are combined yielding a clear but deeply coloured orange solution.88mg (0.4 mmol) NEt$_4$F is added to the stirred solution. The stirring bar is removed immediately thereafter and the vial is closed. Deep red axe blade shaped crystals of [Dy$_2$(H$_2$dapp)$_2$(NO$_3$)$_2$F$_2$](NO$_3$)$_2$ suitable for single crystal X-ray measurements form overnight. Elemental calc. (C, H, N) 33.22 %, 3.37 %, 18.35 %. Found 33.48 %, 2.63 %, 17.26 %. IR / cm$^{-1}$ 3242 (w,b) 2984 (w,b) 1613 (m) 1485 (s) 1381 (m) 1321 (s) 1276 (s) 1243 (m) 1186 (m) 1155 (m) 1089 (m) 1028 (m) 1003 (m) 905 (w) 810 (m) 775 (m) 738 (m) 634 (m) 486 (s) 414 (s)

## 6.10 [Dy$_2$(H$_2$dapp)$_2$(NO$_3$)$_2$O$_2$](NO$_3$)$_2$

1.70g (1.25 mmol) of [Dy$_2$(H$_2$dapp)$_2$(NO$_3$)$_2$O$_2$](NO$_3$)$_2$ is solved in a solution of 25 ml of a 2:1 mixture of DMF and deionised water and 1.25 mmol of LiClO$_4$. Cyclovoltametric experiments are conducted on it. The voltage range is -1.5 to 3.5 V with a sweep rate of 50 mV/s. A few crystals of [Dy$_2$(H$_2$dapp)$_2$DMF$_2$O$_2$](ClO$_4$)$_4$·4H$_2$O grow after one week.

## 6.11 [$^{161}$Dy(OPCy$_3$)$_2$(H$_2$O)$_5$]Br$_3$·2(OPCy$_3$)·2EtOH·2H$_2$O

30 mg (0.811 mmol) of $^{161}$Dy$_2$O$_3$ is dissolved in 4 ml of water and HCl$_{aq}$ is added subsequently while stirring. A sodium hydroxide solution is added until no more white precipitate is obtained. The suspension is centrifuged and the solution is decanted. The white precipitate is washed with deionised water and centrifuged. This is repeated three times. The solution is decanted and the white solid is dissolved 1 ml of deionised water and 58.5 µl (87.2 mg, 0.517 mmol) of a 48% aqueous solution of HBr. 4ml of EtOH were added and 97 mg (0.324 mmol) of tris-cyclohexylphospine are subsequently added with stirring. After one day and slow evaporation clear block shaped crystalline powder of [$^{161}$Dy(OPCy$_3$)$_2$(H$_2$O)$_5$]Br$_3$·2(OPCy$_3$)·2EtOH·2H$_2$O was obtained.

## 6.12 [Gd(OPCy$_3$)$_2$(H$_2$O)$_5$]Br$_3$·2(OPCy$_3$)

0.1 mmol (51 mg) of GdBr$_3$·6H$_2$O is dissolved in a mixture of 8 ml of ethanol and 2 ml of water. The solution is stirred and 0.4 mmol (118 mg) of tris-cyclohexylphospine oxide is added subsequently. The mixture is stirred and heated to 80 °C for one hour and left in a sealed vial. After two days octahedron shaped clear crystals of [Gd(OPCy$_3$)$_2$(H$_2$O)$_5$]Br$_3$·2(OPCy$_3$) are obtained.

## 6.13 [Dy(OP(Cy)$_3$)$_3$Br$_3$]

0.1 mmol (51 mg) of DyBr$_3$·6H$_2$O is dissolved in 10 ml of methanol. The solution is stirred and 0.4 mmol (118 mg) of tris-cyclohexylphospine oxide is added subsequently. The mixture is stirred for an hour and left in a sealed vial. After two days octahedron shaped clear crystals of [Dy(OP(Cy)$_3$)$_3$(Br)$_3$] are obtained. Elemental calc. (C, H) 50.22 %, 7.73 %. Found 49.26 %, 7.34 %. IR / cm$^{-1}$ 3209 (w,b) 2920 (s) 2852 (s) 1442 (m) 1299 (w) 1229 (w) 1087 (s) 1007 (m) 892 (m) 851 (m) 759 (m) 564 (s) 531 (s) 441 (s)

## 6.14 [Dy(OP(Cy)$_2$(Ph))$_4$(Br)$_2$]Br·3MeOH

0.1 mmol (51 mg) of DyBr$_3$·6H$_2$O is dissolved in 10 ml of methanol. The solution is stirred and 0.4 mmol (116 mg) of tris dicyclohexyl(phenyl)phosphine oxide is added subsequently. The mixture is heated at 80 °C for an hour and left in a sealed vial. After two days octahedron shaped clear crystals of [Dy(OP(Cy)$_2$(Ph))$_4$(Br)$_2$]Br·3MeOH are obtained. Elemental calc. (C, H) 55.80 %, 6.13 %. Found 52.80 %, 5.58 %. IR / cm$^{-1}$ 3181 (m,b) 2934 (m) 2884 (m) 1436 (m) 1124 (m) 1073 (m) 995 (m) 890 (m) 825 (w) 685 (s) 515 (s) 418 (m)

# 7 REFERENCES

[1]     C. Hanhart, *kurz & knapp: Quantenmechanik*, Springer Spektrum, Heidelberg, **2020**. 10.1007/978-3-662-60702-2

[2]     B. Hargittai, I. Hargittai: Year of the periodic table: Mendeleev and the others, *Struct. Chem.* **2019**, *30*, 1-7. 10.1007/s11224-018-1266-2

[3]     A. J. Ihde: The Karlsruhe congress: A centennial retrospect, *J. Chem. Educ.* **1961**, *38*, 83-86. 10.1021/ed038p83

[4]     R. Gross, A. Marx, *Festkörperphysik*, Oldenbourg Verlag, München, **2012**

[5]     A. Caneschi, D. Gatteschi, R. Sessoli, A. L. Barra, L. C. Brunel, M. Guillot: Alternating Current Susceptibility, High Field Magnetization, and Millimeter Band EPR Evidence for a Ground S = 10 State in [Mn12012(CH3C00)16(H20)4]*2CH3C00H*4H20, *J. Am. Chem. Soc.* **1991**, *113*, 5873-5874. 10.1021/ja00015a057

[6]     G. Christou, D. Gatteschi, D. N. Hendrickson, R. Sessoli: Single-Molecule Magnets, *MRS Bull.* **2000**, *25*, 66-71. 10.1557/mrs2000.226

[7]     R. Bagai, G. Christou: The Drosophila of single-molecule magnetism: [Mn12O12(O2CR)16(H2O)4], *Chem. Soc. Rev.* **2009**, *38*, 1011-1026. 10.1039/b811963e

[8]     R. Sessoli, D. Gatteschi, A. Caneschi, M. A. Novak: Magnetic bistability in a metal-ion cluster, *Nature* **1993**, *365*, 141-143. 10.1038/365141a0

[9]     L. Bogani, W. Wernsdorfer: Molecular spintronics using single-molecule magnets, *Nat. Mater.* **2008**, *7*, 179-186. 10.1038/nmat2133

[10]    M. Mohammadi, A. Niknafs, M. Eshghi: Controlled gates for multi-level quantum computation, *Quantum Inf. Process.* **2011**, *10*, 241-256. 10.1007/s11128-010-0192-z

[11]    S. T. Liddle, J. van Slageren: Improving f-element single molecule magnets, *Chem. Soc. Rev.* **2015**, *44*, 6655-6669. 10.1039/c5cs00222b

[12]    E. Moreno-Pineda, G. Taran, W. Wernsdorfer, M. Ruben: Quantum tunnelling of the magnetisation in single-molecule magnet isotopologue dimers, *Chem. Sci.* **2019**, *10*, 5138-5145. 10.1039/c9sc01062a

[13]    A. M. Ako, I. J. Hewitt, V. Mereacre, R. Clérac, W. Wernsdorfer, C. E. Anson, A. K. Powell: A Ferromagnetically Coupled Mn19 Aggregate with a Record S=83/2 Ground Spin State, *Angew. Chem. Int. Ed.* **2006**, *118*, 5048-5051. 10.1002/ange.200601467

[14]    O. Waldmann: A Criterion for the Anisotropy Barrier in Single-Molecule Magnets, *Inorg. Chem.* **2007**, *46*, 10035-10037. 10.1021/ic701365t

[15]    E. Ruiz, J. Cirera, J. Cano, S. Alvarez, C. Loose, J. Kortus: Can large magnetic anisotropy and high spin really coexist?, *Chem. Commun.* **2008**, *2*, 52-54. 10.1039/b714715e

[16]    J. D. Rinehart, J. R. Long: Exploiting single-ion anisotropy in the design of f-element single-molecule magnets, *Chem. Sci.* **2011**, *2*, 2078-2085. 10.1039/c1sc00513h

[17]    N. Ishikawa, M. Sugita, T. Ishikawa, S.-y. Koshihara, Y. Kaizu: Lanthanide double-decker complexes functioning as magnets at the single-molecular level, *J. Am. Chem. Soc.* **2003**, *125*, 8694-8695. 10.1021/ja029629n

[18]    C. Görller-Walrand, K. Binnemans, in *Handbook on the Physics and Chemistry of Rare Earths, Vol. 23* (Eds.: K. A. Gschneider Jr., L. Eyring), Elsevier Science, **1996**, pp. 121-283. 10.1016/s0168-1273(96)23006-5

[19]   J. L. Liu, Y.-C. Chen, M.-L. Tong: Symmetry strategies for high performance lanthanide-based single-molecule magnets, *Chem. Soc. Rev.* **2018**, *47*, 2431-2453. 10.1039/c7cs00266a

[20]   K. Dehnicke, A. Greiner: Unusual Complex Chemistry of Rare-Earth Elements: Large Ionic Radii–Small Coordination Numbers, *Angew. Chem. Int. Ed.* **2003**, *42*, 1340-1354. 10.1002/anie.200390346

[21]   Z. B. Goldschmidt, in *Handbook on the Physics and Chemistry of Rare Earths, Vol. 1* (Eds.: K. A. Gschneider Jr., L. Eyring), **1978**, pp. 1-171. 10.1016/S0168-1273(78)01005-3

[22]   D. A. Johnson, in *Inorganic Chemistry in Focus III* (Eds.: G. Meyer, D. Naumann, L. Wesemann), Wiley-VCH Verlag, Weinheim, **2006**, pp. 1-13. 10.1002/9783527609932.ch1

[23]   C. Janiak, H.-J. Meyer, D. Gudat, P. Kurz, E. Riedel, *Moderne Anorganische Chemie*, 5. ed., De Gruyter, Berlin, **2018**. 10.1515/9783110441635

[24]   C. Benelli, D. Gatteschi, *Introduction to Molecular Magnetism : From Transition Metals to Lanthanides*, Wiley-VCH Verlag, Weinheim, **2015**. 10.1002/9783527690541

[25]   S. G. McAdams, A.-M. Ariciu, A. K. Kostopoulos, J. P. S. Walsh, F. Tuna: Molecular single-ion magnets based on lanthanides and actinides: Design considerations and new advances in the context of quantum technologies, *Coord. Chem. Rev.* **2017**, *346*, 216-239. 10.1016/j.ccr.2017.03.015

[26]   K. Futscher: Elementarteilchen, *Phys. J.* **1949**, *5*, 258-267. 10.1002/phbl.19490050603

[27]   G. E. Uhlenbeck, S. Goudsmit: Ersetzung der Hypothese vom unmechanischen Zwang durch eine Forderung bezüglich des inneren Verhaltens jedes einzelnen Elektrons, *Sci. Nat.* **1925**, *13*, 953-954. 10.1007/bf01558878

[28]   D. K. Watson: Many-body formalism for fermions: Enforcing the Pauli principle on paper, *Phys. Rev. A* **2015**, *92*, 013628. 10.1103/PhysRevA.92.013628

[29]   D. R. McMillin: The Pauli Principle: Effects on the Wave Function Seen through the Lens of Orbital Overlap, *J. Chem. Educ.* **2018**, *95*, 1587-1591. 10.1021/acs.jchemed.8b00407

[30]   J. M. D. Coey, *Magnetism and Magnetic Materials*, Cambridge University Press, Cambridge, **2010**. 10.1017/cbo9780511845000

[31]   A. F. Williams, *A Theoretical Approach to Inorganic Chemistry*, Springer, Berlin, **1979**. 10.1007/978-3-642-67117-3

[32]   F. E. Mabbs, D. J. Machin, *Magnetism and Transition Metal Complexes*, Chapman and Hall, **1973**

[33]   S. K. Gupta, R. Murugavel: Enriching lanthanide single-ion magnetism through symmetry and axiality, *Chem. Commun.* **2018**, *54*, 3685-3696. 10.1039/c7cc09956h

[34]   S. Gómez-Coca, D. Aravena, R. Morales, E. Ruiz: Large magnetic anisotropy in mononuclear metal complexes, *Coord. Chem. Rev.* **2015**, *289-290*, 379-392. 10.1016/j.ccr.2015.01.021

[35]   G. Christou: Single-molecule magnets: a molecular approach to nanoscale magnetic materials, *Polyhedron* **2005**, *24*, 2065-2075. 10.1016/j.poly.2005.03.021

[36]   F. Neese, D. A. Pantazis: What is not required to make a single molecule magnet, *Faraday Discuss.* **2011**, *148*, 229-238. 10.1039/c005256f

[37]   J. Sievers: Asphericity of 4f-shells in their Hund's rule ground states, *Eur. Phys. J. B* **1982**, *45*, 289-296. 10.1007/bf01321865

[38]  B. Weber, *Koordinationschemie*, 1 ed., Springer Spektrum, Berlin, **2014**. 10.1007/978-3-642-41685-9

[39]  N. F. Chilton, S. K. Langley, B. Moubaraki, A. Soncini, S. R. Batten, K. S. Murray: Single molecule magnetism in a family of mononuclear β-diketonate lanthanide(iii) complexes: rationalization of magnetic anisotropy in complexes of low symmetry, *Chem. Sci.* **2013**, *4*, 1719-1730. 10.1039/c3sc22300k

[40]  N. F. Chilton, D. Collison, E. J. L. McInnes, R. E. P. Winpenny, A. Soncini: An electrostatic model for the determination of magnetic anisotropy in dysprosium complexes, *Nat. Commun.* **2013**, *4*, 2551. 10.1038/ncomms3551

[41]  D. Aravena, E. Ruiz: Shedding light on the single-molecule magnet behavior of mononuclear DyIII complexes, *Inorg. Chem.* **2013**, *52*, 13770-13778. 10.1021/ic402367c

[42]  N. Ishikawa, M. Sugita, T. Ishikawa, S.-y. Koshihara, Y. Kaizu: Mononuclear lanthanide complexes with a long magnetization relaxation time at high temperatures: A new category of magnets at the single-molecular level, *J. Phys. Chem. B* **2004**, *108*, 11265-11271. 10.1021/jp0376065

[43]  A. Abragam, B. Bleaney, *Electron paramagnetic resonance of transition ions*, Clarendon Press, Oxford, **1970**

[44]  G. Huang, C. Daiguebonne, G. Calvez, Y. Suffren, O. Guillou, T. Guizouarn, B. Le Guennic, O. Cador, K. Bernot: Strong Magnetic Coupling and Single-Molecule-Magnet Behavior in Lanthanide-TEMPO Radical Chains, *Inorg. Chem.* **2018**, *57*, 11044-11057. 10.1021/acs.inorgchem.8b01640

[45]  C. A. P. Goodwin, F. Ortu, D. Reta: Strangely attractive: Collaboration and feedback in the field of molecular magnetism, *Int. J. Quantum Chem* **2020**, *120*, 1-8. 10.1002/qua.26248

[46]  C. A. P. Goodwin, F. Ortu, D. Reta, N. F. Chilton, D. P. Mills: Molecular magnetic hysteresis at 60 kelvin in dysprosocenium, *Nature* **2017**, *548*, 439-442. 10.1038/nature23447

[47]  F.-S. Guo, B. M. Day, Y.-C. Chen, M.-L. Tong, A. Mansikkamäki, R. A. Layfield: A Dysprosium Metallocene Single-Molecule Magnet Functioning at the Axial Limit, *Angew. Chem. Int. Ed.* **2017**, *56*, 11445-11449. 10.1002/anie.201705426

[48]  K. R. McClain, C. A. Gould, K. Chakarawet, S. J. Teat, T. J. Groshens, J. R. Long, B. G. Harvey: High-temperature magnetic blocking and magneto-structural correlations in a series of dysprosium(III) metallocenium single-molecule magnets, *Chem. Sci.* **2018**, *9*, 8492-8503. 10.1039/C8SC03907K

[49]  F.-S. Guo, B. M. Day, Y.-C. Chen, M.-L. Tong, A. Mansikkamäki, R. A. Layfield: Magnetic hysteresis up to 80 kelvin in a dysprosium metallocene single-molecule magnet, *Science* **2018**, *362*, 1400-1403. 10.1126/science.aav0652

[50]  Y.-S. Ding, N. F. Chilton, R. E. P. Winpenny, Y.-Z. Zheng: On Approaching the Limit of Molecular Magnetic Anisotropy: A Near-Perfect Pentagonal Bipyramidal Dysprosium(III) Single-Molecule Magnet, *Angew. Chem. Int. Ed.* **2016**, *55*, 16071-16074. 10.1002/anie.201609685

[51]  M. J. Giansiracusa, A. K. Kostopoulos, D. Collison, R. E. P. Winpenny, N. F. Chilton: Correlating blocking temperatures with relaxation mechanisms in monometallic single-molecule magnets with high energy barriers (Ueff > 600 K), *Chem. Commun.* **2019**, *55*, 7025-7028. 10.1039/c9cc02421b

[52]  K. L. M. Harriman, D. Errulat, M. Murugesu: Magnetic Axiality: Design Principles from Molecules to Materials, *Trends in Chemistry* **2019**, *1*, 425-439. 10.1016/j.trechm.2019.04.005

[53]  J. M. Zadrozny, M. Atanasov, A. M. Bryan, C.-Y. Lin, B. D. Rekken, P. P. Power, F. Neese, J. R. Long: Slow magnetization dynamics in a series of two-

coordinate iron(II) complexes, *Chem. Sci.* **2013**, *4*, 125-138. 10.1039/c2sc20801f

[54] M. Gregson, N. F. Chilton, A.-M. Ariciu, F. Tuna, I. F. Crowe, W. Lewis, A. J. Blake, D. Collison, E. J. L. McInnes, R. E. P. Winpenny, S. T. Liddle: A monometallic lanthanide bis(methanediide) single molecule magnet with a large energy barrier and complex spin relaxation behaviour, *Chem. Sci.* **2016**, 7, 155-165. 10.1039/c5sc03111g

[55] Y. Rechkemmer, J. E. Fischer, R. Marx, M. Dörfel, P. Neugebauer, S. Horvath, M. Gysler, T. Brock-Nannestad, W. Frey, M. F. Reid, J. van Slageren: Comprehensive Spectroscopic Determination of the Crystal Field Splitting in an Erbium Single-Ion Magnet, *J. Am. Chem. Soc.* **2015**, *137*, 13114-13120. 10.1021/jacs.5b08344

[56] E. Lucaccini, M. Briganti, M. Perfetti, L. Vendier, J.-P. Costes, F. Totti, R. Sessoli, L. Sorace: Relaxation Dynamics and Magnetic Anisotropy in a Low-Symmetry DyIII Complex, *Chem. Eur. J.* **2016**, *22*, 5552-5562. 10.1002/chem.201505211

[57] V. S. Mironov, Y. G. Galyametdinov, A. Ceulemans, C. Görller-Walrand, K. Binnemans: Room-temperature magnetic anisotropy of lanthanide complexes: A model study for various coordination polyhedra, *J. Chem. Phys.* **2002**, *116*, 4673-4685. 10.1063/1.1450543

[58] J. Tang, P. Zhang, *Lanthanide Single Molecule Magnets*, Springer, Heidelberg, **2015**. 10.1007/978-3-662-46999-6-1

[59] A. Cornia, M. Mannini, in *Molecular Nanomagnets and Related Phenomena, Vol. 164* (Ed.: S. Gao), Springer, Berlin, **2014**, pp. 293-330. 10.1007/430_2014_150

[60] P. Norman, K. Ruud, T. Saue, *Principles and Practices of Molecular Properties: Theory, Modeling and Simulations*, 1. ed., John Wiley & Sons, Hoboken, **2018**. 10.1002/9781118794821

[61] D. Gatteschi, R. Sessoli, J. Villain, *Molecular Nanomagnets*, Oxford University Press, Oxford, **2006**. 10.1093/acprof:oso/9780198567530.001.0001

[62] J. Dreiser: Molecular lanthanide single-ion magnets: rom bulk to submonolayers, *J. Phys. Condens. Matter* **2015**, *27*, 183203. 10.1088/0953-8984/27/18/183203

[63] L. Escalera-Moreno, J. J. Baldoví, A. Gaita-Ariño, E. Coronado: Spin states, vibrations and spin relaxation in molecular nanomagnets and spin qubits: a critical perspective, *Chem. Sci.* **2018**, *9*, 3265-3275. 10.1039/c7sc05464e

[64] A. Lunghi, F. Totti, S. Sanvito, R. Sessoli: Intra-molecular origin of the spin-phonon coupling in slow-relaxing molecular magnets, *Chem. Sci.* **2017**, *8*, 6051-6059. 10.1039/c7sc02832f

[65] L. Gu, R. Wu: Theory of spin-lattice relaxation in single-molecule magnets: Reasons for the slowness, *Phys. Rev. Lett.* **2020**, *125*, 117203. 10.1103/PhysRevLett.125.117203

[66] S. A. Cotton, P. R. Raithby: Systematics and surprises in lanthanide coordination chemistry, *Coord. Chem. Rev.* **2017**, *340*, 220-231. 10.1016/j.ccr.2017.01.011

[67] S. F. A. Kettle, *Symmetry and Structure: Readable Group Theory for Chemists*, 3. ed., John Wiley & Sons, Chichester, **2007**

[68] B. G. Wybourne, *Spectroscopic Properties of Rare Earths*, Interscience, New York, **1965**

[69] Y.-C. Chen, J.-L. Liu, L. Ungur, J. Liu, Q.-W. Li, L.-F. Wang, Z.-P. Ni, L. F. Chibotaru, X.-M. Chen, M.-L. Tong: Symmetry-Supported Magnetic Blocking at

20 K in Pentagonal Bipyramidal Dy(III) Single-Ion Magnets, *J. Am. Chem. Soc.* **2016**, *138*, 2829-2837. 10.1021/jacs.5b13584

[70] A. De Cian, M. Moussavi, J. Fischer, R. Weiss: Synthesis, Structure, and Spectroscopic and Magnetic Properties of Lutetium(III) Phthalocyanine Derivatives: LuPc2CH2Cl2 and [LuPc(OAc)(H20)2]H20-2CH3OH, *Inorg. Chem.* **1985**, *24*, 3162-3167. 10.1021/ic00214a016

[71] H. Konami, M. Hatano, A. Tajiri: An analysis of paramagnetic shifts in proton NMR spectra of non-radical lanthanide(III)-phthalocyanine sandwich complexes, *Chem. Phys. Lett.* **1989**, *160*, 163-167. 10.1016/0009-2614(89)87576-1

[72] N. Ishikawa, M. Sugita, T. Okubo, N. Tanaka, T. Iino, Y. Kaizu: Determination of Ligand-Field Parameters and f-Electronic Structures of Double-Decker Bis(phthalocyaninato)lanthanide Complexes, *Inorg. Chem.* **2003**, *42*, 2440-2446. 10.1021/ic026295u

[73] N. Ishikawa, T. Iino, Y. Kaizu: Interaction between f-electronic systems in dinuclear lanthanide complexes with phthalocyanines, *J. Am. Chem. Soc.* **2002**, *124*, 11440-11447. 10.1021/ja027119n

[74] N. Ishikawa, T. Iino, Y. Kaizu: Determination of Ligand-Field Parameters and f-Electronic Structures of Hetero-Dinuclear Phthalocyanine Complexes with a Diamagnetic Yttrium(III) and a Paramagnetic Trivalent Lanthanide Ion, *J. Phys. Chem. A* **2002**, *106*, 9543-9550. 10.1021/jp0209244

[75] M. A. AlDamen, S. Cardona-Serra, J. M. Clemente-Juan, E. Coronado, A. Gaita-Ariño, C. Martí-Gastaldo, F. Luis, O. Montero: Mononuclear Lanthanide Single Molecule Magnets Based on the Polyoxometalates [Ln(W5O18)2]9- and [Ln(β2-SiW11O39)2]13- (LnIII = Tb, Dy, Ho, Er, Tm, and Yb), *Inorg. Chem.* **2009**, *48*, 3467-3479. 10.1021/ic801630z

[76] S. Takamatsu, T. Ishikawa, S.-y. Koshihara, N. Ishikawa: Significant increase of the barrier energy for magnetization reversal of a single-4f-ionic single-molecule magnet by a longitudinal contraction of the coordination space, *Inorg. Chem.* **2007**, *46*, 7250-7252. 10.1021/ic700954t

[77] S. Takamatsu, N. Ishikawa: A theoretical study of a drastic structural change of bis(phthalocyaninato)lanthanide by ligand oxidation: Towards control of ligand field strength and magnetism of single-lanthanide-ionic single molecule magnet, *Polyhedron* **2007**, *26*, 1859-1862. 10.1016/j.poly.2006.09.020

[78] M. Gonidec, R. Biagi, V. Corradini, F. Moro, V. De Renzi, U. del Pennino, D. Summa, L. Muccioli, C. Zannoni, D. B. Amabilino, J. Veciana: Surface supramolecular organization of a terbium(III) double-decker complex on graphite and its single molecule magnet behavior, *J. Am. Chem. Soc.* **2011**, *133*, 6603-6612. 10.1021/ja109296c

[79] A. M. J. Lees, A. W. G. Platt: Complexes of lanthanide chlorides with tricyclohexylphosphine oxide. the single crystal X-ray structures and solution properties of pentagonal bipyramidal complexes [Ln(H2O)5(Cy3PO)2]3+·Cy3PO·3Cl- Ln = Dy, Er, *Polyhedron* **2014**, *67*, 368-372. 10.1016/j.poly.2013.09.026

[80] S. K. Gupta, T. Rajeshkumar, G. Rajaraman, R. Murugavel: An air-stable Dy(III) single-ion magnet with high anisotropy barrier and blocking temperature, *Chem. Sci.* **2016**, *7*, 5181-5191. 10.1039/c6sc00279j

[81] J. Liu, Y.-C. Chen, J.-L. Liu, V. Vieru, L. Ungur, J.-H. Jia, L. F. Chibotaru, Y. Lan, W. Wernsdorfer, S. Gao, X.-M. Chen, M.-L. Tong: A Stable Pentagonal Bipyramidal Dy(III) Single-Ion Magnet with a Record Magnetization Reversal

Barrier over 1000 K, *J. Am. Chem. Soc.* **2016**, *138*, 5441-5450. 10.1021/jacs.6b02638

[82] J.-L. Liu, J.-Y. Wu, Y.-C. Chen, V. Mereacre, A. K. Powell, L. Ungur, L. F. Chibotaru, X.-M. Chen, M.-L. Tong: A Heterometallic FeII–DyIII Single-Molecule Magnet with a Record Anisotropy Barrier, *Angew. Chem. Int. Ed.* **2014**, *53*, 12966-12970. 10.1002/anie.201407799

[83] A. B. Canaj, S. Dey, C. Wilson, O. Céspedes, G. Rajaraman, M. Murrie: Engineering macrocyclic high performance pentagonal bipyramidal Dy(III) single-ion magnets, *Chem. Commun.* **2020**, *56*, 12037-12040. 10.1039/d0cc04559d

[84] A. B. Canaj, S. Dey, E. R. Martí, C. Wilson, G. Rajaraman, M. Murrie: Insight into D6h Symmetry: Targeting Strong Axiality in Stable Dysprosium(III) Hexagonal Bipyramidal Single-Ion Magnets, *Angew. Chem. Int. Ed.* **2019**, *58*, 14146-14151. 10.1002/anie.201907686

[85] Y.-N. Guo, G.-F. Xu, W. Wernsdorfer, L. Ungur, Y. Guo, J. Tang, H.-J. Zhang, L. F. Chibotaru, A. K. Powell: Strong Axiality and Ising Exchange Interaction Suppress Zero-Field Tunneling of Magnetization of an Asymmetric Dy2 Single-Molecule Magnet, *J. Am. Chem. Soc.* **2011**, *133*, 11948-11951. 10.1021/ja205035g

[86] L. F. Chibotaru, N. Iwahara: Ising exchange interaction in lanthanides and actinides, *New J. Phys.* **2015**, *17*, 103028. 10.1088/1367-2630/17/10/103028

[87] T. Rajeshkumar, G. Rajaraman: Is a radical bridge a route to strong exchange interactions in lanthanide complexes? A computational examination, *Chem. Commun.* **2012**, *48*, 7856-7858. 10.1039/c2cc33483f

[88] J. D. Rinehart, M. Fang, W. J. Evans, J. R. Long: Strong exchange and magnetic blocking in N23--radical-bridged lanthanide complexes, *Nat. Chem.* **2011**, *3*, 538-542. 10.1038/nchem.1063

[89] Y.-Q. Zhang, C.-L. Luo, B.-W. Wang, S. Gao: Understanding the Magnetic Anisotropy in a Family of N23- Radical-Bridged Lanthanide Complexes: Density Functional Theory and ab Initio Calculations, *J. Phys. Chem. A* **2013**, *117*, 10873-10880. 10.1021/jp4044495

[90] J. D. Rinehart, M. Fang, W. J. Evans, J. R. Long: A N23- Radical-Bridged Terbium Complex Exhibiting Magnetic Hysteresis at 14 K, *J. Am. Chem. Soc.* **2011**, *133*, 14236-14239. 10.1021/ja206286h

[91] S. Demir, J. M. Zadrozny, M. Nippe, J. R. Long: Exchange coupling and magnetic blocking in bipyrimidyl radical-bridged dilanthanide complexes, *J. Am. Chem. Soc.* **2012**, *134*, 18546-18549. 10.1021/ja308945d

[92] F.-S. Guo, R. A. Layfield: Strong direct exchange coupling and single-molecule magnetism in indigo-bridged lanthanide dimers, *Chem. Commun.* **2017**, *53*, 3130-3133. 10.1039/c7cc01046j

[93] L. Ungur, L. F. Chibotaru: Magnetic anisotropy in the excited states of low symmetry lanthanide complexes, *Phys. Chem. Chem. Phys.* **2011**, *13*, 20086-20090. 10.1039/c1cp22689d

[94] R. F. Pfleger, Master thesis, Karlsruhe Institute of Technology (Karlsruhe), **2016**.

[95] S. Schmidt, PhD thesis, Karlsruhe Institute of Technology (Karlsruhe), **2016**. 10.5445/ir/1000068450

[96] E. L. Gavey, Y. Beldjoudi, J. M. Rawson, T. C. Stamatatos, M. Pilkington: Slow relaxation in the first penta-aza Dy(III) macrocyclic complex, *Chem. Commun.* **2014**, *50*, 3741-3743. 10.1039/c4cc00930d

[97] Y. Gil, P. Fuentealba, A. Vega, E. Spodine, D. Aravena: Control of magnetic anisotropy by macrocyclic ligand distortion in a family of Dy(III) and Er(III) single molecule magnets, *Dalton Trans.* **2020**, *49*, 17709-17718. 10.1039/d0dt03370g

[98] J. D. Curry, M. A. Robinson, D. H. Busch: Metal Complexes Derived from Substituted Hydrazones of 2,6-Diacetylpyridine, *Inorg. Chem.* **1967**, *6*, 1570-1574. 10.1021/ic50054a032

[99] D. Wester, G. J. Palenik: Pentagonal-Bipyramidal Complexes. Synthesis and Characterization of Cobalt(II) and Zinc(II) Complexes of Neutral and Dianionic 2,6-Diacetylpyridinebis(2′-pyridylhydrazone), *Inorg. Chem.* **1976**, *15*, 755-761. 10.1021/ic50158a002

[100] M. Sakamoto, N. Matsumoto, H. Okawa: Synthesis and Molecular Structure of Europium(III) Complex with 2,6-Diacetylpyridine Bis(2-pyridylhydrazone), *Bull. Chem. Soc. Jpn.* **1991**, *64*, 691-693. 10.1246/bcsj.64.691

[101] Z.-X. Jiang, J.-L. Liu, Y.-C. Chen, J. Liu, J.-H. Jia, M.-L. Tong: Lanthanoid single-ion magnets with the LnN10 coordination geometry, *Chem. Commun.* **2016**, *52*, 6261-6264. 10.1039/c6cc01695b

[102] E. C. Constable, in *Prog. Inorg. Chem., Vol. 42*, Interscience, New York, **1994**, pp. 67-138. 10.1002/9780470166437.ch2

[103] R. H. Martin: The Helicenes, *Angew. Chem. Int. Ed.* **1974**, *13*, 649-660. 10.1002/anie.197406491

[104] R. Hoffmann: An Extended Hückel Theory. I. Hydrocarbons, *J. Chem. Phys.* **1963**, *39*, 1397-1412. 10.1063/1.1734456

[105] C. C. Addison, N. Logan, S. C. Wallwork, C. D. Garner: Structural Aspects of Co-ordinated Nitrate Groups, *Chem. Soc. Rev.* **1971**, *25*, 289-322. 10.1039/qr9712500289

[106] T. J. Mooibroek: Coordinated nitrate anions can be directional π-hole donors in the solid state: a CSD study, *CrystEngComm* **2017**, *19*, 4485-4488. 10.1039/c7ce01266g

[107] M. Llunell, D. Casanova, J. Cirera, P. Alemany, S. Alvarez, *Shape: Program for the Stereochemical Analysis of Molecular Fragments by Means of Continuous Shape Measures and Associated Tools - Version 2.1*, Universitat de Barcelona, Barcelona, **2013**

[108] C. Rudowicz, J. Qin: Can the low symmetry crystal (ligand) field parameters be considered compatible and reliable?, *J. Lumin.* **2004**, *110*, 39-64. 10.1016/j.jlumin.2004.04.003

[109] L. Ungur, L. F. Chibotaru: Ab Initio Crystal Field for Lanthanides, *Chem. Eur. J.* **2017**, *23*, 3708-3718. 10.1002/chem.201605102

[110] Y.-S. Meng, S.-D. Jiang, B.-W. Wang, S. Gao: Understanding the Magnetic Anisotropy toward Single-Ion Magnets, *Acc. Chem. Res.* **2016**, *49*, 2381-2389. 10.1021/acs.accounts.6b00222

[111] M. Fondo, J. Corredoira-Vázquez, A. M. García-Deibe, J. Sanmartín-Matalobos, J. M. Herrera, E. Colacio: Designing Ligands to Isolate ZnLn and Zn2Ln Complexes: Field-Induced Single-Ion Magnet Behavior of the ZnDy, Zn2Dy, and Zn2Er Analogues, *Inorg. Chem.* **2017**, *56*, 5646-5656. 10.1021/acs.inorgchem.7b00165

[112] C. Das, A. Upadhyay, M. Shanmugam: Influence of Radicals on Magnetization Relaxation Dynamics of Pseudo-Octahedral Lanthanide Iminopyridyl Complexes, *Inorg. Chem.* **2018**, *57*, 9002-9011. 10.1021/acs.inorgchem.8b00979

[113] M. Fondo, J. Corredoira-Vázquez, A. M. García-Deibe, J. Sanmartín-Matalobos, J. M. Herrera, E. Colacio: Tb2, Dy2, and Zn2Dy4 Complexes Showing the

Unusual Versatility of a Hydrazone Ligand toward Lanthanoid Ions: a Structural and Magnetic Study, *Inorg. Chem.* **2018**, *57*, 10100-10110. 10.1021/acs.inorgchem.8b01251

[114] S. Yu, Z. Hu, Z. Chen, B. Li, Y.-Q. Zhang, Y. Liang, D. Liu, D. Yao, F. Liang: Two Dy(III) Single-Molecule Magnets with Their Performance Tuned by Schiff Base Ligands, *Inorg. Chem.* **2019**, *58*, 1191-1200. 10.1021/acs.inorgchem.8b02637

[115] S.-Y. Lin, W. Wernsdorfer, L. Ungur, A. K. Powell, Y.-N. Guo, J. Tang, L. Zhao, L. F. Chibotaru, H.-J. Zhang: Coupling Dy3 triangles to maximize the toroidal moment, *Angew. Chem. Int. Ed.* **2012**, *51*, 12767-12771. 10.1002/anie.201206602

[116] M. Fondo, J. Corredoira-Vázquez, A. Herrera-Lanzós, A. M. García-Deibe, J. Sanmartín-Matalobos, J. M. Herrera, E. Colacio, C. Nuñez: Improving the SMM and luminescence properties of lanthanide complexes with LnO9 cores in the presence of ZnII: an emissive Zn2Dy single ion magnet, *Dalton Trans.* **2017**, *46*, 17000-17009. 10.1039/c7dt03438e

[117] M. Fondo, J. Corredoira-Vázquez, A. M. García-Deibe, S. Gómez-Coca, E. Ruiz, J. Sanmartín-Matalobos: Dysprosium-based complexes with a flat pentadentate donor: a magnetic and ab initio study, *Dalton Trans.* **2020**, *49*, 8389-8401. 10.1039/d0dt01293a

[118] S. K. Malik, R. Vijayaraghavan: Crystal field effects on the saturation magnetic moment of Sm3+ ion in ferronagmetic samarium compounds, *Pramana* **1974**, *3*, 122-132. 10.1007/bf02847119

[119] M. Kanesato, S. Mizukami, H. Houjou, H. Tokuhisa, E. Koyama, Y. Nagawa: Comparison of the bond lengths for the lanthanide complexes of tripodal heptadentate ligands, *J. Alloys Compd.* **2004**, *374*, 307-310. 10.1016/j.jallcom.2003.11.096

[120] M. Seitz, A. G. Oliver, K. N. Raymond: The lanthanide contraction revisited, *J. Am. Chem. Soc.* **2007**, *129*, 11153-11160. 10.1021/ja072750f

[121] S. E. Harris, A. G. Orpen, I. J. Bruno, R. Taylor: Factors Affecting d-block Metal–Ligand Bond Lengths: Toward an Automated Library of Molecular Geometry for Metal Complexes, *J. Chem. Inf. Model.* **2005**, *45*, 1727-1748. 10.1021/ci0500785

[122] C. A. Thuesen, K. S. Pedersen, M. Schau-Magnussen, M. Evangelisti, J. Vibenholt, S. Piligkos, H. Weihe, J. Bendix: Fluoride-bridged {Ln2Cr2} polynuclear complexes from semi-labile mer-[CrF3(py)3] and [Ln(hfac)3(H2O)2], *Dalton Trans.* **2012**, *41*, 11284-11292. 10.1039/c2dt31302b

[123] Q. Zhou, F. Yang, D. Liu, Y. Peng, G. Li, Z. Shi, S. Feng: Synthesis, Structures, and Magnetic Properties of Three Fluoride-Bridged Lanthanide Compounds: Effect of Bridging Fluoride Ions on Magnetic Behaviors, *Inorg. Chem.* **2012**, *51*, 7529-7536. 10.1021/ic300125y

[124] L. E. Sweet, J. F. Corbey, F. Gendron, J. Autschbach, B. K. McNamara, K. L. Ziegelgruber, L. M. Arrigo, S. M. Peper, J. M. Schwantes: Structure and Bonding Investigation of Plutonium Peroxocarbonate Complexes Using Cerium Surrogates and Electronic Structure Modeling, *Inorg. Chem.* **2017**, *56*, 791-801. 10.1021/acs.inorgchem.6b02235

[125] M. Xémard, V. Goudy, A. Braun, M. Tricoire, M. Cordier, L. Ricard, L. Castro, E. Louyriac, C. E. Kefalidis, C. Clavaguéra, L. Maron, G. Nocton: Reductive Disproportionation of CO2 with Bulky Divalent Samarium Complexes, *Organometallics* **2017**, *36*, 4660-4668. 10.1021/acs.organomet.7b00630

[126] X. Zhang, G. R. Loppnow, R. McDonald, J. Takats: {HB(3,5-Me2pz)3}2Sm(η2-O2): First Example of a Lanthanide Superoxo Complex, *J. Am. Chem. Soc.* **1995**, *117*, 7828-7829. 10.1021/ja00134a037

[127] N.-P. Pook, A. Adam: Synthesis, Crystal Structure, and Vibrational Spectra of Five Novel Peroxidocerates(IV) and the Occurrence of a New Complex Unit in K8[Ce2(O2)3(NTA)2]2·20H2O, *Z. Anorg. Allg. Chem.* **2014**, *640*, 2931-2938. 10.1002/zaac.201400376

[128] A. Mustapha, J. Reglinski, A. R. Kennedy: The use of hydrogenated Schiff base ligands in the synthesis of multi-metallic compounds, *Inorg. Chim. Acta* **2009**, *362*, 1267-1274. 10.1016/j.ica.2008.06.026

[129] W. Radecka-Paryzek, V. Patroniak, M. Kubicki: First example of template synthesis of pentaaza macrocyclic ytterbium(III) complex and solvent-controlled supramolecular self-assembly of its dimeric μ-η2:η2 peroxo-bridged derivative, *Inorg. Chem. Commun.* **2004**, *7*, 455-458. 10.1016/j.inoche.2003.12.035

[130] Y.-L. Sang, X.-S. Lin, X.-C. Li, Y.-H. Liu, X.-H. Zhang: Synthesis, crystal structure and antibacterial activity of a novel phenolato- and peroxo-bridged dinuclear cerium(IV) complex with tripodal Schiff bases, *Inorg. Chem. Commun.* **2015**, *62*, 115-118. 10.1016/j.inoche.2015.11.003

[131] D. M. Roitershtein, A. A. Vinogradov, K. A. Lyssenko, I. E. Nifant'ev: Self-assembly of heteroleptic tetranuclear carboxylate complexes of yttrium and lanthanides during hydrolysis and oxidation of rare earth homoleptic carboxylates, *Inorg. Chem. Commun.* **2017**, *84*, 225-228. 10.1016/j.inoche.2017.08.031

[132] M. Niemeyer: Synthesis and Structural Characterization of Several Ytterbium Bis(trimethylsilyl)amides Including Base-free [Yb{N(SiMe3)2}2(μ-Cl)]2 — A Coordinatively Unsaturated Complex with Additional Agostic Yb···(H3C—Si) Interactions, *Z. Anorg. Allg. Chem.* **2002**, *628*, 647-657. 10.1002/1521-3749(200203)628:3<647::Aid-zaac647>3.0.Co;2-l

[133] B. Neumüller, F. Weller, T. Gröb, K. Dehnicke: Lanthanoid-Peroxo-Komplexe mit μ3-η2:η2:η2-(O22—)-Koordination. Die Kristallstrukturen von [Ln4(O2)2Cl8(Py)10] · Py mit Ln = Sm, Eu, Gd, *Z. Anorg. Allg. Chem.* **2002**, *628*, 2365-2371. 10.1002/1521-3749(200211)628:11<2365::Aid-zaac2365>3.0.Co;2-s

[134] V. Patroniak, M. Kubicki, W. Radecka-Paryzek: The First Example of μ-η2:η2-Peroxo-Bridged Macrocyclic Lanthanide Complex. The Crystal Structure of [Lu2{Me2pyo[16]trieneN5}2(μ-η2:η2-O2)Cl2](ClO4)2 Dioxane Solvate, *J. Incl. Phenom. Macrocycl. Chem.* **2004**, *49*, 121-125. 10.1023/b:Jiph.0000031124.82412.40

[135] N. J. C. van Velzen, S. Harder: Deca-Arylsamarocene: An Unusually Inert Sm(II) Sandwich Complex, *Organometallics* **2018**, *37*, 2263-2271. 10.1021/acs.organomet.8b00254

[136] M. P. Coles, P. B. Hitchcock, A. V. Khvostov, M. F. Lappert, Z. Li, A. V. Protchenko: Crystalline amidocerium(iv) oxides and a side-on bridging dioxygen complex, *Dalton Trans.* **2010**, *39*, 6780-6788. 10.1039/c0dt00349b

[137] G. B. Deacon, C. M. Forsyth, D. Freckmann, P. C. Junk, K. Konstas, J. Luu, G. Meyer, D. Werner: Adventitiously Obtained Rare-Earth Peroxide Complexes and Their Structural Characterisation, *Aust. J. Chem.* **2014**, *67*, 1860-1865. 10.1071/Ch14410

[138] G.-C. Wang, Y.-M. So, K.-L. Wong, K.-C. Au-Yeung, H. H.-Y. Sung, I. D. Williams, W.-H. Leung: Synthesis, Structure, and Reactivity of a Tetranuclear Cerium(IV) Oxo Cluster Supported by the Kläui Tripodal Ligand [Co(η5-

C5H5){P(O)(OEt)2}3]-, *Chem. Eur. J.* **2015**, *21*, 16126-16135. 10.1002/chem.201502173

[139] M. Paul, S. Shirase, Y. Morimoto, L. Mathey, B. Murugesapandian, S. Tanaka, S. Itoh, H. Tsurugi, K. Mashima: Cerium-Complex-Catalyzed Oxidation of Arylmethanols under Atmospheric Pressure of Dioxygen and Its Mechanism through a Side-On µ-Peroxo Dicerium(IV) Complex, *Chem. Eur. J.* **2016**, *22*, 4008-4014. 10.1002/chem.201503846

[140] D. C. Bradley, J. S. Ghotra, F. A. Hart, M. B. Hursthouse, P. R. Raithby: Low Co-ordination Numbers in Lanthanoid and Actinoid Compounds. Part 2. Syntheses, Properties, and Crystal and Molecular Structures of Triphenylphosphine Oxide and Peroxo-derivatives of [bis(trimethylsilyl)amido]lanthanoids, *Dalton Trans.* **1977**, 1166-1172. 10.1039/dt9770001166

[141] G.-C. Wang, H. H. Y. Sung, I. D. Williams, W.-H. Leung: Tetravalent Titanium, Zirconium, and Cerium Oxo and Peroxo Complexes Containing an Imidodiphosphinate Ligand, *Inorg. Chem.* **2012**, *51*, 3640-3647. 10.1021/ic202564h

[142] W. J. Gee, J. G. MacLellan, C. M. Forsyth, B. Moubaraki, K. S. Murray, P. C. Andrews, P. C. Junk: Caging Peroxide: Anion-Templated Synthesis and Characterization of a Rare-Earth Cluster, *Inorg. Chem.* **2012**, *51*, 8661-8663. 10.1021/ic301382r

[143] V. Patroniak, M. Kubicki, A. Mondry, J. Lisowski, W. Radecka-Paryzek: Pentaaza macrocyclic ytterbium(III) complex and solvent controlled supramolecular self-assembly of its dimeric µ-η2:η2 peroxo-bridged derivatives, *Dalton Trans.* **2004**, *20*, 3295-3304. 10.1039/b408157a

[144] Y. Huo, Y.-C. Chen, S.-G. Wu, J.-L. Liu, J.-H. Jia, W.-B. Chen, B.-L. Wang, Y.-Q. Zhang, M.-L. Tong: Effect of Bridging Ligands on Magnetic Behavior in Dinuclear Dysprosium Cores Supported by Polyoxometalates, *Inorg. Chem.* **2019**, *58*, 1301-1308. 10.1021/acs.inorgchem.8b02788

[145] K. Griffiths, J. Mayans, M. A. Shipman, G. J. Tizzard, S. J. Coles, B. A. Blight, A. Escuer, G. E. Kostakis: Four New Families of Polynuclear Zn-Ln Coordination Clusters. Synthetic, Topological, Magnetic, and Luminescent Aspects, *Cryst. Growth Des.* **2017**, *17*, 1524-1538. 10.1021/acs.cgd.6b01401

[146] X.-T. Wang, H.-M. Dong, X.-G. Wang, E.-C. Yang, X.-J. Zhao: Two Oxime-Based {LnIII3NiII3} Clusters with Triangular {Ln3(µ3-O2)}7+Core: Solvothermal Syntheses, Crystal Structures, and Magnetic Properties, *Z. Anorg. Allg. Chem.* **2016**, *642*, 1166-1172. 10.1002/zaac.201600253

[147] Y. Zhang, J. Wu, S. Shen, Z. Liu, J. Tang: Coupling Dy3 triangles into hexanuclear dysprosium(III) clusters: Syntheses, structures and magnetic properties, *Polyhedron* **2018**, *150*, 40-46. 10.1016/j.poly.2018.04.042

[148] H. Ke, X. Lu, W. Wei, W. Wang, G. Xie, S. Chen: Unusual undecanuclear heterobimetallic Zn4Ln7 (Ln = Gd, Dy) nano-sized clusters encapsulating two peroxide anions through spontaneous intake of dioxygen, *Dalton Trans.* **2017**, *46*, 8138-8145. 10.1039/c7dt01501a

[149] B.-K. Ling, Y.-Q. Zhai, J. Han, T. Han, Y.-Z. Zheng: A stable dysprosium(iii) complex with a terminal fluoride ligand showing high resolution luminescence and slow magnetic relaxation, *Dalton Trans.* **2020**, *49*, 6969-6973. 10.1039/d0dt01146k

[150] G. Brunet, F. Habib, I. Korobkov, M. Murugesu: Slow Magnetic Relaxation Observed in Dysprosium Compounds Containing Unsupported Near-Linear

Hydroxo- and Fluoro-Bridges, *Inorg. Chem.* **2015**, *54*, 6195-6202. 10.1021/acs.inorgchem.5b00343

[151]  L. Norel, L. E. Darago, B. Le Guennic, K. Chakarawet, M. I. Gonzalez, J. H. Olshansky, S. Rigaut, J. R. Long: A Terminal Fluoride Ligand Generates Axial Magnetic Anisotropy in Dysprosium Complexes, *Angew. Chem. Int. Ed.* **2018**, *57*, 1933-1938. 10.1002/anie.201712139

[152]  J. Dreiser, K. S. Pedersen, C. Piamonteze, S. Rusponi, Z. Salman, M. E. Ali, M. Schau-Magnussen, C. A. Thuesen, S. Piligkos, H. Weihe, H. Mutka, O. Waldmann, P. Oppeneer, J. Bendix, F. Nolting, H. Brune: Direct observation of a ferri-to-ferromagnetic transition in a fluoride-bridged 3d-4f molecular cluster, *Chem. Sci.* **2012**, *3*, 1024-1032. 10.1039/c2sc00794k

[153]  Y.-Z. Ma, L.-M. Zhang, G. Peng, C.-J. Zhao, R.-T. Dong, C.-F. Yang, H. Deng: A series of three-dimensional 3d-4f cyanide heterometallic coordination polymers: synthesis, crystal structure, photoluminescent and magnetic properties, *CrystEngComm* **2014**, *16*, 667-683. 10.1039/c3ce42025f

[154]  S. K. Langley, C. M. Forsyth, B. Moubaraki, K. S. Murray: A fluoride bridged {CrIII4DyIII4} single molecule magnet, *Dalton Trans.* **2015**, *44*, 912-915. 10.1039/c4dt03100h

[155]  A. B. Canaj, M. K. Singh, E. Regincós Marti, M. Damjanović, C. Wilson, O. Céspedes, W. Wernsdorfer, G. Rajaraman, M. Murrie: Boosting axiality in stable high-coordinate Dy(iii) single-molecule magnets, *Chem. Commun.* **2019**, *55*, 5950-5953. 10.1039/c9cc00965e

[156]  K. R. Vignesh, S. K. Langley, K. S. Murray, G. Rajaraman: Quenching the Quantum Tunneling of Magnetization in Heterometallic Octanuclear {TMIII4DyIII4} (TM=Co and Cr) Single-Molecule Magnets by Modification of the Bridging Ligands and Enhancing the Magnetic Exchange Coupling, *Chem. Eur. J.* **2017**, *23*, 1654-1666. 10.1002/chem.201604835

[157]  C. Kölmel, C. Ochsenfeld, R. Ahlrichs: An ab initio investigation of structure and inversion barrier of triisopropylamine and related amines and phosphines, *Theor. Chem. Acc.* **1992**, *82*, 271-284. 10.1007/bf01113258

[158]  M. Gingras, G. Félix, R. Peresutti: One hundred years of helicene chemistry. Part 2: stereoselective syntheses and chiral separations of carbohelicenes, *Chem. Soc. Rev.* **2013**, *42*, 1007-1050. 10.1039/c2cs35111k

[159]  S. Alvarez: A cartography of the van der Waals territories, *Dalton Trans.* **2013**, *42*, 8617-8636. 10.1039/c3dt50599e

[160]  B. Cordero, V. Gómez, A. E. Platero-Prats, M. Revés, J. Echeverría, E. Cremades, F. Barragán, S. Alvarez: Covalent radii revisited, *Dalton Trans.* **2008**, 2832-2838. 10.1039/b801115j

[161]  G. Abbas, Y. Lan, G. Kostakis, C. E. Anson, A. K. Powell: An investigation into lanthanide–lanthanide magnetic interactions in a series of [Ln2(mdeaH2)2(piv)6] dimers, *Inorg. Chim. Acta* **2008**, *361*, 3494-3499. 10.1016/j.ica.2008.03.024

[162]  W. R. Busing, H. A. Levy: Crystal and Molecular Structure of Hydrogen Peroxide : A Neutron-Diffraction Study, *J. Chem. Phys.* **1965**, *42*, 3054-3059. 10.1063/1.1696379

[163]  F. Fehér, I. Von Wilucki, G. Dost: Beiträge zur Kenntnis des Wasserstoffperoxyds und seiner Derivate, VII. Mitteil.: Über die Kristallstruktur des Lithiumperoxyds, Li2O2, *Chem. Ber.* **1953**, *86*, 1429-1437. 10.1002/cber.19530861111

[164]  H. Föppl: Die Kristallstrukturen der Alkaliperoxyde, *Z. Anorg. Allg. Chem.* **1957**, *291*, 12-50. 10.1002/zaac.19572910104

[165] L. Gu, R. Wu: Origin of the anomalously low Raman exponents in single molecule magnets, *Phys. Rev. B* **2021**, *103*, 1-24. 10.1103/PhysRevB.103.014401

[166] S. K. Langley, K. R. Vignesh, K. Holton, S. Benjamin, G. B. Hix, W. Phonsri, B. Moubaraki, K. S. Murray, G. Rajaraman: Mononuclear Dysprosium(III) Complexes with Triphenylphosphine Oxide Ligands: Controlling the Coordination Environment and Magnetic Anisotropy, *Inorganics* **2018**, *6*, 1-17. 10.3390/inorganics6020061

[167] M. Li, H. Wu, Z. Xia, L. Ungur, D. Liu, L. F. Chibotaru, H. Ke, S. Chen, S. Gao: An Inconspicuous Six-Coordinate Neutral DyIII Single-Ion Magnet with Remarkable Magnetic Anisotropy and Stability, *Inorg. Chem.* **2020**, *59*, 7158-7166. 10.1021/acs.inorgchem.0c00616

[168] K. R. Vignesh, D. I. Alexandropoulos, H. Xie, K. R. Dunbar: Six-coordinate mononuclear dysprosium(iii) single-molecule magnets with the triphenylphosphine oxide ligand, *Dalton Trans.* **2020**, *49*, 4694-4698. 10.1039/d0dt00801j

[169] K. N. Shrivastava: Theory of Spin–Lattice Relaxation, *Phys. Status Solidi B* **1983**, *117*, 437-458. 10.1002/pssb.2221170202

[170] S.-S. Liu, Y.-S. Meng, Y.-Q. Zhang, Z.-S. Meng, K. Lang, Z.-L. Zhu, C.-F. Shang, B.-W. Wang, S. Gao: A Six-Coordinate Dysprosium Single-Ion Magnet with Trigonal-Prismatic Geometry, *Inorg. Chem.* **2017**, *56*, 7320-7323. 10.1021/acs.inorgchem.7b00952

[171] L. Scherthan, R. F. Pfleger, H. Auerbach, T. Hochdörffer, J. A. Wolny, W. Bi, J. Zhao, M. Y. Hu, E. E. Alp, C. E. Anson, R. Diller, A. K. Powell, V. Schünemann: Exploring the Vibrational Side of Spin-Phonon Coupling in Single-Molecule Magnets via 161Dy Nuclear Resonance Vibrational Spectroscopy, *Angew. Chem. Int. Ed.* **2020**, *59*, 8818-8822. 10.1002/anie.201914728

[172] M. J. Martínez-Pérez, S. Cardona-Serra, C. Schlegel, F. Moro, P. J. Alonso, H. Prima-García, J. M. Clemente-Juan, M. Evangelisti, A. Gaita-Ariño, J. Sesé, J. van Slageren, E. Coronado, F. Luis: Gd-Based Single-Ion Magnets with Tunable Magnetic Anisotropy: Molecular Design of Spin Qubits, *Phys. Rev. Lett.* **2012**, *108*, 247213. 10.1103/PhysRevLett.108.247213

[173] R. J. Holmberg, L. T. A. Ho, L. Ungur, I. Korobkov, L. F. Chibotaru, M. Murugesu: Observation of unusual slow-relaxation of the magnetisation in a Gd-EDTA chelate, *Dalton Trans.* **2015**, *44*, 20321-20325. 10.1039/c5dt04072h

[174] T. Yoshida, G. Cosquer, D. C. Izuogu, H. Ohtsu, M. Kawano, Y. Lan, W. Wernsdorfer, H. Nojiri, B. K. Breedlove, M. Yamashita: Field-Induced Slow Magnetic Relaxation of GdIII Complex with a Pt−Gd Heterometallic Bond, *Chem. Eur. J.* **2017**, *23*, 4551-4556. 10.1002/chem.201700886

[175] D. C. Izuogu, T. Yoshida, H. Zhang, G. Cosquer, K. Katoh, S. Ogata, M. Hasegawa, H. Nojiri, M. Damjanović, W. Wernsdorfer, T. Uruga, T. Ina, B. K. Breedlove, M. Yamashita: Slow Magnetic Relaxation in a Palladium–Gadolinium Complex Induced by Electron Density Donation from the Palladium Ion, *Chem. Eur. J.* **2018**, *24*, 9285-9294. 10.1002/chem.201800699

[176] Y.-C. Chen, Y.-Y. Peng, J.-L. Liu, M.-L. Tong: Field-induced slow magnetic relaxation in a mononuclear Gd(III) complex, *Inorg. Chem. Commun.* **2019**, *107*, 107449. 10.1016/j.inoche.2019.107449

[177] G. Handzlik, M. Magott, M. Arczyński, A. M. Sheveleva, F. Tuna, M. Sarewicz, A. Osyczka, M. Rams, V. Vieru, L. F. Chibotaru, D. Pinkowicz: Magnetization Dynamics and Coherent Spin Manipulation of a Propeller Gd(III) Complex with

the Smallest Helicene Ligand, *J. Phys. Chem. Lett.* **2020**, *11*, 1508-1515. 10.1021/acs.jpclett.9b03275

[178] A. Bowden, A. W. G. Platt, K. Singh, R. Townsend: Complexes of triphenylphosphine oxide with lanthanide bromides, *Inorg. Chim. Acta* **2010**, *363*, 243-249. 10.1016/j.ica.2009.08.016

[179] A. Bowden, A. M. J. Lees, A. W. G. Platt: Inner and outer sphere coordination of tricyclohexylphosphine oxide with lanthanide bromides, *Polyhedron* **2015**, *91*, 110-119. 10.1016/j.poly.2015.02.008

[180] O. V. Dolomanov, L. J. Bourhis, R. J. Gildea, J. A. K. Howard, H. Puschmann: OLEX2: a complete structure solution, refinement and analysis program, *J. Appl. Crystallogr.* **2009**, *42*, 339-341. 10.1107/s0021889808042726

[181] G. M. Sheldrick: SHELXT – Integrated space-group and crystal-structure determination, *Acta Crystallogr.* **2015**, *A71*, 3-8. 10.1107/S2053273314026370

# 8 APPENDIX

## 8.1 Crystallographic Data

| Compound | [DyL(H$_2$O)$_5$]CL$_3$·5H$_2$O | [DyL(NO$_3$)$_2$]NO$_3$ |
|---|---|---|
| Empirical formula | C$_{19}$H$_{37}$Cl$_3$DyN$_7$O$_9$ | C$_{19}$H$_{19}$DyN$_{10}$O$_9$ |
| Formula weight | 776.40 | 693.94 |
| Temperature/K | 150(2) | 296.15 |
| Crystal system | triclinic | triclinic |
| Space group | P-1 | P-1 |
| a/Å | 8.9853(3) | 9.2539(9) |
| b/Å | 12.6590(5) | 9.8688(10) |
| c/Å | 14.5314(5) | 13.8188(14) |
| α/° | 106.130(3) | 102.958(3) |
| β/° | 100.154(3) | 93.028(3) |
| γ/° | 96.207(3) | 93.607(3) |
| Volume/Å$^3$ | 1541.21(10) | 1224.5(2) |
| Z | 2 | 2 |
| ρcalcg/cm$^3$ | 1.673 | 1.882 |
| μ/mm$^{-1}$ | 2.739 | 3.123 |
| F(000) | 778.0 | 682.0 |
| Radiation | MoKα (λ = 0.71073) | MoKα (λ = 0.71073) |
| 2Θ range for data collection/° | 5.3 to 58.202 | 3.032 to 67.678 |
| Reflections collected | 20147 | 72304 |
| Independent reflections | 7271 [R$_{int}$ = 0.0462, R$_{sigma}$ = 0.0538] | 9844 [R$_{int}$ = 0.0341, R$_{sigma}$ = 0.0208] |
| Data/restraints/parameters | 7271/26/414 | 9844/0/360 |
| Goodness-of-fit on F$^2$ | 1.040 | 1.082 |
| Final R indexes [I>=2σ (I)] | R$_1$ = 0.0317, wR$_2$ = 0.0603 | R$_1$ = 0.0200, wR$_2$ = 0.0436 |
| Final R indexes [all data] | R$_1$ = 0.0400, wR$_2$ = 0.0648 | R$_1$ = 0.0239, wR$_2$ = 0.0453 |
| Largest diff. peak/hole / e Å$^{-3}$ | 0.81/-0.73 | 1.18/-0.85 |

| Compound | [DyL(NO$_3$)$_2$]Cl$_{0.92}$(NO$_3$)$_{0.08}$ | [DyLCl$_2$(H$_2$O)]Cl·MeOH·H$_2$O |
|---|---|---|
| Empirical formula | C$_{19}$H$_{19}$Cl$_{0.92}$DyN$_{9.08}$O$_{6.24}$ | C$_{20}$H$_{25}$Cl$_3$DyN$_7$O$_2$ |
| Formula weight | 669.51 | 664.32 |
| Temperature/K | 150.0 | 293(2) |
| Crystal system | triclinic | monoclinic |
| Space group | P-1 | P21/n |
| a/Å | 9.3609(2) | 7.6057(2) |
| b/Å | 10.0255(3) | 13.6198(2) |
| c/Å | 13.3856(4) | 22.9907(4) |
| α/° | 103.613(2) | 90 |
| β/° | 94.505(2) | 93.1530(10) |
| γ/° | 100.483(2) | 90 |
| Volume/Å$^3$ | 1190.82(6) | 2377.96(8) |
| Z | 2 | 4 |
| ρcalcg/cm$^3$ | 1.867 | 1.856 |
| μ/mm$^{-1}$ | 17.418 | 20.194 |
| F(000) | 656.0 | 1308.0 |
| Radiation | GaKα (λ = 1.34143) | CuKα (λ = 1.54184) |
| 2Θ range for data collection/° | 5.958 to 128.4 | 7.548 to 141.968 |
| Reflections collected | 14085 | 17726 |
| Independent reflections | 5806 [R$_{int}$ = 0.0227, R$_{sigma}$ = 0.0187] | 4550 [R$_{int}$ = 0.0287, R$_{sigma}$ = 0.0334] |
| Data/restraints/parameters | 5806/6/348 | 4550/3/316 |
| Goodness-of-fit on F$^2$ | 1.096 | 1.037 |
| Final R indexes [I>=2σ (I)] | R$_1$ = 0.0314, wR$_2$ = 0.0836 | R$_1$ = 0.0252, wR$_2$ = 0.0550 |
| Final R indexes [all data] | R$_1$ = 0.0320, wR$_2$ = 0.0840 | R$_1$ = 0.0324, wR$_2$ = 0.0577 |
| Largest diff. peak/hole / e Å$^{-3}$ | 1.41/-1.20 | 0.38/-0.54 |

| Compound | [DyL(NO$_3$)Cl(H$_2$O)]Cl·2MeOH | [DyL(NO$_3$)Cl$_2$]·MeOH |
|---|---|---|
| Empirical formula | C$_{21}$H$_{29}$Cl$_2$DyN$_8$O$_6$ | C$_{20}$H$_{23}$Cl$_2$DyN$_8$O$_4$ |
| Formula weight | 722.92 | 672.86 |
| Temperature/K | 293(2) | 200.00(10) |
| Crystal system | monoclinic | monoclinic |
| Space group | P21/n | P21/c |
| a/Å | 16.0852(2) | 8.9838(2) |
| b/Å | 7.53100(10) | 18.2513(2) |
| c/Å | 22.5056(3) | 15.0372(2) |
| α/° | 90 | 90 |
| β/° | 95.2760(10) | 104.5210(10) |
| γ/° | 90 | 90 |
| Volume/Å$^3$ | 2714.72(6) | 2386.83(7) |
| Z | 4 | 4 |
| ρcalcg/cm$^3$ | 1.769 | 1.872 |
| μ/mm$^{-1}$ | 16.988 | 19.204 |
| F(000) | 1436.0 | 1324.0 |
| Radiation | CuKα (λ = 1.54184) | CuKα (λ = 1.54184) |
| 2Θ range for data collection/° | 6.482 to 142.736 | 7.768 to 141.904 |
| Reflections collected | 15458 | 10511 |
| Independent reflections | 5191 [R$_{int}$ = 0.0200, R$_{sigma}$ = 0.0232] | 4492 [R$_{int}$ = 0.0206, R$_{sigma}$ = 0.0226] |
| Data/restraints/parameters | 5191/2/356 | 4492/1/330 |
| Goodness-of-fit on F$^2$ | 1.034 | 1.124 |
| Final R indexes [I>=2σ (I)] | R$_1$ = 0.0235, wR$_2$ = 0.0566 | R$_1$ = 0.0277, wR$_2$ = 0.0687 |
| Final R indexes [all data] | R$_1$ = 0.0273, wR$_2$ = 0.0593 | R$_1$ = 0.0301, wR$_2$ = 0.0701 |
| Largest diff. peak/hole / e Å$^{-3}$ | 0.57/-0.56 | 0.70/-0.37 |

| Compound | [DyL(Ac)$_2$]Cl | [Dy$_2$L$_2$(NO$_3$)$_2$O$_2$](NO$_3$)2·2MeOH |
|---|---|---|
| Empirical formula | C$_{23}$H$_{25}$ClDyN$_7$O$_4$ | C$_{40}$H$_{46}$Dy$_2$N$_{18}$O$_{16}$ |
| Formula weight | 661.45 | 1359.95 |
| Temperature/K | 180.15 | 296.15 |
| Crystal system | triclinic | triclinic |
| Space group | P-1 | P-1 |
| a/Å | 9.5957(9) | 9.8904(11) |
| b/Å | 9.8276(12) | 11.0347(13) |
| c/Å | 13.5030(15) | 13.0057(15) |
| α/° | 96.275(9) | 110.996(4) |
| β/° | 102.452(8) | 105.436(4) |
| γ/° | 97.565(9) | 98.210(4) |
| Volume/Å$^3$ | 1220.1(2) | 1231.8(2) |
| Z | 2 | 1 |
| ρcalcg/cm$^3$ | 1.801 | 1.833 |
| μ/mm$^{-1}$ | 3.217 | 3.098 |
| F(000) | 654.0 | 672.0 |
| Radiation | MoKα (λ = 0.71073) | MoKα (λ = 0.71073) |
| 2Θ range for data collection/° | 3.12 to 54.65 | 4.172 to 55.752 |
| Reflections collected | 8856 | 71600 |
| Independent reflections | 5122 [R$_{int}$ = 0.0400, R$_{sigma}$ = 0.0426] | 5855 [R$_{int}$ = 0.0341, R$_{sigma}$ = 0.0153] |
| Data/restraints/parameters | 5122/2/336 | 5855/5/363 |
| Goodness-of-fit on F$^2$ | 0.986 | 1.125 |
| Final R indexes [I>=2σ (I)] | R$_1$ = 0.0279, wR$_2$ = 0.0655 | R$_1$ = 0.0213, wR$_2$ = 0.0480 |
| Final R indexes [all data] | R$_1$ = 0.0350, wR$_2$ = 0.0675 | R$_1$ = 0.0262, wR$_2$ = 0.0520 |
| Largest diff. peak/hole / e Å$^{-3}$ | 0.80/-1.41 | 2.34/-1.22 |

| Compound | [Dy$_2$L$_2$(NO$_3$)$_2$O$_2$](NO$_3$)$_2$ 4H$_2$O | [Dy$_2$L$_2$(NO$_3$)$_2$F$_2$](NO$_3$)$_2$ 4H$_2$O |
|---|---|---|
| Empirical formula | C$_{38}$H$_{46}$Dy$_2$N$_{18}$O$_{18}$ | C$_{38}$H$_{46}$Dy$_2$F$_2$N$_{18}$O$_{16}$ |
| Formula weight | 1367.93 | 1373.93 |
| Temperature/K | 296.15 | 296.15 |
| Crystal system | monoclinic | monoclinic |
| Space group | P21 | P21 |
| a/Å | 9.5977(9) | 9.5172(6) |
| b/Å | 23.043(2) | 23.0708(15) |
| c/Å | 11.3375(11) | 11.2259(8) |
| α/° | 90 | 90 |
| β/° | 97.586(3) | 96.889(2) |
| γ/° | 90 | 90 |
| Volume/Å$^3$ | 2485.4(4) | 2447.1(3) |
| Z | 2 | 2 |
| ρcalcg/cm$^3$ | 1.828 | 1.865 |
| μ/mm$^{-1}$ | 3.074 | 3.125 |
| F(000) | 1352.0 | 1356.0 |
| Radiation | MoKα (λ = 0.71073) | MoKα (λ = 0.71073) |
| 2Θ range for data collection/° | 4.632 to 44.928 | 4.658 to 51.506 |
| Reflections collected | 33654 | 30571 |
| Independent reflections | 6472 [R$_{int}$ = 0.0868, R$_{sigma}$ = 0.0583] | 9292 [R$_{int}$ = 0.0604, R$_{sigma}$ = 0.0558] |
| Data/restraints/parameters | 6472/1/340 | 9292/831/703 |
| Goodness-of-fit on F$^2$ | 1.227 | 1.064 |
| Final R indexes [I>=2σ (I)] | R$_1$ = 0.0632, wR$_2$ = 0.1480 | R$_1$ = 0.0392, wR$_2$ = 0.0757 |
| Final R indexes [all data] | R$_1$ = 0.0742, wR$_2$ = 0.1532 | R$_1$ = 0.0527, wR$_2$ = 0.0817 |
| Largest diff. peak/hole / e Å$^{-3}$ | 2.22/-5.43 | 1.78/-2.42 |
| Flack parameter | 0.50(4) | 0.50(2) |

| Identification code | [Dy(OP(Cy)$_3$)$_3$(Br)$_3$] | [Dy(OP(Cy)$_2$(Ph))$_4$(Br)$_2$]Br·3MeOH |
|---|---|---|
| Empirical formula | C$_{54}$H$_{99}$Br$_3$DyO$_3$P$_3$ | C$_{78}$H$_{102}$Br$_3$DyO$_7$P$_4$ |
| Formula weight | 1291.47 | 1677.70 |
| Temperature/K | 200.00(10) | 199.99(10) |
| Crystal system | orthorhombic | triclinic |
| Space group | Pca2$_1$ | P-1 |
| a/Å | 28.7878(3) | 14.7590(2) |
| b/Å | 11.56140(10) | 14.7921(2) |
| c/Å | 17.9722(2) | 19.1292(2) |
| α/° | 90 | 106.2280(10) |
| β/° | 90 | 97.1950(10) |
| γ/° | 90 | 98.6860(10) |
| Volume/Å$^3$ | 5981.64(10) | 3901.66(9) |
| Z | 4 | 2 |
| ρcalcg/cm$^3$ | 1.434 | 1.428 |
| μ/mm$^{-1}$ | 10.069 | 8.090 |
| F(000) | 2652.0 | 1714.0 |
| Radiation | CuKα (λ = 1.54184) | CuKα (λ = 1.54184) |
| 2Θ range for data collection/° | 6.14 to 142.186 | 4.888 to 142.874 |
| Reflections collected | 19437 | 72540 |
| Independent reflections | 8453 [R$_{int}$ = 0.0236, R$_{sigma}$ = 0.0281] | 15005 [R$_{int}$ = 0.0225, R$_{sigma}$ = 0.0155] |
| Data/restraints/parameters | 8453/36/631 | 15005/0/845 |
| Goodness-of-fit on F$^2$ | 1.023 | 1.051 |
| Final R indexes [I>=2σ (I)] | R$_1$ = 0.0237, wR$_2$ = 0.0561 | R$_1$ = 0.0248, wR$_2$ = 0.0657 |
| Final R indexes [all data] | R$_1$ = 0.0264, wR$_2$ = 0.0581 | R$_1$ = 0.0258, wR$_2$ = 0.0664 |
| Largest diff. peak/hole / e Å$^{-3}$ | 0.48/-0.39 | 0.59/-0.49 |
| Flack parameter | -0.0079(18) | |